Cytoskeletal Remodeling in Fibrous Environments to Study Pathophysiology

Aniket Jana

Dissertation submitted to the faculty of the Virginia Polytechnic Institute and State University in partial fulfillment of the requirements for the degree of

Doctor of Philosophy

In

Mechanical Engineering

Amrinder S. Nain, Chair

Bahareh Behkam

Mark R. Paul

Timothy E. Long

Rafael V. Davalos

Date: 8.13.2021
Blacksburg, Virginia

Keywords: Extracellular Matrix, Cell-ECM interactions, Nanofibers, Cellular forces, Focal adhesions, Cell migration, Nucleus shapes, Cell division, Electroporation

Cytoskeletal Remodeling in Fibrous Environments to Study Pathophysiology

Aniket Jana

ABSTRACT

Mechanical interactions of cells with their immediately surrounding extracellular matrix (ECM) is now known to be critical in pathophysiology. For example, during cancer progression, while uncontrollable cell division leads to tumor formation, the subsequent metastatic migration of cells from the primary tumor site to distant parts of the body causes most cancer-related deaths. The metastatic journey requires cells to be able to adopt different shapes and move persistently through the highly fibrous native ECM, thereby requiring significant spatiotemporal reorganization of the cell cytoskeleton. While numerous studies performed on flat 2-dimensional culture platforms and physiological 3D gels have elucidated cytoskeletal reorganization, our understanding on how cells adapt to natural fibrous microenvironments and regulate their behavior in response to specific ECM biophysical cues including fiber size, spacing, alignment and stiffness remains in infancy. Here, we utilize the non -electrospinning Spinneret tunable engineered parameters (STEP) technique to manufacture ECM mimicking suspended fibrous matrices with precisely controlled fiber diameters, network architecture, inter-fiber spacing and structural stiffness to advance our fundamental understanding of how external cues affect cytoskeleton-based cellular forces in 3-distinct morphological processes of the cell cycle starting from division to spreading and migration. Mechanobiological insights from these studies are implemented to deliver intracellular cargo inside cells using electrical fields.

Holistically, we conclude that fibrous environments elicit multiple new cell behaviors never before reported. Specifically, our new findings include (i) design of fiber networks regulates actin networks and cell forces to sculpt nuclei in varying shapes: compressed ovals, tear drop, and invaginations, and drive the nuclear translocation of transcription factors like YAP/TAZ. In all these shapes, nuclei remain rupture-free, thus demonstrating the unique adaptability of cells to fibers, (ii) dense crosshatch networks are fertile environments for persistent 1D migration in 3D shapes of rounded nuclei and low density of actin networks, while sparse fiber networks induce 2D random migration in flattened shapes and well-defined actin stress fibers, (iii) actin retraction fiber-based stability regulates mitotic errors. Cells undergoing mitosis on single fibers exhibit significant 3D movement, and those attached to two fibers can have rotated mitotic machinery, both conditions contributing to erroneous division, and (iv) a bi-phasic force response to electroporation that coincides with actin cytoskeleton remodeling. Cells on suspended fibers can withstand higher electric field abuse, which opens opportunities to deliver cargo of varying sizes inside the cell.

Taken altogether, our findings provide new mechanobiological understanding of cell-fiber interactions at high spatiotemporal resolution impacting cell migration, division and nuclear mechanics-key behaviors in the study of pathophysiology.

Cytoskeletal Remodeling in Fibrous Environments to Study Pathophysiology

Aniket Jana

GENERAL ABSTRACT

Cancer, one of the major pathophysiological conditions, progresses within the living body through spreading of malignant cells from the primary tumor to distant secondary sites, ultimately leading to life-ending outcomes. Such spreading of cancer also known as cancer metastasis requires mechanical interactions of cells with their immediately surrounding microenvironment or the extracellular matrix (ECM). Cells utilize their cytoskeleton, a dynamic internal network of filamentous proteins, to adopt various morphologies, exert mechanical forces and physically remodel their local environment as they navigate through the highly fibrous native ECM. While previous research has elucidated how biochemical factors and bulk matrix properties regulate such cytoskeletal organization and single cell behavior, our understanding of how cells adapt to fibrous environments and respond to local biophysical cues like fiber diameter, spacing, alignment and stiffness remains in infancy. Here we use the non -electrospinning Spinneret tunable engineered parameters (STEP) to generate suspended nanofiber networks of tunable geometric and mechanical properties to mimic the native cellular environment. We discover that cells elongated within these ECM-mimicking environments utilize a unique cytoskeletal caging structure to regulate the shape and response of their nuclei in a fiber -diameter and organization-dependent manner. Additionally, we demonstrate that these elongated cell morphologies often observed during metastatic cancer cell movements, is achievable not only in aligned

fibers but can also be induced by dense networks of fibers in a crossing organization. Specifically, such dense crosshatch networks allow cells to migrate persistently at high speeds while cells on sparsely spaced networks demonstrate slower and random movements. As cells elongated during interphase rounded up to undergo division, we find that the underlying fiber-geometry modulates mitotic dynamics through differential levels of actin retraction fiber-mediated stability, leading to significant alterations in orientation of mitotic machinery and mitotic spindle defects. Finally, we utilize these mechanobiological insights on cytoskeletal organization and cell shape control to optimize intracellular delivery of cargo using high-voltage electric fields. We demonstrate suspended cells are capable of withstanding higher electric fields and identify multistage cell contractility recovery dynamics, which correlate with cytoskeletal disruption and reassembly. Taken altogether, our findings provide a comprehensive understanding of the fibrous ECM-mediated regulation of the cytoskeletal organization and its impact in cell migration, division and nuclear mechanics. Knowledge obtained from this study will improve our understanding of cancer metastasis and provide predictive data for *in vivo* cellular response, essential for cytoskeleton-targeting cancer therapies.

Dedicated to my family and friends

Acknowledgement

I am greatly indebted to a number of individuals for their invaluable support during my time at Virginia Tech. I would like to take this opportunity to express my immense gratitude to all of them.

First and foremost, I would like to thank my advisor Dr. Amrinder Nain for his expert guidance and introducing me to exciting research avenues throughout my PhD journey. He has always motivated me to think creatively, work hard and pursue innovative ideas. When I first came to Virginia Tech, I had very limited experience with experimental research and I am very grateful to Dr. Nain for his patience and guiding me to acquire various interdisciplinary research skills. His words of encouragement and constant support have helped me tread through crucial times during my graduate journey. His lessons on scientific writing, professionalism and constructive criticism of my work have contributed immensely in my growth as a researcher. I will always value his mentorship and guidance.

I thank Dr. Behkam, Dr. Davalos, Dr. Long and Dr. Paul for kindly agreeing to serve on my PhD committee and providing valuable feedback on my work. I am really grateful to Dr. Davalos for enabling a very exciting and fruitful research collaboration on cell mechanics and electroporation. It has been a great learning experience for me and has expanded my knowledge domain. I am also grateful to Dr. Behkam for her guidance during our collaborative work on cell migration. I also thank my collaborators Dr. Konstantinos Konstantopoulos, Dr. Rakesh Kapania, Dr. Emil Lou, Dr. Aime Franco, Dr. Jennifer DeLuca and Dr. Nir Gov.

I have been very fortunate to work with some very helpful and supportive colleagues during my time at Virginia Tech. I would like to really thank my fellow labmates over the years: Abinash, Appy, Puja, Jugroop, Daniel, Christian, Sharan, Aldwin, Christopher, Matt, Mason, Jake, Eric, Lauren, Hajar, Irene, Zhou and Ying from both STEP and MicroN BASE labs. I am really grateful to Puja for being an amazing mentor and friend, and teaching me about the various intricacies of biological research. I would like to also thank Philip, and Edward from Bioelectromechanical Systems Lab for their various collaborative efforts. It has been my great pleasure working with all of you. I am especially grateful to two colleagues, Abinash and Appy, who have also been my close friends and roommates. Life in Blacksburg would not have been the same without their companionship and support throughout the ups and downs of this journey. I also want to thank many others in Blacksburg, Saikat, Harsh, Saurav, Arka, Kartik, Anshul, Shantanab, Arit, Ranit, Arnab, Abhijit, Saurabh for being amazing and supportive friends. I am really grateful to Debkalpa for being a constant source of guidance in my academic journey.

Before my time at Virginia Tech, I was very fortunate to be exposed to the field of scientific research and I am really thankful to my early mentors, Dr. Debasis Barman, Dr. Sushanta Kumar Panda and Dr. Prashanta Kumar Das, for their guidance and constantly encouraging me to pursue an academic career.

Finally, I am extremely thankful to my parents, Kartik and Trishna and my sister Arnwesha, for their unconditional love and support throughout all these years. My PhD journey would not have been possible without the countless sacrifices of my parents and while words of gratitude will not justify their immense contribution, I am blessed to have their relentless support and encouragement in my life. I thank them for everything.

Attribution

Chapter 3:

Avery Tran (PhD student, Department of Chemical and Biomolecular Engineering, Johns Hopkins University, United States) generated C2C12 and HT1080 cell lines with lamin A/C knockdown and NLS mCherry expression, performed YAP imaging experiments with HT1080 cells and helped with some of the intensity analysis.

Amritpal Gill (MS student, Department of Mechanical Engineering, Virginia Tech, United States) designed setup for delivery of cell suspension droplets and performed some of the cell spreading/force generation experiments

Chapter 4: Published in *FASEB Journal* (2019)

Intawat Nookaew (Postdoctoral researcher in the lab of Dr. Aime Franco, Department of Physiology and Biophysics, College of Medicine, University of Arkansas for Medical Sciences, Little Rock, Arkansas, United States) is a co-author on the paper and conducted the gene expression analysis.

Jugroop Singh (MS student, Department of Biomedical Engineering and Mechanics, Virginia Tech, United States) is a co-author on the paper and performed some of the cell migration experiments with 3T3 fibroblasts and helped with the migration analysis.

Chapter 5:

Haonan Zhang (MS student, Department of Mechanical Engineering, Virginia Tech, United States) performed some of the long-term and high-speed short-term imaging of the cell division events and helped with the analysis of the division dynamics.

Dr. Nir Gov (Professor, Department of Chemical and Biological Physics, Weizmann Institute of Science, Israel) formulated the predictive models for metaphase plate RMS angular speed as a function of retraction fiber coverage

Chapter 6: Published in *ACS Nano* (2020)

Philip Graybill (PhD student, Department of Mechanical Engineering, Virginia Tech, United States) is an equally-contributing co-first author on the paper and designed and generated the microfluidic devices for electroporation of single cells on the fiber scaffolds, conducted cell-culturing experiments in integrated nanofiber-microfluidic devices and formulated the finite element models in COMSOL. Aniket Jana is an equally-contributing co-first author on the paper and worked on the fabrication of fiber scaffolds, immunofluorescent staining, confocal imaging, membrane bleb analysis and characterization of propidium iodide entry dynamics. Both authors worked together on rest of the experiments, analysis and manuscript preparation.

Table of Contents

List of Abbreviations

ECM: Extracellular matrix

FA: Focal adhesion

SF: Stress fiber

TACS: Tumor associated collagen signature

ANOVA: Analysis of Variance

nN: Nanonewton

PS: Polystyrene

PU: Polyurethane

DMEM: Dulbecco's Modified Eagle's Medium

FBS: Fetal Bovine Serum

FCS: Fetal Calf Serum

YAP: Yes-associated protein

NLS: Nuclear localization sequence

MSD: Mean squared displacement

PRW: Persistent Random Walk

RF: Retraction fibers

MP: Metaphase plate

AR: Aspect Ratio

EP: electroporation

List of Figures

cells (n=49, 40, 36 and 20 for *dense, intermediate, wide* networks and *flat 2D* respectively) for the different substrates, and (iv) polar plots showing angular displacements for cells on varying fiber network porosities and compared with flat 2D (n=40, 40, 20 and 20 for *dense, intermediate, wide* networks and *flat 2D* respectively). Data demonstrates cells moving fastest and with highest persistence on *dense* crosshatch pattern of fibers. **b**) Representative displacement profiles of the leading and trailing edge for the different fiber network categories. Leading and trailing edges are shown in red squares and blue circles respectively in associated time-lapse images (scale bars denote 20 μm and time shown in minutes). **c)** (i) Recoil-to-recoil analysis method to calculate *migration cycle* time, (ii) *migration cycle* time over the different fiber network categories (n=29,50 and 25 for *dense, intermediate, and wide* networks respectively). Note for the *dense* group, data is only shown for 6 μm fiber spacing, as the recoil-to-recoil migration cycle for the 3 μm fiber spacing was not discernable optically, and (iii) migration cycle and retraction *recoil* speeds plotted as function of FAC length showing both metrics to linearly scale with FAC lengths. Inset image shows a fluorescently-labeled cell attached to a 54 μm inter-fiber spacing network and the magnified image of retracting edge showing f-actin stress fiber distribution (red: f-actin stress fiber, blue-nucleus and green: paxillin. Scale bar: 20 μm). Statistical differences between individual inter-fiber spacing categories are superimposed on the data for their respective groups.....**80**

Figure 4.4. **Inter-fiber spacing regulates nucleus dynamics: a)** Representative profile of the deformation of nucleus during retraction of a trailing edge demonstrating rounded nucleus is strained to elongated shape, and after recoil the nucleus relaxes to its original shape. Axis strain is defined as $\varepsilon = \frac{L_i - L(t)}{L_i}$,where L_i is the minor axis length of the nucleus *pre-recoil* and L(t) represents the minor axis length of the nucleus at time t *post-recoil* (Scale bars represent 20 μm). At start of relaxation post-recoil (t=0), minor axis L(t)= L_O. **b)** Normalized nucleus shape recovery data (defined as $\frac{\varepsilon}{\varepsilon_0}$ where $\varepsilon = \frac{L_i - L(t)}{L_i}$ and $\varepsilon_0 = \frac{L_i - L_0}{L_i}$ is the initial nucleus axis strain immediately post-recoil with exponential fits showing that cells on dense networks recover their original shape faster after recoil. Inset shows representative images of the nucleus post recoil and after relaxation (rounded is for *wide* and elongated for *dense* networks). **c)** Relaxation time constants calculated on basis of an exponential decay of nucleus deformation showing stronger recoil in *intermediate* and *wide* networks. Percentage change in nucleus shape (eccentricity (**d**)) and size (projected area (**e**)) during trailing edge recoil. **f)** Nucleus height measured by confocal microscopy quantitates cell nuclei to be thicker in dense regions. Inset shows representative images of nucleus (projected side view from confocal microscopy, scale bar 5 μm). **g)** Nucleus thickness decreases with increase in cell spread area. **h)** Representative temporal plots of nucleus-cell body angular coupling (*included angle*) for the different inter-fiber spacing with inset illustration showing the *included-angle* is defined by the coordination between cell body vector (trailing edge to centroid shown by white star) and nucleus major axis. **i)** Data shows the influence of cell shape (aspect ratio) on the extent of nucleus-cell body coordination. For (**g**) and (**i**) exponential fit to data corresponding to fiber networks with flat 2D data shown as reference. Sample size for b, c, d and e (n=11, 23 and 10: *dense, intermediate* and *wide* networks respectively) for f, g (n=25, 32, 14 & 13: *dense, intermediate, wide* and *flat 2D* respectively) and for i (n=13, 15, 9, 9: *dense, intermediate,*

List of Tables

Chapter 1: Overview

1.1 Examining cell-fiber interactions to understand biological behavior *in vivo*

Cells continuously interact with their surrounding microenvironment, the extracellular matrix (ECM) to gather a diverse range of biochemical and biophysical cues, which are key in their decision-making and ultimate fate during various physiological processes including cell migration, proliferation, differentiation and tissue morphogenesis. Integrin-mediated multiprotein complexes known as focal adhesions, physically connect the ECM to the cell cytoskeleton, allowing cells to exert traction forces and transmit mechanical signals to the nucleus to activate biochemical signaling cascades, through a process commonly referred to as mechanotransduction. While extensive research over the past few decades have demonstrated that mechanical cues are crucial for cell fate determination, our knowledge of such regulation stems from studies performed on 2D tissue culture platforms, which does not adequately recapitulate the *in vivo* setting, where cells are suspended within a three-dimensional matrix. The natural ECM is highly fibrous in nature, comprised primarily of collagen fibrils and bundled fibers of varying diameters, stiffnesses and organized in diverse architectures. *In vivo* cells can utilize various geometric and mechanical cues like fiber diameter, inter-fiber spacing, fiber alignment, network pore sizes and stiffness to regulate their shape and function accordingly. Thus, a detailed investigation of cell-fiber interactions is key to a more holistic understanding pathophysiological phenomenon like cancer metastasis, and can potentially lead to development of novel therapeutic strategies. Our current knowledge of such interactions and the mechanistic effects of individual ECM factors remains highly limited due to

inherent challenges in repeatable manufacturing of fibrous scaffolds *in vitro* with consistent physical properties.

1.2 Research objectives

In this study, we have regularly used the previously reported non-electrospinning Spinneret based Tunable Engineered Parameters (STEP) technique to manufacture suspended networks of nanofibers with a wide range of fiber diameters, inter-fiber spacing, network architecture and structural stiffness, to mimic essential aspects of the native fibrous ECM. Compared to traditional fiber manufacturing techniques like electrospinning, the STEP technique allows precise control on the fiber geometry and mechanical properties and enables systematic investigation of the role of individual fiber parameters in regulating single cell behavior.

The overarching goal of this thesis is to understand the effect of the cellular microenvironment towards the regulation of cytoskeletal organization and response during distinct morphological stages of the cell cycle: division, spreading and migration. Here, we report for the first time that during interphase, cells spreading on aligned and suspended fibrous microenvironments regulate their nuclear morphologies and response via a unique cytoskeletal caging structure, in a fiber diameter, number density and stiffness-dependent manner. Next, we show how dense networks of crossing fibers can induce 3D elongated cellular morphologies with thicker nuclei and a high degree of persistent cell movements, while sparse crosshatch networks caused spread cell shapes with well-developed actin stress fibers and 2D diffusive random-walk based migration. Fiber-geometry mediated control over cell-ECM adhesions during interphase enable for generation of different spatial organization and density of retraction fibers during the rounded mitotic phase and

demonstrate alterations in division dynamics in response to ECM biophysical cues like fiber density and mechanical confinement. Finally, we explored how elongated cells spread on suspended fibers responded to high-voltage external electric fields (relevant in cancer therapeutics), and reported for the first time, multistage mechanical force recovery dynamics, correlating with cytoskeletal disruption and reassembly and geometric orientation-dependent cell viability.

1.3 Organization of the document

This document provides a comprehensive outline of the single cell mechanobiology studies performed using STEP fiber networks. Chapter 2 present a detailed background on the central roles of the cell cytoskeleton and the extracellular matrix (ECM) in driving fundamental cellular processes including cell division, migration, force generation, nuclear shape control and thereby presents the case for a crucial need for investigation of cell-ECM interactions in physiologically relevant fibrous microenvironments. Chapter 3 describes the temporal dynamics of cells spreading in anisotropic shapes within these aligned fiber matrices and reports how the cytoskeletal organization unique to suspended fibrous microenvironments, regulate nuclear shape and response in a fiber curvature, density and stiffness-dependent manner. Chapter 4 extends these findings on elongated cell and nuclear shapes, by describing a previously unreported phenomenon where cells can adopt anisotropic 3D shapes and migrate persistently at high speeds in very dense bidirectional networks of crossing fibers. Chapter 5 utilizes such diverse cell shapes achieved during interphase and describes how cell division dynamics are modulated by the underlying fiber geometry through altered organization of retraction fiber-mediated cell-ECM connections. Chapter 6 explores the previously unreported effect of external electrical cues (specifically

high-voltage, short duration pulsed electric fields used for electroporation-based applications) towards the cytoskeletal and mechanical force response of single cells elongated along suspended fibers. Chapter 7 summarizes the potential impact of our findings and introduces several future research directions.

Chapter 2: Introduction

2.1 Cell-Extracellular matrix interactions in health and disease progression

Cells continually interact with their immediately surrounding microenvironment, the extracellular matrix (ECM) to sense and integrate various biophysical and biochemical cues which are crucial for regulation of fundamental physiological processes like tissue development, homeostasis, wound healing and pathological conditions like cancer[1–3]. Particularly during cancer progression, malignant epithelial cells lose their normal cell-cell junctions and undergo the epithelial-mesenchymal transition (EMT) to achieve mesenchymal phenotypes, featuring anisotropic cell shapes and a high propensity for directed locomotion[4–6]. Cells use their cytoskeletal machinery to dissociate from the site of the primary tumor and migrate through the three-dimensional extracellular matrix, to distant parts of the body leading to tumor cell invasion. In fact tumor metastasis is responsible for 90% of the cancer-related deaths(several hundred thousands) in the U.S.[7,8] Extensive research over the past few decades have described the biophysical nature of the cancer metastatic process, and have demonstrated how mechanobiological principles can be employed in model *in vitro* systems to elucidate impact of the native extracellular matrix towards cancer progression[9]. Thus, detailed characterization of the role of various microenvironmental factors in regulation of mechanical cell behaviors like cytoskeletal dynamics, cell adhesion, force generation, migration and division, is key to advancing clinical knowledge on cancer progression.

2.2 Cell-ECM adhesions and the cytoskeleton

Mechanical interactions of cells with their local microenvironment occur primarily through integrin-mediated adhesions which act as bidirectional links between the cell cytoskeleton

and the extracellular matrix and thereby enable the force transmission between them[10]. The cytoskeleton is a complex inter-connected network of filamentous proteins, which provides essential structure and geometric shape to cells and a key determinant of physical cell function. It consists of 3 major filamentous elements, actin microfilaments, microtubules and intermediate filaments. While the different cytoskeletal elements are structurally and functionally different, they are all generated from repeated subunits and can dynamically change in size by active assembly/disassembly of their subunits. Cell contractility arises primarily from the action of the motor protein myosin II which forms oligomeric complexes along overlapping actin filaments leading to their antiparallel motion and subsequently generates cytoskeletal tension[11–13]. Extracellular transmission of such cytoskeletal contraction through cell-matrix adhesions leads to generation of cellular traction forces. Such contractile force exertion leads to extensive deformation and remodeling of the surrounding ECM and facilitates rapid movement of the cell body during cancer metastasis.

While the actin cytoskeleton is directly connected to the cell membrane and the external environment through various adhesion complexes, it is also linked to the cell nucleus via the linker of nucleoskeleton and cytoskeleton (LINC) complex, composed of the SUN (Sad1p, UNC-84) domain and the KASH (Klarsicht/ANC-1/Syne Homolog) domain proteins[14,15]. Such nuclear-cytoskeletal connections allows for proper spatial positioning of the nucleus within the cell during directed migration and enables transfer of mechanical forces and extracellular signals into the nucleus, leading to activation of molecular signaling pathways and alterations in cellular response, through a process commonly referred to as mechanotransduction[16–18]. Such ability of cells to sense and respond to

mechanical cues is highly important in cancer metastasis and is also a key determinant of cell fate and function during other physiological processes like cell differentiation, proliferation and death. Mechanotransduction is primarily driven by a complex interplay between the cell-ECM adhesions, cell cytoskeleton and mechanical forces within the local microenvironment. Thus, proper understanding of these different factors is key to understanding biochemical alterations within cells in response to mechanical signals during cancer progression.

2.3 Cytoskeletal reorganization during key morphological stages of the cell cycle

The cytoskeletal architecture and the cell-ECM adhesions are highly dynamic and constantly remodeled during the cell cycle, a complex and fundamental process, through which all cells grow and proliferate. While biochemical regulation of the cell cycle is well understood, it is increasingly becoming clear that mechanical cues for the local microenvironment plays a crucial role as well[19,20]. Morphologically, the cell cycle can be subdivided into interphase and various stages of the M (mitotic) phase. Particularly, during interphase, cells can undergo spreading to transform from a rounded state to a flattened contractile morphology and start migrating in polarized shapes. Dynamic remodeling of the cytoskeleton at the onset of mitosis leads to loss of such cell shapes and return of the rounded morphologies. In each of these morphologies, cells remain connected and can interact with their ECM through various cytoskeleton-mediated connections.

2.3.1 Cell spreading leads to contractility generation during interphase

Adherent cells establish their cytoskeletal contractility by transforming to a well-spread state upon contact with an adhesive microenvironment, through a process commonly referred to as cell spreading. The process of cell spreading[21] encompasses several important

events, which are instrumental for force generation, cell migration, and mechanotransduction. At very early stages of the spreading process, cells interact with the local ECM, via the integrin family of transmembrane receptors, which can bind directly to the ECM ligands like fibronectin. Shortly afterwards, integrins bind with the actin cytoskeleton via the adhesion protein talin[22]. As the cells spread further utilizing actin-rich protrusions, an inward movement of the actin cytoskeleton occurs from the leading edge of the cell towards the cell center. This generates tugging forces on the nascent integrin-matrix adhesions, which based on the ECM stiffness, can either lead to integrin unbinding from the matrix, or lead to recruitment of various adhesion proteins[23] like paxillin, vinculin, FAK, to the nascent adhesion sites leading to their maturation into larger (few μm in length) polarized adhesions, also referred to as focal adhesions[10] (FAs). As the focal adhesions mature, concomitantly actin polymerization leads to the generation of actin filaments. Bundles of such filaments crosslinked primarily by α-actinin lead to formation of actin stress fibers[24] (SFs). These stress fibers act in conjunction with the myosin II motors to exert significant traction forces[25] on the matrix and thus constitute the contractile machinery of cells.

2.3.2 Actin stress-fiber mediated cell contractility guides cell migration

Cell migration is a fundamental cellular function which is crucial for various physiological processes including tissue morphogenesis, wound healing and in pathological conditions such as cancer metastasis. During metastatic invasion epithelial cells undergo EMT (epithelial-mesenchymal transition) to escape from the site of the primary tumor and move to distant parts of the body.

While the nature of cell migration vary significantly depending on the cell type and ECM dimensionality, one of the most widely studied is the mesenchymal cell migration particularly on 2D substrates. Mesenchymal migration is a multi-step process which involves extensive mechanical interactions with the underlying extracellular matrix (ECM). To achieve migration, well-spread cells first need to establish a front-rear polarity axis, which will subsequently determine the direction and persistence of cell movements. Such polarized cell shapes typically feature a broad leading edge and a narrow trailing edge. Next, cells advance their leading edge by putting out thin actin–rich membrane protrusions of lamellopodial or filopodial origins, stimulated primarily by the Rho- family GTPases, particularly RAC1 and CDC42. Leading edge protrusions form integrin-based nascent adhesions which mature into larger focal adhesions in response to local transmission of mechanical forces between the cytoskeleton and the extracellular matrix. Formation of such new adhesions increases contractility within the actin stress fibers, while concomitantly a rapid turnover of focal adhesions happens at the rear end through protease activity. Increased actomyosin contractility mediated by RhoA, combined with such FA breakdown ultimately leads to an active retraction of the trailing end of the cell, causing a net cell movement. This cycle of protrusion-adhesion and contraction keeps repeating over time, thereby enabling cells to migrate.

2.3.3. Cell-ECM connections through retraction fibers during cell division

Cell division constitutes a fundamental cellular function, which allows cells to replicate their DNA content and divide into daughter cells. Thus, cell division is key to development of all living tissues and organs and is essential to propagation of life. Additionally, it is also crucial in the context of pathophysiological conditions like cancer, since tumor

formation and development can be largely attributed to uncontrolled division of malignantly transformed cells.

Cell division occurs during the M-phase (mitosis) of the cell cycle and is a highly regulated process which requires precise reorganization and co-ordination of the actin and microtubule cytoskeletons. Entry of mitosis is characterized by drastic changes in cell shape. Particularly, cells lose their spread shapes (during interphase) and round up through an almost complete loss of the classical cell-ECM adhesions and an extensive remodeling of their actomyosin cytoskeleton from a primarily stress-fiber based organization to a cortical localization[26–28]. Internally, within the cell, the mitotic process starts with the directed movement of duplicated centrosomes on either side of the nuclear envelope during prophase. This is followed by the dissolution of the nuclear envelope, also known as the nuclear envelope breakdown (NEBD) during the onset of prometaphase. NEBD enables spindle microtubules to connect to the newly released chromosomes through kinetochore-mediated attachments, and shift them to an equatorial region within the cell to form a condensed plate-like structure. During metaphase, formation of this integrated microtubule-chromosome structure also known as the mitotic spindle is complete, with pairs of sister chromatids situated on the spindle equator directed towards opposite spindle poles. The geometric positioning of the mitotic spindle determines the division axis orientation and subsequent daughter-cell positioning and fate, and thus is of central importance in tissue development and in tumor growth. The next stage or anaphase initiates the segregation of sister chromatids, leading to an increase in separation between the spindle poles. During the latter part of anaphase, an actomyosin-based contractile ring causes a cleavage furrow within the actin cortex. Progressive contraction of this contractile

ring during telophase and cytokinesis, ultimately leads to the formation of daughter cells with segregated DNA.

While environmental cues like soluble factors are known to regulate the mitotic progression, the impact of mechanical cues in determining cell division dynamics remains poorly understood. It is now well known that rounded mitotic cells remain connected to their underlying ECM through thin actin-rich membrane extensions, also known as retraction fibers (RFs). These actin-based RFs emerge from the sites of interphase adhesions and thereby provide essential guidance cues during daughter cell spreading. Recent studies indicate that retraction fibers are mechanically linked to the astral microtubules of the mitotic spindle through a 'cortical mechanosensory complex' which comprises of several key players including active integrins, MISP (Mitotic interactor and substrate of PLK1), caveolin, and few other adhesion complex proteins[29–31].

While a huge body of previously reported studies have elucidated the different mechanisms of spreading, migration and division, it is be noted that they are mostly based on flat 2D cultures or 2D adhesive micropatterns which do not recapitulate the fibrous nature of the native extracellular matrix.

2.4 Biophysical cues within the native extracellular matrix

The native extra-cellular matrix[32,33] (ECM) is a complex 3-dimensional fibrous biopolymer network, enclosed in a viscous macromolecular gel, and forms the immediate microenvironment of living cells. Apart from providing an essential physical substrate for anchorage the embedded cells, the native ECM provides a range of biophysical cues which guides cell adhesions, spreading, mechanical force generation, migration and division. Although the composition of the ECM varies in different regions of the living body, it is

composed primarily of fibrous proteins[34] like collagens, elastin, laminins, fibronectin and hydrophilic and acidic components like proteoglycans (PGs) and glycosaminoglycans (GAGs), which are capable of sequestering water and forming a viscous gel around the fibrous network. Furthermore, based on the network structure and specific composition, natural ECMs are broadly classified into 2 categories: the fibrous connective interstitial matrices[35] and the densely packed pericellular matrices, chief among which being the basement membrane. In the context of fibrous ECM, the major contributing proteins are the fibrillary collagens and elastin. The major varieties of the fibrillar collagens include collagen types I, II, III, V, XII, XXIV, and XXVII. Among them collagen type I and III are expressed most abundantly in various living tissues. Within the ECM, both collagen and elastin exist either as fibrils or fibers, composed of multiple repeats of their structural units ,tropocollagen[36] and tropoelastin, respectively. *In vivo* imaging of native fibrous ECM using second harmonic generation[37] (SHG), third harmonic generation[38] (THG), multiphoton microscopy[39], and electron microscopy has revealed a complex hierarchical network of fibers ,which is comprised of individual fibers (30–70 nm diameter) that can form bundles (100 nm-few microns in diameter)[35,37,40].

ECM fiber type	**Diameter**	**Elastic Modulus**
Collagen fibers	30-100 nm for fibrils ,1-20 µm for fibers/fiber bundles	1.2 GPa for mammalian tendon collagen, 100-360 MPa for rat tail collagen type I fibers
Elastin fibers	100-200 nm for fibrils ,0.3-2 µm for fibers/fiber bundles	~0.2-1 MPa[41] , depending on ECM type
Reticular fibers	20-40 nm fibrils made of collagen mostly	N/A
Fibronectin fibers	10-1000 nm	~1 MPa

Table 2.1: Physical dimensions and mechanical properties of commonly observed ECM fibers, Adapted from Mukherjee, Jana et al.,[42] 2017

While the fibrous nature of the native ECM guides various physiological processes like wound healing and tissue development, it is of central importance in driving cancer progression. The cancer-associated extracellular matrix commonly referred to as the tumor stroma is a highly dynamic microenvironment, which can consist of both dense and loose packing of collagen fibers, featuring differential levels of fibrillar alignment and stiffness. Formation of a dense fibrocollagenous stroma surrounding the tumor, also known as desmoplasia[43], constitutes one of the major features of several invasive carcinomas including breast cancer and is implicated in the initiation and guiding of tumor cell invasion. Recent advancements in second harmonic generation (SHG) and multiphoton microscopy have revealed how constant remodeling of the tumor ECM through actomyosin-mediated cell contractility leads to increased linearization and a radial alignment of the collagen fibers perpendicular to the tumor boundary, thereby enabling the preferential migration of cancer cells along the aligned ECM regions. Such extensive reorganization of collagen fibers is best characterized in the case of breast carcinoma, and is widely referred to as the tumor associated collagen signatures (TACS)[44,45]. Detailed characterization through SHG microscopy has revealed that TACS progresses through 3 major stages. First there is a significant (3-fold) enhancement in collagen content in the regions surrounding the tumor, leading to a highly dense network of randomly oriented collagen fibers, which constitutes TACS1. During the next stage i.e. TACS2, collagen fibers get significantly taut in nature and organize along the tumor boundary. The final stage or TACS3 involves the radial alignment of these taut collagen fibers orthogonal to

the tumor boundary, enabling local invasion of the tumor cells. It is now well appreciated that collagen fiber alignment constitutes one of major markers of invasive tumor cell phenotypes and correlates with poor survival rates in cancer patients.

Intravital (SHG/THG) imaging of the native ECM within various tissues have revealed various details on the organization of collagen fibers. For example, pore sizes within the ECM fiber network are > 100 μm^2 for the loose connective tissues, it is ~ 30-70 μm^2 for loose-medium density ECM and it can go < 1 μm^2 in the spaces between densely packed collagen bundles[46]. Such highly dense fibrous environments can be often observed within the collagen-rich stroma and the packed basement membrane. Intravital characterization of the native collagen rich interstitial ECM by the Friedl group has revealed aligned spaces of the collagen fiber networks with average widths of ~ 10-15 μm[47]. Cells adhering and moving along such networks can interact with single fibers, representing 1D migration or can interact with multiple fibers leading to 3D cell migration.

In summary, the native extracellular matrix, particularly in the context of cancer, is a highly fibrous matrix consisting of fibers with diverse geometric dimensions, mechanical properties and network organization (aligned and crossing), all of which can affect the behavior of interacting cells. Therefore, *in vitro* models mimicking the ECM need to account for both the elastic modulus (N/m^2) of the whole network and the structural stiffness (N/m) of individual ECM fibrils of varying diameters.

2.5 Platforms to study cellular interactions with their microenvironment

Over the years, the most widely substrate for understanding cell-matrix interactions are the flat 2D coverslips made out of glass or plastic. Although these substrates are quite easy to implement in cell culture studies, their lack of any distinct features combined with their

bulk stiffness being several times higher than any normal tissue stiffness, make them quite irrelevant as ECM-mimicking substrates. In their seminal paper, Pelham and Wang[48], demonstrated how stiffness of 2D polyacrylamide gels, can significantly modulate extent of cell spreading and nature of cell migration. Since then, various studies have demonstrated the role of substrate stiffness in regulating cell spreading, cytoskeletal and focal adhesion organization and cell migration. It is to be noted that while these substrates can be used to understand the role of stiffness, they are still 2D featureless in nature. To incorporate aligned features, studies have been performed on micropatterned lines, microgrooves and microchannels, which mechanically confine the cells in 1D morphologies. Although such substrates demonstrate the importance of alignment in guiding cell behavior, they are still unable to recapitulate essential features of the mostly fibrous native ECM. In order to generate nanofibrous environments *in vitro*, a number of fiber manufacturing techniques has been put forward. Out of these various reported techniques, ***electrospinning***[49] is arguably the most widely used method, which allows for the continuous production of fibers, ranging from tens of nanometer to a few microns in diameter. In this process, polymer solution is pumped through a syringe to a needle, where a high electrical voltage (few kV) extrudes polymeric fibers onto a collecting target to form nonwoven fiber mats. Such electrospun fiber networks have been widely used to study cell-fiber interactions in the context of developmental biology, specifically investigating the morphology, proliferation, and differentiation of a variety of cell types and, in more recent years, as novel *in vitro* substrates to mimic the *in vivo* migratory behavior of tumor cells. In 2014, Nelson et al.[50] demonstrated, using aligned and random electrospun fiber architectures, how fiber alignment can have a significant impact on the motility of the

human breast cancer cells (MCF-7, MCF-10A, and MDA-MB-231). Compared to the conventional featureless flat 2D substrates and even randomly oriented fiber networks, cells on aligned fiber architectures demonstrated a significantly higher degree of cell alignment, elongation, and a multifold increase (2-5 times) in the migration rate. Using aligned electrospun nanofibers, Rao et al.[51] demonstrated that OSU-2 (glioblastoma multiforme) cells adopted elongated morphologies on these aligned nanofibers and furthermore the stiffness of the nanofibers induced alterations in the migration rate and focal adhesion dynamics of the cells. In another similar study by Beliveau et al.[52], migration of U87MG (glioblastoma multiforme) tumor cells was investigated on aligned and random fiber networks, and it was observed that aligned topography of the electrospun fibers leads to elongated spindle-shaped cells, featuring well-directed and elongated focal adhesions.

2.6 The STEP technique for ECM-mimicking fibrous environments

Although the electrospun fiber networks have been extensively used to investigate the influence of fibrous topographies on cell morphology, proliferation, growth, differentiation and cell migration, studying cell-fiber interactions at single and collective cell level with high spatiotemporal resolution, in a repeatable manner is quite challenging due to manufacturing challenges associated with controlling fiber diameter, spacing and degree of alignment. In this regard, Spinneret based Tunable Engineered Parameters (STEP) technique pioneered by Nain et al.[53] offers an alternative method for developing highly aligned, tunable, repeatable nanofiber networks for studying cell-fiber interactions. A major factor behind such precise control is due to the fact, that the STEP technique does not require the use of an electric source in fiber fabrication process; rather it relies on a physical pull of a single fiber filament from the extruded droplet from a spinneret.

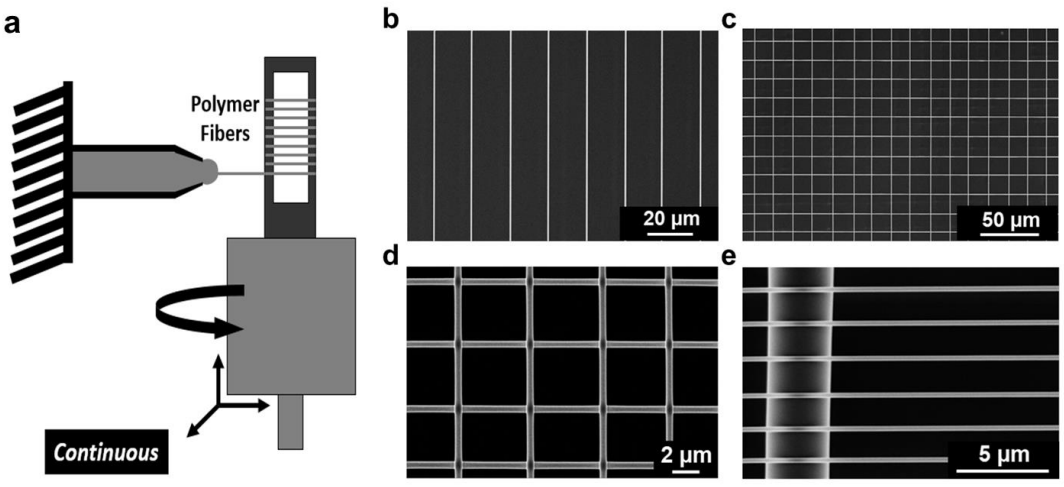

Figure 2.1: The STEP technique for fiber manufacturing, a) Schematic showing fibers pulled from polymer solution droplets, adapted from Mukherjee,Jana et al.,2017 **b)** FESEM images of highly Parallel array of ~ 500 nm diameter PS fibers **c)** Crosshatch network with 18 µm unit cell size **d)** Unit cell size called down to 6 µm, without loss of regularity **e)** 350 nm diameter fibers with a 2 µm inter-fiber spacing deposited on a 3 µm fiber

Typically, polymer solution is pumped through a spinneret (probe) and forms a solution droplet at the probe tip. A rotating substrate contacts the droplet and pulls out solution filaments, which after solvent evaporation and solidification are collected on the substrate in parallel configurations at a desired inter-fiber spacing. By depositing fibers on top of each other in multiple layers, hierarchical assemblies of fiber networks with tunable unit cell dimensions can be generated. Another distinctive feature of the STEP technique, is that the fabricated nanofiber networks can be deposited on hollow substrates, thus making them suspended and more in line with the native ECM. Due to the suspended nature of these nanofibers cells can react to structural features like curvature, topography and structural stiffness (N/m) and changes in these individual fiber properties have the potential to induce significant changes in individual cell response, as quantified by various metrics like cytoskeletal organization, focal adhesion distribution[54], migration rate[55] and nuclear shape index[54].

2.7 Summary and objectives

The native fibrous extracellular matrix provides diverse geometric and mechanical cues which are sensed and transduced by cells to regulate their behavior during various physiological processes like tissue development, wound healing and pathological conditions like cancer metastasis. During cancer metastasis, the ECM gets significantly reorganized near the tumor interface to become highly aligned collagen fiber tracts, which enable directed cell migration in anisotropic shapes. Along their metastatic journey, cells can encounter a diverse range of ECM fiber architectures (including both aligned and crossing fiber arrangements), fiber density, individual fiber sizes and stiffness. While previous studies performed on extracellular regulation of single cell behavior have mostly focused on the role of bulk ECM properties like substrate stiffness, our current understanding of cellular adaptability to such fibrous microenvironments still remains unclear. The STEP technique allows for manufacturing of ECM-mimicking fibrous matrices with tunable geometric (fiber curvature, inter-fiber spacing, network architecture) and mechanical properties (stiffness) and thereby can enable a systemic investigation of the role of such biophysical cues towards regulation of single cell behaviors like cytoskeletal dynamics, force generation, migration, division and nuclear mechanics.

In order to study such regulation, the proposed work in this thesis has been divided into 4 major components. Firstly, we manufacture suspended matrices of aligned fibers with a wide range of diameters (~ 150 nm- 6.6 μm) to mimic the sizes of collagen fibrils and bundled fibers *in vivo* to investigate cytoskeletal and nuclear mechanics during cell spreading in elongated shapes. Here, we report for the first time that cells in suspended environments demonstrate a unique cytoskeletal caging structure surrounding the nucleus,

devoid of apical-basal polarity commonly reported in 2D planar substrates. Fiber diameter and density-dependent mechanical tension within the cytoskeletal cage of elongated cells drives nuclear compression, translocation of the YAP/TAZ transcription factor and induces well-defined deformation or invaginations within the nuclear envelope. To extend our findings and investigate if aligned fiber configuration was a prerequisite for achieving elongated cell and nuclear shapes frequently observed during directed migration of cancer cells, we developed bidirectional crossing fiber matrices with tunable fiber density to mimic the crossing fiber arrangements within the native interstitial matrix. Unexpectedly we observed, cells adhering to dense crosshatch networks developed highly elongated 3D morphologies with thicker nuclei and migrated persistently at high speeds, a previously unknown mechanobiological response of cancer cells to ECM geometry. Interestingly, as cells elongated during interphase rounded up to divide, fiber-geometry dependent organization of retraction fibers led to differential levels of mitotic cell body movements leading to alterations in metaphase plate oscillations, division times and mitotic spindle defects. Finally, we interrogated how elongated cells on suspended fibers respond and adapt to external high-voltage electric fields, commonly used in cancer therapeutics. Using single cell force measurements, we identify for the first time multistage cell contractility recovery dynamics, correlating with cytoskeletal disruption and reassembly, and report geometric orientation-dependent cell-viability. Comprehensive investigation of such ECM-fiber mediated mechanistic regulation of single cell behavior will advance our understanding of the cancer metastatic process and can potentially lead to development and optimization of cancer therapies targeting the cytoskeleton.

Chapter 3:

Sculpting rupture-free nuclear shapes in fibrous environments

3.1 Introduction

The nucleus, as the stiffest cellular organelle [56], plays a central role in mechanotransduction [57]. Proper control of nuclear shapes is one of the primary cellular functions controlling cell migration, differentiation and tissue morphogenesis [58]. Thus, not surprisingly, defects in nuclear shapes are often implicated in various disease states, including progeria, muscular dystrophy, and cancer metastasis [59]. Nuclear shapes are regulated by mechanical forces [14,60] originating from cells' dynamic interactions with their surrounding microenvironment, i.e., the extracellular matrix (ECM), and transmitted to the nucleus by the cell cytoskeleton. The nuclear envelope composed of the lamin intermediate filament networks is critical in sustaining external forces exerted on the nucleus. Lamin network mutations and deficiencies cause significant reduction of the nuclear stiffness [61], leading to nuclear blebbing [62], and mislocalization of DNA repair factors and DNA damage [63].

Mechanical forces primarily act through the actomyosin contractions in the stress fibers to control nucleus shape to induce nucleo-cytoplasmic shuttling of transcription factors like YAP/TAZ, MKL1, and chromatin remodeling proteins such as HDAC [64,65]. The force-mediated nuclear shape changes also induce reorganization and stretching of the internal chromatin domains [66], resulting in altered transcriptional activity and mechanical properties of the nucleus [67]. A growing consensus in the field has been that nuclei rupture as they undergo drastic shape changes, causing mislocalization of signaling molecules (6,12). Large scale mechanical forces, driven by ECM stiffness, mold cell shape, which

controls the nucleus shape; high aspect ratio nuclei induce high curvature at the poles, making them susceptible to rupture [62].

In vivo 3D aligned matrices, observed frequently in both healthy and diseased states, which include tendons [69,70], muscle tissue[71,72] and extracellular regions surrounding metastatic tumors [44,73,74] provide topographic cues for cells to spread uniaxially and migrate persistently by exerting forces [75,76] . Fibrillar matrices composed of individual collagen fibrils range in size from 70 to 300 nm [77–80] that can bundle to larger fibers varying from 1 to 20 μm in diameter [78,80]. Mimicking the native ECM architecture within an in vitro setting, is often highly challenging and flat 2D substrates with and without anisotropic features and 3D gels have been used extensively to study cell behavior[81]. 2D systems have limited physiological relevance, and while 3D collagen gels capture the fibrillar architecture, the inherent heterogeneity in these matrices renders it difficult to understand the role of fiber dimensions and organization in regulation of cytoskeletal and nuclear responses [82,83]. Studies by the Yamada group have demonstrated how single cell behavior in 3D microenvironments can be recapitulated through use of narrow 1D microprinted lines of varying widths (1-40 μm) [84]. Microprinted lines are essentially 2D surfaces, and in our study, we inquired if suspended 1D fibrillar architecture of precisely controlled fiber diameters (150-6000 nm) and interfiber spacing regulated nuclear responses of uniaxial spread cells, as we have previously shown protrusive, contractile, and migratory behavior of uniaxial cells to be sensitive to fiber curvature and spacing [85–91]. In this study, we chose nucleus rupture and the spatial localization of YAP/TAZ as two markers of nuclear response to changes in fiber curvatures. We discovered that cytoskeletal and lamin networks in suspended cells are localized in an almost uniform caging structure

surrounding the nucleus, contrary to the preferential apical localization in flat continuous surfaces. Fiber-curvature driven cytoskeleton tension led to precise sculpting of nucleus shape, including unique teardrop shapes due to actin stress fiber anisotropy and invaginations that ran the length of nucleus. We found that all nucleus shapes, including the sharpest invaginations formed on nanofibers did not undergo rupture events, indicating a remarkable adaptability of nuclei to fibrillar environments. Nuclear translocation of YAP increased with the diameter or fiber density. Overall, we describe cellular mechanosensitivity unique to fiber matrices with implications in pathophysiology.

3.2 Materials and Methods

Fabrication of nanofiber networks

Using the previously reported STEP technique[92,93], suspended fiber nanonets (horizontal arrays of densely spaced (~12 μm) nanofibers of differing diameters (200nm, 350nm, 800nm) deposited on widely spaced (~ 250 μm) vertical support fibers (~2 μm diameter), were manufactured from solutions of polystyrene (MW: 2,000,000 g/mol; Category No. 829; Scientific Polymer Products, Ontario, NY, USA) was dissolved in xylene (X5-500; Thermo Fisher Scientific, Waltham, MA, USA) in 7-13 wt% solutions. Micron scale (≥ 2 μm) fibers were manufactured from 2-5 wt% of high molecular weight polystyrene (MW: 15,000,000 g/mol, Agilent Technologies, Santa Clara, CA, USA). Briefly, the polymeric solutions was extruded through a micropipette (inside diameter: 100 μm; Jensen Global, Santa Barbara, CA, USA) for deposition of aligned fibers on a hollow substrate. Measured (using scanning electron microscopy images) diameters for the 150 nm, 200 nm, 350 nm, 800 nm, 2.5 μm, 3.5 μm and 6.6 μm diameter categories are 153 ± 1.2 nm, 206 ± 2.6 nm, 361 ± 4.5 nm, 808 ± 7.6 nm, 2.50 ± 0.02 μm, 3.48 ± 0.09 μm and 6.62 ± 0.17 μm (values

are shown as Mean ± SEM, n=37, 59, 90, 92, 28, 21 and 25 respectively). For the 350nm diameter category, fiber networks with varying spacing (3-25) μm were used. All fiber networks were crosslinked at intersection points using a custom fusing chamber, to create fixed-fixed boundary conditions.

Cell culturing and experimental procedure

C2C12 mouse myoblasts (ATCC), HT1080 human fibrosarcoma and HeLa cells were cultured in Dulbecco's modified Eagle's medium (Invitrogen, Carlsbad, CA, USA) supplemented with 10% fetal bovine serum (Gibco, Thermo Fisher Scientific) in T25 flasks (Corning, Corning, NY, USA) kept at 37°C and 5% CO_2 in a humidified incubator. For imaging cell spreading dynamics scaffolds containing fiber nanonets were mounted in glass-bottom single well plate. For immunofluorescent staining experiments, cell seeding was performed on fiber scaffolds mounted on glass-bottom six-well plates (Cellvis, Mountain View, CA, USA). Prior to experimentation, fibers were sterilized in 70% ethanol for 10 minutes and functionalized for 1 hour under incubation at 37°C using 4 μg/mL fibronectin in PBS (Invitrogen, Carlsbad, CA, USA). For fluorescent labelling of fibers, rhodamine conjugated fibronectin (Cytoskeleton Inc., Denver, CO, USA) was used with the same concentration and incubation time. Before cell seeding, the test platform was moved into an AxioObserver microscope under incubation conditions of 37°C and 5% CO_2 (Zeiss, Oberkochen, Germany). Without disturbing the closed environment, a droplet (~100 μL) of cell suspension was deposited on the fiber nanonets to begin the experiment.

Live imaging

Time-lapse optical imaging was started immediately before introducing the cell suspension to the fibers. Imaging was performed at 20x 0.8 NA objective in a Zeiss AxioObxerver Z1 microscope with an interval of 1-3 minutes for 1 hour. C2C12 or HT1080 cells expressing NLS (nuclear localization signal) mCherry were imaged every 3 min with a TRITC filter set.

Immunofluorescent staining and imaging

Cells were fixed with 4% paraformaldehyde for 15 minutes at various timepoints (5, 10, 20, 40 and 60 minutes), following initial cell fiber contact. Cells were then permeabilized with a 0.1% Triton X-100 solution, washed in PBS twice and blocked with 5% goat serum (Invitrogen, Grand Island, NY) for 30 minutes. Primary antibodies, diluted in an antibody dilution buffer consisting of PBS with 1% Bovine Serum Albumin and Triton-X 100, were added to the fixed cells and kept either i) overnight at 4^{o} C / ii) at room temperature for 3 hours / iii) at 37^{o}C for 2 hours. Diluted secondary antibodies, along with the conjugated Phalloidin-TRITC (Santa Cruz Biotechnology, Dallas, TX, USA) or Alexa Fluor 647 Phalloidin (Invitrogen) diluted in 1:80 ratio, were subsequently added and stored in a dark place for 45 minutes. Following a 3 times PBS wash, DAPI (4′,6-diamidimo-2-phenylindole) or Hoechst 33342 (Thermo Fisher Scientific) was added for 5 minutes to stain the cell nuclei. Primary antibodies include Anti-Vimentin antibody (1:250, rabbit monoclonal, EPR3776, Abcam), Anti-phospho-Paxillin (1:100, rabbit polyclonal, pTyr31, Invitrogen), Anti-beta tubulin (1:500, mouse monoclonal, 2 28 33, Invitrogen), Anti-Lamin A/C (1:1000, mouse monoclonal, sc-376248, Santa Cruz Biotechnology), Anti-Lamin B1 (1:500, mouse monoclonal, sc-374015, Santa Cruz Biotechnology) and Anti-YAP (1:100, mouse monoclonal, sc-101199, Santa Cruz Biotechnology). Secondary antibodies include

Goat anti-Rabbit IgG Alexa Fluor 488 (1:200, Invitrogen), Goat anti-mouse IgG Alexa Fluor 488 (1:200-1:1000, Invitrogen) and Goat anti-mouse IgG Alexa Fluor 647 secondary antibody (1:500, Invitrogen).

Images were taken using an inverted Zeiss microscope using a 63x objective (NA 1.20, water immersion). Confocal microscopy was performed using a laser scanning confocal microscope (LSM 880, Carl Zeiss Inc.) and images were obtained using a 63x 1.15 NA water immersion objective. Z-stacks were taken with slice thicknesses ranging between 0.3-0.5 μm. Z-stack images were processed in the Zen Blue software (Carl Zeiss Inc).

Generation of knockdown cell lines

Lmna-KD were created using shRNA encoded on pLKO.1 puro plasmid (Addgene #8453) and introduced into C2C12 with 2nd generation lentivirus. Sequences for shRNA was obtained from Broad Institute Genetic Perturbation Platform. The sequence used for this study is GCGGCTTGTGGAGATCGATAA. Viral particles were produced in HEK293T following calcium phosphate transfection using 4.8 μg, 30 μg and 33.6 μg of VSVG (Addgene #14888), psPAX2 (Addgene #12260) and pLKO.1 puro Lmna-shRNA plasmids respectively. After 48 hrs, supernatant containing viral particles were concentrated 100x following 2-hr ultracentrifugation 50,000 g and 4^{o}C. Cells were transduced in full growth media (DMEM supplemented with 10% FBS) containing viral particles for 48 hrs and verified (**Supplementary Fig. 3.S12**) via Western blot using anti-Lmna/c mouse mAb (Cell Signaling Technology #4777).

Pharmacological inhibition

For cytoskeletal inhibition, cells in suspension were incubated with 2 μM cytochalasin D (actin disruption) (Fischer Scientific), 1 μM nocodazole (microtubule disruption) (Sigma Aldrich) and 10-20 μM Y27632 (ROCK inhibition) (Hellobio, Princeton, NJ, USA) for 30 minutes -1 h. For chromatin compaction /decompaction cells were pre-treated with histone demethylase inhibitor (Methylstat, 5 μM, 48 h incubation) (Sigma Aldrich, St. Louis, MO, USA) and histone deacetylase inhibitor valproic acid (VPA, 2 mM, 24 h incubation) (Sigma Aldrich) respectively. At least N=2 replicates were performed for each drug condition.

Analysis of shape metrics

Cells in suspension demonstrate a rounded morphology which evolves as they attach and spread on a substrate. Cell circularity is defined by the relation:

$$\text{Circularity}=4\pi A/P^2$$

where A is spread area (μm^2) and P is perimeter (μm). A perfect circle results in a circularity value of 1.0. As the shape elongates, this value approaches 0.

Polarized cells were manually outlined in ImageJ and the aspect ratio was quantified using the Bounding Rectangle Function.

Analysis of focal adhesion clusters and actin stress fibers

Consistent with our previously reported convention, we quantified the length of the focal adhesion (FA) cluster as the longest continuous length of immunostained paxillin. Intensity profiles for paxillin were generated by performing line scans along the cell-fiber contact region. For averaging purposes, profiles were normalized in 2 steps, i) Intensity (plotted

along y-axis) was normalized with respect to peak intensity of the corresponding profile, ii) Cell length (plotted along x-axis) was normalized with respect to the net length (measured from end-to-end) of the particular cell. Intensity profiles were subsequently averaged using a custom MATLAB routine, using a bin width of 0.01.

Maximum intensity projections of phalloidin stained cells were utilized to count the number of major actin stress fibers emanating from each FA cluster and in the perinuclear region. Orientation of the actin stress fibers were measured with respect to the undeflected nanofiber orientation.

For average actin localization in **Fig. 3.4b**, images of perinuclear regions (17 cells) were averaged using a custom MATLAB routine, and the average image is represented as an intensity heatmap.

Analysis of nucleus shapes and deformations

Confocal z-stacks of DAPI/Hoechst/Lamin stained nuclei were processed in either ImageJ (NIH; https:// imagej.nih.gov/ij/) or Zen Blue (Carl Zeiss Inc). Nucleus projected area was calculated from the top (xy) view at the equatorial plane (plane of the nanonets). The shape (xy) of the nucleus was approximated as an ellipse and quantified by the ellipse eccentricity.

$$\text{Eccentricity} = (1-b^2/a^2)^{0.5}$$

Where 2a and 2b represent the shape of the major and minor axis of the ellipse respectively. The eccentricity value of a perfectly symmetrical circle is 0, while the value increases to 1, with increasing elongation of the ellipse.

Nucleus aspect ratio was measured by manually outlining and using the Bounding Rectangle Function in ImageJ.

Nucleus thickness was measured from the orthogonal side views (xz or yz) generated with the *Ortho* function in Zen Blue, and the maximum z-dimension was considered as the thickness of the nucleus.

To quantify nuclear shapes in 'mismatch' diameter fiber doublets, cross-sectional side views (yz) were generated using *Ortho* function in Zen Blue. A line is then drawn through the nucleus mid-width as shown in (**Fig. 3.4b (iii)**) and the area of the half cross-sections were measured and designated as A_{max} and A_{min} based on larger and smaller area respectively. Nucleus asymmetry index (NAI) is defined by A_{min}/A_{max}. Thus symmetric nuclei will have a NAI of ~1, while teardrop shaped nuclei will have NAI < 1.

To quantify nuclear invaginations in spindle shaped cells attached to single fibers, the deformed region of the nuclear envelope (yz cross-sectional view) was manually outlined in ImageJ and a bell curve ($S = S_0 e^{-y^2/2\sigma^2}$, **Fig. 3.5c**) was fitted to the manual trace using a custom MATLAB (https://www.mathworks.com/) code to evaluate the individual parameters S_0 (invagination depth) and σ (invagination spread).

To quantify the level of curvature of the nuclear surface, a best-fit circle was placed at the apical and basal surface of the cross-sectional view (yz) of the nucleus, in the Zen Blue software. The curvature was defined as the inverse of the radius of this best-fit circle.

Fluorescent Intensity analysis

To compare the basal and apical localization of cytoskeletal and nuclear envelope components, the orthogonal side views of the respective channels were first generated in Zen Blue. Rectangular intensity profiles with a 5 µm width were computed at the cell/nucleus mid-width (**Fig. 3.1e**). The peak intensities at the apical and basal side were subsequently extracted to compute the intensity ratio between basal and apical side.

To quantify the YAP/NLS localization within cells, cells and nuclei were first manually outlined in Zen Blue to get the mean YAP/NLS intensity within the whole cell (I_{cell}) and inside the nucleus (I_{nuc}) and the corresponding projected areas (A_{cell} and A_{nuc}). The average intensity within the cytoplasm (projected area: A_{cyt}) is indirectly quantified from the following relations:

$$I_{cell}*A_{cell} = I_{nuc}*A_{nuc} + I_{cyt}*A_{cyt} ,$$

$$A_{cell} = A_{nuc} + A_{cyt}$$

The intensity ratio $I_{nuc/cyt}$ is quantified by the ratio of the average intensities within the nucleus (I_{nuc}) and the cytoplasm (I_{cyt}).

For NLS intensity analysis (**Supplementary Fig. 3.S9**), rectangular intensity profiles (1 µm width) were taken along the cell length. Fluorescent intensity was normalized with respect to peak intensity of the corresponding profile and centered with respect to the nucleus midpoint.

Calculation of cell adhesion forces

Using our previously reported Nanonet Force Microscopy [94,95] technique, cell-fiber adhesion forces were quantified using a custom MATLAB code. Briefly, taut nanofibers

were approximated as loaded Euler Bernoulli beams with fixed-fixed boundary conditions and with forces exerted at either cell pole (localization of the focal adhesion clusters) at an angle. This direction of force exertion was taken along the average orientation (with respect to the undeflected fibers) of the f-actin stress fibers emanating from the polar FA clusters. Next, experimentally observed nanofiber deflection profiles were compared with the best fit profile from finite-element model predictions and the error between them was minimized iteratively to generate the adhesion forces. In fiber doublets (homogenous diameters), due to the high level of symmetry in fiber deflections on either fiber, magnitude of the net cell force exerted is approximated as twice the magnitude of the cell-adhesion force with each fiber.

Statistical analysis and data fitting

Statistical analysis was performed in GraphPad Prism (GraphPad Software, La Jolla, CA, USA) software. For statistical comparison between multiple groups, ANOVA (along with Tukey's honestly significant difference test) was utilized. For pairwise comparisons with a control group, Student's t-test was used. In all scatter data column plots, error bars represent standard deviation. Unless otherwise mentioned, in all other plots, error bars represent standard error of measurement. For all statistical plots *,**,***,**** represent $p< 0.05$, 0.01, 0.001 and 0.0001 respectively. Data fitting was performed in either MATLAB (for nonlinear fits) or Microsoft Excel (linear fits).

3.3 Results

Suspended cells show uniform nuclear caging of cytoskeletal elements and lamins

We wished to compare the responses of cells plated on flat 2D as opposed to those attached to suspended fibers of varying diameters. We utilized force-measuring nanonets composed

of large diameter (~2000 nm) 'strut' fibers fused to orthogonal small diameter aligned fibers (Nanonet force Microscopy, NFM) [90,94–96]. To investigate the role of fiber diameter, we selected 3 different fiber diameters: 200 nm, 350 nm and 800 nm, while keeping the spacing between large strut fibers constant (~250 μm). Fiber beam stiffness, midspan of a beam scales approximately with ~d^2, thus for constant beam length allows us to directly compare the effects of fiber diameter contributing to increase in stiffness [85,90,96]. We investigated the dynamics of cell spreading and organization of cytoskeletal networks using a custom setup to add cell suspension droplets on the fibronectin-coated fiber networks (**Fig. 3.1a, b**). The inter-fiber spacing (10-12 μm) was chosen to ensure that cells spread along two fibers to form symmetric parallel-cuboidal shapes (**Fig. 3.1b (iii)**). For cells attached approximately midway across the fiber span length, we monitored cell spreading using optical microscopy (**Fig. 3.1c**). For all fiber diameter categories, cells after making initial contact with the fiber networks, began to protrude along the nanofibers. Consistent with our previous findings[86], we observed that protrusions formed during spreading were primarily actin-based, while microtubules and vimentin intermediate filaments localized later during the spreading cycle (**Supplementary Fig. 3.S1 b**). To characterize cell size and shape during spreading, we tracked the cell projected area and the circularity for one-hour for the three diameters. The cell area growth curves for all the fiber diameter categories showed a faster initial incremental phase followed by gradual maturation at longer times (**Fig. 3.1d (i,iii)**), matching growth rate kinetics on 2D substrates[97]. Interestingly, we found that cells achieved steady-state area and circularity faster (~ 40 min) on 200 nm diameter fibers, while cells on larger diameter fibers demonstrated higher spread areas and circularity (**Fig. 3.1d**).

Next, we inquired if classic apical localization of cytoskeletal elements, described in studies on flat surfaces extended to cells attached to suspended nanonets. On 2D substrates, nuclear shapes are shown to be regulated by cell boundary movements which involve both the contractility of the actomyosin cytoskeleton and the mechanical tension of the cell membrane [98,99]. Khatau et al. have furthermore identified the apical perinuclear actin cap as a primary regulator of the nuclear shape [100], while more recently, Ihalainen et al. demonstrated a differential localization[101] of the nuclear lamins (particularly Lamin A/C) towards the apical nuclear envelope. Informed by these studies, we examined the localization of the major cytoskeletal elements (f-actin stress fibers, microtubules and vimentin intermediate filaments) and nuclear lamins (A/C and B1) in cells attached to flat glass surfaces and on our suspended nanonets. We observed that the f-actin, microtubule and intermediate filament cytoskeleton was highly aligned along the fiber axis in elongated cells as compared to their counterparts on flat glass (**Fig. 3.S1 a,c**). Confocal microscopy side-views (xz and yz) at various stages during cell spreading revealed major differences in the localization of the nuclear lamins and the overall organization of the cytoskeletal elements around the nucleus (**Fig. 3.1e (i), Fig. 3.S2**). On flat 2D, our findings on apical-basal localization of Lamin A/C were in agreement with previously reported literature (*Intensity ratio*$_{basal/apical}$ *= 0.35±0.04*), but contrasted on suspended nanonets (*Intensity ratio*$_{basal/apical}$ *= 1.05±0.05*). In a similar manner, cells on flat glass displayed preferential enrichment of different cytoskeletal elements towards the apical side in a 'capping' manner (**Fig. 3.S2a**), with the strongest apical preference observed in case of the vimentin intermediate filaments (*Intensity ratio*$_{basal/apical}$ *= 0.09±0.02*). Contrarily, the cytoskeletal network was nearly

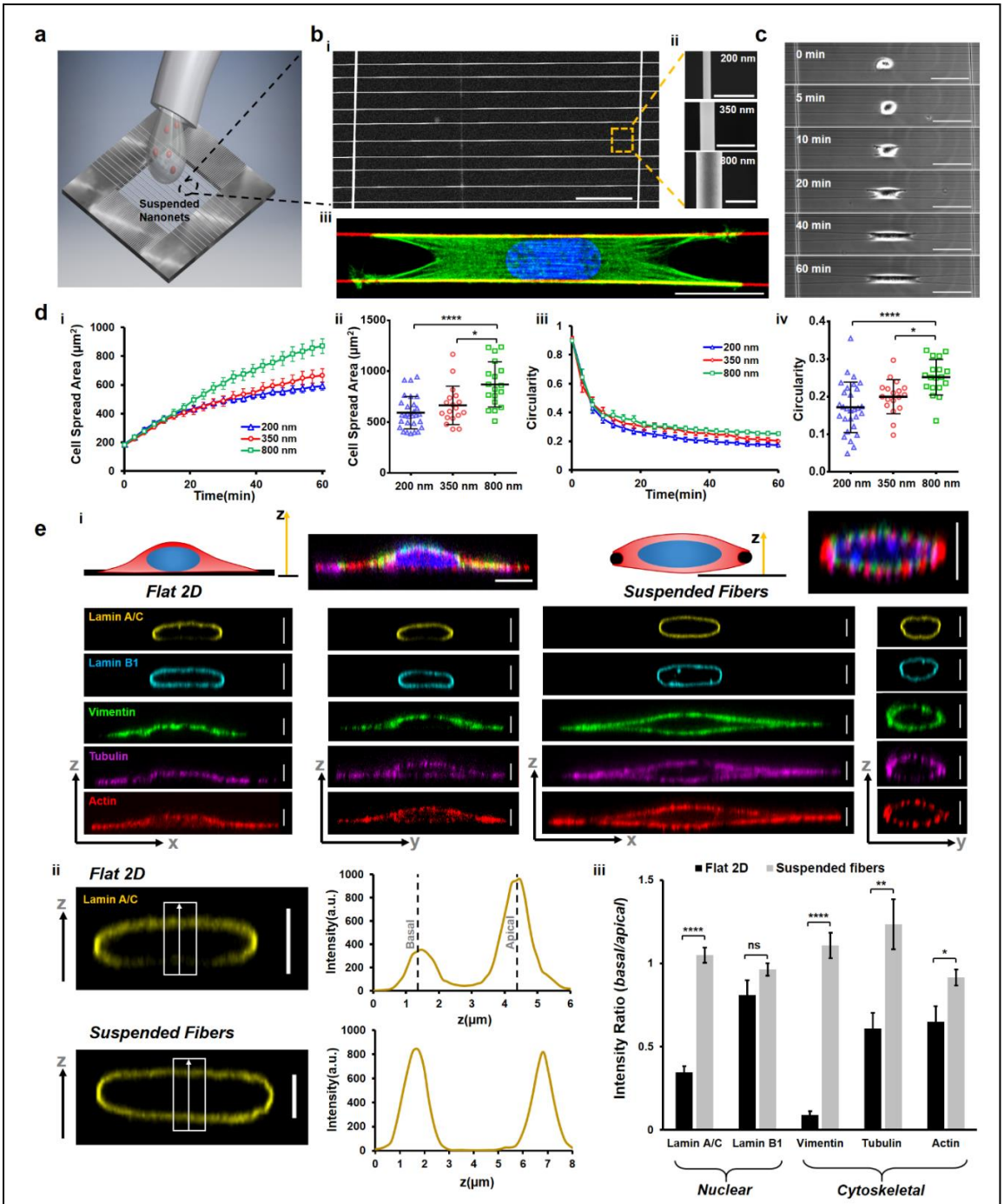

Figure 3.1: Cell spreading on suspended fiber networks: a) Schematic of assay used for studying cell spreading. Cell suspension is dropped on top of suspended nanonets coated with fibronectin and imaged in real-time. b) i) SEM image of suspended nanonet (scale bar, 50 μm) ii) SEM images of 3 different fiber diameters 200, 350 and 800 nm used for the study, (scale bar, 1 μm) and iii) Representative cell (stained for Actin-green, DAPI –blue, and fiber -red) on a 2-fiber (diameter: 350 nm) doublet (scale bar, 20 μm). c) Images from time lapse microscopy showing different phases of cell spreading on a 2-fiber doublet. (scale bar, 50 μm) d, i,iii) Temporal evolution of cell spreading area and circularity respectively (n=16-29 cells per category). d, ii, iv) Statistical comparison of cell spread area and circularity respectively after

1 hour of spreading e) i) Representative immunofluorescence images showing differences in localization of cytoskeletal elements and nuclear envelope proteins between Flat 2D and suspended nanonets. Cytoskeletal elements form a 'caging' structure surrounding the nucleus, while on 2D they 'cap' the nucleus from apical side (scale bars, 5 μm) and ii) Representative confocal side views (xz) along with intensity profiles along the z-direction, first and second intensity peaks correspond to basal and apical surfaces respectively, (scale bar, 5 μm) iii) Comparison of the basal and apical intensity for the different cytoskeletal and nuclear envelope proteins (n=10-11 per category) demonstrating intensity ratio values close to 1 for suspended nanonets (diameter: 200 nm) due to caging of nucleus, absent in cells on 2D.

uniformly distributed around the nucleus in a 'caging' manner on suspended nanonets (intensity ratios ~1, **Fig. 3.1e (iii)**). Overall, we conclude that cytoskeletal caging of the nucleus in suspended nanonets causes uniform distribution of nuclear lamins, which is distinctly different than observations from 2D substrates.

Increase in cytoskeletal tension during cell spreading is fiber-diameter dependent

Since cells were achieving steady-state spreading fastest on the smallest diameters and suspended networks were causing cytoskeletal elements to cage the nucleus, we inquired the role of focal adhesions and actin network in establishing contractile forces. Visualizing cell-fiber adhesions through paxillin immunostaining at various timepoints (5, 10, 20, 40 and 60 min) during cell spreading revealed that focal adhesion (FA) clusters were formed along the entire cell length at early stages (t~10 min), while a preferential localization of the FA clusters occurred to the cell poles with increased spreading (**Fig. 3.2a (i), Fig. 3.S3**). Normalized paxillin intensity taken along the cell length, revealed two distinct peaks (**Fig. 3.2a (ii)**) corresponding to the major FA clusters at either cell pole, consistent with our previous findings[85,90,91]. The transition of adhesion sites from being punctate along the entire cell body to localizing in major clusters at cell poles occurred by the 20-min timepoint (**Fig. 3.2a (ii)**). A closer inspection of the adhesion distribution along the cell

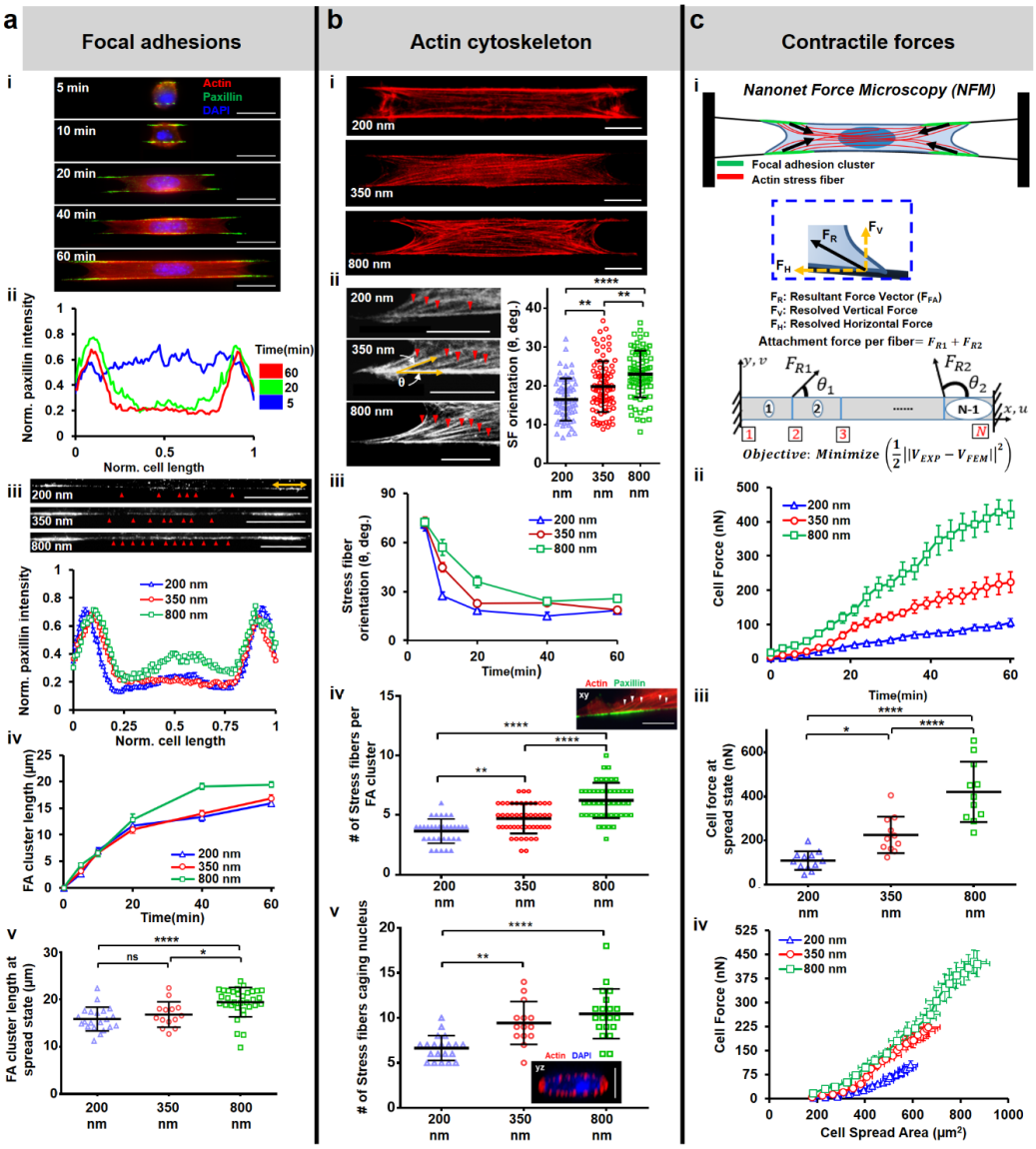

Figure 3.2: Cell contractility during spreading: a) Focal adhesion (FA) organization: i) Representative images showing cells stained for actin (red), paxillin (green) and DAPI (blue) at different timepoints during spreading (fiber diameter: 350 nm), (scale bars, 20 μm), ii) Normalized paxillin intensity (average of 9-12 profiles for each timepoint) showing spatiotemporal reorganization of focal adhesions as cells spread, iii) Differences in FA organization in clusters (yellow arrow) at the poles and along cell body-fiber length (red arrowheads) for different fiber diameters, (scale bars, 20 μm) , iv) Temporal evolution of FA cluster lengths, and v) Comparison of FA cluster lengths at final spread state, n=21, 14 and 33, b) Actin cytoskeleton organization: i) Maximum intensity projections of actin cytoskeleton at spread state (60 min), (scale bars, 10 μm), ii) Stress fiber angle formed at the focal adhesion cluster zones, n=68, 88 and 80, (scale bars, 10 μm), iii) Transient evolution of orientation of the stress fibers during spreading, iv) number of major stress fibers originating from each FA clustering zone, n=33, 49 and 47 and v) number of major stress fibers caging the nucleus, n=20, 14 and 20. Inset are representative images of FA clustering zone, (scale bars, 10 μm) and

nucleus caging with actin networks (scale bars, 5 μm), c) Contractile forces: i) Schematic of force measurement using Nanonet Force Microscopy (NFM) technique, ii) Transient cell attachment force evolution during spreading, (n=11-12 cells each diameter category), iii) Comparison of cell forces at spread state between the different fiber diameters, iv) Relationship between cell forces and cell spread area. Cell forces are computed from both fibers. Sample sizes are given for 200-200, 350-350, and 800-800 nm diameter doublets respectively.

length at 60-min (**Fig. 3.2a (iii)**) revealed smaller paxillin clusters distributed along the cell-fiber length, which became more prominent on larger diameter (800 nm) fibers (red arrowheads). FA cluster lengths were observed to grow in length with cell spread, with the largest 800 nm diameter fibers resulting in the longest cluster lengths at 60-min timepoint (**Fig. 3.2a (iv, v)**).

Our observations that FA clustering occurred in a fiber diameter dependent manner, suggested that the associated cytoskeletal tension might be influenced by fiber diameter as well. We immunostained for the contractile f-actin cytoskeleton (**Fig. 3.2b (i)**) in cells at various timepoints (5, 10, 20, 40 and 60 min) and found that the average angle made by stress fibers anchored to the FA clustering sites at poles progressively decreased as cells spread, with the shallowest angle formed on 200 nm diameter fibers (**Fig. 2b (ii, iii)**). We observed the number of stress fibers originating at each FA cluster zone increased with fiber diameter indicative of increased contractility (**Fig. 3.2b (iv)**). We also investigated the actin cytoskeletal organization in the perinuclear region, since the actin stress fibers in this region directly affect nucleus shape regulation. Appearing as individual dots, surrounding the nucleus, in confocal cross-sections (yz, **Fig. 3.2b (v)**), we found that the number of stress fibers originating from individual FA clustering regions were less than those in the perinuclear region due to convergence of stress fibers emanating from FA

clusters on either side, a behavior unique to anisotropically stretched cells in suspended nanonets (**Supplementary Fig. 3.S4**).

Using NFM, we estimated the forces in cell spreading by monitoring the contractile inward deflection of fibers (**Fig. 3.1c, 3.2c (i)**). Fiber deflections were subsequently converted into attachment forces at the individual FA clusters using inverse methods that minimize the error between computed and experimentally observed fiber deflections (Materials and Methods). The inputs to the computational framework include fiber properties and force vectors that originate from FA clustering zones (**Fig. 3.2a (iii)**) and are directed along the average stress fiber orientation per fiber category (**Fig. 3.2b (ii, iii)**). Consistent with our finding that the number of stress fibers increase with fiber diameter, the computed forces ($F_{cell/fiber} = F_{R1} + F_{R2}$) also increase as cells spread and with increase in diameter (**Fig. 3.2c (ii, iii**)). We also plotted cell force against cell spread area (**Fig. 3.2c (iv)**), and found that for the same area across different diameters, cells attached to larger diameter fibers exerted significantly higher forces. Overall, our data suggest that increasing the fiber diameter causes cells to form larger focal adhesion clusters at the poles that lead to increased number of actin stress fibers resulting in higher cell contractility.

Nuclear translocation of YAP is regulated by nuclear compression

Given our observations on the arrangement of F-actin networks caging the nucleus, we sought to investigate, how the compression forces impacted the nucleus geometry and translocation of various transcription factors including YAP (Yes-associated protein) [102], known for its central role in mechanotransduction. To determine nucleus geometry, we used confocal microscopy on DAPI-stained cells (**Fig. 3.3a (i)**) that were fixed at various timepoints (5, 10, 20, 40 and 60 min). We employed 3 parameters: nucleus projected area

(size in xy plane, top view), nucleus eccentricity (shape in xy plane) and the nucleus thickness (compression in xz plane, side view). Nucleus projected area was found to increase steadily and reach an equilibrium value for all the fiber diameters tested (**Fig. 3.3a (ii), Supplementary Fig. S5a**), with cells in 200 nm nanonets reaching stable areas the fastest. As cells spread, we observed the nuclei to elongate (rise in eccentricity, **Supplementary Fig. 3.S5b**). Not surprisingly, as the nuclei underwent compression from the near spherical shape in rounded cells to the flattened 'pancake' shape (confocal side views, **Fig. 3.3a (i)**), the nucleus thickness reduced significantly over time (**Fig. 3.3a (ii)**), with the minimum thickness in cells attached to 800 nm nanonets (**Fig. 3.3a (iii)**), suggesting that the nuclear compression was primarily driven by the cytoskeletal tension.

To test the relative contributions of the actin and microtubule cytoskeletons in regulating force driven nuclear compression, we treated cells on nanonets with either cytochalasin D (2 μM) or nocodazole (1 μM). As expected, cytochalasin D treatment led to cells of reduced spread area (**Supplementary Fig. 3.S6**) and disrupted actin cytoskeleton as evidenced by loss of stress fibers caging the nucleus (**Fig. 3.3b**). Under these conditions, the nucleus thickness was found to be significantly (~1.5x) higher than the control cells (no drugs). In contrast, disruption of the microtubule cytoskeleton did not significantly alter the nuclear compression levels. Next, we reduced cytoskeletal tension and actin stress fiber formation through the selective ROCK inhibitor Y27632 and observed nuclei of significantly larger thickness (**Fig. 3.3b**), further elucidating the role of the actin cytoskeleton caging network in nucleus shape maintenance.

Informed by these findings, next, we investigated the role of nuclear lamina in sustaining cytoskeletal forces. The nuclear lamina, composed of the nuclear lamins (A, C, B1 and

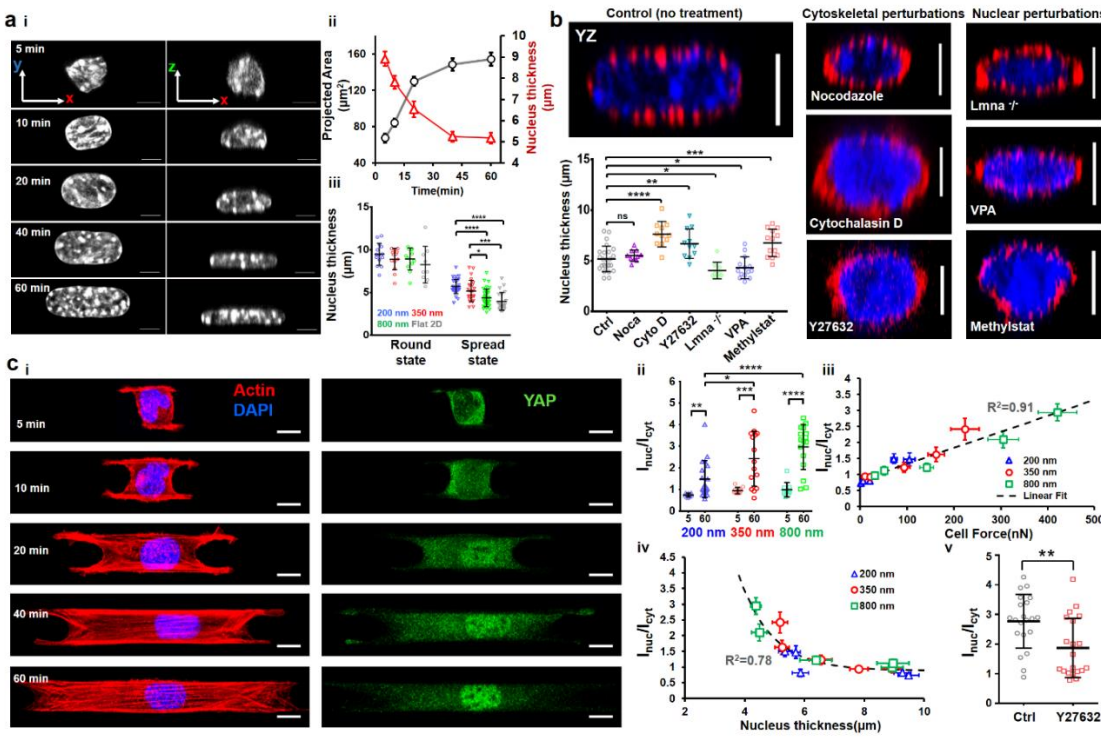

Figure 3.3: Nuclear compression and YAP localization during spreading: a) i) Representative images showing top view (xy) and side view (xz) of nuclei at different timepoints during cell spreading (fiber diameter: 350 nm), (scale bars, 5 μm), ii) Increase in nucleus projected area (xy) and decrease in nucleus thickness (z), indicating nucleus flattening with cell spreading, n=13-32 per timepoint iii) Nucleus thickness comparison between rounded (5 min) and spread (60 min) state, n=14, 13, 12 and 9 (for round state) and n=32, 25, 36 and 22 (for spread state) for 200 nm, 350 nm, 800 nm and Flat 2D respectively, b) Representative cross-section (yz) images of cells under various drug conditions and lamin A/C knockdown, n=25, 10, 11, 11, 9, 14 and 13 (scale bars, 5 μm), Comparison of nucleus thickness with control (no treatment), fiber diameter: 350 nm, c) Nuclear entry of YAP during cell spreading: i) Representative images at various timepoints during spreading, (scale bars, 10 μm) ii) Comparison of nuclear/cytoplasmic YAP between rounded (5 min) and spread state (60 min) for different fiber diameters, n=10-15 cells per timepoint and diameter category iii) Increase in nuclear YAP correlates with cell forces (iv) Increase in nuclear YAP correlates with nucleus thickness, and (v) Nuclear YAP localization decreases with loss of contractility through pharmacological inhibition, n=21 and 20 for control and Y27632 treatment. Fiber diameter: 800 nm.

B2), is a thin intermediate filament meshwork enveloping the nucleus, providing it with essential mechanical support. We generated C2C12 lamin A/C KD cells that had wrinkled nucleus morphologies (**Supplementary Fig. 3.S7**) consistent with observations from previous studies[103]. Fully spread Lamin KD cells, had lower nucleus thickness compared

to control likely due to decreased nuclear stiffness[68]. Next, we altered the chromatin compaction levels by pre-treating cells with the histone deacetylase inhibitor (HDACi) valproic acid (VPA) used for chromatin decompaction and reducing nucleus stiffness or the histone demethylase inhibitor, Methylstat used for chromatin compaction and increasing nuclear stiffness[61,104]. Cells treated with VPA or Methylstat, demonstrated significantly decreased and increased nucleus thickness respectively, as compared to control cells (**Fig. 3.3b**).

Recent studies have shown how cytoskeletal-mediated compressive forces acting on the nucleus can lead to stretching of the nuclear membrane pores[65]. We wanted to inquire if the nuclear entry of YAP correlated with the fiber-diameter driven nuclear compression. Immunostaining for YAP (**Fig. 3.3c (i)**) at various timepoints during cell spreading, showed that YAP localization was primarily cytoplasmic (YAP intensity ratio between nucleus and cytoplasm I_{nuc}/I_{cyt} <1) during early stages of cell spreading (5-10 min) but with increase in cytoskeletal tension at later stages of cell spreading, a significant increase in the nuclear entry of YAP was observed (**Fig. 3.3c (ii)**). Interestingly, we observed that nuclear YAP translocation ratio was independent of cell shape, but dependent upon force and nucleus thickness (**Fig. 3.3c (iii, iv)**). Thus, reducing nuclear compression through contractility inhibition (Y27632 treatment) resulted in a significant decrease in the nuclear translocation of YAP (**Fig. 3.3c (v)**).

Mismatch diameter fiber networks sculpt asymmetric nuclear shapes and invaginations

Cells in the native fibrous ECM, can interact simultaneously with fibers of different diameter combinations. Hence, we interrogated force dynamics and YAP localization in

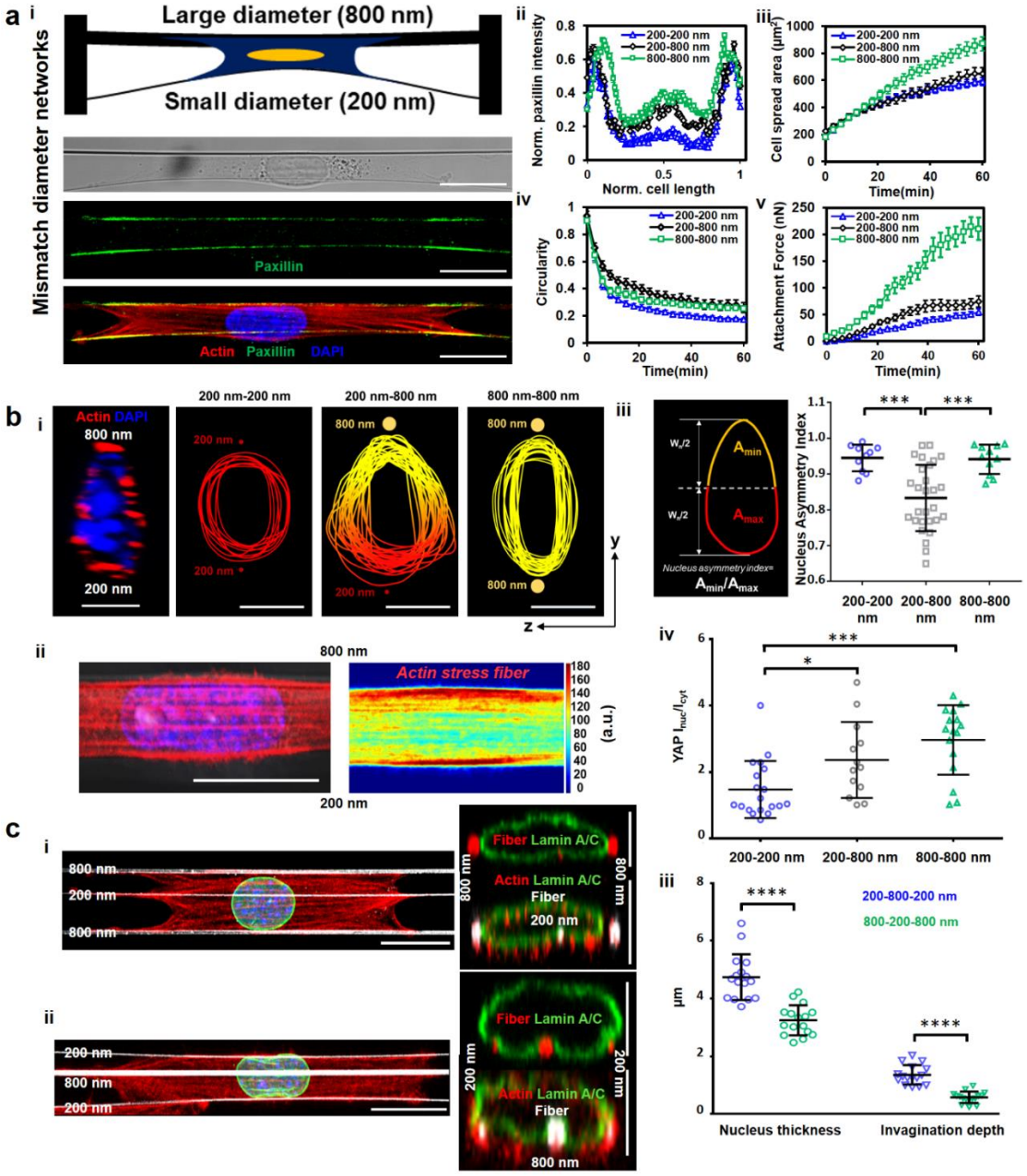

Figure 3.4: Sculpting nucleus shapes using mismatch diameter networks a i) Cells attached to a small diameter (200 nm) fiber coupled on other side to a large diameter (800 nm) fiber, (scale bars, 20 μm) ii) Mismatch fiber combination leads to enhanced focal adhesion organization along smaller diameter fiber, n=10-14 per category, (iii) Increased cell spread area compared to 200-200 nm networks iv) Altered cell shape, n=12-17 per category, v) Force exertion on 200 nm diameter fiber in 200-800 nm mismatch configuration is higher than in 200-200 nm configuration, n=10-12 per category, b i) Mismatch (2-fiber , 200-800 nm) networks induce asymmetric (teardrop) nucleus shape, nuclear cross-sections (yz) perpendicular to cell length are used (scale bars, 5 μm), (ii) Teardrop shapes are formed due to higher density of actin stress fibers at the 800 nm diameter side of cell, n=17 cells, iii) Analysis of teardrop shapes using Nucleus Asymmetry Index, n=10,28 and 11 for 200-200, 200-800 and 800-800

combinations respectively, iv) nuclear/cytoplasmic YAP in mismatch diameter networks, n=19,13 and 16 for 200-200, 200-800 and 800-800 combinations respectively c) i,ii 3-fiber Mismatch (800-200-800 nm and 200-800-200 nm) can induce 'invaginations' in nucleus (yz-cross sections, nuclear envelope stained for lamin A/C, green, fibers, red) , second representative cross-section for each category, is included to demonstrate cytoskeletal caging, actin (red), Lamin A/C (green), fibers (white) and nucleus (blue), (scale bars, 10 µm for top views, 5 µm for cross-sectional views) iii) Comparison of the nucleus thickness and the depth of the invaginations show that 200 nm diameter outer fibers in 200-800-200 nm triplets exert low force causing overall thicker nuclei with larger invaginations due to middle 800 nm diameter fiber , n=16 for both categories.

mismatch diameter nanonets. To this end, we developed a strategy using our STEP platform to deposit nanonets in two mismatch-diameter combinations (2-fiber 200-800 nm doublets, and 3-fiber triplets (200-800-200 nm, and 800-200-800 nm). We reasoned that cell spreading on 200-800 nm doublets would proceed as described in Fig. 1, with cells spreading faster on 200 nm side leading to trapezoidal shaped cells with longer base on 200 nm diameter side. Unexpectedly, we found symmetric spreading on both diameters (**Fig. 3.4a**), but enhanced focal adhesion clustering (with respect to the 200 nm-200 nm counterparts) along the cell-fiber interface on 200 nm fiber side (**Fig 3.4a (i, ii)**) that was similar to the focal adhesion clustering on 800 nm nanonets (**Fig. 3.2a (iii)**). Increased cell adhesion sites on the 200 nm fiber side caused cells to spread more, have higher circularities, and exert larger forces on the 200 nm diameter fiber compared to their counterparts on 200-200 nm nanonets (**Fig. 3.4a (iii-v)**).

Intrigued by the altered force exertion by cells on mismatch nanonets, next, we inquired if YAP localization inside the nucleus was affected as well. First, we investigated the differences in nucleus cell shapes and unexpectedly discovered asymmetric nuclear shapes (tear drop, confocal side view) with the tapered end towards the 800 nm diameter fiber (**Fig. 3.4b (i)**). Analyzing the actin stress fiber distribution across the cells attached to

mismatch diameter doublets revealed a higher density near the larger diameter fibers potentially being the cause of increased nucleus compression (**Fig. 3.4b (ii), Supplementary Fig. 3.S8**). To quantify the teardrop shapes, we defined the nucleus asymmetry index (NAI, **Fig. 3.4b (iii),** Materials and Methods) as A_{min}/A_{max}, where A_{max} and A_{min} are the areas of the larger and smaller regions with respect to the nucleus mid-width line (**Fig. 3.4b (iii)**) respectively. Cells adhering to mismatch doublets demonstrated significant asymmetry (NAI ~ 0.8, **Fig. 3.4b (iii)**), compared with symmetric nuclei on 200-200 and 800-800 nm nanonets (NAI ~ 0.95). Furthermore, the nuclear localization of YAP was found to be significantly enhanced in mismatch diameter fiber networks, as compared to the 200-200 nm, but less than 800-800 nm nanonets (**Fig. 3.4b (iv)**).

Next, we generated 3-fiber nanonets (triplets) that provided symmetric same diameter outer fibers and a mismatch diameter inner fiber (200-800-200 nm and 800-200-800 nm) that resulted in symmetric cell shapes (**Fig. 3.4c (i,ii)**). However, we noted that the shape of nucleus on outer fibers was flattened and at inner fiber had nucleus distortions (invaginations). Visualizing confocal cross-sections (yz) of nuclei, immunostained for Lamin A/C (nuclear envelope marker) revealed several interesting aspects of the overall nuclear geometry. First, the nucleus thickness observed on these mismatch 3-fiber nanonets, demonstrated a similar trend as compared to the same diameter 2-fiber nanonets. Nuclei in cells on 200-800-200 nm nanonets were significantly thicker than those on 800-200-800 nm, just as the nucleus thickness in 200-200 nm nanonets was higher than 800-800 nm nanonets (**Fig. 3.4c (iii)**)). Second, in 3-fiber triplets, we observed the extent of invagination in 200-800-200 nm combination was greater due to lower force exertion of the outside 200 nm diameter fibers (**Fig. 3.4c (iii)**). Overall, our data suggests that nucleus

shape, YAP localization and nucleus invaginations are regulated by the diameter combinations of fibers external to the cell.

Single fibers sculpt curvature-dependent nuclear invaginations

Our observation that single fibers induced nucleus invaginations running along the nuclei length prompted us to investigate the role of curvature in physical indentation of the nucleus. To interrogate this behavior, we utilized a simplified model system of single cell spreading on a single fiber (**Fig. 3.5a**). Immunostaining for the focal adhesions (paxillin) revealed, that similar to the parallel-cuboidal shape cells spread on 2-fiber nanonets, major focal adhesion clusters localized to the poles of the spindle shape cells (**Supplementary Fig. 3.S9a (i)**). We also observed that majority of the actin stress fibers caged the nucleus (**Supplementary Fig. 3.S9a (ii)**), causing local invaginations in the nucleus (**Fig. 5b (i)**). We confirmed that the dynamics of cell spreading and FA cluster formation was similar to our prior observations on 2-fiber nanonets (**Supplementary Fig. 3.S9b (i,ii)**). Next, we varied the fiber diameter over a broad range (~150 nm (high curvature) to > 6,000 nm (low curvature) to understand the extent of fiber-induced local invaginations (**Fig. 3.5b (i)**) in nuclei. We compared the radius of curvature (R_i, **Fig. 3.5b (ii)**) of the nuclear membrane at the invagination site with the radius of best-fit projected circle on the apical side of the nucleus (R_o). With increasing diameters, we found the curvature ratio R_i/R_o linearly scale with the fiber diameter (**Fig. 3.5b (ii)**). We also found the nucleus aspect ratio reduced significantly with increase in fiber diameter indicating a change in nucleus shape from elongated on small diameter fibers to flattened on larger diameter fibers (**Fig. 3.5b (iii)**). With increase in diameters, we observed a drop in the cell aspect ratios (**Supplementary Fig. 3.S9c**), with cells adhering to the 150 nm diameter fibers forming long protrusions and

having the highest aspect ratios. Fluorescent labelling of the fiber (conjugated fibronectin, red) and the nuclear envelope (Lamin A/C, green) revealed, the nucleus to be locally deformed at the location of fiber, thus allowing us to sculpt invaginations of varying sizes and shapes (**Fig. 3.5c (i)**). We quantitated the effective shapes (**S**) of nuclear invaginations with a bell curve defined by $S = S_0 e^{-y^2/2\sigma^2}$, where S_0 denotes the invagination depth (z–direction) and σ is related to the lateral spread (y-direction) of the invagination. We found that nuclear invaginations on lower diameter fibers of high curvatures were typically ~ 2 μm deep (S_0) and narrow (σ ~ 0.4 μm), and with increase in fiber diameters, the size (depth and lateral spread) of these invaginations was found to increase (**Fig. 3.5c (ii)**). However, the sharpness ratio (ratio of S_0 and σ) was the highest for low diameter fibers, which decreased with increase in diameter, indicating smoother nuclear deformations. For all tested diameters, our data showed a strong linear fit between nucleus invagination shapes and fiber diameter.

Next, we wanted to investigate the effect of fiber diameter on the spatial localization of YAP. On the lower diameter nanofibers, cells primarily demonstrated a cytoplasmic YAP localization (**Fig. 3.5d (i)**) with the nucleus/cytoplasmic intensity ratio less than of ~ 1 (**Fig. 3.5d (ii)**). However, with increase in fiber diameters to micron-scale, we observed significantly enhanced YAP localization within the nucleus (**Fig. 3.5d (ii)**). Interestingly, despite various levels of nuclear deformations in both nanofibers and microfibers, the nuclei demonstrated no signs of rupture, as confirmed by no appreciable leakage of NLS (nuclear localization sequence) in cells expressing NLS mCherry (**Fig. 3.5d (iii), Supplementary Fig. 3.S10**). Quantification of NLS localization revealed an average

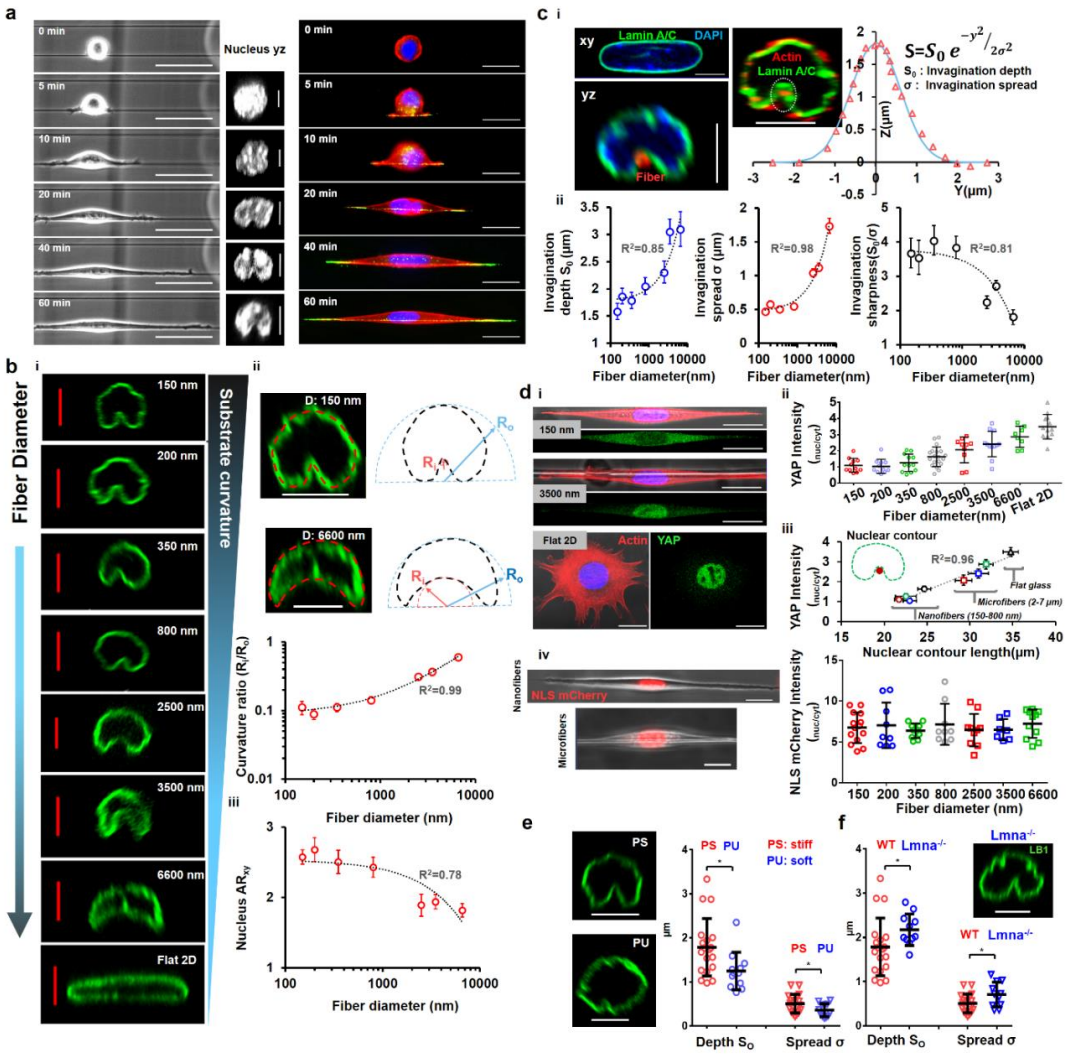

Figure 3.5: Sculpting nucleus invaginations using curvature of single fibers a) i) Timelapse images showing different phases of cell spreading on a 1-fiber system causing cells to spread in elongated spindle shapes, (scale bars, 50 μm), Confocal side views of representative cells at various spreading time points demonstrate the fiber–mediated nuclear deformations (scale bars, 5 μm) , cytoskeletal and focal adhesion arrangement in spindle-shaped cells at various timepoints, actin (red), paxillin (green) and nucleus (blue), (scale bars, 20 μm) b) i) Representative images showing effect of substrate curvature (fiber diameter) on the invagination shape/size, (scale bars, 5 μm) ii) representative images of the deformed nucleus shape on two diameters (150 and 6000 nm, scale bars: 5 μm) and methodology for comparing invagination shapes, Fiber diameter dependence of Curvature ratio: Radius of curvature at the invagination side (R_i) divided by radius of curvature at the nucleus apical side (R_0), n=12,10,17,10,10,9 and 9 respectively, (iii) Nucleus aspect ratio (top view, xy) as a function of fiber diameter, n=14,10,10,11,10,6 and 6 respectively c) i) Nucleus in spindle cells exhibit invaginations near sites of external fibers (red circle), Representative image showing cytoskeletal caging of nucleus in spindle cell, actin (red) and Lamin A/C (green), (scale bars, 5 μm), Invagination shape (shown in white circle) can be approximated with a bell curve, ii)

invagination depth and spread increase with fiber diameter, while invagination sharpness decreases with increase in fiber diameter, n=9-19 cells per diameter category d) i) Representative stained images showing YAP localization in cells on nanofibers, microfibers and Flat 2D, (scale bars, 20 µm) ii) Comparison of YAP localization (I_{nuc}/I_{cyt}) in cells on different fiber diameters and Flat 2D, n=11,11,12,19,10,12,8 and 12 cells respectively, iii) YAP localization as a function of nuclear contour length (n=10-13 cells for each substrate category) , circles represent nanofibers, squares represent microfibers, Flat 2D is marked with triangle iv) Representative cells expressing NLS mCherry, showing primary nuclear localization of NLS on both nanofibers and microfibers , (scale bars, 20 µm) , NLS localization is predominantly in the nucleus in cells attached to fibers of all diameters, n=7-14 cells for each diameter category e) influence of fiber stiffness in regulation of invagination size, n=19,12 for PS and PU respectively, (scale bars, 5 µm) and f) influence of impaired nuclear lamina on invagination size in cells attached to 350 nm diameter fibers, n=19,11 for control, Lamin A/C KD respectively (scale bars, 5 µm). All R^2 values shown are calculated for linear fits. Sample sizes (4b (ii), 4c (ii), 4d (iv)) are given for 150 nm, 200 nm, 350 nm, 800 nm, 2500 nm, 3500 nm and 6600 nm respectively.

nuclear/cytoplasmic intensity ratio > 6 for all fiber diameters, demonstrating NLS to be primarily localized to the nucleus.

Next to investigate the effect of material stiffness, independent of fiber curvature, we used polyurethane (E: 10-100 MPa) and polystyrene (E: 1-3 GPa) fibers of ~350 nm diameters, and observed a significant decrease (**Fig. 3.5e**) in the size of the nuclear invaginations in softer polyurethane fibers. We also inquired the role of lamin A/C in nucleus invaginations, and found that impairing the nuclear envelope caused by knockdown of lamin A/C resulted in significantly larger nuclear deformations (**Fig. 3.5f).** Inhibiting f-actin based contractility through Y27632 treatment resulted in thicker nuclei with significantly smaller nuclear invaginations (**Supplementary Fig. 3.S9b (iv)**).

Multiple fibers of same diameter sculpt nucleus shapes

Since single fibers were causing significant invaginations in the nuclei, we inquired if multi-fiber networks (≥3) of same diameter caused multiple similar sized invaginations.

We deposited 350 nm diameter fibers at low (~3 μm) inter-fiber spacing (**Fig. 3.6 (i)** images shown for single cell attached to five and eight fibers). We found that cell and nucleus aspect ratios (at the spread state) were reduced with the increase in the number of fibers (**Fig. 3.6 (ii)**). Also, the increased compression mediated by the cytoskeletal caging caused a significant reduction in nucleus thickness and invagination depth (**Fig. 3.6 (iii)**). Additionally, these deformations failed to generate ruptures in the nucleus, as confirmed by the spatial localization analysis of NLS (**Supplementary Fig. 3.S10**). We also quantified the shapes of nuclei at the apical and basal sides in cells attached to flat 2D, 1-fiber, two- fiber, and multiple fiber systems by quantifying the curvature of the nuclear envelope at the apical and basal side (**Fig. 3.6 (iv)**). Consistent with previous literature[101,105], our results indicate that on flat continuous surfaces, the nucleus is mostly pancake-shaped, which differs from cells on suspended 2-fiber parallel doublets, where the nucleus is mostly ellipsoid shaped, with equivalent curvatures on both apical and basal sides. In multifiber networks, we found the nucleus shape to have a flatter surface (low curvature) at the basal side, primarily due to cell attachment to multiple underlying fibers. In comparison, presence of the fiber-induced invaginations in the spindle-shaped cells results in a much shaper curvature (inward) at the basal side. Concurrent with our previous findings that increasing the number of fibers results in increased cell contractility[94], we found that for the same diameter, increasing the number of fibers results in a decrease in nucleus thickness (**Fig. 3.6(v)**). Interestingly, enhanced nuclear compression caused by cell attachment to multiple fibers led to a significant increase in the nuclear

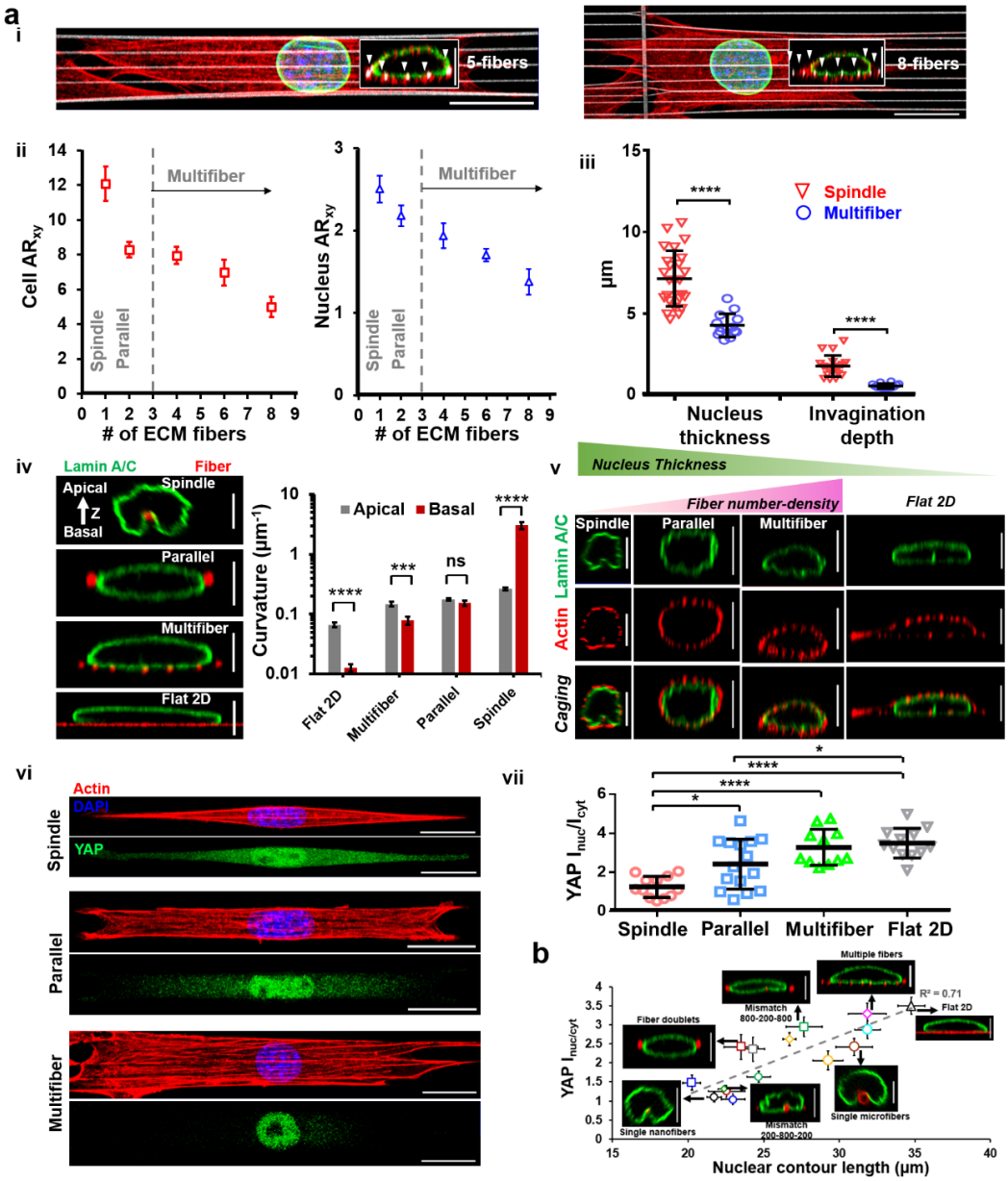

Figure 3.6. Nuclear geometry and YAP localization in cells attached to multiple fibers of same 350 nm diameter a) i) Representative images of cells attached to 5 and 8 fibers (350 nm diameter) respectively, stained for actin (red), Lamin A/C (green) and nucleus (blue). Fibers are coated with rhodamine fibronectin (pseudo-colored white), Insets are cross sections (yz), showing the cytoskeletal caging of the nucleus with fibers identified with white arrowheads (scale bars, 20 μm and 5 μm for main and inset images respectively), ii) comparison of the cell and nuclear aspect ratio (xy top view) as a function of the number of interacting fibers, n=10, 24, 6, 7 and 5 iii) nucleus thickness (n=25,14) and invagination depth (n=19,14) in spindle (1 fiber) versus multifiber (≥ 3 fibers) systems, and iv) Representative nuclear cross sections (yz) demonstrating shape sculpting over different substrates, Analysis of curvatures at the apical and basal side of the nucleus for the different substrates, note, only curvature magnitude is

considered here, spindle basal curvature being inward, is of opposite sign as compared to all other categories, n=11, 16, 11 and 18 for Flat 2D, multifiber, parallel (2-fiber) and spindle (1-fiber) respectively, v) Representative images showing the caging effect and nuclear compression as a function of fiber-number density, Flat 2D is shown for reference, actin (red), Lamin A/C (green) (scale bars, 5 μm), vi, vii) Comparison of YAP localization between spindle, 2-fiber, multifiber systems and flat 2D, n=12, 15, 11 and 12 respectively, Representative cells are stained for actin (red), YAP (green) and nucleus (blue), (scale bars, 20 μm). b) YAP localization across single, 2 fiber and multifiber configurations of all diameters and interfiber spacing in the study showing positive correlation between YAP localization and increase in contour length (n=8-16 cells for each substrate category), small and large circles represent nanofibers and microfibers, squares represent fiber doublets (same diameter and mismatch), polygons represent 3-fiber mismatch and multifiber configurations, Flat 2D is marked with triangle.

translocation of YAP, as compared to spindle and parallel-cuboidal cells attached to single or two fibers of the same diameter, respectively (**Fig. 3.6 (vi-vii)**). To understand how different fiber configurations led to altered nuclear entry of YAP, we computed the stretching of the nuclear contour (yz cross-section) due to local invaginations (single fibers) or compression (fiber doublets) or both (multiple fibers) and observed a distinct increase in the contour length in cells attached to micron-scale fibers or multiple fibers. In general, nuclear YAP localization for different fiber configurations and Flat 2D demonstrated a strong dependence on the nuclear contour length (R^2=0.71, **Fig. 3.6b**).

Overall, our observations show that the organization of contractile f-actin network in spindle cells on single fibers induces nucleus invaginations in a diameter dependent manner, while the same f-actin network in cells attached to multiple fibers, leads to higher levels of nuclear compression but reduced local invaginations, and causes distinct YAP translocation to the nucleus. Irrespective of the shape, sharpness and number of invaginations, we find that nuclei of cells attached to fibrous matrices remain rupture-free.

3.4 Discussion

Nucleus shapes have been studied in a wide range of *in vitro* settings, but the role of physiological fibrous ECM such as those found in skeletal muscle tissue and around metastatic tumors [35,78,79], in controlling nucleus shapes remain poorly described. Fibrous ECM environments are composed of a mix of diameters (individual nanoscale fibrils that combine into larger hundreds of nanometer or micron-scale bundles) distributed in a wide range of orientations and inter-fiber spacing. In ECM regions with a large number of contact sites (small pore size), cells sense confinement, and with few contact points (large pore size), cells make contact with only single fibers [106–108]. With differing contact points across multiple diameters, cell contractility is altered [90], resulting in changes in overall cell [89,91] and nucleus shape. Here, using nanofiber networks of precisely controlled geometries and fiber diameters, we explore the mechanosensitivity of cells to fibrous microenvironments. Our method of precisely controlling the external fibrous environment led to exquisite sculpting of nucleus with and without invaginations across multiple cell lines (C2C12 mouse myoblasts, HT1080 human fibrosarcoma and HeLa cells, **Supplementary Fig. 3.S11**). Irrespective of the shape or sharpness of the invaginations, we found nuclei to remain rupture free and fiber-diameter driven contractility and network organization to regulate translocation of mechanosensitive YAP to the nucleus.

To understand fiber diameter driven contractility and associated nucleus shape changes, we estimated the increase in contractility as rounded cells spread along the fibers. While the cell spreading behavior on fibers was similar to reported flat 2D behavior [109], the spreading rates were fiber diameter dependent, with cells attached to thinnest fibers achieving steady-state spread areas the earliest. In the spread state, although actin,

microtubules and vimentin localize at the apical side in cells on 2D, we found them to *cage* the nucleus with no apical-basal preference in suspended cells. Even in cells spreading on single or multiple fibers, where regions of cell contact with fibers act as pseudo-basal regions, we observed a uniform distribution of Lamin A/C expression (**Supplementary Fig. 3.S9d**). In all diameter combinations, focal adhesions were preferentially localized to the poles as cells spread on the fibers, consistent with their localization pattern during spreading at the peripheries in cells on flat 2D and the poles in cells on micropatterned substrates [110]. The clustering of focal adhesions to the poles occurred early in the cell spreading phase (~20 min), resembling those observed in 3D cell-derived matrices (37, 38). Additionally, our observations that the lengths of FA clusters at the poles and the number of focal adhesions along the cell-fiber contact length increased with fiber diameter, may potentially explain the slower spreading observed on larger diameter fibers.

Cell contractility increased with diameter, and we compared forces, estimated using Nanonet Force Microscopy (NFM) with other force measurement techniques using two metrics: traction stress and tension per stress fiber. The average stress per FA cluster (Force/ FA $cluster_{area}$, where FA $cluster_{area}$ = FA $cluster_{length}$ * $Diameter_{fiber}$) was found to be ~8, 9, and 7 nN/μm^2 for 200-200, 350-350, and 800-800 nm doublets, respectively, which is similar to the reported values of stress per focal adhesion in the literature (~6 nN/μm^2) [113,114]. We approximated the tension in individual stress fibers by assuming their arrangement to be similar to be mechanical springs in parallel. Dividing the force per FA cluster at spread state (60 min time point) with the number of stress fibers associated with each cluster, we obtained the tension in each stress fiber to be ~7, 11, and 15 nN for 200-200, 350-350, and 800-800 nm doublets, respectively, which agree with reported values

(2-10 nN) (41, 42). The ability to estimate spreading forces allowed us to examine the extent of nucleus compression as a function of fiber diameter. Since 800-800 nm doublets were exerting the highest forces, not surprisingly, the nuclei in these networks had the highest compression that matched the thickness of nuclei on flat 2D[105,117]. Loss of actin tension via cell treatment with cytochalasin D alleviated nucleus compression, a behavior consistent with previous findings [118], while the loss of microtubules via nocodazole treatment did not affect the nucleus compression. On the other hand, reduction in stiffness of the nucleus and lamin A/C KD resulted in increased compression while stiffening the nucleus reduced nucleus compression. Previous studies have shown that nucleus flattening causes stretching of the nuclear pore complexes [65] (NPCs), which lead to the nucleo-cytoplasmic shuttling of various transcription factors, including YAP/TAZ [65] and HDAC3 [67]. Across the tested diameters, our studies concluded that YAP localization increased with cell spreading due to increasing contractility. Importantly, our studies showed that for similar levels of contractility but different spread areas, YAP translocation remained similar.

We also generated *in vitro* fibrous environments of a mix of diameter combinations to mimic ECM heterogeneous fibrous environments. First, we generated 200-800 nm fiber diameter mismatch doublets to study altered cell spreading, contractility, and nucleus shape. Unlike FA clustering patterns observed during cell spreading on homogenous doublets (200-200 or 800-800 nm), unexpectedly, we found a higher density of focal adhesion sites on the 200 nm diameter that matched the adhesion sites' pattern on the 800 nm diameter fiber, resulting in delayed cell spreading. Moreover, the 200 nm diameter fibers deflected more than the corresponding deflection in a 200-200 nm homogenous doublet, resulting in increased contractility. Confocal side views (yz) in mismatch doublets

showed the nuclei to have a remarkable teardrop shape (~60% cases), with the broad end towards the 200 nm diameter. Intensity analysis of f-actin stress fiber distribution across the cell body in mismatch doublets revealed a higher density of stress fibers towards the 800 nm diameter fiber, thus contributing to the increased compression of nucleus. We then proceeded to generate triplets composed of two same diameter outer fibers and a third middle fiber of different diameter (200-800-200 nm, and 800-200-800 nm). We observed the 800 nm diameter fiber to induce large invaginations in the nucleus in 200-800-200 nm triplets, which is consistent with the finding that the outer larger diameter pairs caused significant nucleus compression due to higher contractility. The effect of middle fiber in either of these triplets did not affect cell spreading behavior.

Nucleus invaginations have been previously reported using micropillars at sites of contact [119,120]. In contrast, here we demonstrate that the invagination in the nucleus occurs across the entire length of the nucleus. Naturally, we inquired if these invaginations' size depended on the fiber diameter. Our earlier work has shown that cells attached to < ~100 nm diameter fibers remain rounded, while those attached to larger diameters form elongated spindle shapes[86]. Thus, we chose the fiber diameters to range from 150-6600 nm. Immunostaining for actin and paxillin revealed that actin stress fibers connecting the FA clustering zones straddled the nucleus, thus causing compression of the nucleus and invaginations. The high curvature (low diameter) fibers caused the sharpest invaginations (S_0/σ), which transitioned to smooth wider invaginations with increase in diameter. Despite such extreme nuclear invaginations during cell spreading, no nuclear rupture events were detected. Recently, single migrating cells have been shown to undergo nucleus rupture when they are subjected to confinement of ~3 μm [121]. Our studies, on the other hand were able to get the nucleus to

compress to a height of ~4 μm. Under these conditions, we show that while fiber curvature and compression directly contribute to YAP localization, they are insufficient to cause nucleus rupture. Increasing the number of fibers of the same diameter (350 nm) further decreased the nucleus' height, due to increased contractility, resulting in reduced invagination depth compared to a single 350 nm diameter fiber. However, these conditions still remained insufficient to cause nuclei to rupture during cell spreading.

3.5 Conclusion

Here, we demonstrate sculpting of nucleus shapes and its functional response using *in vivo* mimicking fibrous environments through regulation of cell contractility in a fiber-diameter and number-density manner. The nuclei remain robust mechanical organelles capable of withstanding extensive shape changes and invaginations without undergoing rupture. We envision that control of nuclear 3D shape in these environments will yield new fundamental insights on the ECM-mediated alterations in the sub-nuclear chromatin organization and overall gene expression during cancer metastasis, wound healing, cell differentiation, and myogenesis.

Supplementary Material

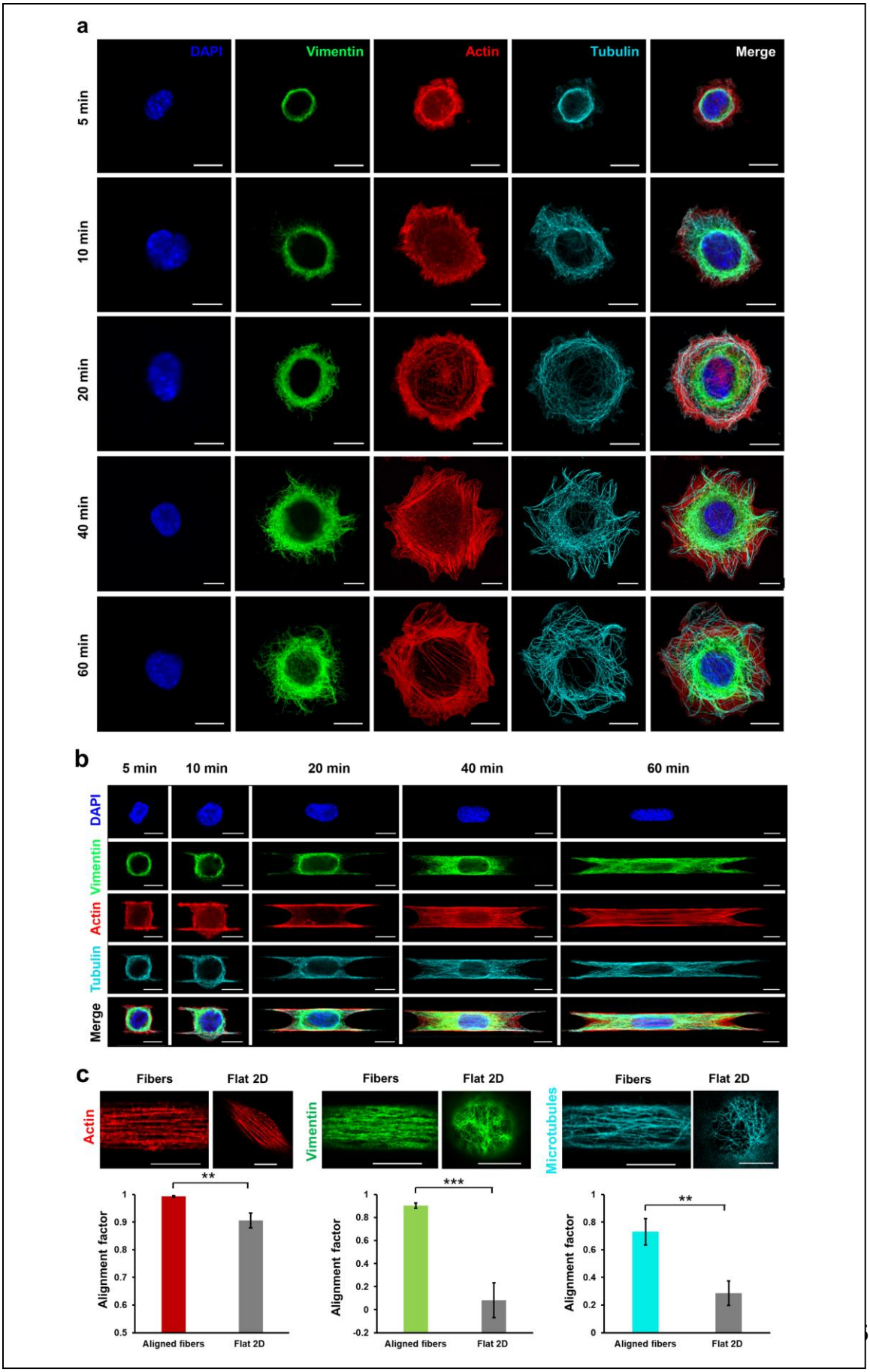
a
DAPI
Vimentin
Actin
Tubulin
Merge
5 min
10 min
20 min
40 min
60 min
b
5 min
10 min
20 min
40 min
60 min
DAPI
Vimentin
Actin
Tubulin
Merge
c
Fibers
Flat 2D
Actin
Vimentin
Microtubules
**
***
**
Alignment factor
Aligned fibers
Flat 2D

Supplementary Figure 3.S1. Cytoskeletal alignment in suspended fibers a,b) Representative cells showing cytoskeletal organization at different timepoints during spreading on flat glass and suspended fiber doublets (fiber diameter: 350 nm) respectively, cells are stained for actin (red), vimentin intermediate filaments (green), microtubules (cyan) and nuclei (blue), cells on fibers show entry of microtubules and intermediate filaments into the protrusions as spreading progresses, scale bars represent 10 µm c) Comparison of the alignment of the cytoskeletal elements in the perinuclear region, between flat glass and suspended fibers (fiber diameter: 350 nm). Alignment factor is defined as cos(2α) where α is the orientation of the actin stress fiber or individual pores within the microtubule or intermediate filament meshwork, with respect to the primary cell orientation, Alignment factor ~ 1 for perfect alignment and ~ 0 for random alignment, scale bars represent 10 µm, n=5-6 cells for aligned fibers and Flat 2D respectively.

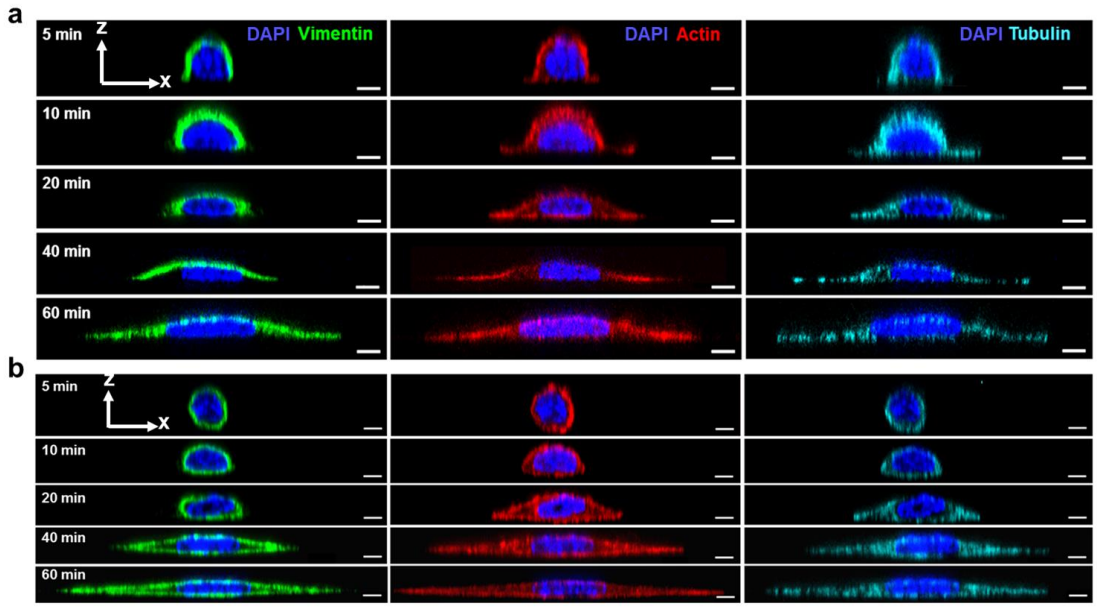

Supplementary Figure 3.S2. Spatiotemporal localization of cytoskeletons a) Confocal side views (xz) showing 'Capping' localization of the cytoskeletal elements at various timepoints during cell spreading on flat glass b) 'Caging' localization observed in suspended fibers (fiber diameter: 350 nm), actin (red), vimentin intermediate filaments (green), microtubules (cyan) and nuclei (blue), all scale bars represent 5 µm

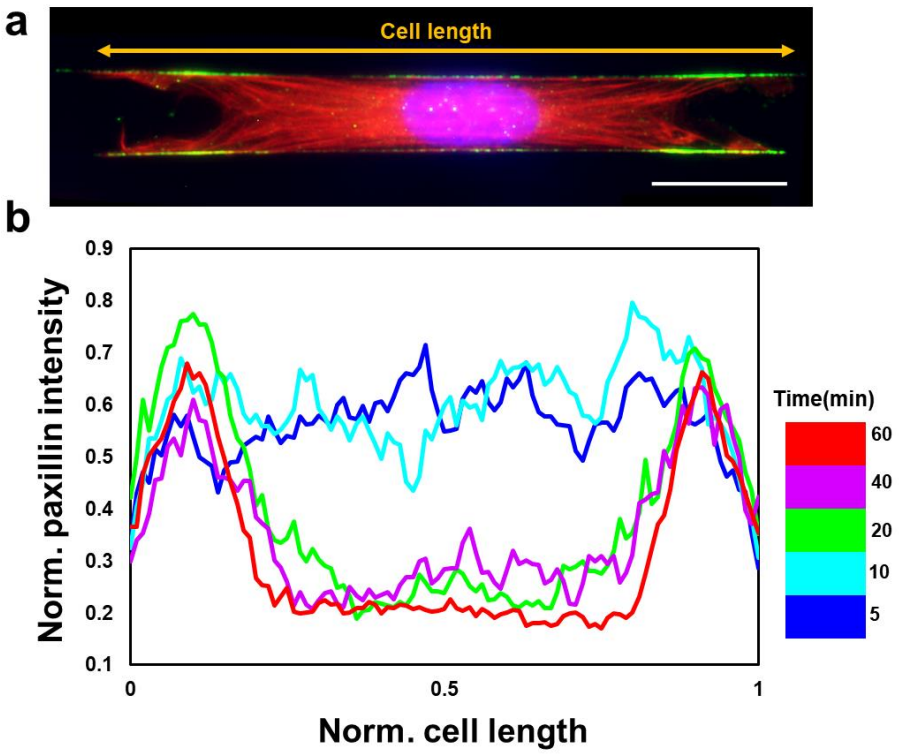

Supplementary Figure 4.S3. Evolution of focal adhesion organization over the course of cell spreading a) Representative spread cell showing focal adhesion clustering at cell poles, scale bars represent 20 µm, b), Average profiles (n=9-12 for each timepoint) are shown, Paxillin intensity is normalized with respect to the peak intensity of each profile, Cell length normalization was performed with respect to the entire length of the cell as shown in part a, In the spread state, two intensity peaks demonstrate the focal adhesion clustering, Data is shown for 350 nm diameter category

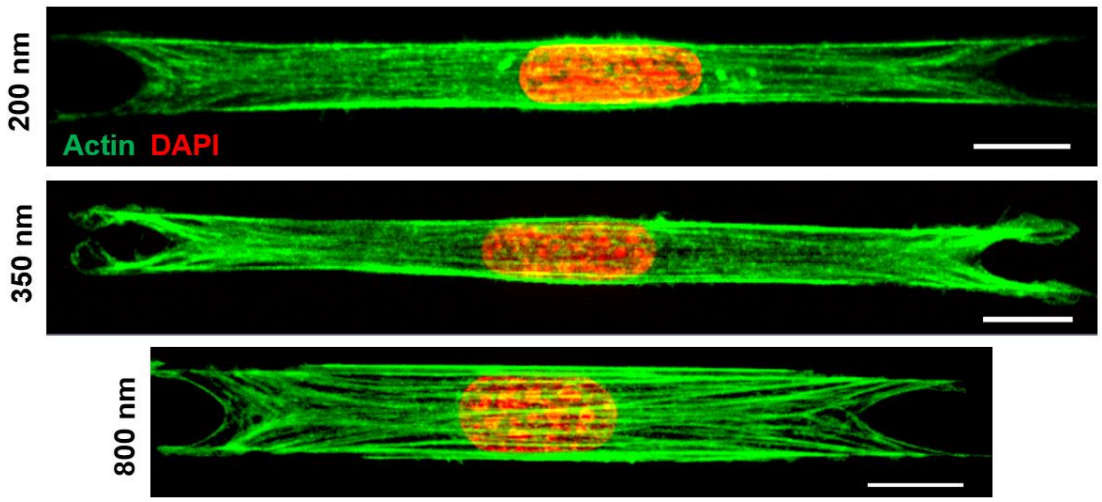

Supplementary Figure 3.S4: Stress fiber organization in spread cells, Maximum intensity projections of representative cells demonstrating stress fibers emerge from focal adhesion clusters on either side and converge to become almost parallel to the cell orientation, in the perinuclear region. Actin and DAPI are pseudo-colored in green and red for better visualization. Scale bars represent 10 µm.

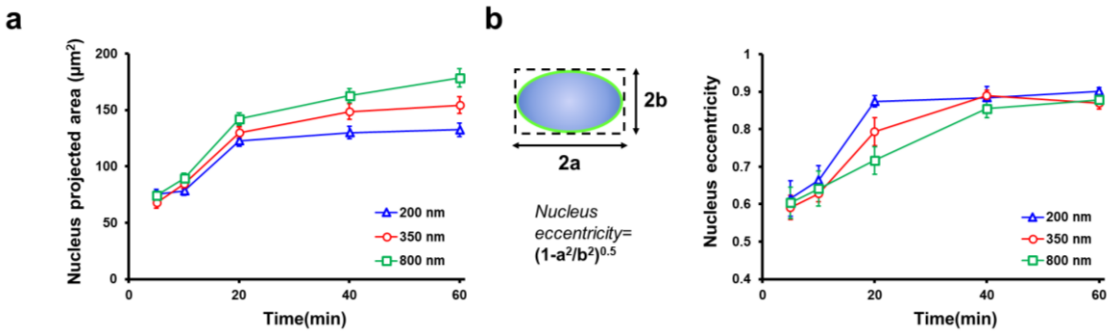

Supplementary Figure 4.S5: Nucleus geometry during cell spreading a,b) Evolution of nucleus projected area (xy) and eccentricity as function of spreading time and shown for the different diameter fiber doublets, respectively, n=17-34 per timepoint for each diameter

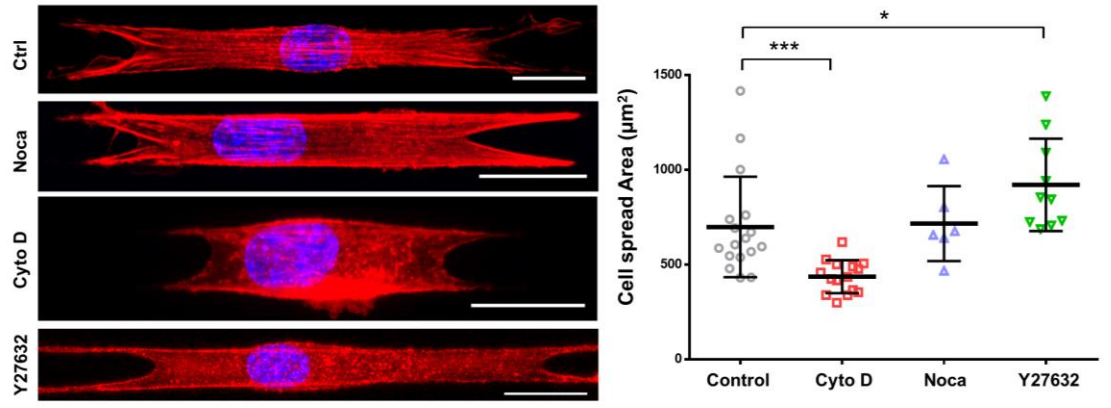

Supplementary Figure 3.S6: Effect of cytoskeletal inhibition on cell spreading, Representative images showing control (no treatment), cytochalasin D, nocodazole and Y27632 treated cells, fiber diameter: 350 nm, scale bars represent 20 µm. Comparison of the cell spread area under different drug conditions, n=17,15,6 and 10.

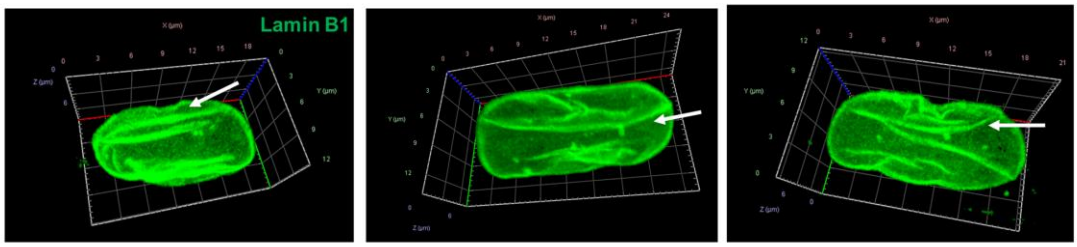

Supplementary Figure 3.S7: Morphological alterations in Lamin A/C KD cells a) 3D isometric views showing wrinkled morphologies of Lamin A/C KD cells, white arrows indicate wrinkles, Lamin B1 is shown in green

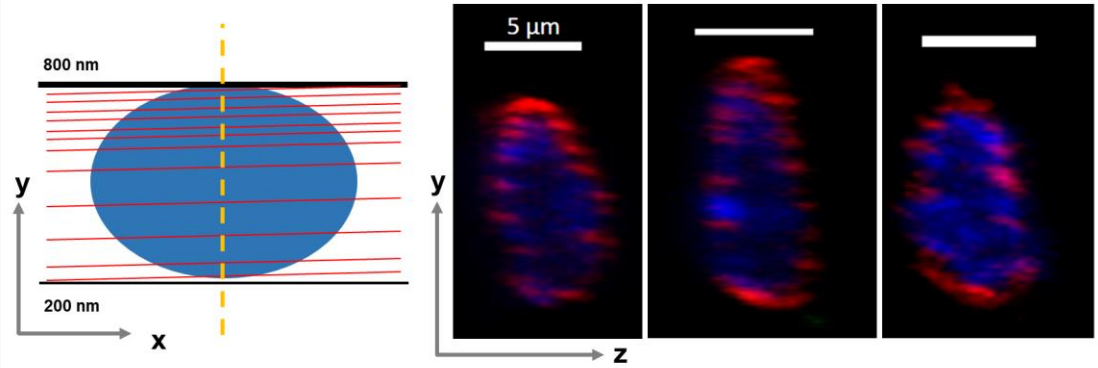

Supplementary Figure 3.S8 : Asymmetric organization of actin stress fibers leading to teardrop shaped nuclear cross-sections. Specifically higher density of stress fibers towards the 800 nm fiber side leads to greater reduction in nucleus thickness

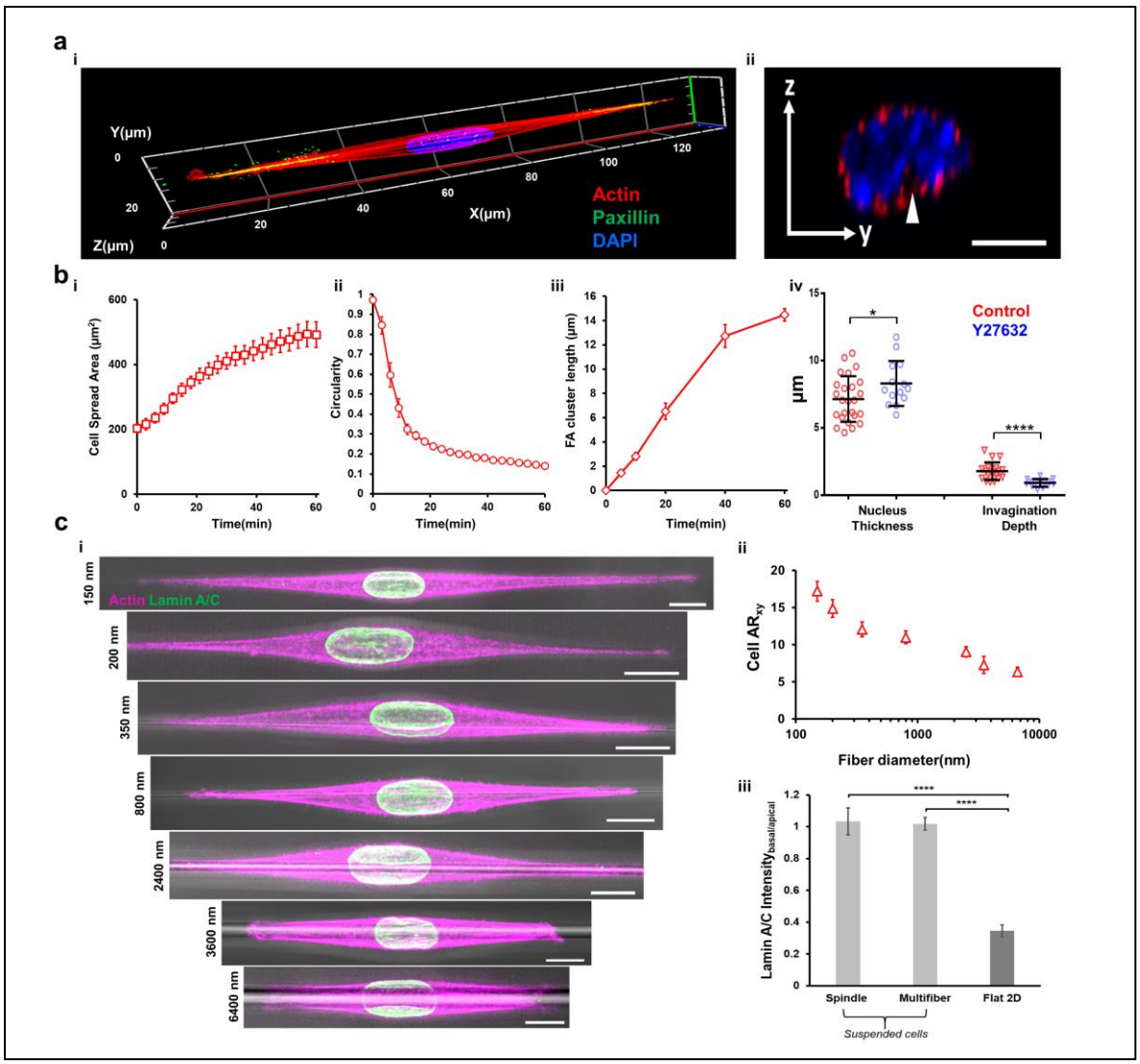

Supplementary Figure 3.S9. Cell and nucleus shapes in spindle cells: a) i) 3D isometric view of spindle cell stained for actin (red), paxillin (green, shown with yellow arrows) and nucleus (blue) ii) Representative confocal side views (yz) showing stress-fiber mediated caging of nucleus in spindle shaped cells, scale bars represent 5 μm b) i.ii) Temporal evolution of cell spread area and circularity for spindle cells, n=15 cells, fiber diameter: 350 nm, iii) Focal adhesion cluster (FAC) length evolution during cell spreading, n=34.47,32,17 and 34 for 5, 10,20,40 and 60 min respectively, iv) Effect of cell contractility inhibition on nucleus thickness and invagination size in spindle cells, (fiber diameter: 350 nm) c) i) Representative images showing variation of cell/nucleus shape as the fiber diameter is varied from 150-6600 nm. Actin (magenta) and lamin A/C (green) are overlaid with the brightfield channel to show underlying fibers, scale bars represent 10 μm ii) Cell aspect ratio as a function of fiber diameter, n=14,10,10,11,10,6 and 6 for 150,200,350,800,2500,3500 and 6600 nm respectively iii) Localization of lamin A/C at the basal (contact points with fiber) and apical surfaces for spindle (1-fiber) and multifiber configurations, Flat 2D is included for comparisons (n=5-10 cells).

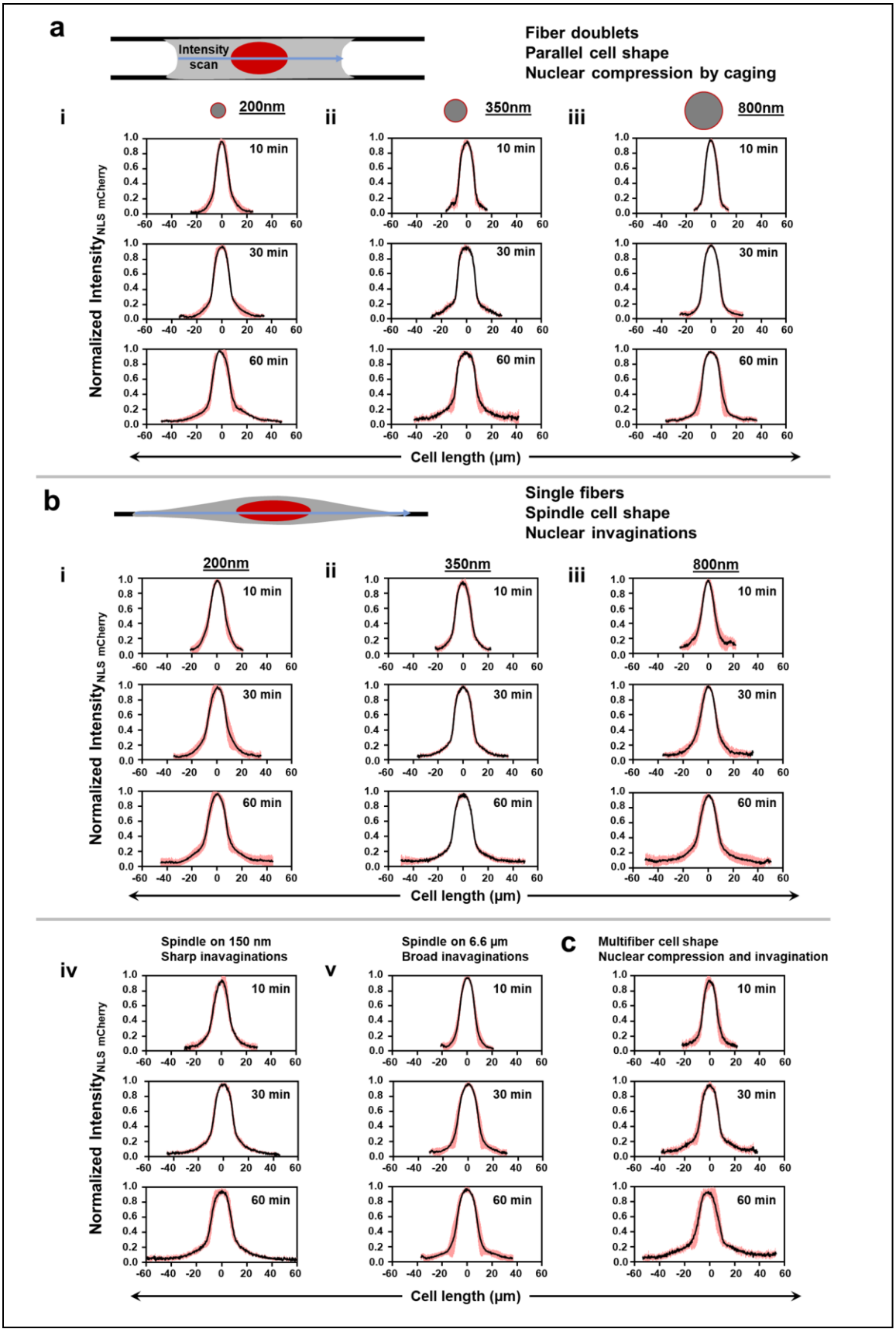
a
Intensity scan
Fiber doublets
Parallel cell shape
Nuclear compression by caging
i
200nm
ii
350nm
iii
800nm
10 min
30 min
60 min
Normalized Intensity NLS mCherry
Cell length (µm)
b
Single fibers
Spindle cell shape
Nuclear invaginations
iv
Spindle on 150 nm
Sharp inavaginations
v
Spindle on 6.6 µm
Broad inavaginations
c
Multifiber cell shape
Nuclear compression and invagination

Supplementary Figure 3.S10. NLS localization in aligned fibers a) i,ii,iii) NLS intensity profiles, along cell length at different spreading timepoints (~ 10,30,60 min) corresponding to fiber doublets with 200 nm , 350 nm and 800 nm respectively, Schematic illustrates the direction of intensity scans b) i,ii,iii, iv and v) Spatiotemporal NLS localization for spindle shaped cells corresponding to fiber diameters: 200, 350 ,800, 150 and 6600 nm respectively c) Intensity analysis for multifiber (D: 350 nm) cells, n=10 cells for each timepoint and substrate category. Error bars represent standard deviation.

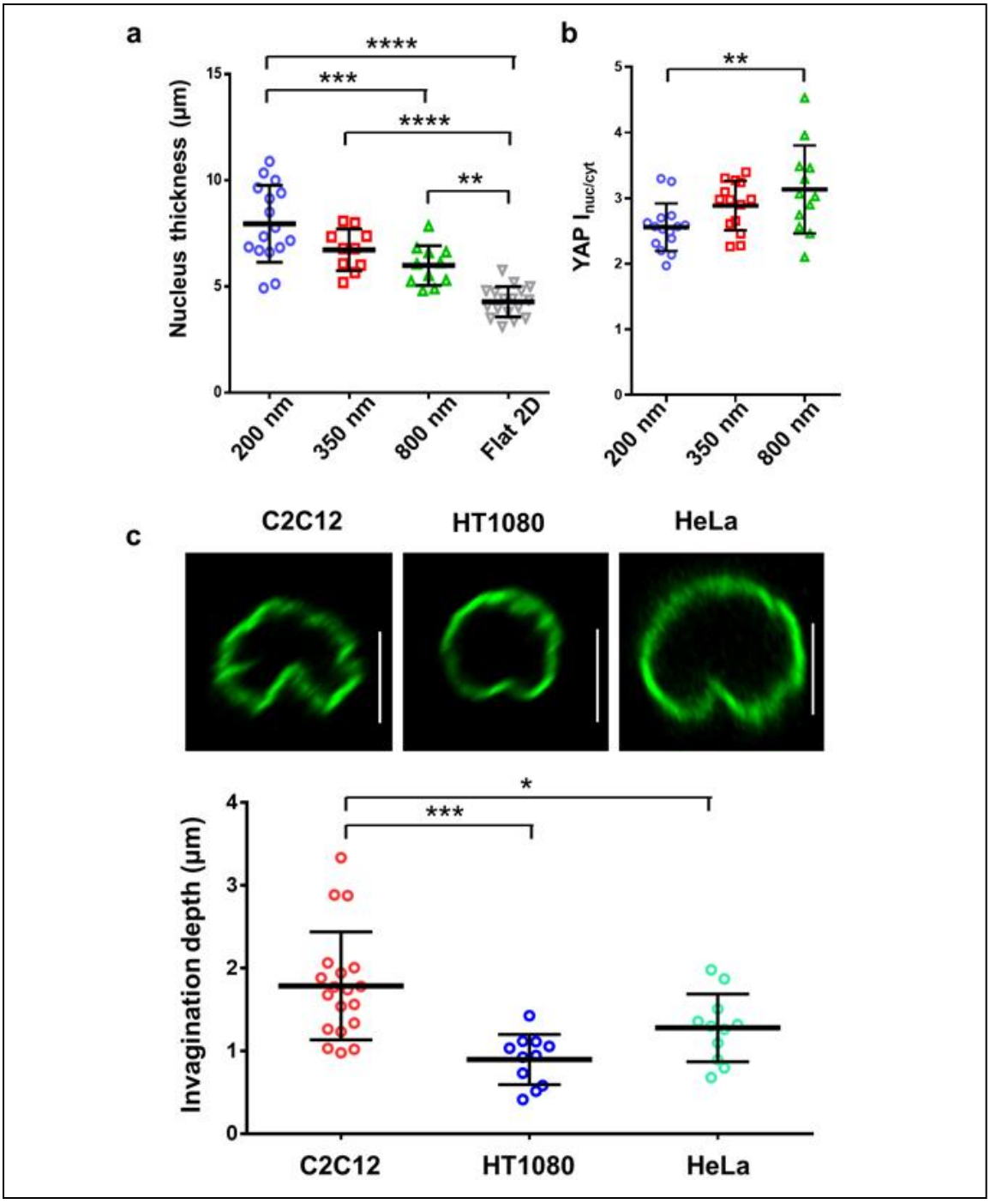

Supplementary Figure 3.S11. Nucleus shape regulation mode is independent of cell line: a) Fiber diameter dependence of nucleus thickness in HT1080 fibrosarcoma cells b) Enhanced nuclear translocation of YAP for HT1080 cells in 800 nm networks. c) Nuclear invaginations are observed in spindle cells for all cell types tested (C2C12, HT1080 and HeLa), comparison of the invagination depths in the different cell types for 350 nm diameter single fibers, scale bars represent 5 µm.

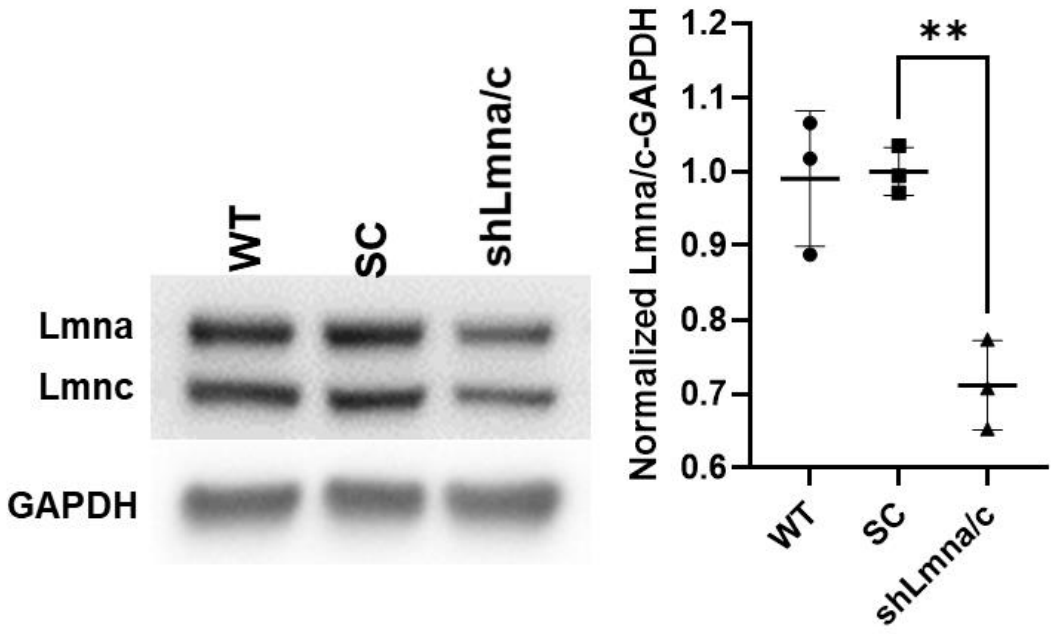

Supplementary Figure 3.S12: Western blot showing partial knockdown of Lamin A/C in C2C12 cells. SC stands for scramble with null expression.

Chapter 4:

Crosshatch nanofiber networks of tunable interfiber spacing induce plasticity in cell migration and cytoskeletal response

4.1 Introduction

Cell migration plays a critical role in the development, repair and disease biology. Notably, in cancer, cell metastasis from tumors often portends unfortunate life-ending outcomes. Migratory metastatic cells take advantage of both biophysical and biochemical cues present in the surrounding extracellular matrix (ECM) to achieve persistent migration. While it is easy to visualize how the aligned (parallel) arrangement of ECM individual strands or groups of strands favor cells to invade neighboring stroma followed by persistent migration, we inquired if alignment was the only fiber configuration capable of promoting and sustaining persistent migration that is observed along the metastatic journey? This seemingly straightforward question has been difficult to resolve due to challenges in imaging deep inside the body over long periods,[122,123] and recapitulation of structures *in vitro.*[83] Thus, it is not uncommon to find illustrations of fibrous ECM interfacing with tumors depicting the existence of both aligned fibers and non-aligned configurations of varying pore sizes and lengths that are able to support persistent migration.[2,124–130]

*In vivo, c*ells migrate through fibrous ECM or on top of the dense basement membrane of varying porosities.[38,46,131–134] Currently, a large number of *in vitro* strategies exist to investigate cell migration. Perhaps the most widely used method involves culturing cells on featureless flat 2D substrates that describe cell migration to occur in short phases of cell motion interspersed with random changes in the migration direction and periods of cell

inactivity. These steps collectively are described by classic random walk.[135,136] To achieve persistent cell migration, a number of strategies (micropatterned stripes, microchannels, microgrooves, etc.) [107,137–143] have been devised, which mechanically confine cells to have aligned 1D morphologies. To investigate cell migration in a 3D environment, cells are embedded in a 2.5 or 3D gel systems, and gels with built-in anisotropy recapitulate persistent migration.[35,82,144–146] The given complexity and the inter-connectivity of ECM biophysical parameters (stiffness, fiber size and alignment, pore size, and architecture) [35,37,44,79,106,147–154] makes it exceedingly difficult to elucidate the role of individual parameters in persistent cell migration. Thus, it is not surprising that in a recent commentary it was noted that there are generally no accepted methods to cross-validate *in vitro* findings, and to compare them with *in vivo* behavior.[83]

While many *in vitro* strategies (including by us) have demonstrated anisotropic migration using aligned geometries, the contributions of other configurations including crosslinked networks of varied inter-fiber spacing remain unclear. Here, using our previously reported non-electrospinning spinneret-based tunable engineered parameter (STEP) technique,[92,155–157] we use nanofiber crosshatch networks of tunable inter-fiber spacing to interrogate at high spatiotemporal resolutions the plasticity of single cell migratory behavior and cytoskeleton arrangement in Hras 1 murine cell line. We chose Hras 1, as it is derived from an aggressive follicular thyroid cancer, a tumor with highly invasive capacity and propensity to metastasize to distant sites, primarily the lungs.[158] This tumor has increased levels of lysyl oxidase (Lox) enzyme that crosslinks the collagenous ECM, thus imparting collagen fibers increase stability and stiffness; known promotors of tumor progression.[74] Using crosslinked nanofibers in a two-layer fiber system, we show that

contrary to intuition, dense (low inter-fiber spacing) crosshatch networks that resemble 2D flat surfaces, cause cells to migrate persistently (1D) in 3D shapes, whereas increasing inter-fiber spacing recapitulates 2D shapes and random walk migration. Furthermore, through high spatiotemporal resolution microscopy and genome sequencing, we show that inter-fiber spacing is a regulator of focal adhesion clustering, nucleus thickness and strain, f-actin stress fiber organization and differential upregulation of metabolic pathways. Using multiple migratory cell lines (mouse NIH 3T3 fibroblasts, and human smooth muscle cells, mesenchymal stem cells and cancerous MDA-MB-231 cells), we find similarities in the migratory phenotype, and show that alignment is not the only requisite biophysical configuration for achieving high-speed persistent migration.

4.2 Materials and Methods

Fiber network fabrication and characterization

Preparation of nanofiber networks

Polystyrene ((PS) molecular weight: 2,000,000 $g.mol^{-1}$, Scientific Polymer Products Inc., Ontario, NY, Catalog# 829) was dissolved in xylene (Fisher Scientific, Pittsburgh, PA, Catalog# X5-500) to form a 10 wt% solution. Isotropic crosshatch networks of nanofibers, with tunable inter-fiber spacing and a uniform fiber diameter of ~ 500 nm, were then fabricated using the STEP technique. Briefly, PS was dissolved in p-xylene for at least a week to prepare a polymeric solution for fiber spinning. The solution was extruded through a micropipette (inside diameter ~100 μm, Jensen Global, Santa Barbara, CA, USA) to deposit suspended and aligned fibers in parallel and crosshatch patterns.[159] Fused-fiber networks were created using a custom fusing chamber.[160]

AFM characterization of fiber networks

Fused fiber networks on hollow stainless steel scaffolds (3mmx3mm hollow square region), were mounted on a plastic wedge with a 12^{o} incline that was subsequently placed in the substrate holder of an Atomic Force Microscope (Veeco, Plainview, NY). A tipless SiN AFM cantilever (AppNano, Mountain View, CA, Catalog# FORTA-TL-10) was used to measure the stiffness in contact mode. Cantilever stiffness (2 N/m) was measured by thermal tuning (average value from 8 independent tests). Deflection sensitivity (nm/V) was obtained using the standard approach of probing a hard surface (stainless steel surface used) in contact mode. Using the above two parameters, Force-distance (F-d) curves were directly obtained from the Deflection error (V) vs z (distance) plots generated in contact mode AFM. The bending stiffness of the fiber networks were then evaluated from the slope of the linear region in the F-d curves.

Cell culture, imaging and RNA extraction

Cell seeding

The nanofiber networks were mounted in individual wells of a six-well plate and sterilized with 70% ethanol for 10 min, followed by rinsing them twice with Phosphate Buffered Saline (PBS). Subsequently, the networks and flat glass were functionalized by coating with 4 µg/ml of fibronectin (Sigma-Aldrich, Catalog# F1141-1MG) for one hr at 37 ^{o}C. Hras1 cells were obtained from an Hras^{G12V}/Pten KO murine thyroid tumor.[158] Cells were confirmed to be mycoplasma negative by PCR, and the cell line was authenticated using short tandem repeat (STR) DNA profiling (DDC Medical). Cells were cultured in F12 medium (Fischer Scientific) supplemented with 10% fetal bovine serum in T25 flasks kept

at 37°C and 5% CO_2 in a humidified incubator. 3T3 fibroblasts (ATCC, Catalog# CRL-1658) were cultured in Dulbecco's modified Eagle Medium (DMEM) supplemented with 10% fetal calf serum at 37°C and 5% CO_2 in a humidified incubator. MDA-MB-231 cells (ATCC, Catalog# HTB-26) were cultured in Leibovitz (L15) medium supplemented with 10% fetal calf serum at 37°C in a CO_2-free environment. Smooth muscle cells (gift from University of Pittsburgh)[161] were cultured in smooth muscle basal cell medium (Cell Applications Inc., San Diego CA) at 37°C and 5% CO_2 in a humidified incubator. Bone Marrow-derived human Mesenchymal Stem Cells, hMSCs (Lonza Inc, Basel, Switzerland) were cultured in supplemented growth medium (Lonza Inc) at 37°C and 5% CO_2. The functionalized nanofiber networks were seeded with a low concentration (~$7*10^4$ cells/ml, 50 µl added to each well) of cells and allowed to attach and spread on the fiber networks for 1 hour followed by addition of 2 ml of media and 2% penicillin-streptomycin to each well to prevent contamination during the experiments. Time-lapse optical microscopy for migration characterization was subsequently performed for at least 8 hours with an interval of either 5 or 10 minutes, using a 20x (Plan-Apochromat 0.8 NA) objective.

Fluorescent imaging

Fixed immunofluorescent staining was performed on the cells for F-actin, focal adhesion protein paxillin and nucleus. Cells were fixed with 4% paraformaldehyde for 15 minutes followed by permeabilization in 0.1% Triton X-100 in PBS solution for 15 minutes and blocking in anti-goat blocking buffer (Invitrogen, Carlsbad, CA), for 30 minutes. Rabbit anti-paxillin primary antibody (Tyr31, Invitrogen, Carlsbad, CA, Catalog#44-720G; RRID: AB_843415) was diluted in antibody dilution buffer in 1:200 dilution ratio and was added to the substrates containing the fixed cells and refrigerated for 1 hour. Afterward

goat anti-rabbit secondary antibody (Alexa Fluor 488, Invitrogen, Carlsbad, CA, Catalog# A-11008; RRID: AB_143165), diluted in 1:200 ratio was added with the rhodamine-conjugated phalloidin (Santa Cruz Biotechnology, Dallas, TX, Catalog# sc-301530), diluted in 1:80 ratio. Samples were stored in a dark place for 45 minutes followed by 3 PBS washes. Subsequently, DAPI (4′,6-diamidimo-2-phenylindole , Thermo Fisher Scientific,Waltham, MA, Catalog# D1306) was added for 5 minutes to stain the cell nuclei. Images were taken with an inverted Zeiss microscope (Axio Observer.Z1) using either a 40x (0.75 NA) or 63x (1.2 NA water immersion) objective Confocal microscopy was performed using a laser scanning confocal microscope (LSM 880, Carl Zeiss Inc.) and images were obtained using a 63x 1.15 NA water immersion objective.

RNA extraction protocol

The total RNA was extracted (from three independent experiments) from the cells using the Ambion® RNAqueous®-Micro Kit (Thermo Fisher Scientific, Catalog# AM1931) and the manufacturer's recommended protocol was followed. Briefly, cells were seeded on the fiber networks (3, 6, 18, 36 and 54 µm) attached to individual wells of a 6-well plate (glass bottom, Mattek Corporation). The 6^{th} well acted as the control well, where cells were seeded on the flat glass. Cells were cultured until 40-50% confluency. Afterwards, cell media was aspirated from the wells and fiber networks were transferred quickly (~5 second transfer time) to a new sterile 6-well plate using a pair of tweezers (UV sterilized, RNase free), and immediately lysed with the lysis solution from the kit. Control cells were lysed directly in the wells. Following RNA isolation with the kit, extracted RNA was eluted with a total volume of 50µl of eluate. The RNA in the elution solution was then transferred to an RNase free microcentrifuge tube and stored at -80 ^{o}C for further processing.

Quantification and statistical analysis

Analysis of aspect ratios, cell shapes and areas

The aspect ratio (Figure 4.2c) was defined as the ratio of the maximum and minimum dimensions of the cell and was intended to quantify the degree of polarization of the cell body in a certain direction. Cells stained for actin were manually outlined in ImageJ (https://imagej.nih.gov/ij/). 'Bounding Rectangle' function in ImageJ was subsequently used to evaluate the maximum horizontal and vertical dimensions of the outlined cell. Widths of individual cells were measured at ~25 positions along the cell length and mean width vs. length profiles (corresponding to each fiber network category, Figure 4.2a) were generated by averaging (using a bin size of 5 μm) the individual profiles. Cell areas (Figure 4.2b) and perimeters were measured by manually outlining the cells in ImageJ.

Analysis of cell profiles and slope of leading edge

Cells were not of the same lengths. To calculate the mean cell shape profile representing each inter-fiber spacing, we first calculated the average cell length for each inter-fiber spacing category. Then the individual cell profiles in each inter-fiber spacing category were normalized (stretched/shortened) with respect to the respective average length. Finally, the mean profile (Figure 4.2a) for each inter-fiber spacing was obtained by averaging the individual normalized profiles. To calculate the slopes of leading edges, mean profiles of each inter-fiber spacing were superimposed to coincide at x=0 μm.

Analysis of focal adhesion clusters and actin stress fibers

We report FAC lengths (Figure 2d) as the longest continuous length of paxillin clustering. These lengths were generated from manual measurements of the fluorescently-labeled

paxillin focal adhesion clusters in Axiovision (Zeiss) software. Straight lines were drawn from end to end of the major stress fibers in ImageJ and the orientation of such lines with respect to the net cell orientation were considered as the stress fiber orientations (Figure 5d).

Analysis of cell migration

Single (not in contact with neighboring cells) motile cells were chosen randomly from the timelapse videos and their centroids were tracked, using the 'Centroid' function in ImageJ, every 10 minutes for 8 hours. The centroid data was subsequently processed using a custom MATLAB (https://www.mathworks.com/) code to evaluate the migration rate, angular displacement and mean squared displacements (MSD) over each 10-minute interval. The migration rate (Figure 4.3a ii) for a cell was calculated every 10-minutes over an 8-hour experiment (48 measurements) and the measurements were then averaged for each cell to obtain the final migration rate. Migration persistence (Figure 4.3a iii) is defined as: (net cell displacement)/ (length of total path of cell motion) Angular displacement (Figure 4.3a iv) is defined as the change in migration direction after each time interval. It is evaluated from the following equation: $cos\theta = \frac{(x_n - x_{n-1})(x_{n+1} - x_n) + (y_n - y_{n-1})(y_{n+1} - y_n)}{\sqrt{(x_n - x_{n-1})^2 + (y_n - y_{n-1})^2}\sqrt{(x_{n+1} - x_n)^2 + (y_{n+1} - y_n)^2}}$ where (x_{n-1}, y_{n-1}), (x_n, y_n) and (x_{n+1}, y_{n+1}) represent the x and y co-ordinates of the cell centroid at $(n-1)^{th}$, n^{th} and $(n+1)^{th}$ time points (n=2,3….48) and θ represents the angular displacement. Mean square displacement ((Figure 3a iii) for a time interval τ is defined by the following equation: $MSD(\tau) = \langle (x(t+\tau) - x(t))^2 + (y(t+\tau) - y(t))^2 \rangle$,where x and y are the co-ordinates of the cell centroid and t denotes time. Experimental MSD values were fitted against the exponential function $MSD(\tau) \sim \tau^{\alpha}$, where α denotes the scaling exponent, to

determine the nature of cell's diffusive motion. Cell migration was also evaluated using the persistent random walk (PRW) model. [135,162] Mean square displacement for a time interval τ is defined by the following equation: $MSD(\tau) = 4D\left(\tau - P\left(1 - e^{-\tau/P}\right)\right) + 4\sigma^2$ where D is the diffusion coefficient, P is the persistence time and the last term denotes the noise in the cell position detection. Persistence length is calculated as persistence time (P) multiplied by the average speed.

Analysis of leading and trailing edges

For individual cells, we chose the most active leading and trailing edge regions and tracked their positions over time using the 'Manual Tracking' plugin of ImageJ. Displacements for each of the leading and the trailing edges (Figure 3b) are normalized to their individual starting positions respectively.

Nuclear movement, nuclear shape, area, eccentricity and thickness

To investigate the movement of the cell nucleus (Figure 4h,i), the cell nucleus was stained using the CellLight Nucleus-GFP, BacMam 2.0 reagent (Thermo Fischer Scientific, Waltham, MA, Catalog# C10602). Cells were incubated with the reagent overnight for at least 16 hours and timelapse imaging was performed afterwards with either 5 or 10 min interval for 4 hours. Throughout our analysis, we have approximated the nucleus to be an elliptical body and specifications of the nuclear shape were calculated using the 'Fit ellipse' function of ImageJ. The nucleus eccentricity (Figure 4.2f) was defined as $\sqrt{1 - \frac{b^2}{a^2}}$,where 2a and 2b denote the lengths of the major and minor axes of the ellipse respectively. The nucleus areas (Figure 4.2e) and perimeters were recorded by manually outlining the nuclei

in ImageJ. Z-stack images of the cell nucleus were taken using a confocal microscope, with a slice thickness of 0.36 μm, and the nucleus thickness (Figure 4f) was directly measured from the orthogonal cross-section (x-z or y-z section) images.

Genome-wide analysis of gene expression

The RNA was extracted from cell grown at each condition as described in the RNA extraction protocol. Libraries were prepared using the standard Illumina RNA-seq protocol and the sequencing was performed using a Hiseq 3000 system. The sequencing data for the RNA-seq analysis is deposited in the NCBI SRA database under accession SRP131388. RNA-seq data was handled and processed following the basis of our previous work.[163] The statistical analysis for differential gene expression compares the different inter-fiber spacing size with flat using DESeq2 method.[164] The functional enrichment analysis over Gene Ontology gen-set were performed and the selected results were plotted in a heatmap (Figure 6) using PIANO package.[165]

Statistical analysis and data fitting

Statistical analysis for the microscopy data was performed using the Graphpad Prism (GraphPad Software, La Jolla, CA) software. Typically, D'Agostino and Pearson omnibus normality test was utilized to test the normality of the data. Based on the normality of the data, either Analysis of Variance (along with Tukey's HSD for multiple comparisons) or the non-parametric Kruskal-Wallis test (along with the Dunn's multiple comparison test) was used to test the statistical significance between groups. For comparisons between only two groups, Student's t-tests were utilized. Data fits were performed in either MATLAB (for nonlinear fits) or Microsoft Excel (linear fits). Standard values for reporting

significance (****, p<0.0001;***, p<0.001; **, p<0.01; *, p < 0.05) were used. Unless otherwise mentioned error bars represent standard error of measurement.

4.3 Results

Crosshatch inter-fiber spacing regulates cell morphology

We wanted to determine the role of network inter-fiber spacing in regulating cell morphology (cell and nucleus size and shape). We generated 5 different categories of crosshatch fiber networks with inter-fiber dimensions: 3, 6, 18, 36 and 54 µm (Mean ± SE , n=100 per category): 2.6±0.09, 6.0±0.26, 17.8±0.3, 35.6±0.48, and 53.5±0.42 µm respectively. Supplementary figure S1), with flat 2D culture serving as the control (**Fig. 4.1a**). For interpretation of statistical differences, we categorized the fiber networks into three major characteristically similar groups: ***Dense*** (3 and 6 µm), ***Intermediate*** (18 and 36 µm) and ***Wide*** (54 µm). Although cells on wide fiber networks (~54 µm) attained a symmetric kite shape characterized by well-defined branching of the cell body along each fiber axis, on *intermediate* networks, we observed cells with increased branching at multiple fiber intersections (**Fig. 4.1b**). Interestingly on the 18-µm networks, we observed that cells had a broad leading and a narrow trailing edge, which strikingly resembled the flat 2D morphology (Supplementary figure S2). With a further decrease in unit-cell size (*dense networks*), unexpectedly, we found the cells to have elongated shapes, similar to those observed in cells moving through dense collagen gels or cell-derived matrices.[112] For

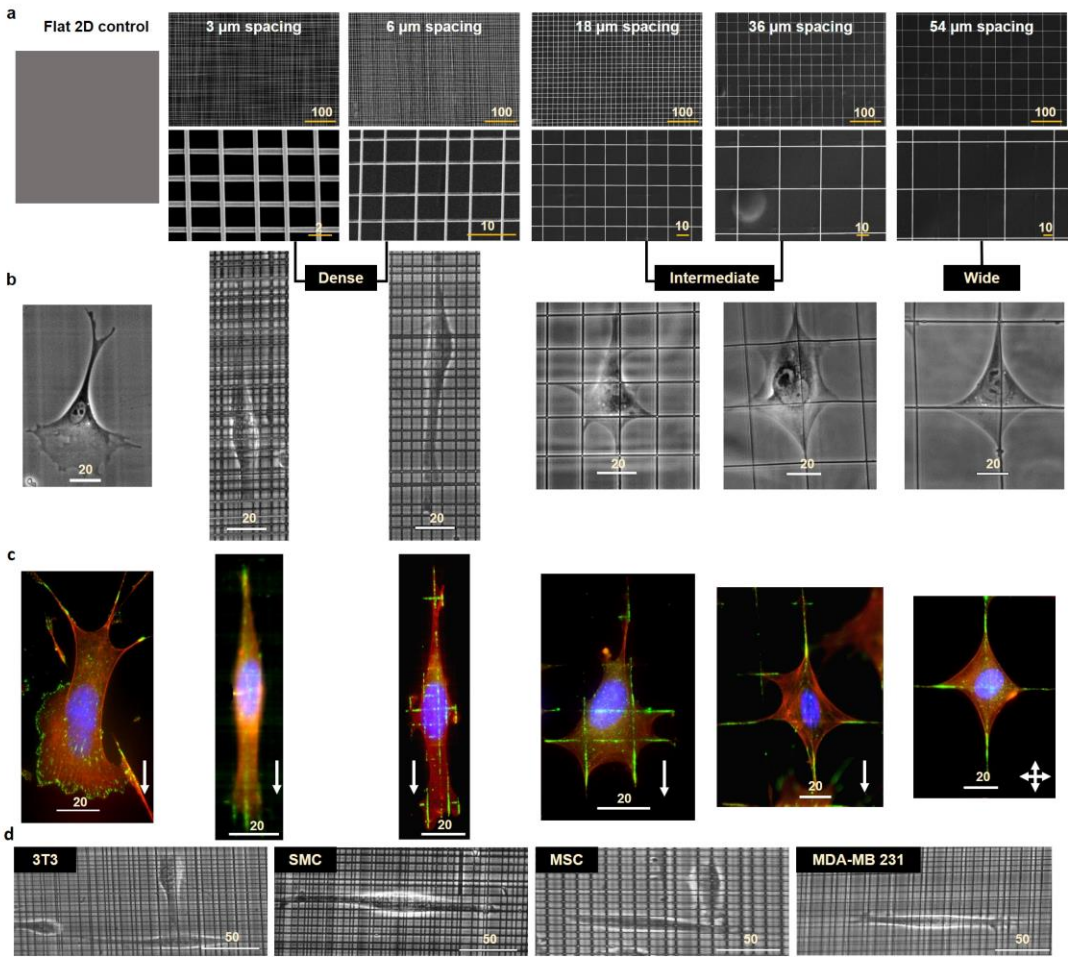

Figure 4.1. **Nanofiber networks and the corresponding cell morphologies**: **a)** SEM images of 500 nm diameter fiber networks with bottom panel showing high magnification images. Also shown is a cartoon of the flat control substratum. **b)** Representative phase-contrast images of cell morphologies obtained on the different substrata. **c)** Assembly of focal adhesions visualized by staining for the focal adhesion protein, paxillin (shown in green), f-actin stress fibers in red and nucleus in blue. White arrows denote cell migration direction. In the case of the 54-µm fiber networks, cells exhibit no bias in direction of migration. Characteristically similar fiber categories are grouped as *Dense* (3 and 6 µm), and *Intermediate* (18 and 36 µm), while 54 µm network is designated as *Wide*. **d)** Cells of different migratory lineages behave similarly on fiber networks (example shown for *dense* network). All scale bars shown in µm.

all inter-fiber spacing networks, cells were found to interact with both fiber layers as observed by time-lapse imaging. To visualize the cell-fiber adhesion areas, we performed immunostaining for paxillin[166], a major focal adhesion marker. While paxillin adhesions

were distributed throughout the cells on the 2D flat substrata, on fibers, they were observed to be concentrated in focal adhesion clusters (FACs, **Fig. 4.1c**), consistent with our previous observations. [85,91] The observed migratory phenotype was not unique to Hras 1, as other commonly used cell lines with migratory potential: NIH 3T3 fibroblasts, human smooth muscle cells (SMCs), human bone mesenchymal stem cells (MSC), and human breast adenocarcinoma MDA-MB 231 cells (**Fig. 4.1d**) also exhibited similar behavior, thus generalizing our findings.

Next, we biophysically phenotyped cell shape on fiber networks using metrics of area, aspect ratio, and eccentricity. First, a comparison of the average slope of the leading edge of cell shape showed a close match between the 18-μm unit-cell spacing and the flat 2D substrate (**Fig. 4.2a**). Lower slope values indicate elongated cell bodies, whereas the higher slopes, associated with cells on *intermediate* and 2D flat substrata, indicate spread cell shapes. Cells on *dense* networks had lower cell spread areas and higher aspect ratios (**Fig. 4.2b, 4.2c**). Cells cultured on the 3-μm inter-fiber spacing had the most elongated cell bodies and the lowest spread area, a morphology often associated with invasive cells, and resembling cells undergoing epithelial to mesenchymal transition (EMT). Next, quantitating the FAC-migratory behavior revealed that increasing length of FACs with inter-fiber spacing (inset, **Fig. 4.2d**) resulted in a bi-phasic migratory response (R^2=0.90, **Fig. 4.2d**). Cells on flat substrate had the shortest FAC but their high number density compared to cells on 3 and 6 μm likely caused the drop in migration rate. On the other hand, longer FACs at higher spacing contributed to slowing of cells due to line arrangement of adhesion sites that needed to be disengaged during migration. We also observed that

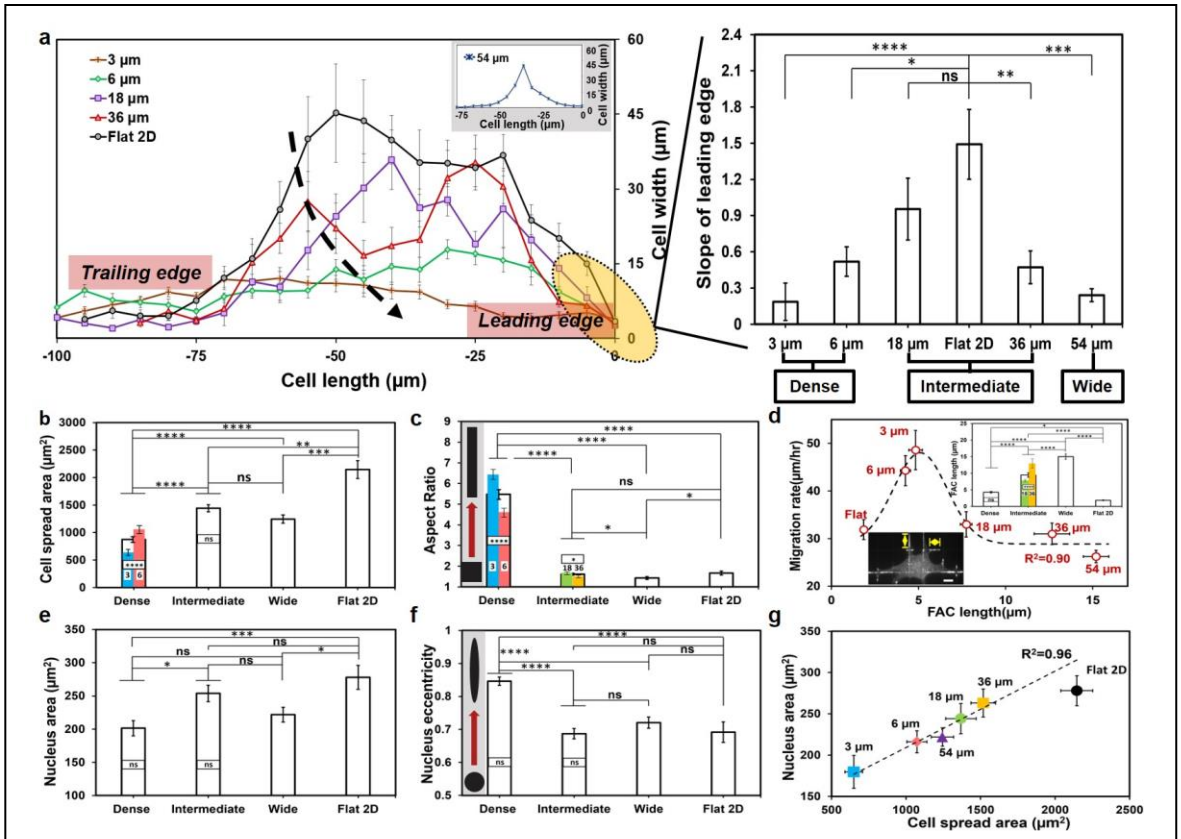

Figure 4.2. Inter-fiber spacing regulates cell/nucleus morphologies and focal adhesion cluster lengths: a) Cell width versus cell length profiles (top-view of cell, shown only half due to symmetry) for each category along with the measured slopes of the profiles at the leading edges (n=13, 7, 8, 10, 9 and 9 for 3, 6, 18, 36, 54 µm and Flat 2D, respectively). Cells on dense networks have lower slopes indicating elongated cell bodies. **b)** Cell spread areas on networks of increasing inter-fiber spacing (n=107,101,84 and 50 for *dense*, *intermediate*, *wide* networks and flat 2D, respectively). **c)** Aspect ratios of the cells on varying fiber networks show cells to be highly elongated on dense networks (n=107,101,84 and 50 for *dense*, *intermediate*, *wide* networks and flat 2D respectively). Inset in grey box shows schematic of geometry change (square to elongated rectangle) with increase in aspect ratio. **d)** Paxillin focal adhesion cluster lengths (FACs) increase with fiber network porosity leading to a bi-phasic migratory response (n=11,17,20,10,13 and 12 for 3, 6, 18, 36, 54 µm and Flat 2D, respectively). Inset shows FAC data for different cateogries and a representative image with yellow arrows depicting FAC mesasurement (Scale bar 10 µm). Nucleus area **(e)** and nucleus eccentricity **(f)** are regulated by the underlying network porosity with smallest size and highest eccentricity found in dense networks (n≥40 per category). Inset in grey box shows schematic of geometry change (circle to elongated oval) with increase in eccentricity. **g)** Cell and nucleus areas are positively correlated. Linear fit to data corresponding to fiber networks with flat 2D data shown as reference. Error bars represent standard error of measurement. Statistical differences between individual inter-fiber spacing categories are superimposed on the data for their respective groups.

cells on *dense* networks had the lowest nucleus areas (**Fig. 4.2e**), and highest eccentricity (**Fig. 4.2f**). Altogether, we found cell and nucleus areas linearly correlated across all fiber network spacing (R^2= 0.96, **Fig. 4.2g**). While previous studies have relied on printing adhesion proteins and patterned surfaces to achieve control on cell shape,[167–170] here we demonstrate that varying the geometric inter-fiber spacing alone is sufficient to control cell morphology.

Network inter-fiber spacing regulates cell motility

We next sought to determine if the dynamics of cell migration (speed, persistence, angular displacements and cell body movement) was driven by spacing of the fiber networks. We determined the mean squared displacement (MSD, **Fig. 4.3a(i)**) exponents and found a scaling exponent of ~1.4 for cells on intermediate and wide spacing, indicative of migratory behavior resembling a diffusive random walk, similar to that observed on flat 2D substrate. However, on *dense* networks (3 and 6 μm), we obtained a scaling exponent of ~1.8 signifying a persistent migratory behavior similar to migratory behavior observed in presence of physical constraints such as microchannels, grooves, 1D stripes or fibrillar tracks [107,138,140]. Migration rate (**Fig. 4.3a(ii)**) and persistence (**Fig. 4.3a(iii)**) were inversely related to inter-fiber spacing. Cells on *dense* networks not only moved faster, but with higher persistence, demonstrating smaller angular displacement during migration (**Fig. 4.3a(iv)**). Interestingly, we observed that the migratory behavior of cells on flat 2D matched closely with the cells migrating on networks with *intermediate* (18 and 36 μm) spacing. This is consistent with our finding that cell shapes in these categories (especially

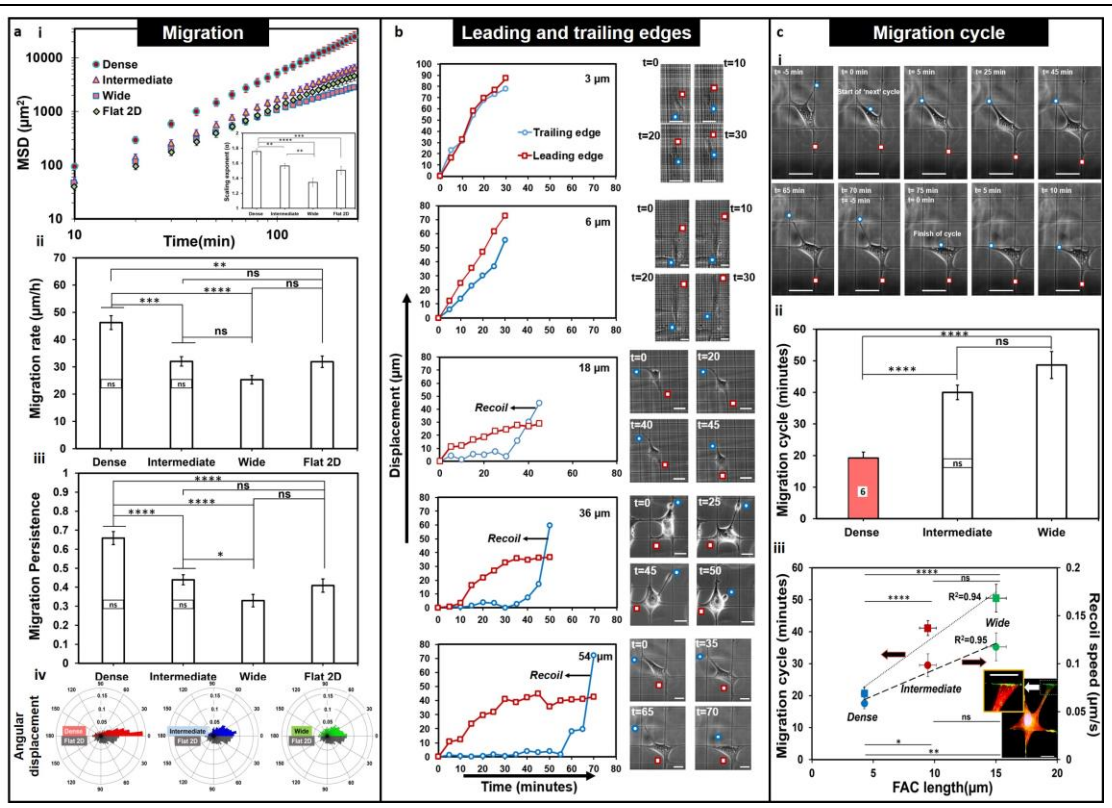

Figure 4.3. **Inter-fiber spacing regulates cell migration: a)** (i) mean squared displacement (MSD) vs. time (t) plots corresponding to *dense*, *intermediate*, and *wide* fiber network categories and Flat 2D. Inset shows the scaling relation MSD ~ t^{α} ,where α is the scaling exponent that is used to fit the data. (ii) migration rate of single cells (n=59, 40, 44 and 29 for *dense*, *intermediate*, *wide* and *flat 2D* respectively), (iii) persistence of single cells (n=49, 40, 36 and 20 for *dense*, *intermediate*, *wide* networks and *flat 2D* respectively) for the different substrates, and (iv) polar plots showing angular displacements for cells on varying fiber network porosities and compared with flat 2D (n=40, 40, 20 and 20 for *dense*, *intermediate*, *wide* networks and *flat 2D* respectively). Data demonstrates cells moving fastest and with highest persistence on *dense* crosshatch pattern of fibers. **b**) Representative displacement profiles of the leading and trailing edge for the different fiber network categories. Leading and trailing edges are shown in red squares and blue circles respectively in associated time-lapse images (scale bars denote 20 μm and time shown in minutes). **c)** (i) Recoil-to-recoil analysis method to calculate *migration cycle* time, (ii) *migration cycle* time over the different fiber network categories (n=29,50 and 25 for *dense*, *intermediate, and wide* networks respectively). Note for the *dense* group, data is only shown for 6 μm fiber spacing, as the recoil-to-recoil migration cycle for the 3 μm fiber spacing was not discernable optically, and (iii) migration cycle and retraction *recoil* speeds plotted as function of FAC length showing both metrics to linearly scale with FAC lengths. Inset image shows a fluorescently-labeled cell attached to a 54 μm inter-fiber spacing network and the magnified image of retracting edge showing f-actin stress fiber distribution (red: f-actin stress fiber, blue-nucleus and green: paxillin. Scale bar: 20 μm). Statistical differences between individual inter-fiber spacing categories are superimposed on the data for their respective groups.

in 18 μm category) resembled cell shapes on 2D flat substrata. Altogether, we report that crosshatch fiber networks of varying inter-fiber spacing are able to achieve precise control on migratory behavior: 1D highly persistent to diffusive 2D random walk.

Next, to understand the mechanics of how cells migrated on fiber networks of varying spacing, we investigated the dynamics of trailing and leading edges (shown by blue and red circles respectively in **Fig. 4.3b**). We observed that the trailing edge served as an *anchor point* for the advancing leading edge. Thus, as the leading edge advanced, the trailing edge elongated over time and subsequently it was observed to detach and retract in a *'recoil*' manner at the rate of 10^{-2}-10^{-1} μm/s. These rates are equivalent to those observed for the fast phase of fibroblast trailing edge retractions cultured on 2D glass substrates.[171] This mechanism, a well-documented aspect of 2D cell migration, matched well with the cells migrating on *intermediate* and the *wide* fiber network categories. However, on the *dense* networks the motion of the trailing edge was much smoother (slower *recoil*) compared to intermediate and wide spacing. We quantified the time taken between successive trailing edge retractions to determine *migration cycle*, **Fig. 4.3c(i)**. Migration cycle time increased with increased inter-fiber spacing (**Fig. 4.3c(ii)**) and increased FAC lengths (R^2=0.94, **Fig. 4.3c(iii)**). Similarly, the *recoil* speed was found to increase with FAC length (R^2=0.95), thus suggesting that the longer FAC lengths associated with well-defined f-actin stress fibers originating from the adhesion sites (inset in **Fig. 4.3c(iii)**) were causing stronger recoils.

Nucleus dynamics response to network porosity

We next sought to determine the dynamics of nucleus shape change in response to fiber network spacing. Nuclei underwent distinct and rapid deformation with the *recoil* of the

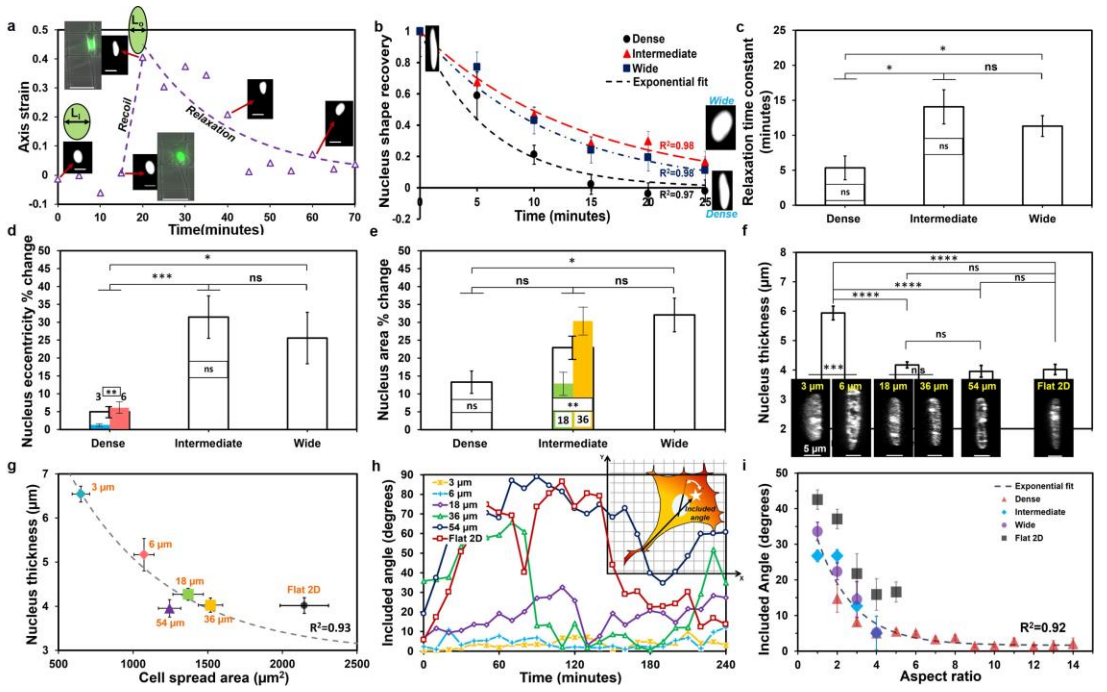

Figure 4.4. **Inter-fiber spacing regulates nucleus dynamics: a)** Representative profile of the deformation of nucleus during retraction of a trailing edge demonstrating rounded nucleus is strained to elongated shape, and after recoil the nucleus relaxes to its original shape. Axis strain is defined as $\varepsilon = \frac{L_i - L(t)}{L_i}$,where L_i is the minor axis length of the nucleus *pre-recoil* and L(t) represents the minor axis length of the nucleus at time t *post-recoil* (Scale bars represent 20 μm). At start of relaxation post-recoil (t=0), minor axis L(t)= L_O. **b)** Normalized nucleus shape recovery data (defined as $\frac{\varepsilon}{\varepsilon_0}$ where $\varepsilon = \frac{L_i - L(t)}{L_i}$ and $\varepsilon_0 = \frac{L_i - L_0}{L_i}$ is the initial nucleus axis strain immediately post-recoil with exponential fits showing that cells on dense networks recover their original shape faster after recoil. Inset shows representative images of the nucleus post recoil and after relaxation (rounded is for *wide* and elongated for *dense* networks). **c)** Relaxation time constants calculated on basis of an exponential decay of nucleus deformation showing stronger recoil in *intermediate* and *wide* networks. Percentage change in nucleus shape (eccentricity (**d**)) and size (projected area (**e**)) during trailing edge recoil. **f)** Nucleus height measured by confocal microscopy quantitates cell nuclei to be thicker in dense regions. Inset shows representative images of nucleus (projected side view from confocal microscopy, scale bar 5 μm). **g)** Nucleus thickness decreases with increase in cell spread area. **h)** Representative temporal plots of nucleus-cell body angular coupling (*included angle*) for the different inter-fiber spacing with inset illustration showing the *included-angle* is defined by the coordination between cell body vector (trailing edge to centroid shown by white star) and nucleus major axis. **i)** Data shows the influence of cell shape (aspect ratio) on the extent of nucleus-cell body coordination. For (**g**) and (**i**) exponential fit to data corresponding to fiber networks with flat 2D data shown as reference. Sample size for b, c, d and e (n=11, 23 and 10: *dense*, *intermediate* and *wide* networks respectively) for f, g (n=25, 32, 14 & 13: *dense*, *intermediate*, *wide* and *flat 2D* respectively) and for i (n=13, 15, 9, 9: *dense*, *intermediate*, *wide* and *flat 2D* respectively). Included angle and aspect ratios are calculated every 10 minutes over the 4-hour experimental time (25 measurements) and then averaged across cells of similar aspect ratios. Statistical differences between individual inter-fiber spacing categories are superimposed on the data for their respective groups.

trailing edge. We quantitated the changes in nucleus shape (major and minor axes, projected area) within a *migration cycle*, and found nucleus shape changes to be pronounced on *intermediate* and *wide* inter-fiber spacing networks. On these networks, at the start of the *migration cycle*, the nucleus was observed to be rounded (low eccentricity), which transitioned to an elongated shape (high eccentricity) during *recoil* of the trailing edge and returned to rounded morphology as the trailing edge reattached (**Fig. 4.4 a,b** (R^2=0.98 for both *wide* and *intermediate* networks)). This is in contrast to cells on dense networks that maintain high eccentricity, elongated nuclei, at all times. In general, the recovery time constant ($\boldsymbol{strain \sim e^{-t/\tau}}$ where $\boldsymbol{\tau}$ is the recovery time constant) for nucleus shape dynamics was found to increase with the inter-fiber spacing, thus, signifying a larger deformation with stronger trailing edge *recoil* (**Fig. 4.4c**). The extent of the nucleus shape change was estimated in terms of the percent change of the nucleus eccentricity and it was found that trailing edge retractions in *intermediate* and *wide* networks involved up to ~35% eccentricity change of the nucleus (**Fig. 4.4d**), whereas on *dense* networks, it was significantly reduced (~5%). Similarly, the change in nucleus area increased with network inter-fiber spacing (**Fig. 4.4e**). We observed large (~30%) changes in areas only on the 36 and 54 μm fiber categories presumably due to high forces generated during recoil to compress the nucleus. Next, we interrogated the thickness of nuclei on different fiber network categories using confocal microscopy. Reconstruction of nucleus height using z-stack images showed the nuclei to be significantly thicker in *dense* networks (**Fig. 4.4f**). Furthermore, nucleus thickness was found to decrease with the increase in cell spread area (R^2=0.93, **Fig. 4.4g**). Since *intermediate* and *wide* fiber spacing were causing

nuclei to undergo shape changes, we interrogated the angular coupling between nucleus and cell body vector (defined as *included angle* (inset in **Fig. 4.4h**) signifying the extent of co-alignment between nucleus and cell body during migration. We found that increasing inter-fiber spacing resulted in larger nucleus angular spins (**Fig. 4.4h**) similar to the studies described previously on flat substrates,[172] while with increasing aspect ratio of cells (signifying persistent migration on denser networks), the extent of nucleus-cell body coordination increased (included angle decreases, R^2=0.92, **Fig. 4.4i**). Altogether, our data shows that nucleus thickness, shape, deformation and the degree of change in angular orientation during *migration cycle* are controllable through the choice of inter-fiber spacing.

Cell spreading and symmetry breaking dynamics

Next, we wanted to investigate how cells adopted highly elongated geometries on dense fiber networks. We monitored the cell spreading behavior from the moment the cells first started interacting with the fibrous networks (**Fig. 4.5a**). Cells cultured on dense networks formed transient short-lived protrusions resulting in delayed spreading (**Fig. 4.5b**). We calculated the temporal evolution of the projected spread area of the cells (**Fig. 4.5c**) and found that all inter-fiber spacing demonstrated an almost linear growth of the projected area (with slowest on the 3-μm category), which is in accordance with cell spreading on flat substrata and in gel systems.[109,173,174] Furthermore, we observed that on *dense* networks, spreading occurred with continuous growth in aspect ratio signifying anisotropic shapes, whereas cells on *intermediate* and *wide* categories continually protrude along all fiber axes and spread mostly in an isotropic fashion (aspect ratio ~1). Next, we looked at

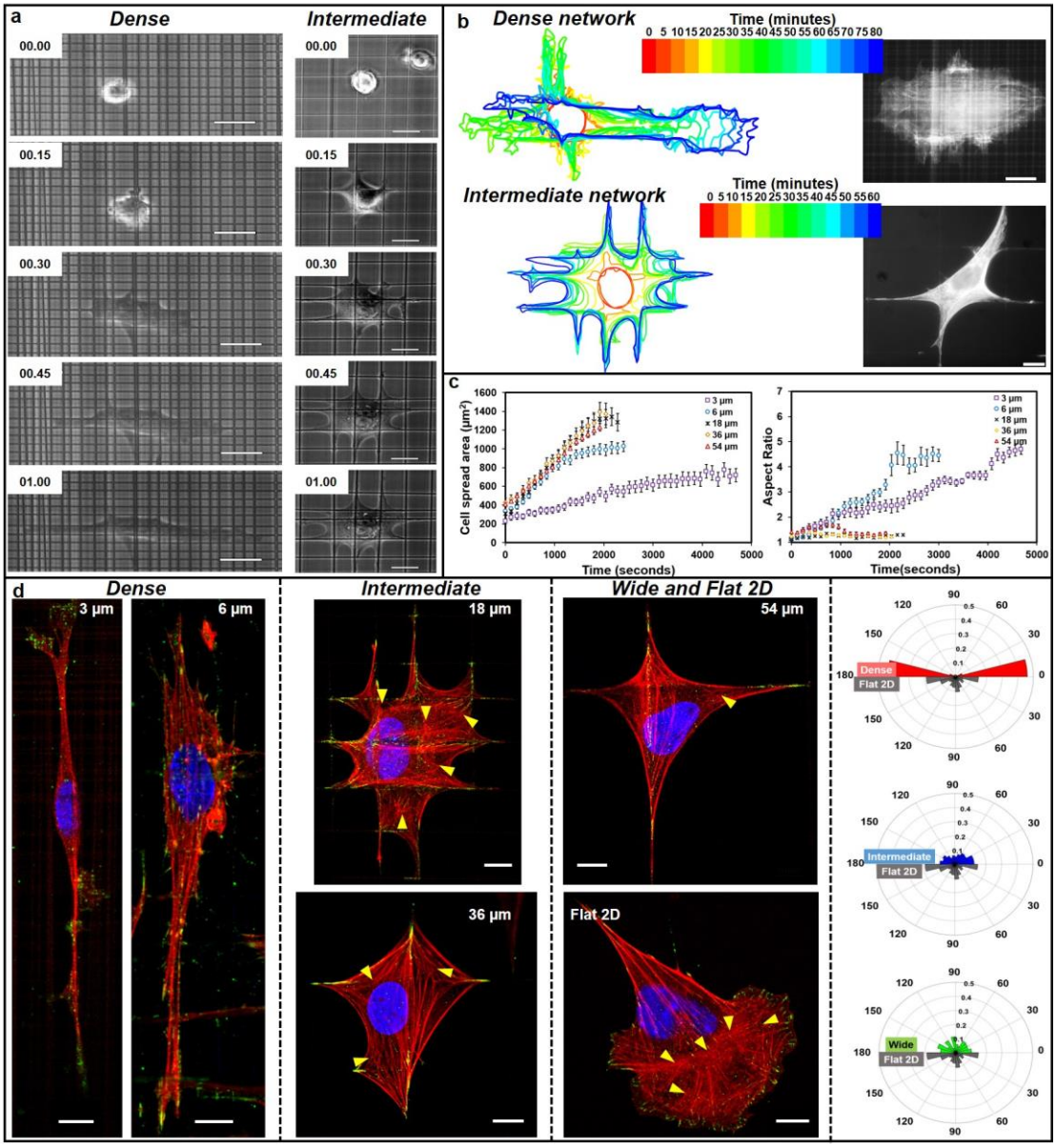

Figure 4.5. Inter-fiber spacing regulates cell spreading and f-actin stress fiber organization: a) Phase contrast time-lapse images showing *anisotropic* and *isotropic* cell spreading on 6 and 18 μm representing *dense* and *intermediate* fiber networks, respectively. **b)** Transient profiles outlining cell spreading on *dense* and *intermediate* networks. On *dense* networks, cells form multiple short-lived protrusions in all directions (inset image) before elongating in a primary direction, whereas on *intermediate* networks cells protrude and extend isotropically. **c)** Analysis of cell spread area and associated aspect ratio (length/width) of cells spreading on fibers of varying network porosities (n= 8-11 per category). **d)** Immunostained images of f-actin stress fibers (red), focal adhesion paxillin (green) and nucleus (blue) on all fiber categories and the flat 2D substratum. Cells cultured on the 3 μm porosity networks lack dominant stress fibers. Yellow arrows indicate clustering (meshwork) of stress fibers, with *intermediate* spacing matching the stress fiber distribution found in cells on flat 2D

substrata. All scale bars are 20 µm. Polar plots of f-Actin stress fiber distribution demonstrating highly aligned stress fibers in *dense* networks and isotropic distribution of stress fibers in *intermediate* and *wide* categories resembling those on flat substrates (n=25,24,11 and 10 for *dense, intermediate, wide* and *flat 2D* respectively,15-20 stress fibers analyzed for each cell).

the organization of f-actin stress fibers once cells had completely stretched. We observed stress fibers to be aligned along the cell body axis in *dense* networks and isotropically distributed as meshwork (shown by yellow arrows) in *intermediate* and *wide* networks similar to those observed on flat 2D substrata (**Fig. 4.5d** and Supplementary Fig. S3). Interestingly, on the 3 µm network of fibers, we did not observe a large number of dominant stress fibers, similar to reported observations of cells in 3D morphologies[84]. Altogether, our data suggests that the inter-fiber spacing of crosshatch networks of fibers is a regulator of cell spreading dynamics and actin cytoskeleton organization.

Gene expression analysis

To determine whether growth on different fiber networks could drive transcriptional reprogramming, we performed RNASeq analysis on independent replicates grown on the different fiber networks. The upregulation of genes related to cytoskeletal rearrangement and cell-cell adhesion were concordant with the observed phenotypes described (**Fig. 4.6a**). Interestingly, we observed a generalized decrease in transcriptional activity, compared to flat control (**Fig. 4.6b**). Previous studies have shown that nuclear shape and size can influence gene transcription, and access of transcriptional machinery to DNA.[175–177] Surprisingly, gene families associated with transcriptional activity are suppressed, and we do not observe dynamic changes concordant with changes in nucleus shape and size observed between cells on the different fiber networks. However, we observed

upregulation of multiple genes in pathways regulating translation and protein expression, suggesting functional changes in cell behavior may be due to post-transcriptional modifications. Further, upregulation of genes involved in metabolic processes (BP-GO:0008152) was observed in cells grown on all fibers compared to a flat surface. These data suggest that inter-fiber spacing is sufficient to induce changes in gene expression, which may be independent of changes in nuclear morphology. The resulting gene expression changes appear to be primarily involved with driving post-transcriptional alterations related to translation and protein modifications, whereas generalized transcriptional upregulation is not altered. Together, all these data suggest that biophysical alterations within the tumor microenvironment may be sufficient to modulate transcriptional programming that could increase the expression of genes implicated in

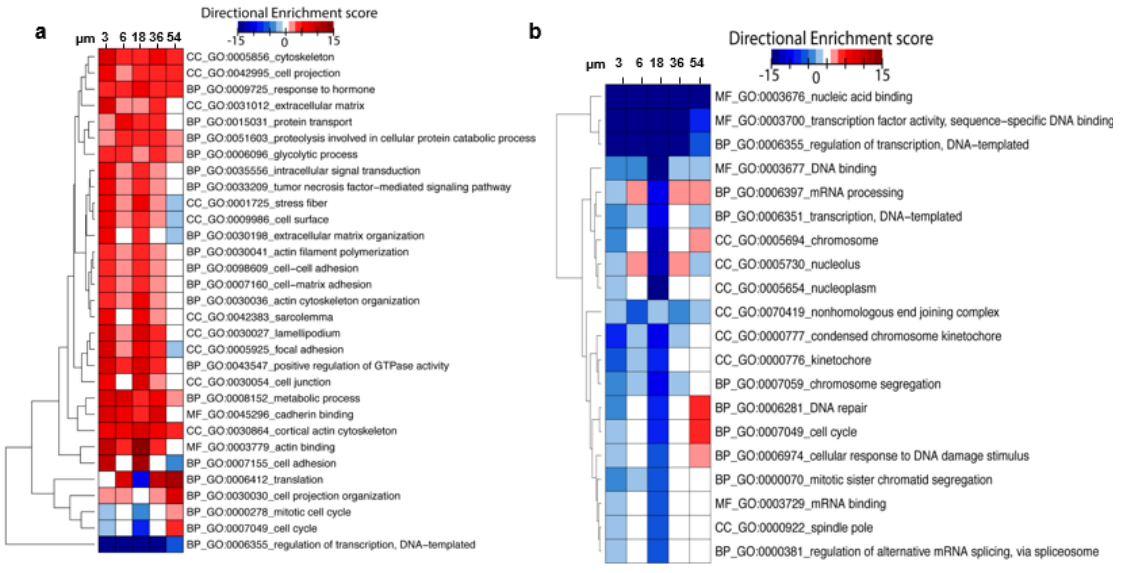

Figure 4.6. **Inter-fiber spacing regulates gene expression: (a)** Hierarchical clustering and GO enrichment analysis of gene families related to cellular phenotypes in cells cultured on fiber networks of different inter-fiber spacing. **(b)** Hierarchical clustering and GO enrichment analysis of gene families primarily downregulated during growth on fiber networks. Downregulated networks are primarily associated with transcription. Directional enrichment scores are reported with respect to flat 2D control.

enhanced pathogenic and tumorigenic potential in transformed cells.

4.4 Discussion

The immediate environment surrounding a cell offers a variety of biophysical cues of confinement, rigidity, topography (isotropic and anisotropic) and porosity.[178] Here, we have explored how in the context of crosshatch network of fibrous environments found in dermis[128], basement membrane[132], muscular hydrostats [148], and the loose connective tissue[38],, different levels of inter-fiber spacing can result in different morphologies and associated migration dynamics. Firstly, we observed that at very high inter-fiber spacing (*wide*: ~54x54 μm), cells form symmetric kite shapes and have reduced migration rates and persistence due to formation of significantly large FACs. With decrease in inter-fiber spacing to *intermediate* (18 and 36 μm), we observed that the cell morphologies and migratory behavior were very similar to those obtained on traditional flat 2D substrata (**Fig. 4.2, 4.3**). Encouraged by our ability to recapitulate 2D migratory behavior on suspended network of fibers, we inquired if making the fiber networks denser would still maintain this behavior, as we presumed that decreased inter-fiber spacing would translate to increased number of contact points similar to that available on a featureless 2D substratum. Unexpectedly, we found that the increased contact points caused multiple transient short protrusions leading to elongated cell bodies and anisotropic migration. We found that cell elongation occurred much earlier during the cell-spreading process (**Fig. 4.5b**) and since cells were probing both directions, we observed polarized cells in both principal directions. Once polarized, the cells did not break symmetry on *dense* networks and migrated almost exclusively in the direction of polarization. However, with increasing inter-fiber spacing, cells were able to more readily change direction resembling random walks.

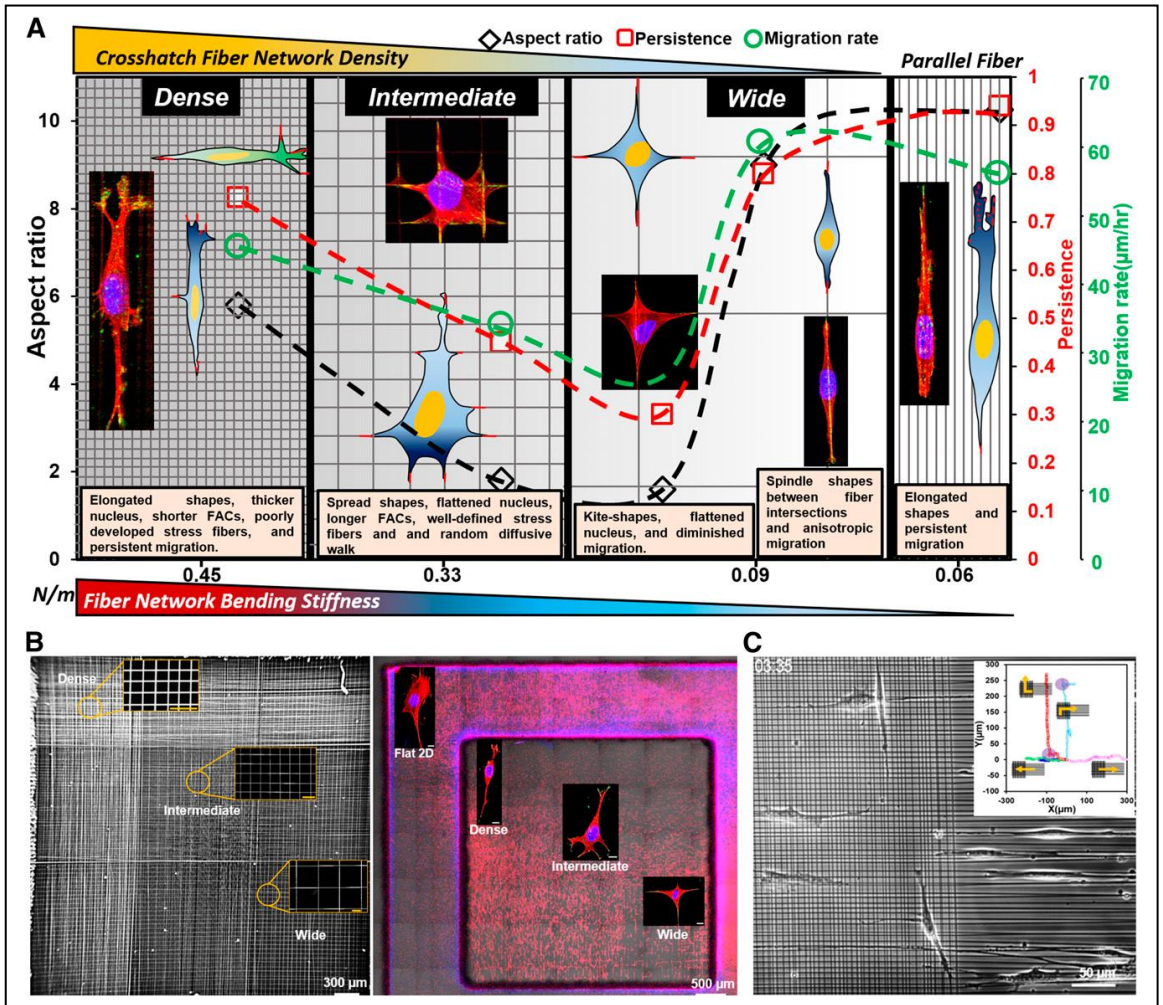

Figure 4.7. Fiber network based migration platform. a) Migration phase diagram based upon inter-fiber spacing and bending stiffness (N/m) regulates single cell migratory phenotype in 1D, 2D and 3D cell shapes. Data is plotted for various inter-fiber spacing against parallel arrangement of fibers (shown on extreme right). On average, cells were found to engage with three parallel fibers, resulting in estimation of equivalent stiffness by summation of stiffness of individual fibers (springs in parallel). **b)** SEM image (left) of a single scaffold with three fiber network categories. Middle and right fluorescence microscopy images show images of the cells seeded on fibers of varying crosshatch densities and the flat 2D control. Scale bars in inset images in SEM panel are 20 μm and stained images are 10 μm. c) Custom suspended fiber networks to study cell shape and migration changes as cells transition between aligned and crosshatch networks [pattern adapted from Doyle et al. 2009]. Inset shows representative migration trajectories demonstrating cells maintaining elongated shapes and persistent migration on both networks along with cases in which cells can turn directions shown by purple circles

3D persistent migration can be obtained using cell-derived matrices, 1D microprinted fibrillar lines or mechanically confining cells using microgrooves/microposts, while 2D random migration is typically obtained using flat, featureless substrates with no confinement. Here, we demonstrate that our method recapitulates random 2D and persistent 3D migration by simply varying the inter-fiber spacing in suspended crosshatch network of fibers. Our method of achieving persistent migration is independent of the requirement of aligned topographical cues. Cells on networks of suspended crosshatch fibers make contact with both layers (shown by paxillin adhesions on both layers: Supplementary figure S3). On *dense* networks, cells maintain elongated shapes that have significantly longer persistence lengths (Dense: *92.5 μm*, Intermediate: *29.8 μm*, Wide: *12.16 μm*, Flat 2D: *19.95 μm*, calculated using persistent random walk (PRW) model, Supplementary figure S5[135,162]). Interestingly, cells on *dense* networks (i) align along both principal axis of crosshatch networks (Supplementary movie M1-3), and (ii) can make right angle turns, thus changing their migratory direction (Supplementary movie M5). Our quantitation of leading-trailing edge displacements (**Fig. 3.3b**) of cells migrating in *dense* networks matches the 3D migration profiles and cell shapes reported in the literature using cell-derived matrices and narrow 1D microprinted fibrillar lines[107]. Furthermore, cell migratory behavior on *dense* networks in 3D shapes matches the reported migration speed patterns and cell shapes obtained in narrow microgrooves.[179] However, our findings diverge from cell behavior observed on 2D crosshatch microprinted patterns, which report similarities in cell shapes across *dense, sparse* and smooth 2D substrates, while the migration rates across *dense* and *sparse* remain similar.[180,181] We speculate the differences from our method arise due to the absence of *curvature* in microprinted lines and cells presumably

making contact with the underlying flat substrate. Suspended fibers not only provide *curvature* as a cue to cells but also ensure that cells interact only with fibers.

Our observation of cells of multiple lineages (fibroblasts, cancer cells, smooth muscle cells and mesenchymal stem cells) having high aspect ratios and 3D shapes moving persistently (1D) on *dense* networks (**Fig. 4.1**) compares well with the reported morphology and behavior of cells in 3D collagen gels and cell derived matrices.[107,112,182] Co-alignment between nucleus and cell body vectors, a hallmark of persistent migration is recapitulated *in vitro* using anisotropic topographical cues of varying widths,[183,184] while here, in contrast, we show that *dense* crosshatch fiber environments can achieve similar behavior. With increase in inter-fiber spacing, cells on *intermediate* and *wide* network categories have a loss of the co-alignment that leads to random migration as observed in cells on 2D flat substrata. Additionally, we also found that cells on *dense* networks had thicker nuclei (**Fig. 4.5f**), exhibited lower time constants during shape recovery after *recoil* (**Fig. 4.5c**) and lacked well-defined f-actin stress fibers (**Fig. 4.6d**). These findings suggest that *dense* networks induce 3D morphologies of compliant (soft) cells that migrate anisotropically; a mechanical signature that is often associated with higher invasive potential. [185,186] Interestingly, plotting the migratory behavior across the bending stiffness (N/m, Supplementary Fig. S4) of crosshatch networks shows that cells in elongated shapes having thicker 3D bodies migrate faster at high stiffness values (*dense* networks) and slower on lower stiffness values (*intermediate and wide* networks, **Fig. 4.7a**). Contrastingly, cells having elongated shapes similar to *dense* networks, but cultured on multiple parallel fibers or on single parallel fibers in spindle shapes move faster at lower stiffness.[85,152] Thus, we

emphasize the need to conjointly examine geometric arrangement of fibers and their stiffness for a comprehensive description of the migratory phenotype.

Surprisingly, we found that isotropic environments can not only induce plasticity in migration, but also lead to transcriptional modifications that may enhance transformation. We report the upregulation of multiple metabolic pathways in response to growth on fibers and report that the observed transcriptional changes were primarily in gene ontologies related to post-transcriptional modifications and modulation of metabolic capacity. Further, we did not observe general transcriptional upregulation that correlated with nuclear size and shape presumably due to similarities in morphology across the different substrates (**Fig. 4.2 e, f**). Instead, we observed more specific upregulation of pathways related to translation and post-translational modification of proteins, including upregulation of metabolic pathways. These data support that physical cues in the microenvironment can alter transcriptional output, seemingly independent of nuclear shape changes, and modulate the metabolic capacity of tumor cells. These observations support targeting the tumor microenvironment (TME) through therapeutic intervention to decrease tumor cell growth and motility[187,188]. A dense TME has been shown in previous studies to limit therapeutic efficacy and many dense tumors are resistant to chemotherapy. It has been proposed that this is due to decreased delivery of drug to the tumor site due to transport barriers to drug delivery. However, our data reveal a potential additional mechanism of resistance, whereby metabolic programming within the tumor cells is changed based on the tumor microenvironment, and may contribute to therapeutic resistance. Our current and future studies are aimed at discerning the mechanisms of drug resistance in our *in vitro* models of thyroid cancer, and to determine whether growth on

varying inter-fiber spacing changes the sensitivity of tumor cells to molecular inhibitors. Finally, while we did not identify transcriptional and metabolic changes that have been previously reported in regards to nuclear shape changes[175–177], we cannot exclude the possibility that chronic stresses and strain to nuclear shape associated with repeated cycles of attachment and recoil that were observed may have contributed to some of the transcriptional reprogramming and expression changes observed. We believe short to long term future studies using our platform provides novel quantifiable metrics to dissect whether acute nuclear shape changes versus chronic stresses to nuclear shape associated with motility and recoil forces lead to distinct transcriptional responses.

4.5 Conclusion

Here, we report the development of a new ECM mimicking crosshatch nanofibrous platform for studying 1D, 2D, and 3D cell migration. Our method of using crosshatch suspended fibrous environments of tunable inter-fiber spacing regulates plasticity in cell migration and cytoskeletal arrangement, thus allowing us to identify crosshatch fiber density driven rules in cell migration. Notably, we show that dense crosshatch spacing much like aligned fibers is a fertile environment that induces fast persistent migration in 3D shapes, a known signature of softer invasive cancer cells, while wider crosshatches induce random migration in 2D shapes of cells with higher contractility. We demonstrate that aligned geometries are not the only requisite biophysical configuration that can elicit elongated cell shapes and sustain persistent migration. The flexibility of our approach permits using a *single* scaffold with tunable crosshatch inter-fiber spacing, thus allowing simultaneous recovery of 1D, 2D and 3D cell morphologies and migratory patterns at desired locations (**Fig. 4.7b**) that are currently recapitulated using a wide variety of *in vitro*

methods. Non-electrospinning STEP platform can also generate custom ‘fibrous’ networks matching patterns reported in the literature[107] to compare cell shape and migration mode changes (**Fig. 4.7c**). In doing so, we overcome the well noted current challenges of cross-validating migratory phenotypes across platforms, quantitative microscopy at high spatiotemporal resolutions and easy access to desired cells for detailed molecular profiling.[83] We envision that extending the platform to include co-cultures and biochemical cues along with the ability to estimate the physical forces exerted by cells (Nanonet Force Microscopy),[90,189] will yield new mechanotransduction knowledge in the metastatic invasion, regenerative wound repair and stem cell migrational homing.

Supplementary Material

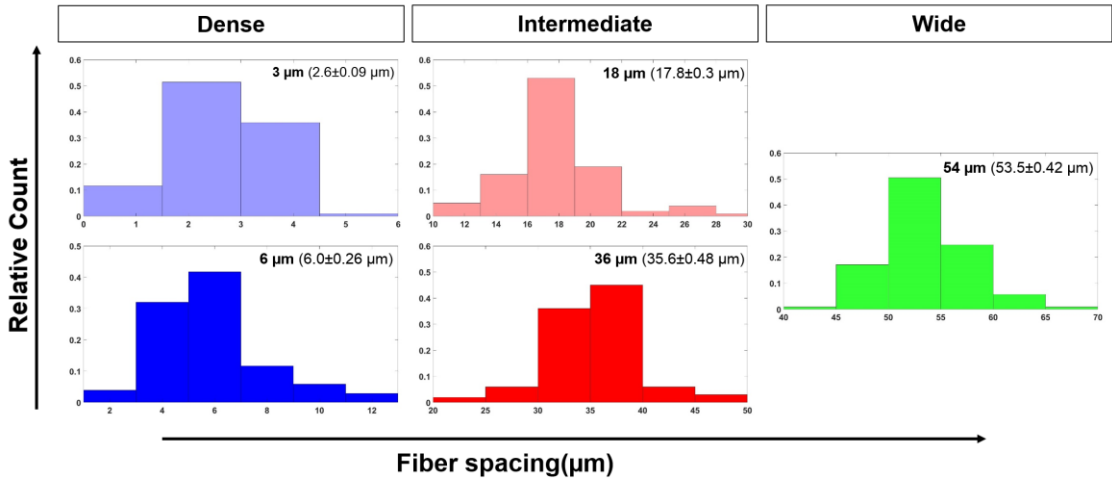

Supplementary Figure 4.S1: Inter-fiber spacing of individual fiber network Categories: Histograms are based on relative count; n=100 measurements taken for each network category. Data in parenthesis is shown as Mean±SE.

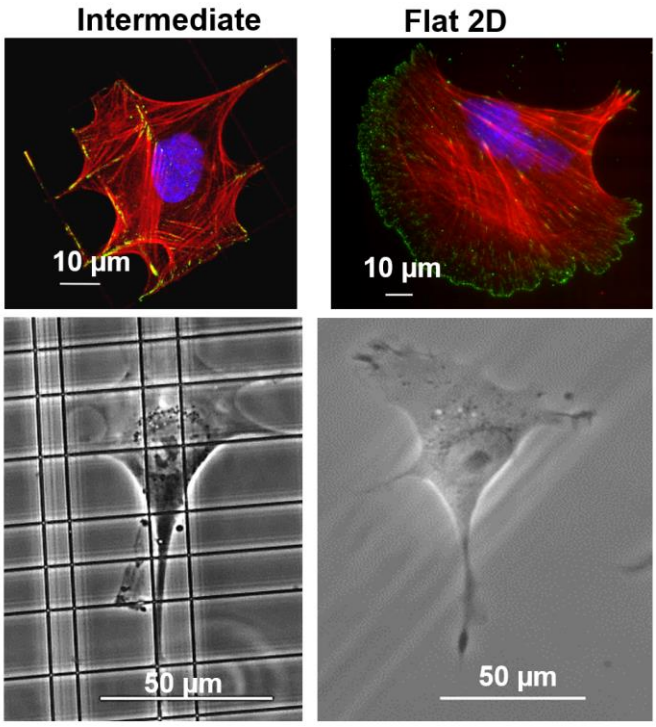

Supplementary Figure 4.S2: Overall cell shape (broad leading edge with tapering trailing edge) is consistent between flat glass and the 18 µm spacing fiber networks. Top panel: Fluorescently labelled (red: actin, green: Paxillin and blue: DAPI) fixed cells on intermediate fiber networks and Flat glass respectively. Bottom panel: Phase images of different cells attached to the fibers and on the flat 2D substratum.

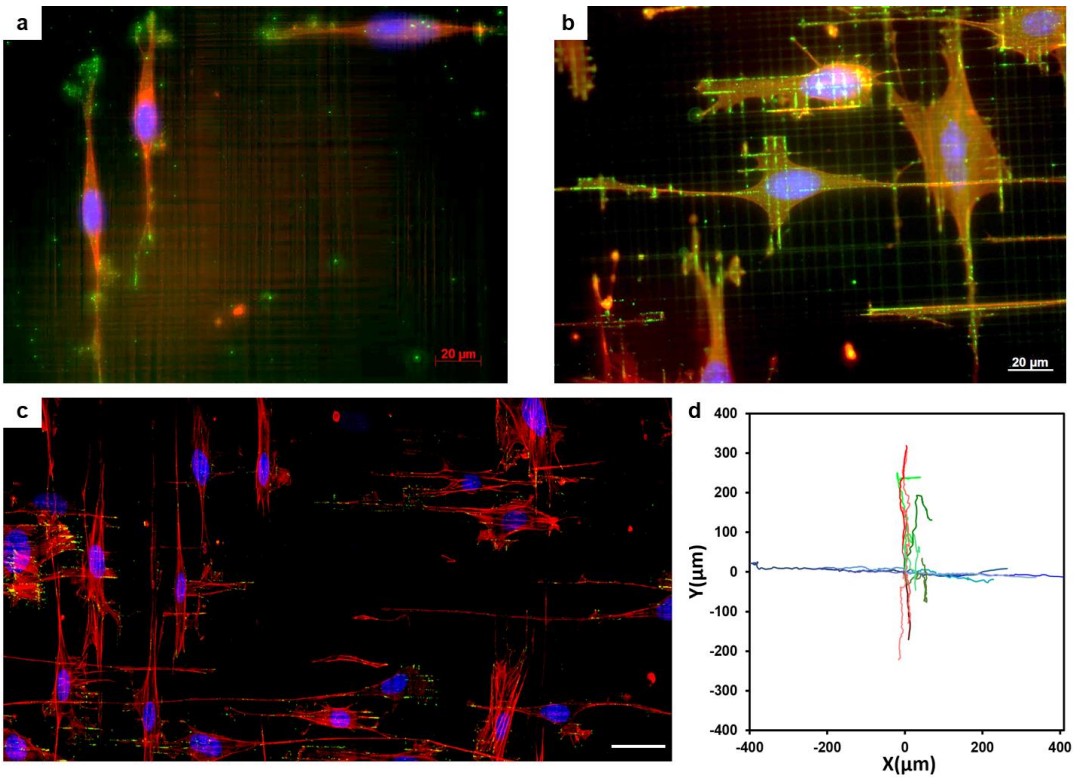

Supplementary Figure 4.S3: **Cells sense both layers. (a, b)** Cells form focal adhesions on both layers of *dense* networks, as shown by paxillin staining (green). **(c)** Representative fixed-stained image of cells on a *dense* fiber network showing cells in both north-south and east-west orientations (red: actin, blue: nucleus and green: paxillin). Scale bar is 50 µm. **(d)** Migration trajectories of cells tracked at 5-minute intervals for at least 6 hours on *dense* fiber networks. Cells move in both directions and can make right angle turns.

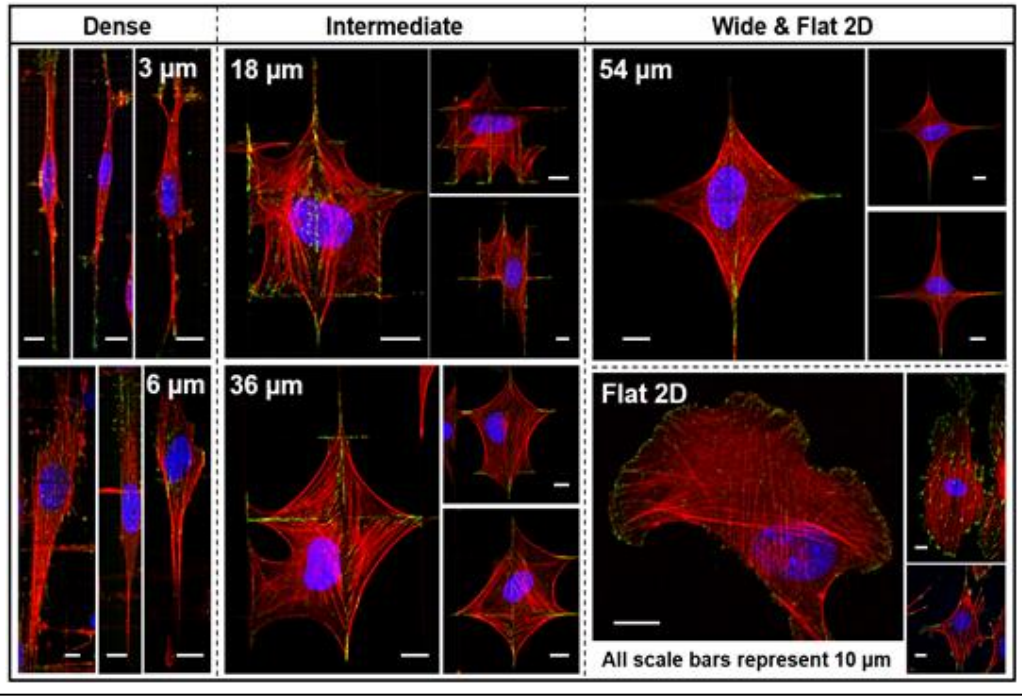

Supplementary Figure 4.S4: Stress fiber organization in the different fiber network categories. All scale bars represent 10 µm

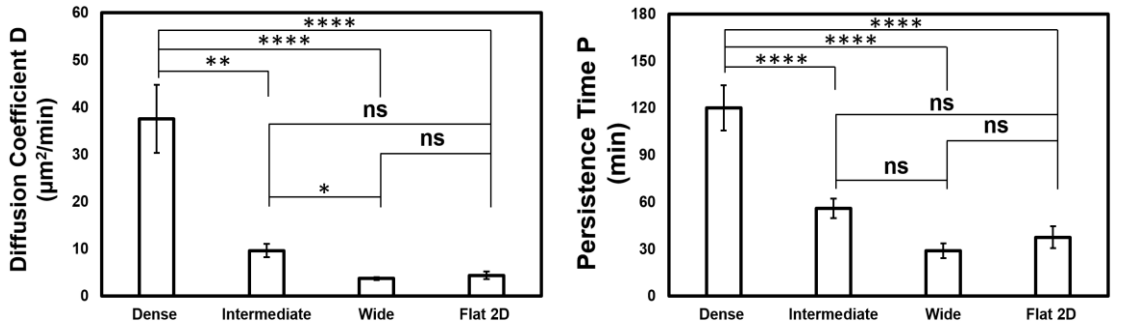

Supplementary Figure 4.S5. **Migration analysis using persistent random walk (PRW) model.** Diffusion coefficient (D) and persistence time calculated for all inter-fiber spacing and flat 2D using PRW model. Sample size is 29, 29, 17 and 13 for *dense*, *intermediate, wide,* and *Flat 2D* respectively.

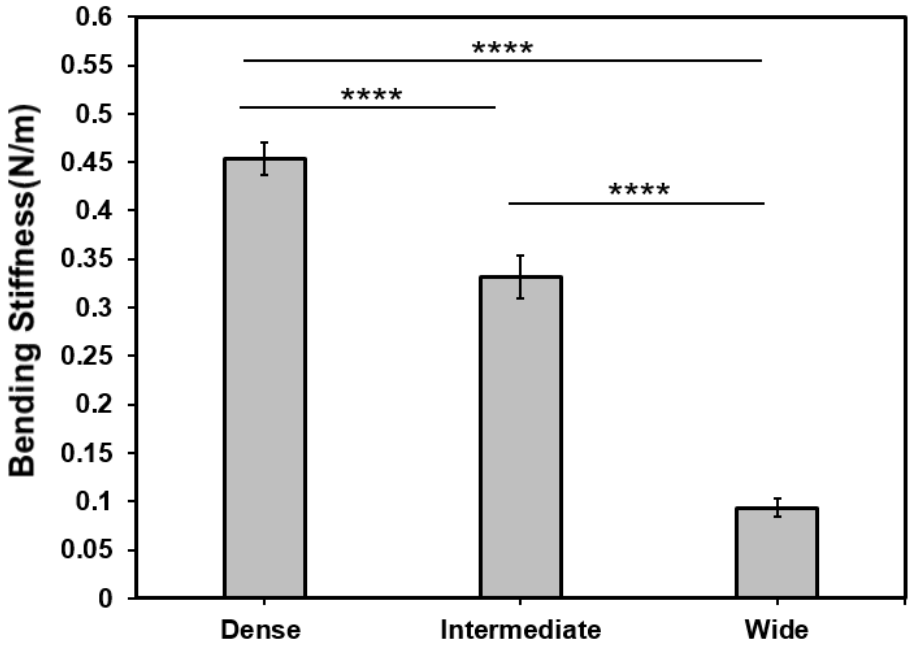

Supplementary Figure 4.S6. Bending stiffness (N/m) measured by AFM of the crosshatch networks (n=12, 14, and 11 for *dense*, *intermediate*, and *wide* networks)

Chapter 5:

Retraction fiber-driven stability governs mitotic rules in suspended fibrous environments

5.1 Introduction

The mitotic spindle is a remarkable biological machine responsible for proper segregation of chromosomes during cell division[190]. Its positioning determines the cell division axis orientation and is thereby crucial for tissue morphogenesis. Defects in spindle positioning are often implicated in developmental disorders and cancer progression[191]. Mitotic spindle positioning depends upon the cell shape and spatial organization of cell-matrix focal adhesions (FA) present during interphase[27,29,30,192]. Mitosis progresses with a series of morphological changes, the primary of which being the mitotic cell rounding[28,193]. In the rounded state, cells almost completely lose their adhesions and are connected to the ECM via thin actin-rich structures, referred to as retraction fibers[26,192]. Retraction fibers act as mechanical links to stabilize the orientation of the mitotic spindle[29,194,195], and to facilitate spreading of daughter cells following cytokinesis through re-establishment of FAs[26].

In vivo extracellular matrices (ECM) are typically fibrous in nature, consisting of individual fibrils and bundled fibers ranging in sizes from few hundreds of nm to several microns[153,196,197], and organized in a diverse range of fiber densities and network architectures which include both aligned configurations (ECM surrounding metastatic tumors[44]) and crossing fiber arrangements (loose connective tissues[47]). Cells in these native fibrous 3-dimensional environments form elongated cell-matrix adhesions that differ significantly from the low aspect ratio adhesions formed on flat 2D surfaces[82,198]. 2D

adhesive micropatterns of varying shapes designed to control cell shapes have shown cell rounding to occur in a mostly unrestricted manner. On the other hand, natural ECM imposes mechanical confinement, requiring cells to generate forces for overcoming confinement and proceeding with rounding up and mitosis[199,200]. Since fibrous ECM elicits differential FA organization and imposes confinement, we inquired if rules of mitotic progression mostly developed through studies on 2D extended to suspended fibers that mimic the natural ECM.

We used our previously reported non-electrospinning 'Spinneret Tunable Engineered Parameters' (STEP) technique to generate aligned and crosshatch networks of suspended fibers, to achieve diverse interphase cell shapes with controlled FA clustering sites[93,92], and retraction fibers. During mitosis, retraction fibers held rounded cells in position with different levels of stability dependent upon the number of FA clustering sites. We develop mitotic progression rules in retraction fiber-driven low to high stability and find a dramatic switch from monopolar to multipolar spindle defects with increased stability. We conclude that mitotic progression rules in biologically relevant fibrous microenvironments are radically different than the stereotypical 2D systems, and tightly linked with focal adhesion clustering.

5.2 Materials and Methods

Manufacturing nanofiber networks

Suspended fiber networks were generated from solutions of polystyrene (MW: 2,000,000 g/mol; Category No. 829; Scientific Polymer Products, Ontario, NY, USA) dissolved in xylene (X5-500; Thermo Fisher Scientific, Waltham, MA, USA) at 7 wt%, using our

previously reported STEP technique. Horizontal arrays of 250 nm fibers with inter-fiber spacings between 3-25 μm were deposited on large diameter (~2 μm) vertical support fibers placed ~ 350 μm apart. Support fibers were generated from 5 wt% solutions of polystyrene (MW: 15,000,000 g/mol, Agilent Technologies) dissolved in xylene. Crosshatch networks were prepared with orthogonal layers of 250 nm fibers with an inter-fiber spacing of ~50 μm. Fiber networks were bonded at intersection points using a custom fusing chamber.

Cell culturing and cell division synchronization

HeLa cells expressing Histone H2B GFP were cells were cultured in Dulbecco's modified Eagle's medium (Invitrogen, Carlsbad, CA) supplemented with 10% fetal bovine serum (Gibco, Thermo Fischer Scientific) in T25 flasks (Corning, Corning, NY, USA) and maintained at 37°C and 5% CO_2 in a humidified incubator. Nanofiber networks were first sterilized with 70% ethanol for 10 minutes, followed by functionalization with 4 μg/mL of fibronectin in PBS (Invitrogen, Carlsbad, CA). For select imaging experiments, fibers were coated with rhodamine-conjugated fibronectin (Cytoskeleton Inc.).

To synchronize divisions, cells were treated with 9 μM of the Cdk1 inhibitor RO-3306 for 20 h. Cells were subsequently released for division after 2 times wash with complete culture media. To capture cells at metaphase, paraformaldehyde (4%) fixation was performed ~ 1 h following drug washout.

Live imaging

Time-lapse optical imaging was performed every 5 minutes for extended periods of time (~12-16 h) to track multiple cell division events. Imaging was performed with a 20x 0.8

NA objective in a Zeiss AxioObxerver Z1 microscope. GFP fluorescence was captured using a FITC filter set. Experiments were performed under incubation conditions of 37°C and 5% CO_2 (Zeiss, Oberkochen, Germany).

Immunofluorescent staining and imaging

Cells were fixed with 4% paraformaldehyde for 15 minutes. Following 2 times PBS wash, permeabilization was performed with a 0.1% Triton X-100 solution. Permeabilized cells were washed with PBS (2x) and blocked with 5% goat serum (Invitrogen, Grand Island, NY) for 45 minutes. Primary antibodies were diluted in an antibody dilution buffer consisting of PBS with 1% Bovine Serum Albumin and Triton-X 100, and stored overnight at 4^{o} C. Primary antibodies include Anti-beta tubulin (1:500, mouse monoclonal, 2 28 33, Invitrogen), Anti-Hec1 (1:1000, human monoclonal) and Anti-phospho-Paxillin (1:100, rabbit polyclonal, pTyr31, Invitrogen). Secondary antibodies diluted in antibody dilution buffer was added along with the conjugated Phalloidin-TRITC (Santa Cruz Biotechnology) or Alexa Fluor 647 Phalloidin (1:40-1:80, Invitrogen), and stored in a dark place for 45 minutes. Secondary antibodies include donkey anti-human IgG Alexa Fluor 555 (1:600), Goat anti-mouse IgG Alexa Fluor 405 (1:500, Invitrogen) and Goat anti-mouse IgG Alexa Fluor 647 secondary antibody (1:500, Invitrogen). Confocal microscopy was performed using a laser scanning confocal microscope (LSM 880, Carl Zeiss Inc.) with optimal imaging settings and z-slice thicknesses ranging from 0.36-0.5 µm.

Cell shape metrics

To quantify cell shape during interphase, manual outlining of phalloidin stained cells were performed in Image J (NIH; https:// imagej.nih.gov/ij/) and aspect ratio (cell length by

width) was computed using the Bounding Rectangle function. Cell circularity is defined by $4\pi A/P^2$, where A is spread area (μm^2) and P is perimeter (μm) of the cell. A circularity value of 1.0 was achieved for perfectly circular cells. For elongated or contoured shapes, this value is reduced and falls between 0 and 1.

To compute cell heights during mitosis, complete z-stacks were processed in the Zen Blue (Carl Zeiss Inc) and orthogonal cross-section views (xz and yz) generated using the 'Ortho' function were used.

Scoring of mitotic defects

Cells stained for microtubules and DNA were visually inspected under a 40x objective to categorize as bipolar, monopolar or multipolar based on the number of spindle poles. At least 300 cells over 3-4 independent experiments were considered for each fiber category and Flat glass and the average proportion of observed bipolar, monopolar and multipolar cells are reported.

Quantifying cell rounding forces

Outward deflections of nanofibers during cell rounding were converted to force (nN) values using our previously reported Nanonet Force Microscopy[90]. Briefly fibers are modelled as Euler Bernoulli beams with fixed-fixed boundary conditions, and subjected to point loads at cell-fiber contact regions.

Statistical analysis

Statistical analysis was performed in GraphPad Prism (GraphPad Software, La Jolla, CA, USA) software. Statistical comparison among multiple groups were performed using one-

way ANOVA along with Tukey's honestly significant difference test. Pairwise statistical comparisons were performed using Student's t-test. Error bars in scatter data plots indicate standard deviation. *,**,***,**** represent $p< 0.05$, 0.01, 0.001 and 0.0001 respectively.

5.3 Results

Focal adhesion clustering controls metaphase plate oscillations

We wanted to inquire if the focal adhesion patterns on fibers correlating with different cell aspect ratios (AR), determined the dynamic orientation of the metaphase plate. We generated suspended nanofiber (fiber diameter ~ 250 nm) networks in both aligned and crosshatch geometries to achieve control on cells of diverse AR and FA clusters (**Fig. 5.1a**). Tuning the inter-fiber spacing (4 μm -25 μm) in the aligned networks resulted in 3 elongated high AR cell shapes, i) one-fiber spindle (1F-elongated) shapes of cells attached to single fibers and having two major FA clusters, ii) 2 fiber-rectangular (2F-elongated) attached to two fibers and having four FA clusters, and iii) multifiber-rectangular (MF-elongated) attached to ≥ three fibers with multiple FA clusters. Crosshatch networks of inter-fiber spacing ~ 50 μm induced symmetric polygonal kite-shaped cells with four FA clusters. Quantification of the ARs during interphase revealed highest elongated geometries in the 1F-elongated and 2F-elongated categories (AR~9, **Supplementary Fig. 5.S1**), followed by the MF-elongated shapes (AR ~ 5) and finally the 2F-kite shape and 2D-rounded cells on flat 2D having AR close to 1. Using HeLa cells expressing Histone H2B GFP, we investigated the dynamics of mitotic progression (Fig. 5.1a). As cells balled up during mitosis, we observed them to be held in place by actin retraction fibers

originating at the FA cluster sites and connecting to the cell cortex. Consistent with previously reported literature[201], we observed that following mitotic entry,

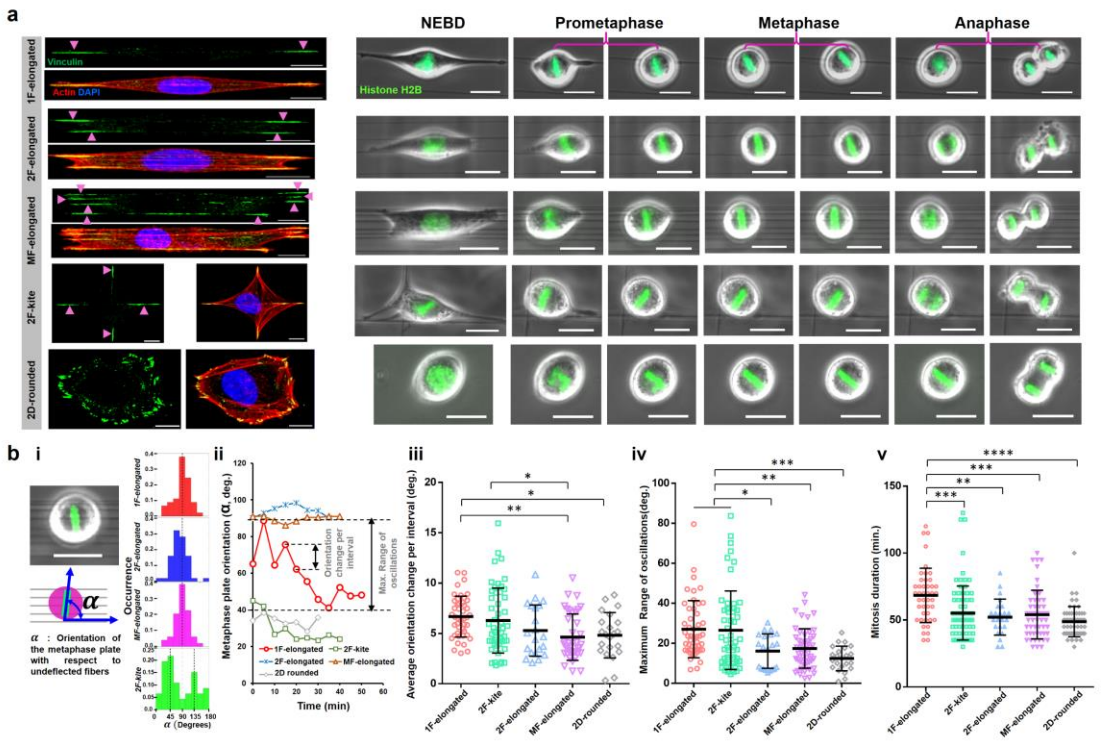

Figure 5.1: Cell division in suspended fiber environments. (a) Time-lapse images showing representative cases of mitotic progression, corresponding to 5 distinct interphase cell shapes: needle (1-fiber), 2F-rectangular (2 fibers), MF-rectangular (≥3 fibers), 2F-kite (2 orthogonal fibers) and 2D-rounded (glass coverslips). Cells are fluorescently stained with actin (red), vinculin (green) and nucleus (blue), Scale bars represent 10 μm and 20 μm respectively, (b,i) Illustration showing convention for metaphase plate orientation (α), (ii) Analysis of individual temporal profiles of metaphase plate orientation using orientation change per interval maximum range of metaphase plate oscillations (iii,iv) Statistical comparison across all fiber configurations and 2D for metaphase plate dynamics, (v) mitosis duration analysis showing 1F-elongated to be slowest.

the metaphase plate (MP) exhibited significant fluctuations about its mean position. We characterized the fluctuations of the MP orientation with respect to the undeflected fibers (α, **Fig. 5.1b(i)**). In aligned fiber networks, we found the orientation profiles to be centered around 90^o (i.e. orthogonal to the cell elongation during interphase, Fig. 1c(i) and **Fig. S1**) in good agreement with Hertwig's rule. Interestingly, in the case of 2F-kite shaped cells attached to crosshatch networks with AR~1, the temporal profiles (**Supplementary Fig.**

5.S2) were mostly centered around either 45^{o} or 135^{o}, indicating a preferential alignment of the MP diagonally between the two orthogonal fibers and sites of cell adhesion.

A closer inspection of the individual temporal profiles (**Fig. 5.1b(ii)**) indicated significant changes in the orientation of MPs during mitosis. We quantified the degree of orientation changes using two metrics: i) absolute orientation change of the MP per time interval, and ii) maximum angular range of MP rotations. Across all elongated shapes, we observed that the 1F-elongated shaped cells with two FA clusters demonstrated significantly higher orientation changes (**Fig. 5.1b(iii)**) and the highest angular range of MP rotations (**Fig. 5.1b(iv)**). Incidentally, similar levels of dynamic activity of the MP was also observed in symmetric 2F-kite shaped cells with four FA clusters. Intrigued by the differences in MP dynamics, and the curious similarity between 1F-elongated and 2F-kite shapes, next, we investigated the durations for mitosis completion (nuclear envelope breakdown to anaphase completion, **Fig. 5.1b(v)**). We found that 1F-elongated cells took significantly longer average times (68.4±3 min, mean±sem) to divide, as compared to other suspended cell shapes (50-55 min) or on traditional flat glass coverslips (48.8±1.5 min).

Spatial organization of retraction fibers modulates mitotic cell shape and dynamics

Our observations of increased metaphase plate orientations and mitotic times in 1F-elongated cells prompted us to inquire on the role of retraction fiber-driven stability in mitotic outcomes. From timelapse videos, we had observed rounded cells held in position by retraction fibers (schematically shown in **Fig. 5.2a(i), Supplementary Fig. 5.S3a**). Using confocal microscopy, we analyzed the TOP (xy, **Fig. 5.2a(ii)**), SIDE (zy, **Fig. 5.2b**), and FRONT (xz, **Fig. 5.2c(i)**) views and identified retraction fibers to appear as actin-rich hotspots in the averaged intensity heatmaps of the cell cortex. 1F-elongated cells attached

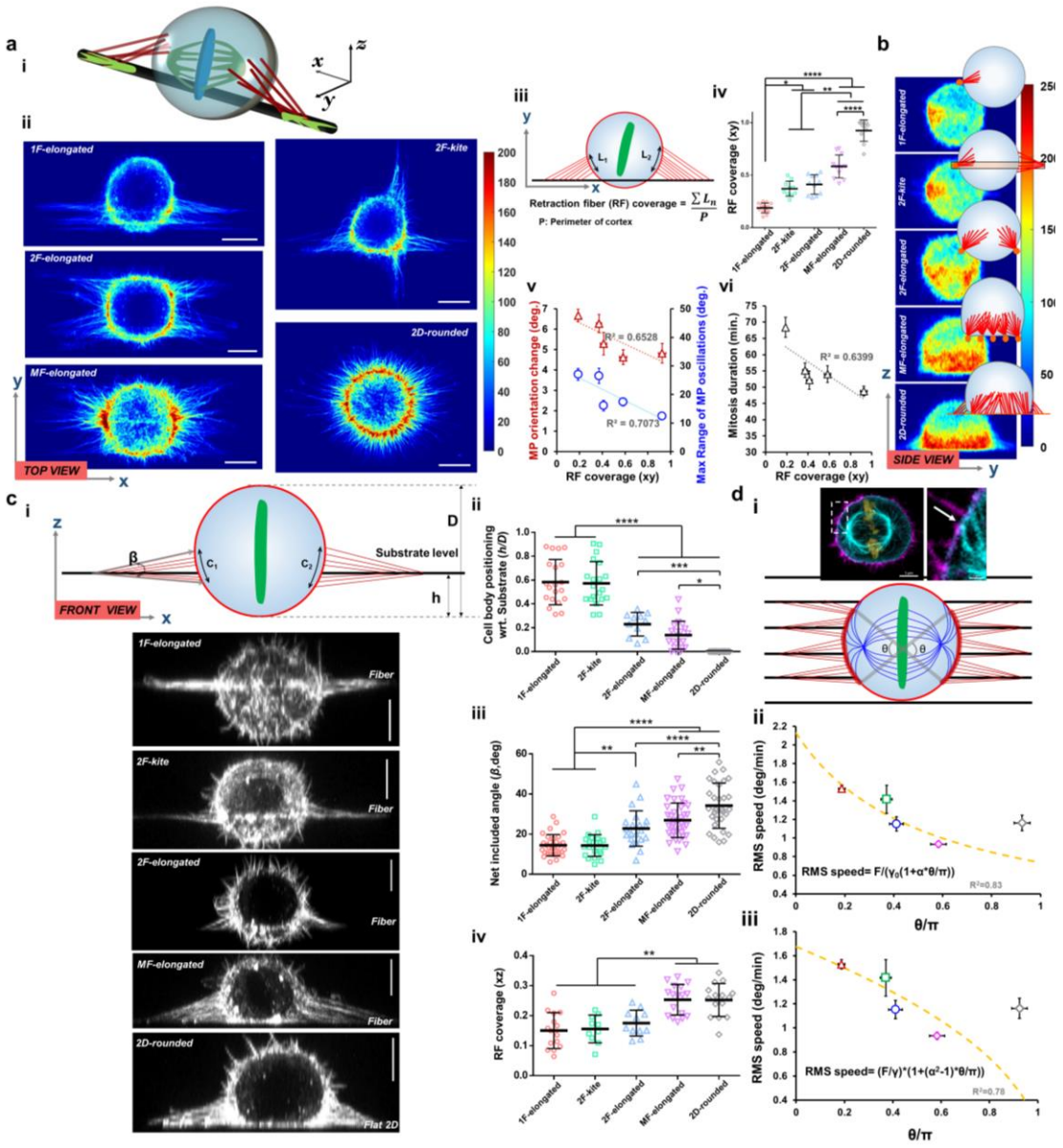

Figure 5.2. Retraction fiber-based stability and positioning of mitotic rounded cell bodies. (a,i) 3D schematic of rounded cell body held in place by retraction fibers in a single-fiber category, (ii) Average hotspots of retraction fibers from confocal microscopy of top view across various fiber configurations and 2D (n=10 per category), (iii)schematic describing retraction fiber coverage metric, (iv) retraction fiber coverage across fiber configurations and 2D in xy plane, (v) metaphase plate orientation and maximum range of oscillations decrease with increasing retraction fiber coverage, (vi) mitosis duration decreases with increasing fiber coverage. (b) Average hotspots of retraction fibers from confocal microscopy of side view across various fiber configurations and 2D (n=10 per category). (c, i) Representative images showing front view of mitotic cells across various fiber configurations and 2D, schematic shows the retraction fiber organization from the front view of cells, (ii) cell body positioning

(h/D ratio defined in c(i)) across all fiber configurations and 2D, (iii) net included angle (β, defined in c(i)) across all fiber configurations and 2D, (iv) retraction fiber coverage in xz plane across all fiber configurations and 2D, (d, i) Representative image and schematic showing the mechanical linking of the astral microtubules and the cell cortex at the sites of the retraction fibers, (ii,iii) Model formulations based on reduced forces and increase effective friction respectively

to single fibers, through two major FA clusters, were connected by two major sets of retraction fibers during mitosis. Interestingly, 2F-kite shaped cells despite having four FA clusters during interphase, in the rounded mitotic state were found to be anchored by two dominant sets of orthogonally arranged retraction fibers. To quantitate the spatial localization of retraction fibers, we introduced a new metric: retraction fiber coverage, defined as the fraction of the cortical perimeter to which retraction fibers were localized along two principal equatorial planes (**Fig. 5.2a(ii)** for TOP view, and **Fig. 5.2c(v)** for FRONT view). Averaged over both planes, the 1F-elongated cells had a retraction fiber coverage of only ~0.19 and 0.15 while cells on Flat 2D had an average value of ~ 0.92 and 0.25 for TOP and FRONT views, respectively. Not surprisingly, plotting MP orientation changes per interval and maximum angular range, as a function of retraction fiber coverage demonstrated reduced MP oscillations with increasing retraction fiber coverages (**Fig. 5.2a(v)**). Coincidentally, mitosis time decreased with increasing number of retraction fibers (**Fig. 5.2a(vi)**), indicating a role of mechanical stability in mitosis.

Next, given our observations of altered patterns of retraction fibers, we wanted to investigate the 3D shapes of mitotic cells. Quantification of the mitotic cell heights and aspect ratios revealed that multifiber and flat 2D cases supporting largest number of focal adhesion clusters and retraction fibers caused cell bodies to be non-spherical, i.e. the bodies

had reduced heights (**Supplementary Fig. 5.S3**). Our observations are in excellent agreement with previous studies on flat 2D, which also report shorter cell heights than widths[202]. To relate the spatial arrangement of retraction fibers and cell body with respect to fiber axis, we introduced new metrics: i) number of retraction fibers associated with a single FA cluster, ii) location of rounded cell with respect to substrate, and iii) net included angle (β), defined as the angular spread of the retraction fibers about their attachment sites. Quantification of the number of major retraction fibers emanating from individual FA clusters revealed an average of 10-12 retraction fibers per category (**Fig. 5.2c(ii)**). Interestingly, analysis of the cortical distribution of retraction fibers revealed that in case of 1F-spindle and 2F-kite, retraction fibers were mostly positioned along the nanofiber plane, in contrast to the MF-rectangular or the 2D-rounded category, where they were organized at a steeper angle between the mid-cortical level of the rounded cell and the underlying substrate. Thus not surprisingly, the net included angle and the retraction fiber axial distribution were found to be significantly higher in MF-elongated and the 2D-rounded categories **(Fig. 5.2c (iii,iv))**. Additionally, we observed that the rounded mitotic cell was positioned roughly in the mid-cortical level for 1F-spindle and 2F-kite shapes (h/D ratio~ 0.5-0.6), while rounded cells on multiple fibers typically were positioned on top of the fiber plane (h/D ratio~0.1) similar to cells on Flat 2D (Fig. 2a(ii), **Fig. 5.2c(v)**).

Next we wanted to compare our experimental observations of metaphase plate stability at higher levels of retraction fiber coverage, with predictions from theoretical models. Here, we present two formulations, with both models based on the force interactions between the actin cortex and astral microtubules (**Fig. 5.2d(i)**). The first formulation takes into account the higher effective friction experienced by the interacting microtubules, in the region of

the cell cortex covered by the retraction fibers. Thus the root-mean-square (RMS) angular velocity of the metaphase plate (quantified from distributions of the angular velocity, **Supplementary Fig. 5.S4**) scales with the microtubule-cortex forces (F) as, $\sqrt{\langle v^2 \rangle} = \sqrt{\langle F^2 \rangle / \gamma^2}$, where γ is the friction coefficient, which is given by $\gamma=\gamma_0(1+(\theta/\pi)\alpha)$, where $\alpha>1$ denotes the higher effective friction in the cortical region attached to the retraction fibers. Thus the RMS speed of the metaphase plate depends directly on the retraction fiber coverage as

$$\sqrt{\langle v^2 \rangle} = \frac{F}{\gamma_0\left(1+\left(\theta/\pi\right)\alpha\right)}.$$

The second formulation is based on the reduction of the forces exerted by the astral microtubules on the cortex due to being "stuck" on adhesion complexes where the retraction fibers emanate. The central approximation is that microtubules are less mobile when in contact with a cortex area that has retraction fibers linked to it. Thus the mean square force (microtubule-cortex) can be given as:

$$\langle F^2 \rangle = \left[\left(1 - \theta/\pi\right) + (\theta/\pi)\alpha^2\right]F^2$$

and the corresponding RMS speed $\sqrt{\langle v^2 \rangle} = \sqrt{\langle F^2 \rangle / \gamma^2} = \frac{F}{\gamma}\sqrt{[1 + (\theta / \pi)(\alpha^2 - 1)]}$

Our fitting results demonstrate α is effectively zero ($1.48*10^{-6}$), which brings the dependence of the MP RMS speed on retraction fiber coverage as $\sqrt{\langle v^2 \rangle} = \frac{F}{\gamma}\sqrt{[1 - (\theta / \pi)]}$.

Both of the proposed models fit our experimental data quite well (R^2=0.83 and 0.78 respectively, **Fig. 5.2d (ii,iii)**) and demonstrate how increasing the retraction fiber coverage (θ/π) results in a significant reduction in overall movements of the metaphase plate.

Overall, we found that the spatial organization of retraction fibers in fibrous microenvironments, regulated the 3D positioning and shape of mitotic cells and led to varying levels of mechanical stability of the metaphase plate.

Dynamics of daughter-cell positioning

Since metaphase spindle dynamics and mitotic times were governed with the organization and density of retraction fibers, we inquired if the orientation of cell division axis and the subsequent positioning of the dividing daughters were also affected. We quantified the orientation of the division axis with respect to the underlying fiber orientation. Interestingly, 1F-elongated cells, being the least stable cells demonstrated the widest spread (**Fig. 5.3a**) in their division axis orientation as compared to the 2F-rectangular or MF-rectangular cell shapes. Consistent with average metaphase plate orientations, 2F-kite shaped cells showed a distinct peak (~ 67%) in the 30-60^o region, indicating the division axis to be symmetrically located between the two orthogonal fibers. On Flat 2D substrates, due to the isotropic distribution of retraction fibers the division axis distribution was observed to be mostly random, in agreement with previous reports[203].

Additionally, following mitotic exit by formation of the cytokinetic furrow, we observed that the orientation of the cell division axis to be highly dynamic. We tracked the orientation of the cell division axis from late metaphase (see methods for defining cell division axis orientation) till the time taken by daughter cells to begin spreading (**Fig. 5.3b**).

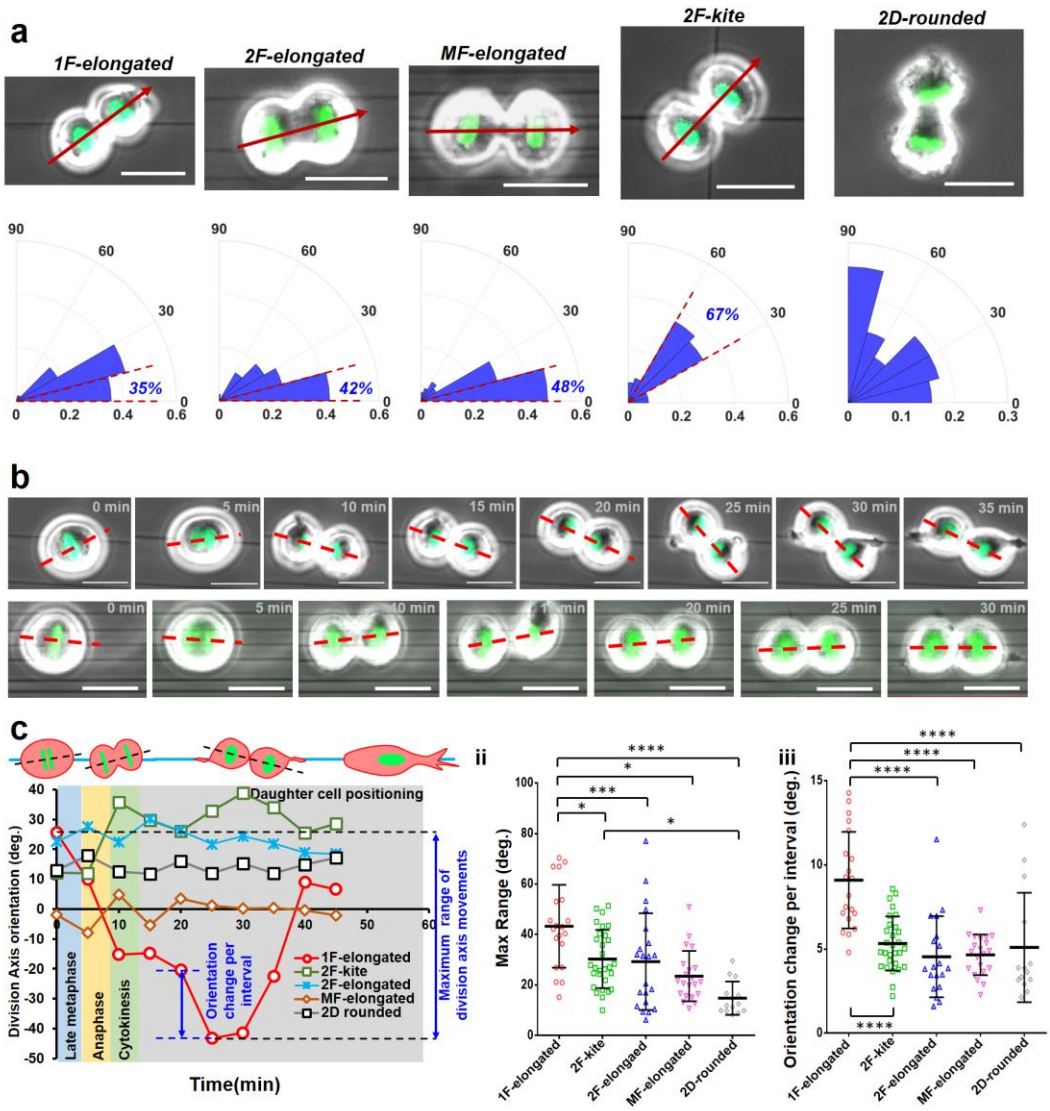

Figure 5.3: Division axis orientation and daughter cell positioning on suspended fibers: (a) Polar histograms of cell division axis orientations (marked by red arrow) in for different fiber geometries, absolute acute angle magnitudes of orientation are used, n=45, 41, 62,105 and 50 for 1F-elongated, 2F-elongated, MF-elongated, 2F-kite and 2D rounded, respectively. Percentage of cells in 0-15^{o} sector for aligned geometries, and 30-60^{o} for crosshatch geometry, (b) Timelapse images showing the representative dynamics of cell division axis (red dashed line) in single fibers versus multiple fibers. (c) i) Representative profiles showing the variations of division axis orientation and subsequent positioning of daughter cells, (ii,iii) Statistical comparison of the max range of division axis movements and orientation change per interval, for the different substrate categories.

As with previous analysis (**Fig. 5.1**), we utilized two major parameters: maximum range of orientation change in the total time period and average orientation change during individual imaging intervals (**Fig. 5.3c(i)**). We found that daughter cells of 1F-elongated cells, were

the most unstable as they underwent the maximum degree of motion before achieving steady state positioning (**Fig. 5.3c(ii,iii)**). High-speed timelapse microscopy demonstrated that the fluctuations in daughter cell positioning were primarily mediated by the retraction fibers. Not surprisingly, cells attached to multiple fibers (MF-rectangular shape), demonstrated significantly reduced fluctuations in daughter cell spreading, due to increased stability via multiple groups of retraction fibers. Overall, we found that increased levels of retraction fiber connections results in stable positioning of the daughter cells following mitotic exit.

Cell confinement causes force buildup to affect mitosis

Mitosis proceeds with cells rounding up and exerting outward forces, and natural ECM environments impose confinement. We wanted to inquire the role of confinement in mitotic progression, and found that the 2F-elongated cells often got trapped (confined) within the two parallel fibers resulting in outward push of the fibers (**Fig. 5.4a**). To quantify the extent of confinement, we analyzed the positioning of the rounded cell with respect to the fiber plane (**Fig. 5.4b**) from cross-sectional side views(yz) and observed that in a significant proportion (~35%) of cells, the fibers were located roughly at the mid-cortical level (h ~ D/2, **Fig. 5.4b**). We took advantage of such entrapment of the mitotic cell between 2-parallel fibers (2F-rectangular shape during interphase, **Fig. 5.4c**) to estimate the rounding forces during mitosis using Nanonet Force Microscopy[90,94,95,189] (NFM). During interphase, cells are in their natural contractile state and thus deflect the fibers inward. However, following mitotic entry, as cells progressively round up in this entrapped configuration, they push out the fibers to cause distinct outward deflections (Fig. 3a, yellow arrows). Consistent with previously reported literature[202,204], we observed a steady increase

in the rounding forces from nuclear envelope breakdown, with peak mitotic forces of ~12-14 nN averaged over multiple cells. Following mitotic exit (anaphase completion), rounding forces dropped sharply, with outward fiber deflections becoming negligible. Finally, with daughter cell formation and spreading, fiber deflections were again found to be inward, indicating transition into the contractile state. In the case of unconfined cells (**Figs. 5.1** and **5.2**), we observed the balled-up cells to be sitting on top of fibers and held in position by retraction fibers. Knowing the average number of retraction fibers (**Fig. 5.2**) and the forces associated with almost complete balled-up state of the cell, allowed us to approximate the tension in each retraction fiber (~230 pN) by assuming retraction fibers to be springs in parallel.

Next, we wanted to understand the effect of mechanical confinement in the overall mitotic progression. Interestingly, we found that mitotic cells under confinement were significantly taller (increased cell height, **Fig. 5.4d(i,ii)**) with a higher aspect ratio (**Fig. 5.4d(iii)**) as compared to their unconfined counterparts. We found that confinement caused a significant drop in metaphase plate (MP) fluctuations (**Fig. 5.4d(iv)**), which coincided with faster mitotic progression (**Fig. 5.4d(v)**) and higher inter-kinetochore stretching (**Supplementary Fig 5.S5b**) and increase in the angle of division axis (**Fig. 5.4d(vi,vii)**). The increase in angle caused the daughter cells to spread on adjacent fibers and can be potentially attributed to a spatial repositioning or 'tilt' in 3D space caused by the cortical-deformation induced physical constraints. Indeed quantification of the metaphase plate orientation in the xz-plane for confined cells revealed a significantly higher tilt angle as compared to their unconfined counterparts (**Supplementary Fig. 5.S5).** Overall, external mechanical confinement achieved with fiber-doublets allowed us to

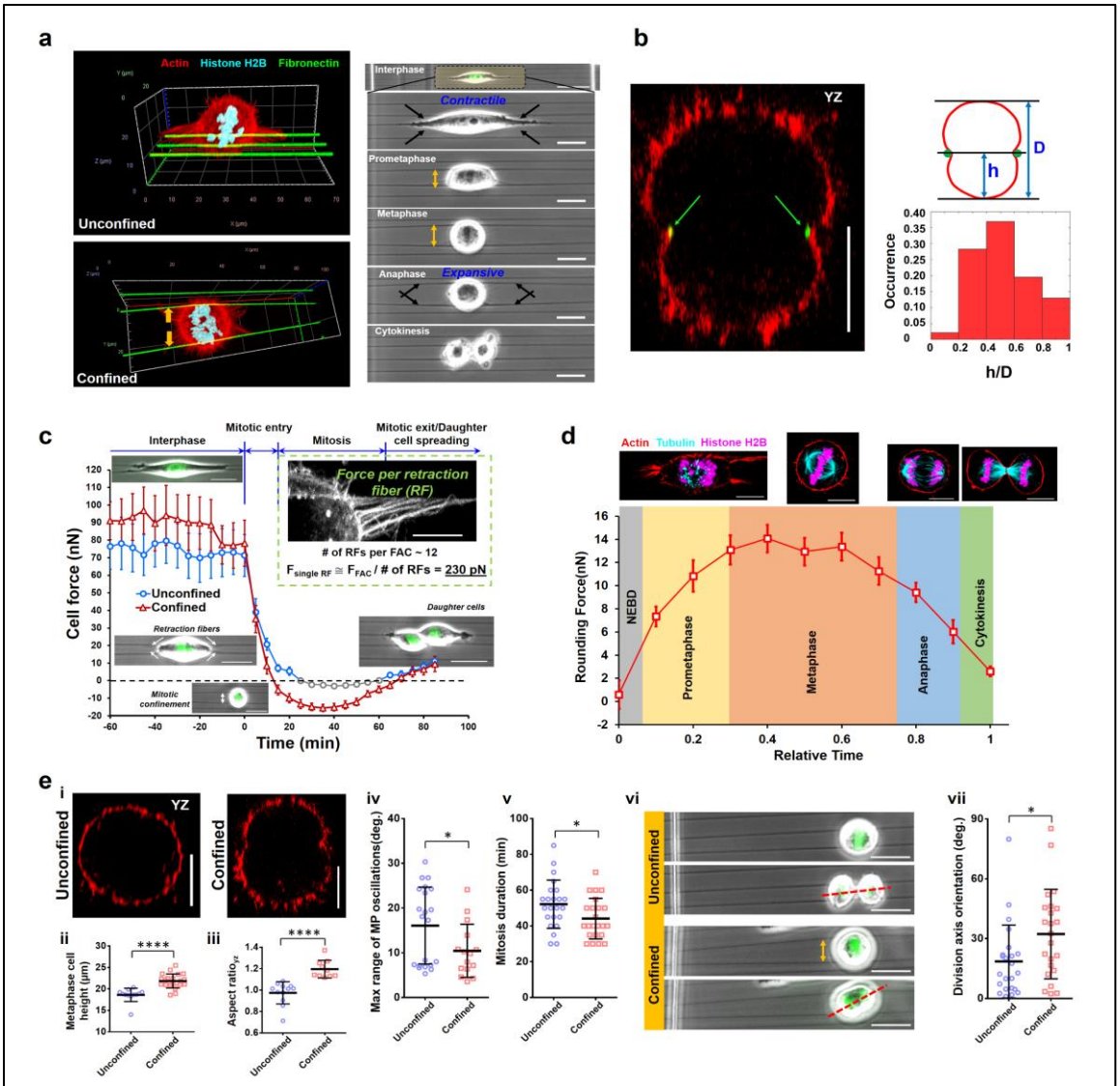

Figure 5.4: Forces in cell division. (a) Isometric views of a representative cells positioned on top of the fiber network (unconfined category) and confined between 2-fibers (confined category). Actin (red), fibers (green), chromosomes (cyan). During mitosis, the contractile forces change direction from inward pointing to outward pointing as cell balls up and pushes the fiber outwards (yellow arrows). Scale bars 20 μm. (b) Side view (yz) of a representative confined cell. Actin (red) and fibers (green) are indicated by green arrows. Illustration showing the positioning of the cell with respect to the fiber plane, h: height of rounded cell below the fiber plane, D: Net cell height, Scale bar is 10 μm. (c) Average rounding forces of confined and unconfined cells in two-fiber category. Inset shows analysis of approximating tension in each retraction fiber (n= 20 per category). Forces for the retraction fiber analysis are taken from the unconfined force profiles and divided by four to obtain force per focal adhesion cluster length. (d) Force profiles during cell rounding and mitosis are normalized for time taken from NEBD to cytokinesis (n=23). (e,i) Representative side views of unconfined and confined cells at metaphase, Scale bars are10 μm, (ii,iii,iv,v) Comparison of metaphase cell height, aspect ratio, maximum range of metaphase plate (MP) oscillations and mitotic duration between the

unconfined and confined categories, respectively, (vi) Representative images showing mechanical confinement re-orients division axis, and vii) Comparison of cell division axis orientation (with respect to undeflected fibers) between unconfined and confined category respectively.

characterize mitotic rounding forces, which we found accelerate mitotic progression by increasing stability of the metaphase plate.

Mitotic fidelity is influenced by fiber geometry

Our observations that controlling interphase cell shape and adhesion geometry can significantly affect the metaphase plate dynamics, mitotic duration and daughter cell positioning led us to inquire if the mitotic spindle machinery was affected by fiber geometry as well. To this end we synchronized divisions of HeLa cells by treatment and washout with the Cdk1 inhibitor RO-3306 and fixed mitotic rounded cells at metaphase[205,206]. We immunostained the rounded cells for different components of the mitotic spindle machinery (**Fig. 5.5a**): microtubules (β-tubulin), kinetochores (Hec1) and the chromosomes (Histone H2B). We quantified the net length and width of the mitotic spindle (**Fig 5.S3**) and did not observe differences between the overall spindle shape across fiber networks and also with conventional flat glass substrates. Since kinetochore stretching is directly associated with regulation of mitotic timing[207], we wanted to estimate the extent of stretching by analyzing the inter-kinetochore separation distances(***δ*** in **Fig. 5.5b**). Our observations reveal that the inter-kinetochore separation distance was reduced in the 1F-elongated cells (**Fig. 5.5c**), thus, potentially explaining the slower mitotic progression in these cells (**Fig. 5.5d**).

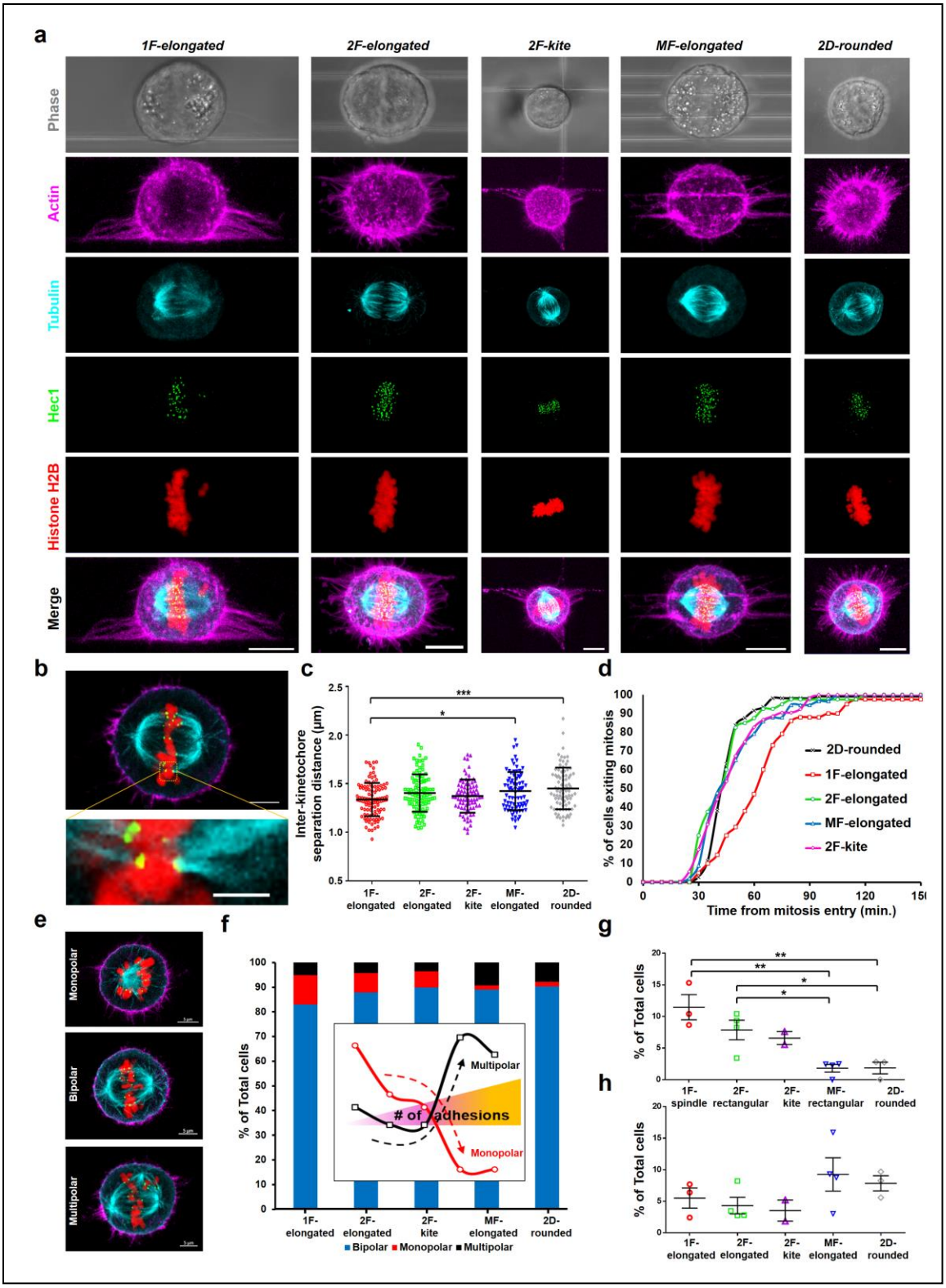
a
1F-elongated
2F-elongated
2F-kite
MF-elongated
2D-rounded
Phase
Actin
Tubulin
Hec1
Histone H2B
Merge
b
c
Inter-kinetochore separation distance (μm)
***
*
1F-elongated
2F-elongated
2F-kite
MF-elongated
2D-rounded
d
% of cells exiting mitosis
Time from mitosis entry (min.)
2D-rounded
1F-elongated
2F-elongated
MF-elongated
2F-kite
e
Monopolar
Bipolar
Multipolar
f
% of Total cells
Multipolar
# of adhesions
Monopolar
Bipolar
Monopolar
Multipolar
g
% of Total cells
**
**
*
1F-spindle
2F-rectangular
2F-kite
MF-rectangular
2D-rounded
h
% of Total cells
1F-elongated
2F-elongated
2F-kite
MF-elongated
2D-rounded

Figure 5.5: Mitotic spindle machinery in different fiber geometries: (a) Cells are fixed at metaphase and stained for the actin cortex (magenta), microtubules (cyan), kinetochores (green) and chromosomes (red). Maximum intensity projected images are shown. Brightfield images show the respective fiber networks. (b) Representative image showing a pair of kinetochores attached to both ends of a single chromosome via microtubules. (c) Comparison of the inter-kinetochore separation distance between the different cell shapes. (d) Cumulative profiles showing the mitotic progression for the different categories. (e) 3 major categories of mitotic spindles based on the number of observable poles. (f) Relative occurrence of monopolar, bipolar and multipolar spindles in the different cell shape categories. (g,h) Comparison of monopolar and multipolar defects in the different substrate categories.

Next, we wanted to investigate if the assembly of the mitotic spindle was affected by the underlying fiber geometry. Similar to previously reported classification of mitotic spindles, we also observed 3 major types of outcomes (**Fig. 5e**): i) bipolar (2 symmetrically positioned spindle poles for normal chromosome segregation), ii) monopolar (1 spindle pole, defective chromosome segregation), and iii) multipolar (at least 3 spindle poles, defective chromosome segregation)[208]. To understand the relative occurrence of these spindle types, we sampled at least 300 cells (from multiple independent experiments) for each cell shape category and observed significant differences in the relative occurrences of the mitotic spindles. Increasing the stability during mitosis (increasing the number of fibers) resulted in increased percentage of bipolar segregation (**Fig. 5.5f**). Contrarily, decreasing the stability during mitosis (1F-elongated and 2F-kite) resulted in significantly higher percentage of monopolar spindles (**Fig. 5.5f, 5.5g**). Unexpectedly, we found increased incidences of multipolar defects at high stability during mitosis (MF-elongated and 2D-rounded, **Fig. 5.5h**). Overall, we found that number of focal adhesions and associated retraction fiber-mediated stability contributed to mitotic spindle integrity and chromosome segregation outcomes.

5.4 Discussion

It is now well-appreciated that the orientation of the mitotic spindle is regulated by interphase cell shape and adhesion organization. Here, we inquired about the role of mechanical stability in establishing mitotic rules for cells attached to suspended and physiologically relevant ECM-mimicking nanofibers of well-controlled geometries. We demonstrate that the positioning and stability of the mitotic spindle are regulated by the spatial organization of the actin-rich retraction fibers unique to organization of focal adhesions.

To understand the interplay of elongated cell shape and adhesion organization, we designed aligned fiber networks with tunable inter-fiber spacing, so that cells interacted with either single fibers, fiber doublets or multiple fibers (MF-rectangular shape). Consistent with observations on elongated cells on micropatterns, cells on aligned fibers divided along the fiber axis[191]. Our observations that the metaphase plate can undergo significant levels of oscillations, are in agreement with previous studies which also report similar movements over the course of the division process[201]. However, unique to fibers was the observation that the most elongated shape demonstrated the widest spread in the cell division axis orientation and metaphase plate movements, which contrasted findings from previously reported literature[27]. These differences can be explained from the fact that cells dividing on single fibers are mechanically stabilized by only two sets of retraction fibers.

Recent studies have demonstrated how astral microtubules existing at either end of the mitotic spindle, is mechanically linked to the cell cortex and the retraction fibers via the integrin-dependent cortical mechanosensory complex[29]. Furthermore, during mitotic entry since retraction fibers emanate from interphase adhesion sites, such organization dictates

the preferential recruitment of integrins and other key players of the cortical mechanosensory complex including caveolin-1, FAK, LGN-NuMA, dynein and MISP, to the cell cortex[29–31]. Selective enrichment of such complexes in the cortical regions connected to retraction fibers, ultimately directs proper positioning of the mitotic spindle. Our theoretical formulation of the mitotic spindle stability, is based on such mechanical interactions/links between the astral microtubules and the cortical complexes and thus predicts a constraining effect on metaphase plate movements at higher cortical coverage by retraction fibers.

Previous studies have shown how retraction fibers exert appreciable levels of forces on the mitotic cell body and their spatial organization can dictate the ultimate orientation of division axis irrespective of interphase cell shape[195]. Alternatively, loss of retraction fibers mediated by knockdown (KD) of β_5-integrins, can lead to random orientations of the mitotic spindle[209]. We also interrogated the organization of retraction fibers and found them to control the position of the rounded cell body with respect to the fiber axis. Cells on single fibers (1F-elongated) had two sets of retraction fibers that originated at the two poles (focal adhesion cluster sites) leading to the least stable configuration. Surprisingly, a large number of cells attached to two-fiber crosshatches underwent mitotic events by positioning half-way between the two fibers (angle of 45 degrees). In both these configurations, the retraction fibers were found to contact the cell body off-centered from the fiber axes, thus, positioning the rounded cell body relative to fiber axes (highest h/D ratio, Fig. 2). Increasing the number of parallel fibers (two and multi-fibers) resulted in retraction fibers to be above the fiber axes, causing the rounded cell body to be positioned

above the fiber axes (reduced h/D ratio). In case of cells being confined in two-fiber category, the retraction fibers were found to be closer to the fiber axis plane.

The tension in the retraction fibers emerging from the cell midbody[209], can cause substantial sagging of mitotic rounded cells on flat surfaces, resulting in a flattened morphology (cell height/width < 1)[202,210]. For cells rounding on top of multiple fibers (MF-elongated shape) the retraction-fiber mediated forces led to flattened shapes with local cortical deformations at the cell-fiber interface. However, for cells attached to individual fibers (1F-elongated) or orthogonal fibers (2F-kite), we observed circular cross-sections of mitotic cells (aspect ratio ~1). Such differences in mitotic cell shapes can potentially explain why multipolar defects are more prevalent in the slightly flattened mitotic cells on multiple fibers or flat surfaces while monopolar defects are more common for the highly circular mitotic cells observed on single fibers[211].

Mitotic cell rounding is associated with a multi-fold increase in the cortical tension[212] and the intracellular hydrostatic pressure[202], which manifest as outward expansive forces required to undergo cell rounding within confined microenvironments like solid tumors[20,213]. Failure to counteract mechanical confinement can lead to spindle defects[214], delayed cell division[215] and even cell death. While these rounding forces are essential for normal mitotic progression, challenges in manipulation and confinement of rounded cells during mitosis, make the force measurements challenging. Currently, the rounding-cell force measurements have been made using involving AFM cantilevers[202] and micropillar arrays[204]. Our use of fiber doublets with an inter-fiber spacing of ~ 10 μm enables confinement of cells during mitotic rounding offers a straightforward approach without the need of any external manipulation. Our method allows us to estimate force signature from

interphase to all stages of mitosis, followed by daughter cell forces. In line with reported transient evolution of forces as cells undergo mitosis, we find a monotonous decrease from baseline force values, after nuclear envelope breakdown, followed by a constant peak level of forces during metaphase and a gradual increase during anaphase and cytokinesis. Average rounding forces of ~ 12 nN recorded in our fiber doublets during metaphase are similar to the peak forces observed by Sorce et al. using micropillar based lateral confinement assays[204] but lower than the magnitudes (~80nN) observed in AFM confinement assays. These differences can be attributed to the much larger contact area between mitotic cells and AFM cantilevers, as compared to the regions of cell contact with individual nanofibers. A unique advantage of our method is the ability to identify the contractile load carried by each retraction fiber group to estimate the average mechanical tension associated with individual retraction fibers. Modeled as springs in parallel, our estimated value of ~230 pN tension in single retraction fibers is in excellent agreement with previously reported values using optical tweezers (250 pN)[195].

Mechanical confinement can induce a diverse range of alterations in the mitotic dynamics. Under conditions of extreme vertical confinement[199] using agar gels placed apart at separations less than 7 μm, mitotic cells fail to round up properly and demonstrated significantly delayed division completion. Similar results were obtained under AFM cantilever mediated confinement[216], with mitotic progression significantly inhibited in cells experiencing >100 nN external forces. Moreover, studies performed in dense 3D gels[217] have demonstrated how cell-ECM force interactions can alter the cell division axis orientation and even the overall shape of the mitotic spindle. Interestingly, mechanically confined cells in our fiber doublets demonstrated significantly reduced mitosis completion

times as compared to their unconfined counterparts. Such observations are consistent with previous reports[215] which also demonstrate accelerated mitotic progression under conditions of low confinement (5-10 nN) using AFM cantilevers.

5.5 Conclusion

Here, we demonstrate retraction fiber driven stability governs mitotic rules in ECM-mimicking suspended fibrous microenvironments. The dramatic switch between monopolar and multipolar defects by simply changing the number of fibers highlights the importance of fiber geometry. Fiber diameter regulates cell contractility through alterations in the size of focal adhesion clusters and number density of cell-spanning actin stress fibers. Thus, we emphasize the need to include ECM-mediated regulation of cell division, which will likely impact pathophysiological outcomes.

Supplementary Material

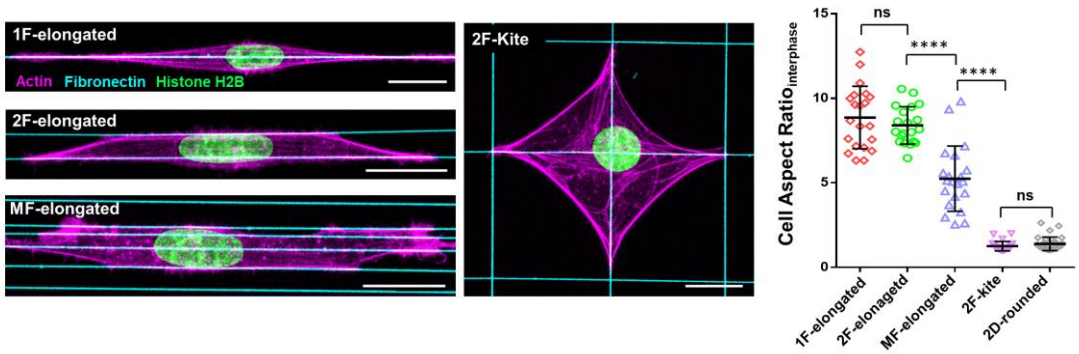

Supplementary Figure 5.S1: Cell shapes during Interphase: Representative stained images and cell aspect ratio quantification corresponding to 1F-elongated, 2F-elongated, MF-elongated, 2F-kite and 2D-rounded

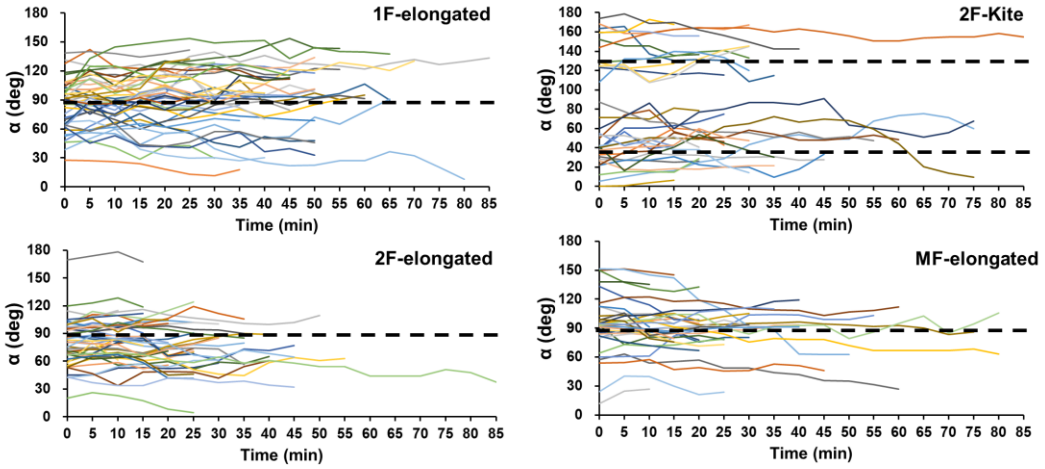

Supplementary Figure 5.S2: Compilation of individual profiles showing temporal dynamics of metaphase plate movements for the different fiber geometries

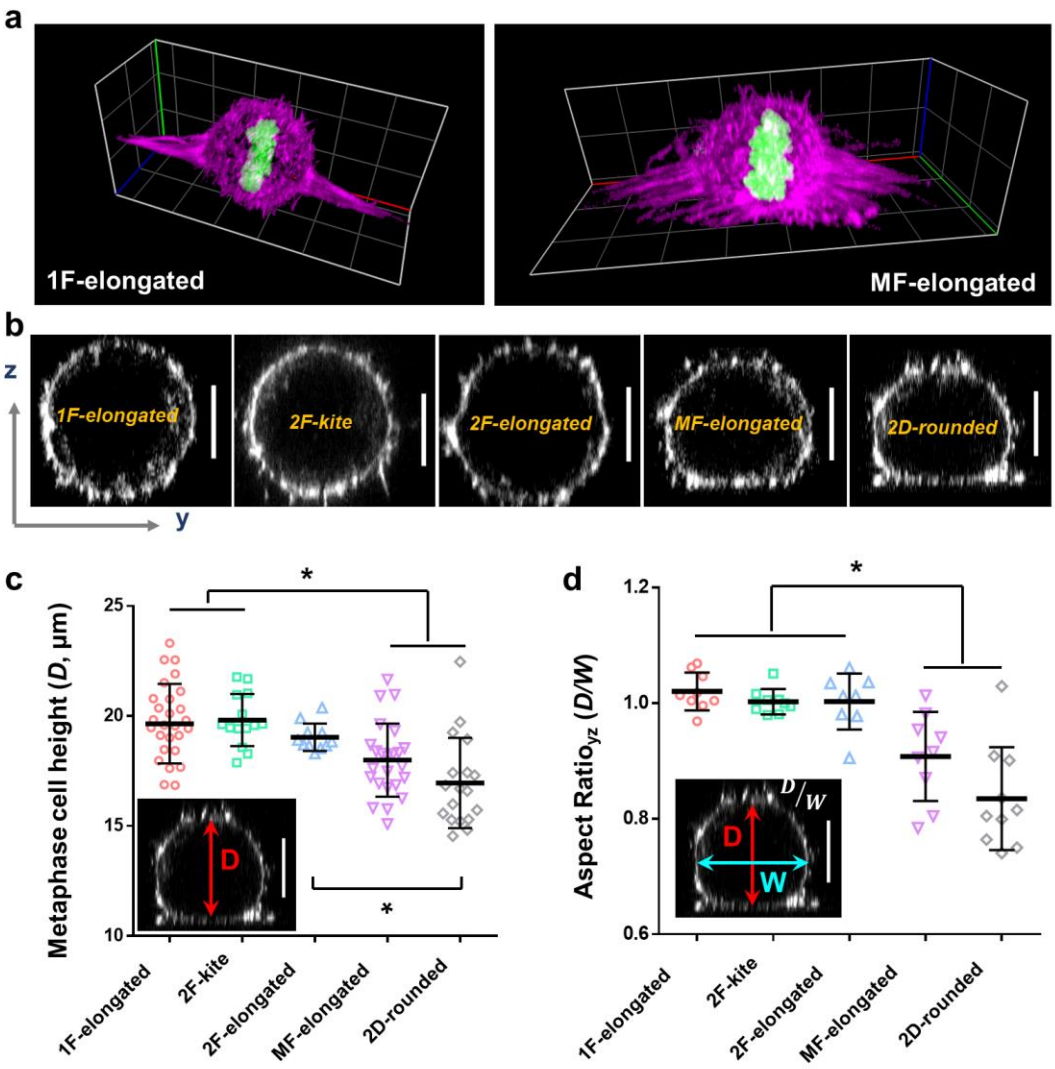

Supplementary Figure 5.S3: Regulation of mitotic cell shapes through retraction fiber organization, a) Isotropic views showing retraction fiber organization of cells attached to single fibers and multiple fibers, Cells are stained for actin (magenta) and histone H2B (green), b) Representative YZ cross-sectional side-views corresponding to different substrate categories, c,d) Quantification of metaphase cell heights and Aspect ratio(yz) corresponding to different substrate categories

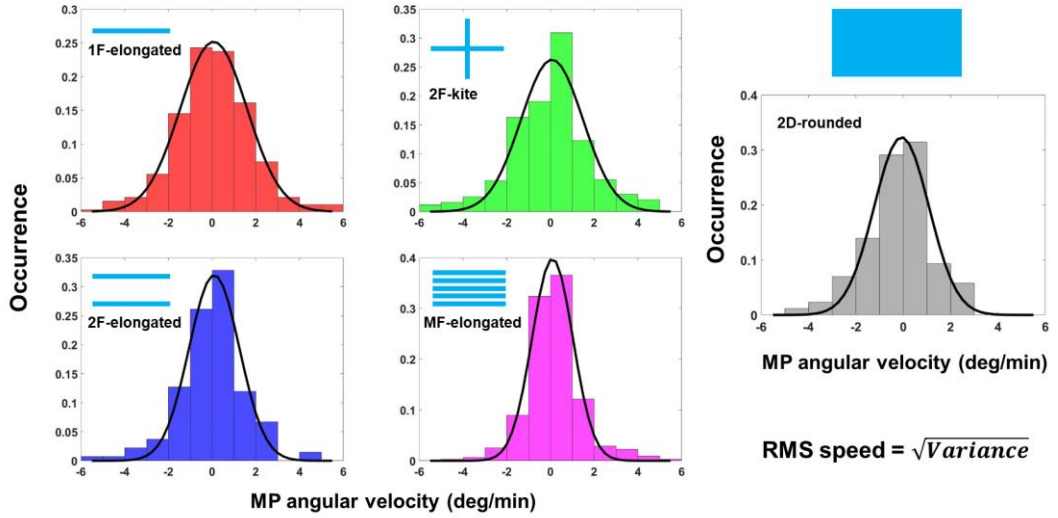

Supplementary Figure 5.S4: Probability distributions of the metaphase plate angular velocity for the different substrate categories

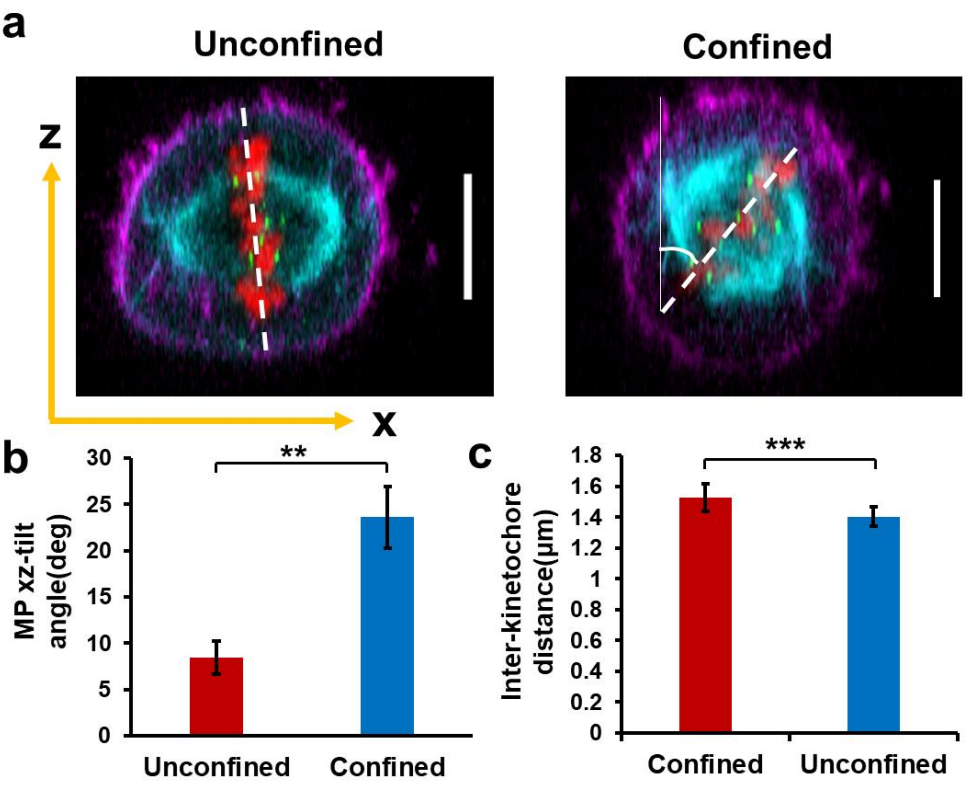

Supplementary Figure 5.S5: Effect of mechanical confinement on 3D orientation of metaphase plate a) Representative XZ cross-sectional images for unconfined and confined cells b,c) Statistical comparison of MP tilt angle and inter-kinetochore distance for unconfined and confined category cells

Chapter 6:

Single Cell Forces after Electroporation

6.1 Introduction

Exogenous electric fields, applied as short, high-voltage pulses can disrupt the cell through a process known as electroporation. Electroporation increases membrane permeability, enabling molecular and ionic diffusion across the cell membrane.[218,219] Electroporation techniques such as gene transfection,[220] electrofusion,[221] and electrochemotherapy[222] exploit a transient increase in membrane permeability, while irreversible electroporation induces cell death through a loss of homeostasis for nonthermal tumor ablation[223–225].

Developed over five decades, the classical theory on electroporation focuses on the mechanisms and timescales of membrane disruption[218,226–228]. While it is now widely accepted that hydrophilic pores, electrically-altered lipids, and modulated voltage-gated ion channels increase membrane permeability within microseconds of intense electric field application, the mechanisms and timescale (minutes to hours) of membrane resealing remain only partially understood[219,229–231]. Recently, there is a growing appreciation that pulsed electric fields cause disruption to the cell cytoskeleton[232–251].The cytoskeleton generates contractile forces that maintain tensional homeostasis required for survival while also dynamically connecting to the cell membrane. Studies show that chemically- or physically-disrupting the cytoskeleton alters membrane permeability after electroporation[236,252,253] and affects cell viability[237,246,247,249]. Electric fields may also decrease the elastic modulus of cells[237,254]. However, the dynamic changes in cell contractility and tensional homeostasis after electroporation have not been quantified yet.

Here, we use a custom-built device to enclose suspended extracellular matrix-mimicking fibers that act as force sensors (Nanonet Force Microscopy, NFM[96,160,255]), enabling us to causally link cell contractility, shape, and viability of single cells undergoing electroporation. We describe a biphasic mechanical response and remodeling of the cytoskeleton post-electroporation. Our analysis of multiple cell types, reveals three distinct stages during the recovery process: an initial loss in contractility immediately post-electroporation (Stage 1), a biphasic force response (Stage 2), and a final force recovery stage to pre-electroporation contractility (Stage 3). Cytoskeletal staining reveals that the biphasic response is concurrent with actin-mediated bleb retraction and is most pronounced when the electric field direction is parallel to the axis of cell elongation, which interestingly also results in higher cell viability. Altogether, our data suggest targeted opportunities to optimize electroporation for genetic engineering, gene therapy, and molecular medicine.

6.2 Materials and Methods

Device Fabrication and Fiber Deposition

Scaffold bases consisting of a hollow square region (See Fig. 1. Outer scaffold dimensions: 8 x 8 mm; inner region: 3 x 3 mm) were laser cut from ~250 μm-thick polystyrene coverslips (Fisher Scientific). Using our previously reported non-electrospinning Spinneret based Tunable Engineered Parameters (STEP) technique, we fabricated force-sensing nanofiber networks consisting of a horizontal array of densely-spaced (inter-fiber spacing: 14.5 ± 0.7 μm) small diameter (~250 nm, 233 ± 4 nm) nanofibers deposited on a vertical array of widely-spaced (inter-fiber spacing: 279 ± 9 μm) large diameter (diameter ~2 μm, 1.92 ± 0.11 μm) support fibers. Fiber networks were fused at their junctions using a custom fusing chamber. The 250 nm-diameter fibers were prepared using a 7 wt% solution of

polystyrene (MW: 2,000,000 g/mol; Category No. 829; Scientific Polymer Products, Ontario, NY, USA) in *p*-xylene (X5-500; Thermo Fisher Scientific, Waltham, MA, USA), while a 2 wt% solution (Polystyrene MW: 15,000,000 g/mol; Category No. PL2014-9001, Agilent Technologies, Santa Clara, CA, USA) was used for the large, 2 μm support fibers. Individual fiber diameter and inter-fiber spacing were confirmed *via* Scanning Electron Microscopy (SEM) images. Mechanical properties of the fibers are listed in Table 6.S3.

A single channel in polydimethylsiloxane (PDMS) was bonded to a glass coverslip to contain a plastic scaffold placed between two electrodes spaced 1-cm apart. A master mold for the PDMS channel was fabricated on a glass slide using acrylic. A 1/16" acrylic sheet was laser-cut to form the channel region (30 x 10 x 1.6 mm), and epoxied onto the glass slide. Acrylic walls surrounding the channel region were laser cut from 3/16" acrylic and epoxied in place. PDMS was mixed in 10:1 (wt/wt) base to cross-linker, degassed, and cast-molded using the master mold. After curing at 80 °C for 2-3 hours, the PDMS was removed from the mold and inlet and outlet holes were punched with a 0.75 mm biopsy punch. Before bonding to a glass cover slip, high-vacuum grease (Dow Corning, Midland, MI) was used to tack the scaffold in place on the glass slide. Bonding of the PDMS to the cover slip was achieved using a plasma cleaner (Harrick Plasma). To complete the device assembly, stainless steel acupuncture needles (diameter 0.18 mm) were carefully inserted through the device at a spacing of 1 cm and epoxied in place. The assembled device was placed under vacuum until use.

Cell Culture and Experimental Procedure

The glioblastoma cell line U251 (Sigma-Aldrich) was cultured according to standard practices in growth media consisting of Dulbecco's Modified Eagle Media (DMEM) with

L-Glutamine, 4.5 g/L Glucose and Sodium Pyruvate (Corning) supplemented with 10% Fetal Bovine Serum (FBS, R&D Systems) and 1% Penicillin Streptomycin (Gibco). Growth media had a conductivity of 12.8 mS/cm, an osmolarity of 355 mOsm, and contained 1.95 mM calcium. U251 cells tested negative for mycoplasma. Cells were passaged at 70-90% confluency. Both C2C12 mouse myoblasts (ATCC) and HeLa cells[256] were cultured in growth media consisting of DMEM with L-Glutamine, 4.5 g/L Glucose and Sodium Pyruvate (Corning) supplemented with 10% Fetal Bovine Serum (FBS, R&D Systems). VAMT cells were cultured in RPMI 1640 medium supplemented with 10% Fetal Bovine Serum (FBS, R&D Systems). Chinese hamster ovary (CHO-K1, ATCC) cells were cultured in growth media consisting of DMEM/F12 (Dulbecco's Modified Eagle Medium: Nutrient Mixture F-12, Thermo Fischer Scientific) supplemented with 10% Fetal Bovine Serum (FBS, R&D Systems). Thyroid cancer cells[257] (isolated from young mouse tumors) were cultured in F12 medium (Ham's F-12 Nutrient Mixture, Thermo Fischer Scientific) supplemented with 10% Fetal Bovine Serum (FBS, R&D Systems).

To prepare a device, the device was sterilized with ethanol, washed with PBS, and incubated for 45 minutes with 4 μg/ml Fibronectin in PBS. Cells were trypsinized, centrifuged at 150 x *g* for 5 minutes, and resuspended in media at 0.1 x10^6 cells/ml. Cells in suspension were added to the device and incubated at 37 °C and 5% CO_2 for 20-40 minutes. The device was then transferred to the microscope and incubated for 2 hours at 30 °C and 5% CO_2 before data collection. Contractile force experiments were performed on a Zeiss microscope (Zeiss AxioObserver Z1) with an incubation chamber maintaining a 30 °C and 5% CO_2 environment throughout the entirety of the experiments. The incubation temperature was decreased from standard 37 °C incubation to 30 °C to remove

the potential of thermal damage caused by Joule heating during pulsing (Fig. S3e-f, See Mitigation of Thermal Effects subsection of the Methods). Brightfield data was captured at 20x (phase objective, 0.8 NA) at intervals of 2 minutes. For each experiment, approximately 25 to 50 locations on the fiber network were imaged every 2 minutes. Imaging locations frequently contained more than one cell. For U251 experiments, twenty minutes of baseline data were collected before electroporation and cells were maintained in growth media for the duration of the experiment. For consistency with U251 experiments, experiments with other cell types were all performed in DMEM growth media (devices flushed ~20 minutes pre-experiment for cells not cultured in DMEM growth media). Ten minutes of baseline data were collected before pulsing.

To prepare cells for treatment in calcium-free DMEM, cells were seeded in complete growth media and allowed to adhere and spread on the fibers for at least 2 hours under incubation at 37°C and 5% CO_2. After incubation, devices were removed from the incubator and flushed thoroughly (2x, each flush with 2x device volume) with calcium-free DMEM (DMEM with 4.5g/L Glucose and without L-Glutamine, Sodium Pyruvate, Calcium Chloride. Gibco, 21068-028). The free calcium concentration was measured to be approximately 50 µM (Cell Biolabs Inc., MET-5121), and free calcium was not chelated to prevent alterations in cell morphology[258,259]. The device was then immediately placed on the microscope, incubated at 30°C and 5% CO_2 as in the other experiments. A brief acclimation period of approximately 20 minutes was given prior to data collection. Baseline (pre-electroporation) images were acquired for 10 minutes before applying the electroporation pulses. Cells were maintained in calcium-free DMEM for the duration of the experiment.

Sample Size and Inclusion Criteria

We analyzed U251 cells from three independent experiments for each voltage (500 V, 1000 V, 1500 V) and orientation (∥, ⊥) condition. Table 6.1 presents the number of cells analyzed for the force analysis from each independent experiment. For each voltage and orientation tested, three independent experiments were conducted, with 20 or more total cells analyzed where possible. Ultra-low viability for the 1500 V ⊥ condition limited sample number. Cells selected for analysis were well-centered on the fibers (for the duration of the experiment), had no interference from other cells, were adhered to nanofibers with fixed endpoints (orthogonal fibers well-fused), and showed an elongated and contractile phenotype. We performed three independent experiments of the 1000 V ∥ condition in calcium-free DMEM and analyzed the response of 24 cells. Additionally, we performed two control ("sham") experiments (Fig. 6.S2f). For our force analysis on additional cell types presented in Fig. 6, we analyzed ≥ 8 cells from a single experiment for each cell type. C2C12 cells were electroporated at 2000 V due to their greater resistance to electroporation effects.

Table 6.1: Sample size for force analysis of U251 cells.

Condition	Number of cells analyzed per independent experiment			Total Cells Analyzed
	Exp1	Exp2	Exp3	
500 V ∥	6	6	9	21
1000 V ∥	9	6	11	26
1500 V ∥	9	11	8	28
500 V ⊥	7	7	9	23

1000 V ⊥	8	6	8	22
1500 V ⊥	0*	0*	4	4
1000 V ∥ Ca^{+2}-free	13	7	4	24
Control (Sham)	8	5	-	13

* no cells viable for analysis

Viability of U251 cells post-electroporation was analyzed from at least three independent experiments for each voltage (500 V, 1000 V, 1500 V) and orientation (∥, ⊥, 2D Flat). Table 2 presents the number for cells analyzes for each independent experiment. Viability was assessed 180 minutes post-electroporation for 500 V experiments and 240 minutes post-electroporation for 1000 V and 1500 V experiments. (Note, 2D Flat data were collected from experiments investigating the ⊥ or ∥ orientations.)

High-resolution brightfield data of individual cells enabled us to assess viability without the need for conventional live/dead staining. Viability was assessed at the single-cell level from brightfield data based on several criteria. Cells considered viable had (visually) intact membranes, had re-spread on the fibers, and were able to apply contractile forces to the fibers (i.e. deflected parallel nanofibers). Cells considered "dead" did not have (visually) intact membranes (cell lysis), did not re-spread on the fibers, and did not apply contractile forces (no fiber deflections). Using these criteria, cells considered "viable" were very distinct from cells considered "dead." Fig. 6.S3b shows several examples of "viable" *vs* "dead" cells. As shown in this Fig., cell death generally occurred immediately following electroporation, suggesting necrosis (accidental cell death). For all experiments, all cells elongated between two parallel fibers with the characteristic elongated shape shown in Fig. 6.1c were included in the viability analysis.

Table 6.2: Sample size for analysis of cell viability following electroporation.

Condition	Number of cells analyzed per independent experiment							Total Cells analyzed
	Exp1	Exp2	Exp3	Exp4	Exp5	Exp6	Exp 7	
500 V ∥	66	55	112	-	-	-	-	233
500 V ⊥	68	25	37	26	25	-	-	181
500 V 2D Flat	34	26	32	103	-	-	-	195
1000 V ∥	60	62	60	33	27	48	126	416
1000 V ⊥	39	45	93	21	-	-	-	198
1000 V 2D Flat	37	23	42	-	-	-	-	102
1500 V ∥	101	65	71	-	-	-	-	237
1500 V ⊥	33	74	201	-	-	-	-	308
1500 V 2D Flat	15	24	20	93	48	126	-	326

Electroporation Parameters

Cells were electroporated with a high voltage pulse generator (BTX ECM 830, Harvard Apparatus). Ten, 100 µs square-wave pulses were delivered at 500 V, 1000 V, or 1500 V to the device electrodes. Pulses were delivered at a frequency of 1 Hz. Measured current and voltage waveforms approximated ideal square waves (Fig. 6.S1a,b). Voltage waveforms were not affected by pulse number. Electrical current increased slightly with pulse number due to Joule heating. Finite Element modeling of the electric field within the device indicated that at applied voltages of 500 V, 1000 V, and 1500 V, the cells within the scaffold region-of-interest (cut-out region of scaffold, 250 µm from edges) experienced

electric field magnitudes of 441 ± 12 V cm^{-1}, 882 ± 23 V cm^{-1}, and 1323 ± 35 V cm^{-1} respectively for the parallel orientation, and 455 ± 12 V cm^{-1}, 911 ± 24 V cm^{-1}, and 1366 ± 36 V cm^{-1} respectively for the perpendicular orientation. See the Finite Element Modeling subsection of the Methods for more details.

Pulse application resulted in micron-diameter bubble formation on both electrodes, but did not result in electrical arcing. Undesired electrochemical effects were minimized by incorporating a large volume of fluid outside the electrode region (~2.5 times the volume of fluid between the electrodes), and locating the fiber network region several millimeters away from both electrodes. Media pH was minimally affected by electroporation (No electroporation (Sham): 7.11 ± 0.06; 1500 V: 7.16 ± 0.06. pH measured 3 hours after electroporation).

Immunostaining and Confocal Microscopy

Cells were fixed and stained for actin, paxillin, and microtubules according to standard practices. Cells were fixed with 10% Formalin for 10 minutes, permeabilized with 0.1% Triton-X 100 in PBS for 15 minutes, and blocked with 5% goat serum in PBS for 30 minutes. Focal adhesion antibody (Paxillin, TYR31) (5µg/ml) and microtubule antibody (beta tubulin) (1 µg/ml) were prepared in an antibody dilution buffer (PBS with 10 mg/ml BSA and 1 µl/ml Triton X-100) and were added to the cells and incubated at room temperature for three hours. The device was washed with PBS and antibody dilution buffer supplemented with actin stain (rhodamine phalloidin, sc-301530; Santa Cruz Biotechnology, Dallas, TX, USA) diluted in a 1:80 ratio and secondary antibodies (Alexa Fluor 488 Goat Antibody (Green), Alexa Fluor 647 Goat Antibody (Cyan) both diluted in a 1:400 ratio) were added for 45 minutes at room temperature while protected from light.

The device was then washed with PBS and 300 nM DAPI diluted in PBS was added to the device for 5 minutes in the dark. The device was then washed with PBS and imaged using a 63x (1.15 NA) water-immersion objective on a confocal microscope (Zeiss LSM 880). The z-slice thickness was kept at either 0.36 μm or 0.5 μm.

Cell volume calculations were performed in MATLAB from z-stacks of fluorescent images (stained for actin, microtubules, and the nucleus) of fixed cells at various time points (pre-pulse, 0.5, 2, 8, 16, 32, and 128-minutes) after electroporation. (n = 6, 10, 8, 13, 7, 9 and 5 cells corresponding to pre-pulse, 0.5, 2, 8, 16, 32, and 128-minute timepoints respectively.) In MATLAB, images were converted into grayscale and subsequently binarized using a custom MATLAB routine to calculate the projected cell area as shown in Fig. 6.S3c. Cell volume was calculated as volume = Σ(projected cell area)*z-slice thickness.

Bleb analysis was performed in ImageJ. Bleb area was measured on the z-slice corresponding to the bleb's greatest diameter (n = 82, 126, 214, 131 and 23 blebs from 12, 12, 13, 11 and 4 cells for 0.5, 2, 8, 16 and 32-minute timepoints respectively). A membrane roughness ratio (Fig. 6.4e) was used to quantify the increased length of the cell contour along the nanofiber due to the presence of blebs, and was measured as the ratio of the contour length to the cell end-to-end length (n = 6, 14, 16, 9, 10 and 6 for -2 (pre-pulse), 0.5, 2, 8, 16 and 32-minute timepoints respectively). Non-electroporated cells demonstrated negligible blebbing and thus had a roughness ratio very close to 1. Bleb analysis for calcium-free experiments (Fig. 6.S5a,b) followed the same procedure, however brightfield images were used to calculate the roughness ratio.

Membrane Permeability Imaging

To experimentally confirm membrane disruption by electroporation, we used YO-PRO-1 and Propidium Iodide (PI), both membrane-impermeant dyes. Membrane disruption by electroporation was visually demonstrated by the fluorescence of the membrane-impermeant dye YO-PRO-1 (1000 V ‖ condition shown in Fig. 6.2a). For clarity in Fig. 6.2a, we used a background subtraction technique (*via* a gaussian-blur) and a lower intensity threshold to remove background YO-PRO-1 signal and thus these images are for illustration purposes only. Experiments were performed with 1 µl/ml (1 µM) YO-PRO-1 (Thermo Fisher Scientific) in media.

We visualized the spatial distribution of PI uptake during the first 60 seconds after electroporation at 1000 V (‖: 882 V/cm; ⊥: 911 V/cm). A high concentration of PI (0.17 mg/ml) (Fisher Scientific) was used as in similar studies[260] to enable high frame-rate data collection (short exposure times) while maintaining strong fluorescence signal. We added media containing PI immediately prior to imaging and electroporating the cells. Ten, 1000 V pulses were delivered at 1 Hz. Images were captured at 1.2 s intervals at 63x magnification.

Force Calculation

Contractile force was calculated in MATLAB by comparing the deflection profile of the fiber with the best fit profile of a loaded fixed-fixed beam subjected to the cell forces at an angle, α_{Force}, measured as the angle between the resultant force vector and the undeflected nanofiber direction. Details on force analysis formulation and numerical scheme have been published previously[96]. The cell's applied load to the fiber is assumed to be at each endpoint of the cell's protrusions where the f-actin stress fibers are anchored to the nanofibers *via* focal adhesions (Fig. 6.1e).

The direction of the resultant force, α_{Force}, is estimated based on physiological structures from fixed cells. Elongated cells (cell before electroporation or long after electroporation) have well defined stress fibers which are ~12.4° from the horizontal (Fig. 6.1e, bottom left). In instances where stress fibers were not present in recovering cells, we deferred to the angle of the dominant retraction fibers, (Fig. 6.1e bottom center) known for their force bearing capabilities[203,261]. In cases where neither stress fibers nor retraction fibers are visible, and the cell is highly rounded, we took the resultant angle to be the bisection of the angle created by the membrane at the point of attachment to the fiber (Fig. 6.1e, bottom right). For these situations, mechanical forces must be applied in-line with the membrane, thus, the resultant force would be the sum of the vectors radiating outward along the membrane, resulting in half the angle formed by the membrane. For a completely spherical cell, the half angle created by the membrane would point the force vector directly to the cell centroid. We fixed cells and imaged their cytoskeleton under no-electroporation conditions and 0.5, 2, 8, 16, 32, 128 minutes after electroporation at 1000 V ‖. When α_{Force} was averaged for each cell, we arrived at the plot in Fig. 6.1f (n=119). When cell length (L) is less than 63.4 μm in length, the angle of force application increases, and can be approximated as linear. Minimizing error for the data results in the following best fit:

$$\alpha_{Force}(L) = \begin{cases} 12.4 + .54(63.4 - L), & L < 63.4 \\ 12.4, & L \geq 63.4 \end{cases} \quad (1)$$

Where α_{Force} is in degrees and L is in μm. At each timepoint during cell recovery, the cell length was computed and the corresponding force angle was an input to the finite element model.

The deflection profiles were measured by marking the fiber endpoints and eight points along the fiber length including the two endpoints of the cell. Fiber properties used in the computation of contractile force can be found in Table 6.S3. Cell elongation was defined to be the length between a cell's endpoints on a fiber.

Finite Element Modeling

COMSOL 5.4 was used to model the electric field distribution in the device. We used the AC/DC module to perform a steady-state simulation. Computational models of the electric field within the device are shown in Fig. 1d and Fig. S2. Our models indicated that the scaffold region-of-interest (cut-out region of scaffold, 250 μm from edges) experienced electric field magnitudes of 0.88 V cm^{-1} for every 1 V delivered when the scaffold was in the parallel orientation, and 0.91 V cm^{-1} for every 1 V delivered when the scaffold was in the perpendicular orientation. Cells adherent to the glass slide (2D flat) experienced electric field magnitudes of 0.93 V cm^{-1} and 0.90 V cm^{-1} for every 1 V delivered when the scaffold was in the parallel orientation and perpendicular orientation respectively. Scaffold rotation is the cause of the slight increase in the electric field in the perpendicular orientation.

COMSOL was used to model the induced transmembrane potential (ITP) on cells. An accurate cell volume was reconstructed using 3D Slicer from a z-stack images of a fixed, actin-stained cell. Cell volume was meshed using 3-Matic. We performed a steady state model and neglected the effect of electroporation-induced conductivity changes to the cell membrane[262]. Over the volume, the Laplace equation (2) was solved:

$$\nabla^2 V = 0 \qquad (2)$$

where V is voltage. A contact impedance boundary condition was used to model the boundary condition across the cell membrane:

$$n \cdot J = \frac{\sigma_m}{d_m}\left(V - V_{ref}\right) \quad (3)$$

where σ_m and d_m are the conductivity and thickness of the cell membrane respectively and V and V_{ref} are the voltages on either side of the cell membrane. Model parameters are presented in Table S4.

Mitigation of Thermal Effects

We performed experiments at 30 °C to mitigate thermal effects due to Joule heating. We analytically and experimentally determined Joule heating to be no greater than 8 °C (Fig. S3). We calculated the worst-case scenario for Joule heating by assuming that all electrical energy was immediately converted to thermal energy to cause an instantaneous temperature rise[260]. Worst-case Joule heating was calculated for the delivery of 10 pulses at 1500 V using the equation:

$$\Delta T = IVt_{on}/(C_p\, m) \quad (4)$$

where ΔT is the change in temperature within the device, V is the voltage applied (measured), I is the current through the device (measured), C_p is the specific heat capacity of the media (approximated as water: 4.184 kJ/(kg·K)), and m is the mass of the media being heated. Mass is calculated as $m = \rho lwh$, where ρ is the density (approximated as water: 1 kg/m^3), l is distance between electrodes (1 cm), w is width of the channel (1 cm), and h is height of the channel (1.6 mm). We calculated that the worst-case scenario Joule heating would cause a temperature rise of less than 8 °C

Fiber optic temperature probe measurements within the device demonstrated that at the maximum electroporation condition of 10 pulses at 1500 V cm^{-1}, temperature rise was under 7 °C (Fig. 6.S3e-f). Our analytical temperature rise calculation is thus in good agreement with experiments. The rapid temperature rise was quickly dissipated by the surrounding fluid in the channel, and the temperature returned to within 2 °C of the pre-treatment temperature within a few minutes.

Statistical Analysis

All data is presented as mean ± SEM. Statistical analysis was performed in JMP and Graphpad Prism. Student t-tests were performed to determine significance between data sets. The significance level for Student t-tests was $\alpha = 0.05$.

6.3 Results

Microfluidic chip integrates force-sensing nanofibers.

We fabricated a custom microfluidic device that integrates the nanofiber scaffold between two needle electrodes spaced 1 cm apart (**Fig. 6.1a**). Using the previously reported non-electrospinning STEP technique,[53,263] we generated suspended polystyrene nanofiber networks: 250 nm-diameter nanofibers spaced 15 µm apart were fused to larger, 2 µm-diameter orthogonal fibers spaced 275 µm apart. Rotation of the nanofiber scaffold 90 degrees reoriented the electric field from a "parallel" configuration that aligned the electric field direction from being parallel to the nanofibers to a "perpendicular" orientation that

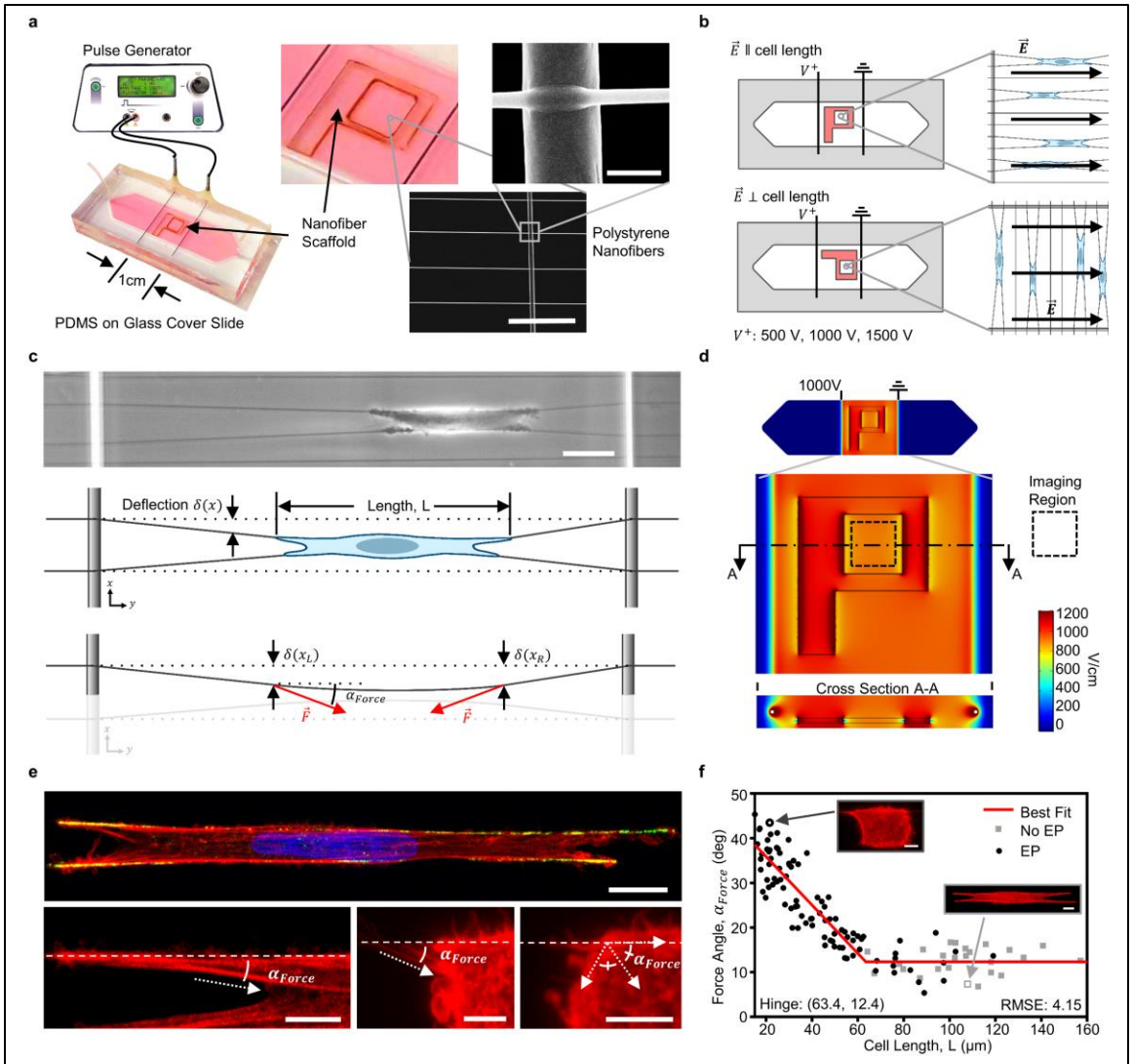

Figure 6.1. Nanofiber force sensing. a) A microfluidic PDMS device encloses a nanofiber network spun on a hollow substrate. The cells are electroporated via a high-voltage pulse generator connected to two needle electrodes. Precisely-controlled nanofiber networks are fabricated using the STEP technique: ⌀250 nm fibers (15 μm spacing) are deposited orthogonal to ⌀2 μm fibers (275 μm spacing) and fused at their intersections. Scale bar 20 μm (lower), and 1 μm (upper). b) *Parallel orientation*, cell long-axis aligned with the electric field; *Perpendicular orientation*, cell long-axis perpendicular to the electric field. c) Single cells attach to parallel nanofibers, causing visible fiber deflection. Scale bar 25 μm. The deflecting fiber is modeled as a fixed-fixed beam with two point-loads, $\vec{F}$, located at the attachment points of the cells and at an angle α_{Force}. d) A finite element model indicates that the electric field is approximately uniform within the region of interest at the center of the scaffold. e) An elongated

cell shows f-actin stress fibers (red) and focal adhesions (green) along the fibers. Contractile force is applied along the f-actin stress fibers (e, bottom left), retraction fibers (e, bottom center), or at the bisection of the membrane angle (e, bottom right). The dashed lines indicate fiber location. Scale bars 10 μm (top) and 5 μm (bottom). f) The angle α_{Force} is well approximated by a two-segment line when plotted against cell length. For cells longer than 63.4 μm, α_{Force} is constant at 12.4°. For cells shorter than 63.4 μm, α_{Force} is approximated as a linear function of cell length. Inset images show a round and elongated cell with corresponding data points. Scale bars 5 μm. EP, electroporation.

placed the nanofibers perpendicular to the field (**Fig. 6.1b**). We refer to these orientations simply as the parallel (∥) and perpendicular (⊥) orientations. Cells elongate between adjacent nanofibers and deflect them according to the cell's inherent contractility (Fig. 1c). In this study, we subjected human glioblastoma cells (U251, Sigma-Aldrich) to ten, 100 μs square-wave pulses at 1 Hz delivered at 500 V, 1000 V, or 1500 V, generating approximately uniform electric fields across the scaffold region (**Fig. 6.1d, Fig. 6.S1c-f**). At applied voltages of 500 V, 1000 V, and 1500 V, our models indicated that the scaffold region-of-interest (cut-out region of scaffold, see Fig. 1d) experienced electric field magnitudes of 441 ± 12 V cm^{-1}, 882 ± 23 V cm^{-1}, and 1323 ± 35 V cm^{-1} respectively for the parallel orientation, and 455 ± 12 V cm^{-1}, 911 ± 24 V cm^{-1}, and 1366 ± 36 V cm^{-1} respectively for the perpendicular orientation. The contractile force of a cell was calculated by the deflection of the flexible nanofibers[94,160]. To calculate the contractile force from fiber deflection, we model a deflecting nanofiber as a fixed-fixed beam with two point-source loads, $\vec{F}$, acting at the two primary adhesion sites, one at either end of the cell[54,160,264,265] The direction of the force application, α_{Force}, was determined from the orientation of the actin stress fibers, actin-rich retraction fibers, or as specified in the

Methods (**Fig. 6.1e**). In general, α_{Force} is approximately linearly-dependent on the cell length (L) for L < 63.4 μm, but constant (~12.4°) for L ≥ 63.4 μm (**Fig. 6.1f**).

Contractility as a biophysical metric of electroporation

Almost immediately after electroporation, cell elongation decreased and membrane blebs formed. In the parallel orientation, cell rounding became appreciable with increasing field strengths (**Fig. 6.2a**). Interestingly, in the perpendicular orientation, cells largely retained their elongated morphology (**Fig. 6.2b**) unless the field strength was high (1500 V), which resulted in high levels of blebbing and cell rounding. Membrane blebbing decreased over a span of several minutes, after which the cells re-spread along the fibers. We quantified the temporal dynamics of the cell length, average fiber deflection (measured at cell attachment points), and contractile force response for different field strengths both in the parallel (**Fig. 6.2c**) and perpendicular orientations (**Fig. 6.2d**).

In the parallel orientation, all applied voltages immediately reduced the average contractile force, and showed complete recovery within 1-2 hours (**Fig. 6.2c**). Increasing the applied voltage caused a larger decrease in the cell force (**Fig. 6.2e**) and length (**Fig. 6.2f**). Unexpectedly, we discovered a transitory biphasic rebound in the cell contractile force immediately after the initial decrease in force post-electroporation, as indicated by the black arrows in **Fig. 6.2c**. Analysis of individual force responses in the parallel orientation reveals that a majority of the cells (50 of 75 of sampled cells, 67%) underwent a multi-stage force response, discussed in detail later in this paper.

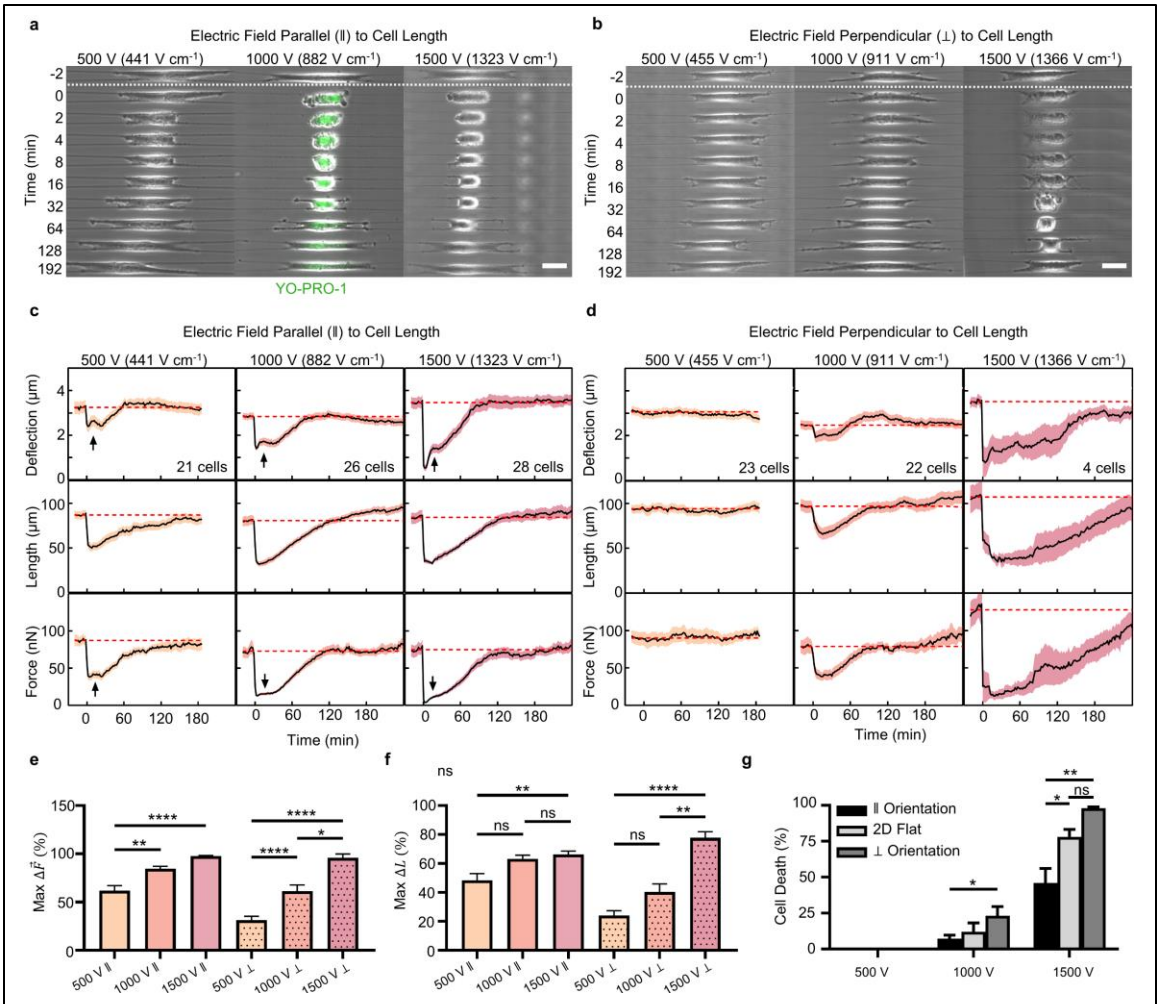

Figure 6.2. Cell shape and contractile force response to electroporation. a-b) Cell responses to electroporation at 500 V, 1000 V, 1500 V in the (a) parallel orientation (441 V cm^{-1}, 882 V cm^{-1}, and 1323 V cm^{-1} respectively) and (b) perpendicular orientation (455 V cm^{-1}, 911 V cm^{-1}, and 1366 V cm^{-1} respectively). The onset of membrane disruption by electroporation is visualized for 1000 V ∥ by the inclusion of YO-PRO-1 (green, background subtraction and thresholding used to remove background signal, see Methods). Cells show rounding, membrane blebbing, and an eventual return to a characteristic elongated state in a voltage- and orientation-dependent manner. Scale bars are 25 μm. c-d) Average fiber deflection, cell length, and contractile force post-EP for cells in the parallel (c) and perpendicular orientation (d). Cells in the parallel orientation show rapidly decreased length and contractility, and recovery within 1-2 hours. For the perpendicular orientation, no response occurs at 500 V, a moderate response occurs at 1000 V, and an extreme response is seen at 1500 V. Unexpectedly, fiber deflection and force plots show a transitory increase shortly after electroporation (see arrows on plots) indicating multiple stages in the recovery process. Error bands show standard error. e-f) Maximum percent decrease in force and cell length is greatest at high voltages. g) Electroporation at high electric fields causes significant cell death, particularly in the perpendicular orientation.

In the perpendicular orientation, higher electric fields caused a greater decrease in force (**Fig. 6.2e**) and length (**Fig. 6.2f**) after electroporation, however cell response was quite different from the parallel orientation. Contractile force and cell length did not change after electroporation of 500 V, similar to steady-state cell behavior observed in control (sham) experiments (**Fig. 6.S2f**). Application of 1000 V ⊥ decreased contractile force and elongation, but this decrease was smaller (**Fig. 6.2e, Fig. 6.S2a-b**), more gradual, and recovery occurred sooner than 1000 V ∥. Few cells survived 1500 V ⊥, but surviving cells showed higher-than-average pre-pulse contractility (Fig. S3a), had dramatically reduced force and lengths after treatment, and had a long recovery to near pre-electroporation conditions. Interestingly, cell death (**Fig. 6.S3b**) was higher for cells treated in the perpendicular orientation than in the parallel orientation (**Fig. 6.2g, Table 6.S2**). At 1500 V, the percent cell death increased dramatically from 46 ± 10% (∥ orientation) to 98 ± 1% (⊥ orientation). At the end of data collection post-electroporation (3-4 hours), we did not find any significant differences in cell length or contractile force compared to pre-electroporation values for either cell orientation (**Fig. 6.S2c,d**).

Contractility reveals a multi-stage cell recovery post-electroporation

The recovery process can be divided into the following stages (**Fig. 6.3a-b**): a cell-rounding stage (Stage 1) of decreasing force and cell rounding, a biphasic stage (Stage 2) characterized by a transient rebound of force and subsequent relaxation, and a cell-spreading stage (Stage 3) during which the cell recovers its pre-electroporation force and length. In **Fig. 6.3c**, we show the multi-stage dynamics of contractile force and fiber deflection for a single cell in each treatment condition. We found that this response occurs

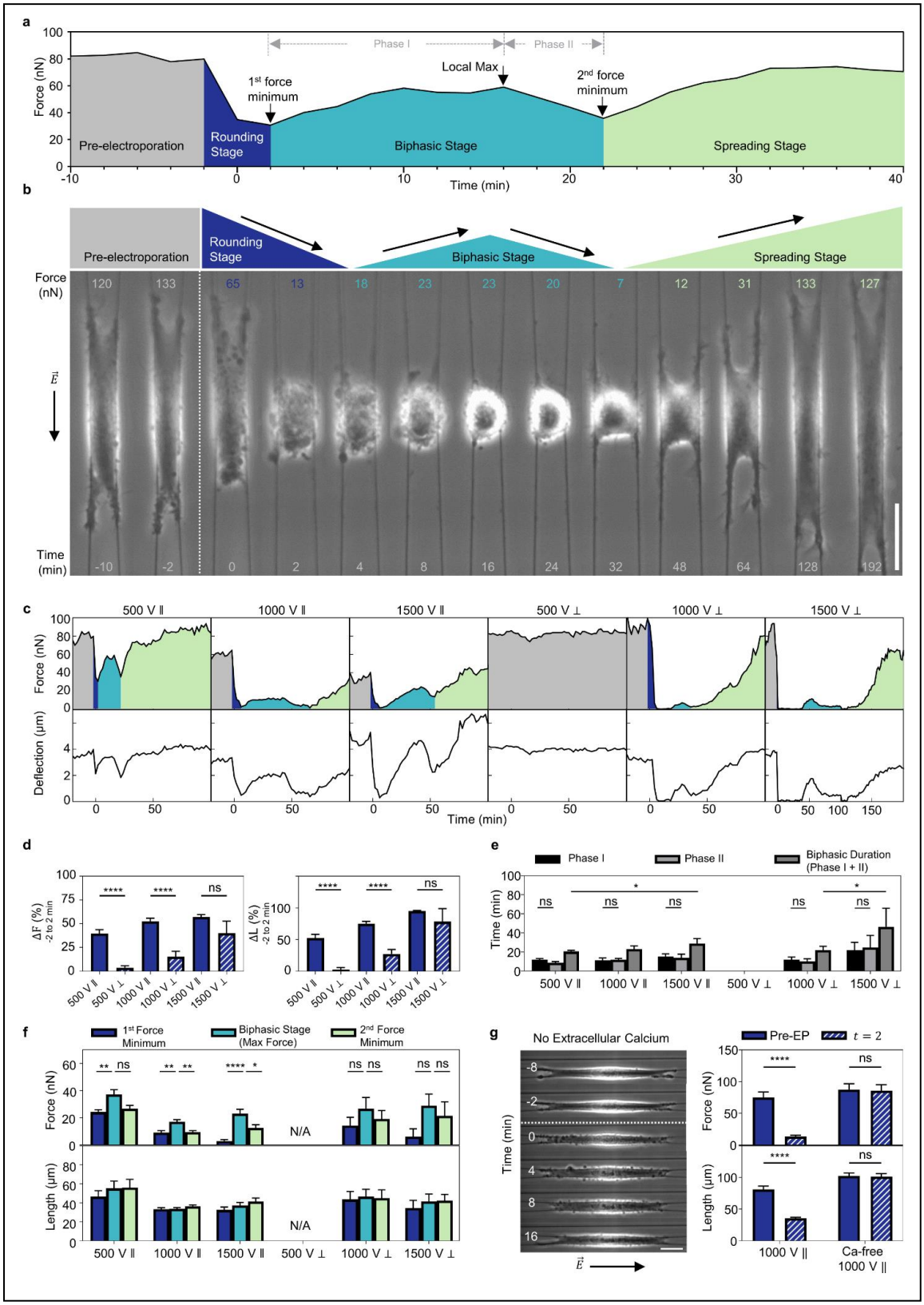
a
Force (nN)
Time (min)
Phase I
Phase II
1st force minimum
Local Max
2nd force minimum
Pre-electroporation
Rounding Stage
Biphasic Stage
Spreading Stage
b
Force (nN)
Time (min)
120 133 65 13 18 23 23 20 7 12 31 133 127
-10 -2 0 2 4 8 16 24 32 48 64 128 192
c
500 V ∥
1000 V ∥
1500 V ∥
500 V ⊥
1000 V ⊥
1500 V ⊥
Force (nN)
Deflection (μm)
Time (min)
d
ΔF (%) -2 to 2 min
ΔL (%) -2 to 2 min
e
Phase I
Phase II
Biphasic Duration (Phase I + II)
Time (min)
f
1st Force Minimum
Biphasic Stage (Max Force)
2nd Force Minimum
Force (nN)
Length (μm)
N/A
g
No Extracellular Calcium
Time (min)
Pre-EP
t = 2
Force (nN)
Length (μm)
1000 V ||
Ca-free 1000 V ||

Figure 6.3. Electroporated cells show a biphasic force recovery. a) A sample contractile force profile for a cell treated at 500V ||. The cell-rounding stage (Stage 1) begins after electroporation and ends at the first force minimum. Contractile forces increase during phase I of the biphasic stage (Stage 2) before decreasing again in phase II. The cell-spreading stage (Stage 3) begins after the second force minimum during which the cell recovers its pre-electroporation contractility. b) Images of a cell showing a multi-stage response (1000 V ||). Corresponding force values are presented for each image and the stages of recovery are schematically represented above. Scale bar 25 μm. c) Contractile force and deflection for a representative cell from each treatment demonstrating a multi-stage response. Note a minimal response for 500 V ⊥. d) Cells in the perpendicular orientation have significantly less change in force and length in the first two minutes after electroporation, except at very high voltages (1500 V). e) The biphasic stage lasts 20-30 minutes (longer for 1500 V ⊥) with higher voltages causing slightly longer durations. The duration of phase I is nearly equivalent to phase II. f) Force significantly increases during the biphasic response. The first and second minimum values are not significantly different. During the biphasic stage, cell length does not change significantly. g) Image sequence of a representative cell electroporated (1000 V ∥) in calcium-free media. Scale bar 25 μm. Cell force and length remain unaffected in calcium-free DMEM during the first two minutes after electroporation (1000 V ||).

more frequently in the parallel orientation (for example, 20 of 26 cells for 1000 V ∥ (77%) *versus* 8 of 22 cells for 1000 V ⊥ (36%)). See **Table 6.S1** for all percentages.

Stage 1: Recovery begins with a cell-rounding stage that typically occurs within the first 5 minutes (longer for 1500 V ⊥) after pulsing and is characterized by a rapid reduction of force. Cell extremities retract along the fibers (via actin retraction fibers (**Fig. 6.1e**)) causing rounding and membrane blebbing (**Fig. 6.3b**, t=0-2 min). At 500 V and 1000 V, cell length decreases significantly more in the parallel orientation than the perpendicular orientation during the first two minutes post-electroporation (**Fig. 6.3d**). Since calcium is known to breakdown cell focal adhesions[266] and is also an important ion regulating cell response to electroporation,[267] we repeated experiments in calcium-free DMEM (see Methods). For electroporation of 1000 V ∥ in serum-free media with no extracellular calcium, cells universally remained elongated on the fibers shortly after electroporation

(**Fig. 6.3g**), in stark contrast to the ubiquitous rounding that occurred after the same electroporation conditions in standard cell culture media.

Stage 2: The biphasic stage begins at a force minimum following the cell rounding stage, in a state of high membrane blebbing. A significant increase of contractile force (**Fig. 6.3f**) occurs during the first half of this stage (phase I), averaging 11 ± 1 nN or 14% of the average pre-electroporation value. Some cells show force increases up to 40 nN or 48% of the average pre-electroporation force value. The maximum force during this stage is reached when nearly all membrane blebs have disappeared (**Fig. 6.3b**, *t* =16-24 min). Following the local force maximum, contractility decreases (**Fig. 6.3b**, *t* =16-32 min) to a local minimum value that is not statistically different from first minimum (phase II) (Fig. **6.**3f). The duration of phase I and phase II are nearly equal (**Fig. 6.3e**). During the entire biphasic stage, cell length remained almost unchanged (**Fig. 6.3f**). The total duration of the biphasic stage increased with increasing field strength (**Fig. 6.3e**) in both the parallel orientation (500 V: 21 ± 1 min; 1000 V: 25 ± 3 min; 1500 V: 32 ± 4 min) and in the perpendicular orientation (500 V: no response; 1000 V: 22 ± 1 min; 1500 V: 47 ± 19 min).

Stage 3: The cell spreading phase is characterized by a gradual recovery of contractility as the cell re-spreads along the fibers (**Fig. 6.3b**, *t* =32-216 min). Cells eventually recover their pre-electroporation elongation as well as their pre-electroporation contractile force.

Cytoskeletal reorganization drives cell contractile response post-electroporation

The cytoskeleton plays a major role in regulating the contractile response of cells. We performed immunofluorescent staining for the major cytoskeletal components, actin

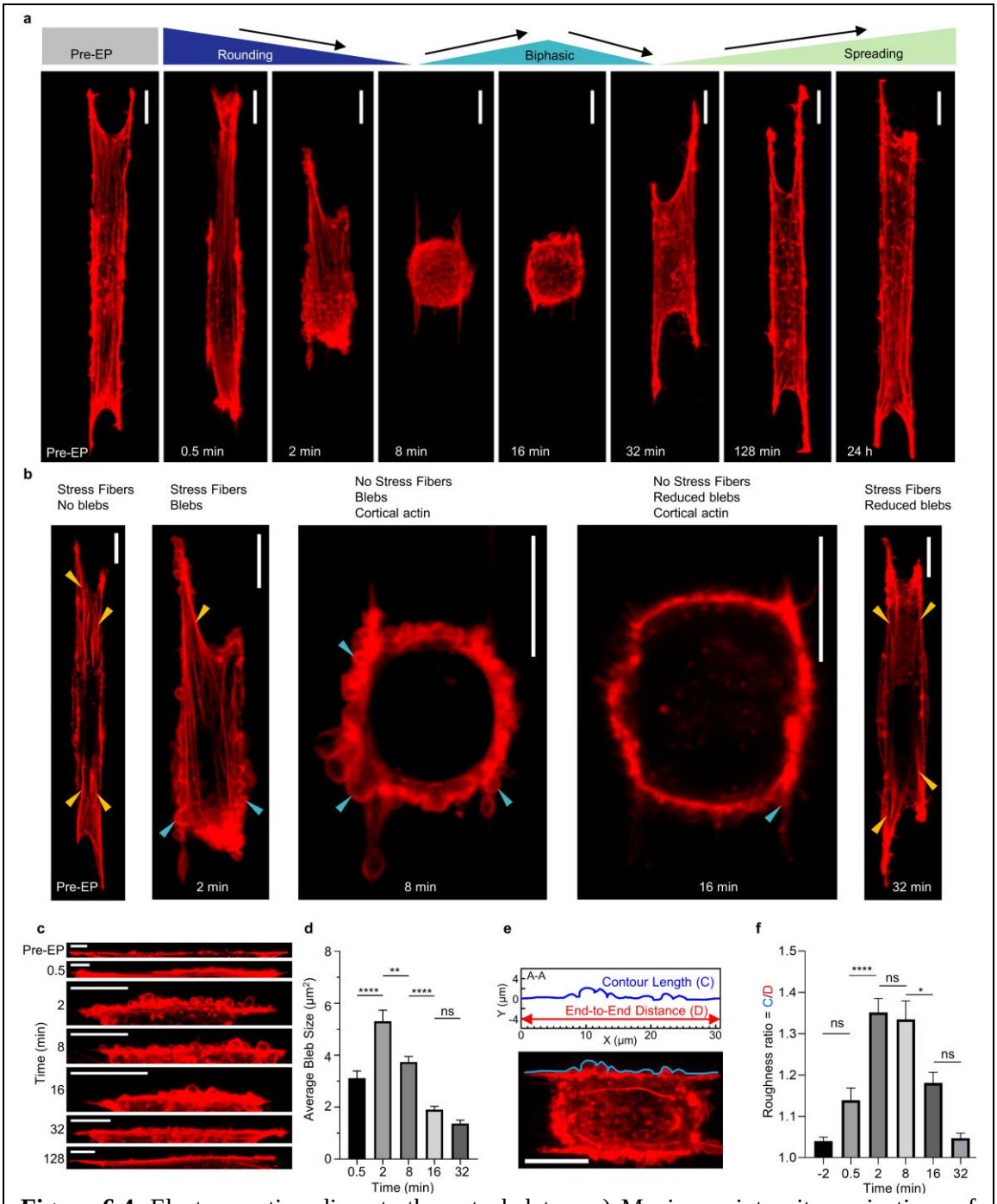

Figure 6.4. Electroporation disrupts the cytoskeleton. a) Maximum intensity projections of cells stained for actin before electroporation and during various stages of recovery post-electroporation (1000 V ||). b) A single confocal z-slice taken in the nanofiber plane. Pre-EP, actin cytoskeleton consists primarily of well-defined stress fibers (yellow markers). During the cell-rounding stage (2,8 min), both stress fibers and blebs (blue markers) are present. During the biphasic stage (8,16 min), cells are rounded with cortical actin and no stress fibers. Eventually, stress fibers begin to reform (32 min) and blebbing is reduced as the cell enters the cell-spreading stage and regains its characteristic cytoskeletal structure. c,d) Bleb size analysis. Large blebs form immediately after electroporation (maximum at 2 min), but are reduced to

baseline values within 32 minutes. e,f) Membrane roughness is quantified by the ratio of the contour length of the membrane along the nanofiber by the cell length end-to-end distance. Membrane roughness is at its maximum at 2 minutes after electroporation and returns to pre-EP values after 32 minutes. All scale bars 10 μm. EP, electroporation.

(**Fig. 6.4**) and microtubules (**Fig. 6.S4**), on fixed cells at various timepoints post-electroporation (1000 V ǁ; 0.5, 2, 8, 16, 32, 128 min and 24 hrs) and compared cytoskeletal structure with non-electroporated cells. Non-electroporated cells show well-developed actin stress fibers and continuous microtubules aligned with cell elongation (**Fig. 6.4a-b**, **Fig. 6.S4**). During the cell-rounding stage (**Fig. 6.3b, Fig. 6.4a-b**, 0.5 and 2 min timepoints) as cells begin to detach from the fibers and decrease in length, the aligned actin fibers and microtubules get disrupted and blebs form on the cell membrane. By 8 minutes, the f-actin stress fibers are nearly non-existent, and cells take on a rounded shape with the actin primarily localized at the cortex or on actin-rich retraction fibers originating from prior adhesion sites along the nanofibers. Throughout the cell-rounding stage and at the early phases of the biphasic force response stage (2, 8 min post-electroporation), we observed high levels of membrane blebbing (**Fig. 6.3b**) with very large individual blebs (up to 20-30 μm^2 projected area). Using two metrics for blebbing, bleb size[268] and membrane "roughness" (see Methods for details), we found blebbing to be maximal at two minutes post-electroporation, with significant decreases by 16 minutes, and baseline values by 32 minutes (**Fig. 6.4c-f**). Also, at 32 minutes, we observed the formation of actin stress fibers, indicating the start of Stage 3 (cell-spreading stage) of force recovery. At 128 min, electroporated cells show a fully recovered cytoskeletal structure with well-defined actin stress fibers and aligned, continuous microtubules. Blebbing dynamics in calcium-free media followed similar trends, but the bleb recovery was faster (**Fig. 6.S5a,b**).

Cell membrane permeability aligns with electric field orientation

Given our observations that the electric field orientation with respect to cell shape altered cell responses in contractile force and cell length, we wanted to determine how orientation affected membrane permeability. Using propidium iodide (PI) as a marker of membrane permeability, we visualized the temporal dynamics of PI uptake during and after the application of ten, 1000 V pulses delivered at 1 Hz. We found that PI entered cells at both the anodic (hyperpolarized) and cathodic (depolarized) sides of the cells (with respect to electric field): near the cell's endpoints (protrusions) in the parallel orientation

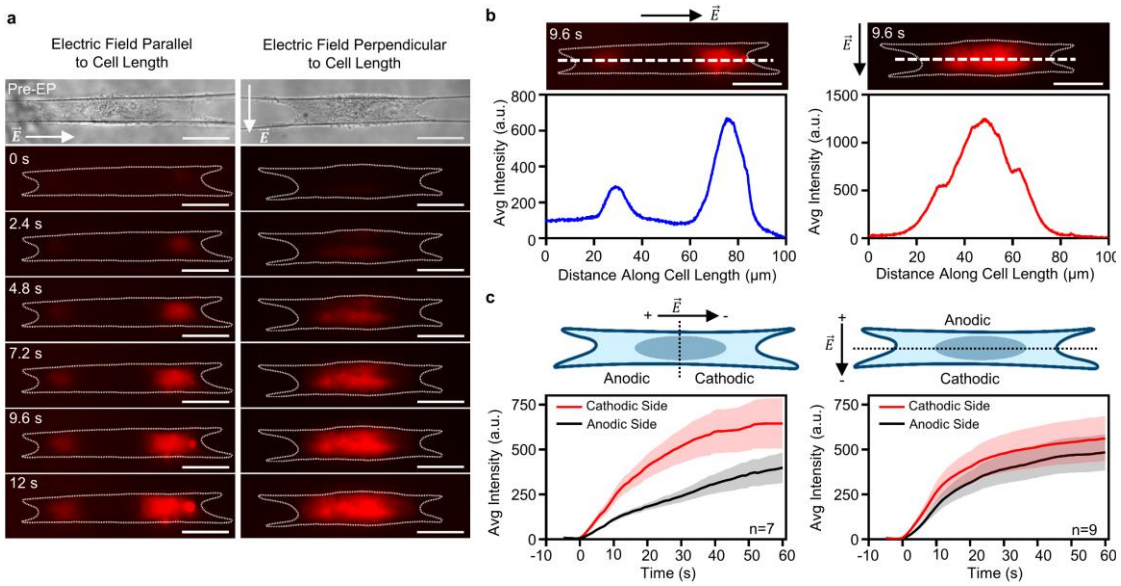

Figure 6.5. Cell orientation affects membrane permeability after electroporation. a) Cells show uptake of propidium iodide (PI) during and after the application of ten, 1000 V pulses (∥: 882 V cm^{-1}; ⊥: 911 V cm^{-1}) delivered at 1 Hz. Time $t = 0$ indicates the end of the first pulse. PI uptake reveals distinct spatial distributions of membrane permeability for the parallel and perpendicular orientations. In the parallel orientation (a, left column), PI uptake is located near the cell attachment points. However, in the perpendicular orientation (a, right column), uptake is near the central sidewalls. White dashed lines show cell boundary pre-electroporation. The time series indicates that membrane permeability and the influx of PI precedes cell rounding. Scale bars 20 μm b) Representative intensity plots taken along the cell length (large white dashed lines) demonstrate the distinct spatial distributions of membrane permeability in the parallel and perpendicular orientations. c) PI uptake is biased toward the cathodic (depolarized) side of the cell. Error bands show standard error. (Figure 6.5 c).

and along the cell's width in the perpendicular orientation (**Fig. 6.5**). Incidentally, we observed that PI uptake was biased toward the cathodic side of the cell (**Fig. 6.5c**) with the initial rate of fluorescence intensity change (a.u./s) nearly two times greater compared to the anodic side in the parallel orientation (22.9 ± 3.7 *vs* 10.7 ± 1.1 a.u./s), while the perpendicular orientation showed a smaller but still significant difference between the cathodic and anodic side (26.1 ± 5.7 *vs* 18.5 ± 3.7 a.u./s). To investigate if PI uptake was dependent upon calcium in the buffer, we repeated experiments in calcium-free media at 1000 V. We found that the temporal uptake of PI in calcium-free media at 1000 V followed similar trends as in regular media at 1000 V (**Fig. 6.S5c,d**) with no significant difference in PI uptake 60 seconds after electroporation (**Fig. 6.S5e**).

Cell contractility and not necessarily cell shape is sensitive to pulsed electric fields

We wanted to inquire if our findings of cell shape and force recovery were generalizable to other cell types, so we investigated electroporation effects to five other cell lines: VAMT cells (human mesothelioma), human thyroid cancer cells, CHO-K1 cells (Chinese hamster ovary), C2C12 cells (mouse myoblasts), and HeLa cells (human cervical cancer). We performed electroporation experiments with cells in the parallel orientation (**Fig. 6.6 a, b**). Although the magnitude of contractile force pre-electroporation varied between cell lines, all cell lines demonstrated a rapid and significant loss in force after electroporation, followed by an eventual recovery of force in 1 to 2 hours. Importantly, experiments with all cell types showed instances of cells undergoing biphasic force responses (Stage 2) during recovery (**Fig. 6.6c**). Furthermore, we found that contractile force is a much more sensitive indicator of cell recovery compared to cell shape (length) alone, as HeLa and CHO cells showed minimal rounding, but a significant loss of contractile force after

electroporation. Overall, our experiments with additional cell types, healthy and cancerous, demonstrate that the loss of contractile force after electroporation was cell-line independent, while a severe loss of cell shape was cell-line dependent.

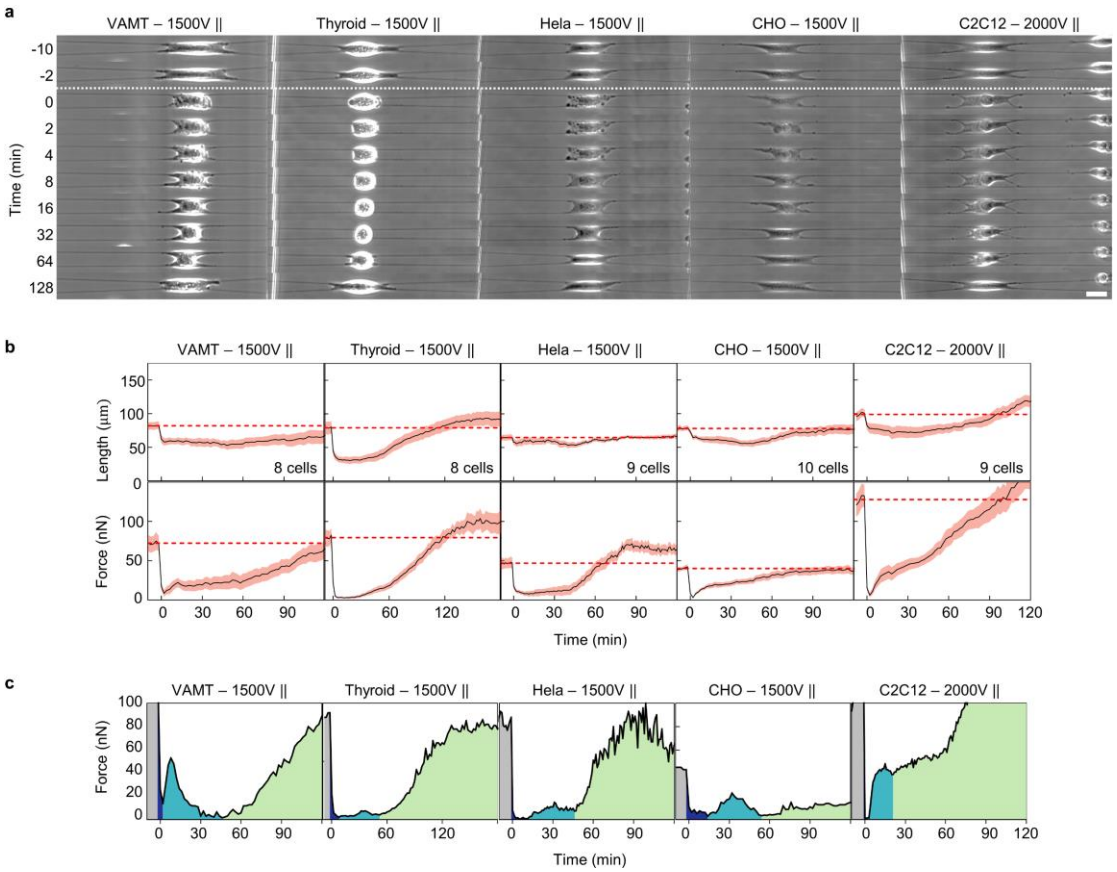

Figure 6.6: Electroporation experiments on five additional cells lines conducted at 1500 V or 2000 V in the parallel orientation. a) Brightfield images of cell responses to electroporation. Scale bar is 25 µm. b) Cell length and contractile force responses for five cell types after electroporation. Note that the cell contractile force is more dynamic than the cell shape. All cell types demonstrate a robust loss and recovery of forces post-electroporation, but do not necessarily show any significant changes in the cell shape. c) An example of a multi-stage response for each additional cell type.

6.4 Discussion

Despite the extensive development and use of electroporation technologies in various biological applications, the dynamics of mechanical recovery to tensional homeostasis in

cells post-electroporation remain poorly understood. Complementary to membrane-centric approaches to electroporation reported in literature, here we provide a mechanobiological investigation of electroporated cells by measuring the contractile forces of single cells adherent to extracellular matrix-mimicking suspended fibers. Our network of suspended nanofibers constrains cells to be elongated, in high-aspect ratio shapes with inherent mechanical, biological, and spatial anisotropy, properties that we investigate with two electric field directions (Fig. 6.1). We demonstrate that both electric field magnitude and direction significantly impact the contractile response of cells, which exhibits three distinct stages (Fig. 6.2): an initial loss in contractility immediately post-electroporation (Stage 1), a biphasic force response (Stage 2), and force recovery to pre-pulse contractility (Stage 3).

Cells attached to our parallel network of fibers form clusters of focal adhesions at their extremities, and upon electroporation, the adhesions are broken, leading to cell rounding (Stage 1). Our observations of minimal cell rounding in the absence of extracellular calcium (Fig. 6.3g) implicates extracellular Ca^{2+}-induced focal adhesion disassembly as a possible contributing factor to the cell-rounding stage. It is well established that electroporation disrupts the transmembrane Ca^{2+} gradient[267,269] and causes an influx of extracellular calcium inside the cell, and that locally-elevated intracellular calcium levels can lead to disassembly of focal adhesions within minutes[266,270–272] This conclusion is reinforced by our observation that significant PI uptake occurs prior to cell rounding (Fig. 6.5). To disambiguate the role of serum and calcium in cell rounding, we performed experiments in both serum-free and calcium-free media. Our findings that cell rounding was observed after electroporation in calcium-containing DMEM (1.8mM calcium, no serum), and minimal rounding in calcium-free media further confirm the role of calcium

in cell rounding (Fig. 6.S5f). Cell rounding after electroporation has been previously attributed to colloid-osmotic swelling,[244,254,273,274] and our results suggest that extracellular calcium is an additional factor driving the loss of cell adhesion. Incidentally, we found some evidence that cells with higher levels of pre-pulse contractility undergo a faster cell-rounding stage, suggesting a 'slingshot effect' caused by the contractile actin stress fibers that accelerate the rounding process (Fig. 6.S2e). Independent of the magnitude of pre-pulse contractility, we observe a rapid loss of actin stress fibers and microtubule structure following the electric field treatment, as prior studies have also noted[232,234,254,275]. Cytoskeletal disruption was concomitant with the formation of blebs, with peak bleb size observed at 2 minutes post-electroporation (1000 V ∥) corresponding closely with maximal loss of cell contractility. Bleb elimination by 32 min (1000 V ∥) post-electroporation is in reasonable agreement with the timescales of membrane resealing previously reported[228,230,236,276,277].

Membrane disruption during electroporation is driven by an induced transmembrane potential (ITP), causing pore formation if ITP values exceed a "critical" threshold (~ 0.2-1 V)[219,226,278–282]. Our simple ITP models (Fig. 6.S6, steady-state, constant membrane conductivity) predict pore formation (ITP ≥1.0 V) for all conditions except 500 V perpendicular, in good agreement with our experimental results demonstrating loss of contractility and cell length for these conditions. However, a maximal ITP value of 0.5 V for cells treated at 500 V in the perpendicular orientation indicates minimal (or no) electroporation, a result consistent with minimal changes to contractile force or length and no YO-PRO-1 uptake observed (data not shown). Incidentally, our experiments showed that PI uptake was asymmetric with a bias toward the cathodic (depolarized) side of the

cell, a finding consistent with previous studies but not explained by our ITP models or electroporation theory[283,284]. Our models indicate that cells in the parallel orientation should have greater overall disruption compared to the perpendicular orientation due to higher ITP values. However, our experiments revealed higher cell viability for cells electroporated in the parallel orientation. Modifying our model to include dynamic membrane conductivity[285–287], electric field disruption near the nanofibers, pore characteristics (number and radii),[287] and/or total mass transport across the membrane[288,289] might reconcile the differences between experimental viability results and model predictions. Cell shape-change after pulsing, which is more rapid and prominent after electroporation in the parallel orientation, may also contribute to increased viability in this orientation, as rounding may promote cell recovery by reducing membrane tension or by reducing the cell's surface area, thereby reducing transport across the disrupted membrane.

As cells become rounded at the end of the cell-rounding stage (Stage 1), the contractility measurements demonstrate a biphasic response with a significant rise in forces but with a minimal change in cell length during the first half of this stage (Stage 2). Although the exact mechanisms responsible for the biphasic force response remain unknown, we suggest three likely contributing factors. First, during the initial phase of force recovery, contractility increases as blebbing decreases. Bleb reduction by contraction of cortical actin likely contributes to the increased contractility we observe[290,291]. Second, cell volume may decrease slightly after electroporation (Fig. 6.S3c-d) likely due to cytoskeleton tension-mediated water efflux[292,293], thus leading to an increase in force. Third, increased levels of intracellular Ca^{2+} have been shown to cause aggregation of endoplasmic reticulum Ca^{2+} sensor STIM1, which then leads to the recruitment of the force-bearing focal adhesion

protein, talin, and could thereby account for the increased cell contractility in the first phase of this biphasic stage[294]. The reduced contractility seen in phase II is most likely indicative of a reorganization of actin, possibly from a bleb-reduction configuration to a spreading configuration, yet the specific mechanisms are unknown.

Irrespective of the electric field strength and orientation, cells that were viable post-electroporation (see Methods for viability criteria) had fully-restored contractility typically within the first 1-3 hours post-electroporation (Stage 3). Such timescales for cell contractile recovery fall within the reported range of cytoskeletal recovery times (minutes to hours[234,235,241,250,254,295]). Cell force recovery has been previously investigated in the context of rapid mechanical stretching events[296–301], and not for electroporation, which we show here. While mechanical stretching and electric field treatment are fundamentally different cues, the cellular contractility response to perturbation bear similarities. Studies show that rapid mechanical stretching disrupts tensional homeostasis leading to rapid disruption of the actin cytoskeleton, followed by recovery of cell contractility either in single or multi-stages. For example, Nekouzadeh *et al*. demonstrated that rapid stretching (20% strain at 800%/s) induced a multi-stage recovery process: a stage of rapid force increase and relaxation (>1 min), a force plateau stage, and finally a gradual active force recovery stage that lasted around 20 minutes[301]. Loss and recovery of cell force was attributed to cytoskeletal fluidization (depolymerization of the actin cytoskeleton) and cytoskeletal re-solidification (actin stress fiber recovery) respectively. While these force response patterns resemble the multi-stage force dynamics reported by us, we note the importance of membrane disruption linked with integrity of cytoskeletal networks in electroporation. The large-scale bleb formation and recession observed in our studies post-electroporation is

synchronized with disruption and formation of actin fibers (Fig. 6.4), which might explain why the timescales of electroporation-mediated biphasic force recovery (few minutes) differ from the stretch-mediated shedding of forces occurring typically within a few seconds. Additionally, while mechanical stretching induces a loss in contractility without affecting the overall cell shape, electroporation-mediated disruption can have a loss of cell shape (rounding) followed by recovery (spreading). Such substantial cell shape recoveries may further explain the longer timescales of force recovery (2-3 hours) compared with mechanical stretching (~30 minutes)[298,301].

6.5 Conclusion

In conclusion, the prevailing paradigm in electroporation emphasizes membrane disruption and resealing as the key metrics in cell recovery, yet from our study across multiple cell types, it is increasingly clear that cytoskeletal dynamics play a significant role in cell shape and force recovery. Our ECM-mimicking nanofiber-based platform demonstrates that mechanical force recovery is a robust metric to evaluate cell recovery after electroporation. We anticipate our mechanobiological approach to cell recovery will yield insights clarifying the relationship between membrane dynamics (permeability, tension, composition) and cytoskeletal dynamics (structure, contractility), and show how these properties impact cell survival. Fundamental knowledge on the relationship between cell mechanics and membrane permeability may link membrane resealing times with the force response, knowledge that may reveal the mechanisms of pore resealing and enable optimizations for electroporation technologies such as gene transfection. We expect that a better understanding of the mechanical response to electroporation will present target-

opportunities in reversible electroporation applications such as genetic engineering, gene therapy, and molecular medicine.

Supplementary Material

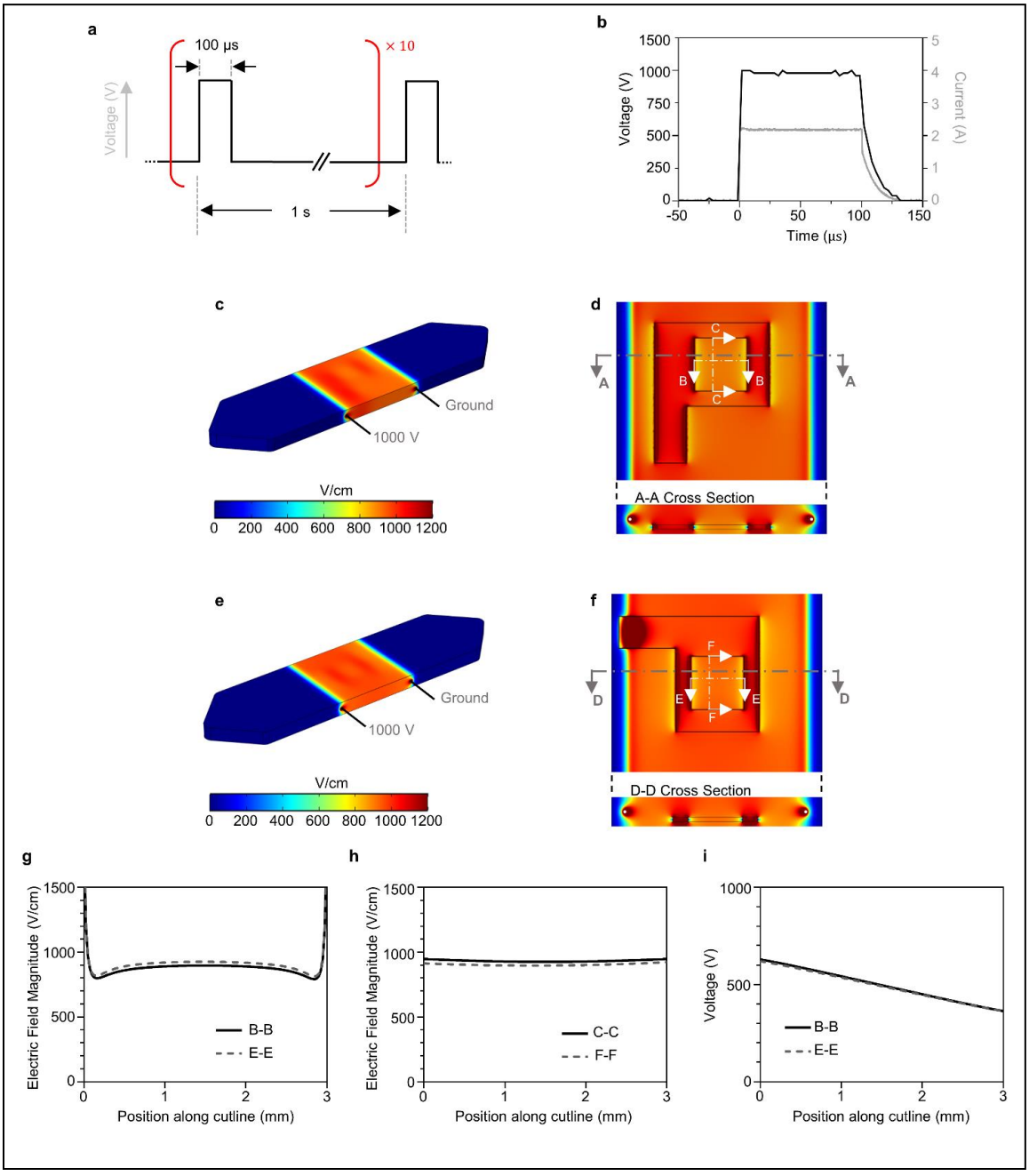

Supplementary Figure 6.S1. Electroporation waveforms and the electric field within the device. a) Cells were treated with ten, 100 µs square wave pulses at 1 Hz. b) Actual voltage and current waveforms measured during the first pulse. Pulses approximate idealized square waves. c) A finite element model shows the electric field distribution along the walls of the fluidic channel (c,e) and in the plane of the nanofiber scaffold (d,f). In c) and d) the scaffold is modelled in the parallel orientation while e) and f) are modelled with the scaffold in the perpendicular orientation. The nanofiber region within the scaffold has an approximately uniform electric across the center of the scaffold. g) Along the cutlines B-B and E-E the electric field magnitude is mostly constant, with asymptotic regions near the edges. h) Along cutlines C-C and F-F, electric field is quite uniform. i) The voltage drop is nearly linear along cutlines B-B and E-E. The generated electric fields over the region of interest were approximately 441 V cm^{-1}, 882 V cm^{-1}, and 1323 V cm^{-1} respectively across the scaffold region in the parallel orientation and 455 V cm^{-1}, 911 V cm^{-1}, and 1366 V cm^{-1} respectively across the scaffold region in the perpendicular orientation.

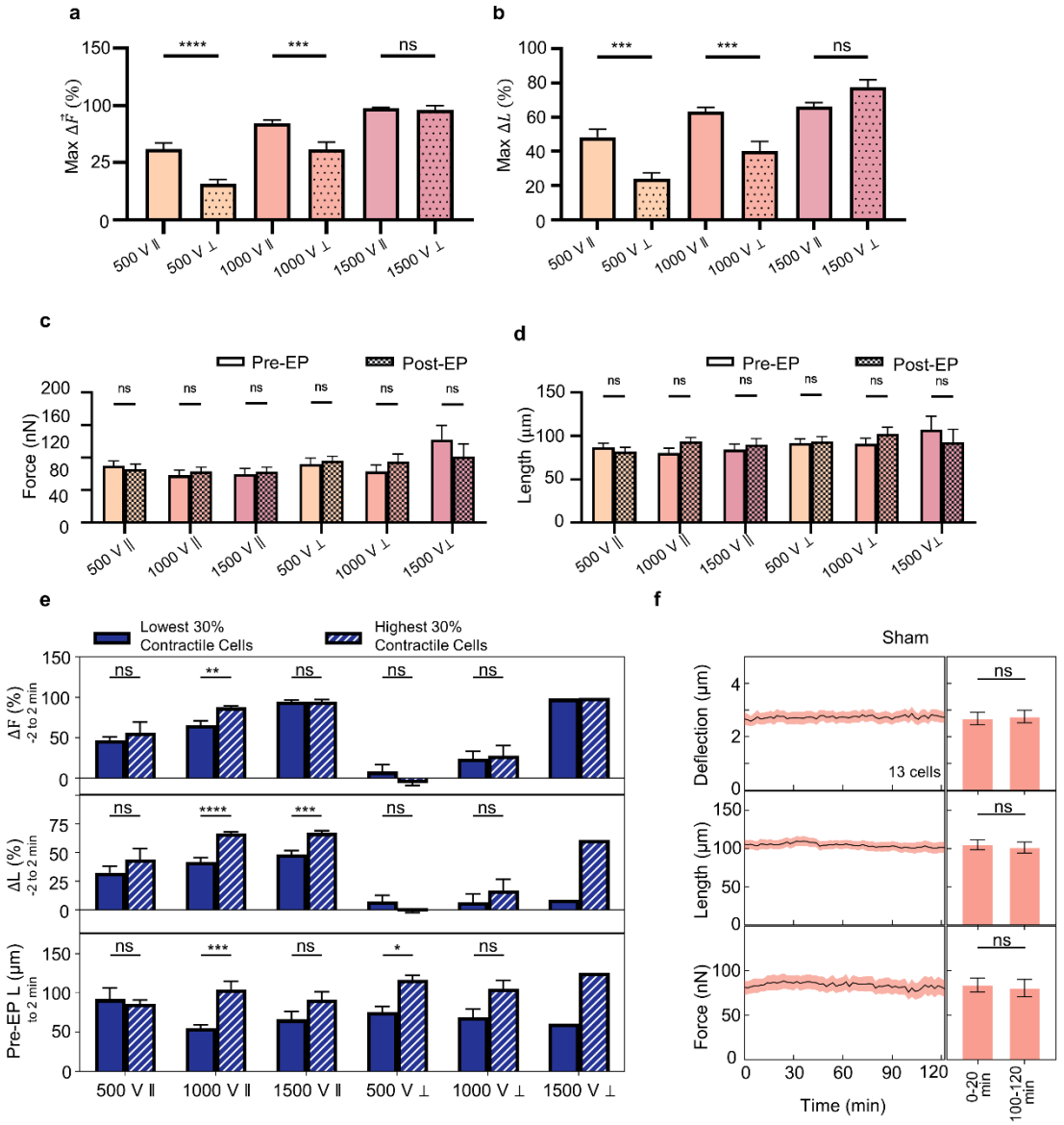

Supplementary Figure 6.S2. Force and length changes after electroporation. a-b) Data from Figure 6.2e-f, re-ordered to show significant differences due to electric field orientation. c-d) Cells post-electroporation do not show significant differences in contractile force or length compared to pre-electroporation values. Post-electroporation data collected at 180 min for 500 V and 240 min for 1000 V and 1500 V. e) For a given voltage and field orientation, high and low contractile cells show a similar force response in the first two minutes after EP. In the parallel orientation, the high contractile cells show a larger decrease in cell length immediately after electroporation when compared with low contractile cells, suggesting that contractility might increase the rate of rounding. However, high contractile cells also tend to also have longer initial lengths, so the rate of rounding may be dependent on both cell contractility and cell length. Stats not available for 1500 V ⊥ (n=1 for both bars). f) Response of control cells ('sham exposure') kept at the same culture conditions as electroporation experiments. Over the course of 2 hours cells, demonstrated steady-state levels of contractility and maintained consistent cell shapes. EP, electroporation.

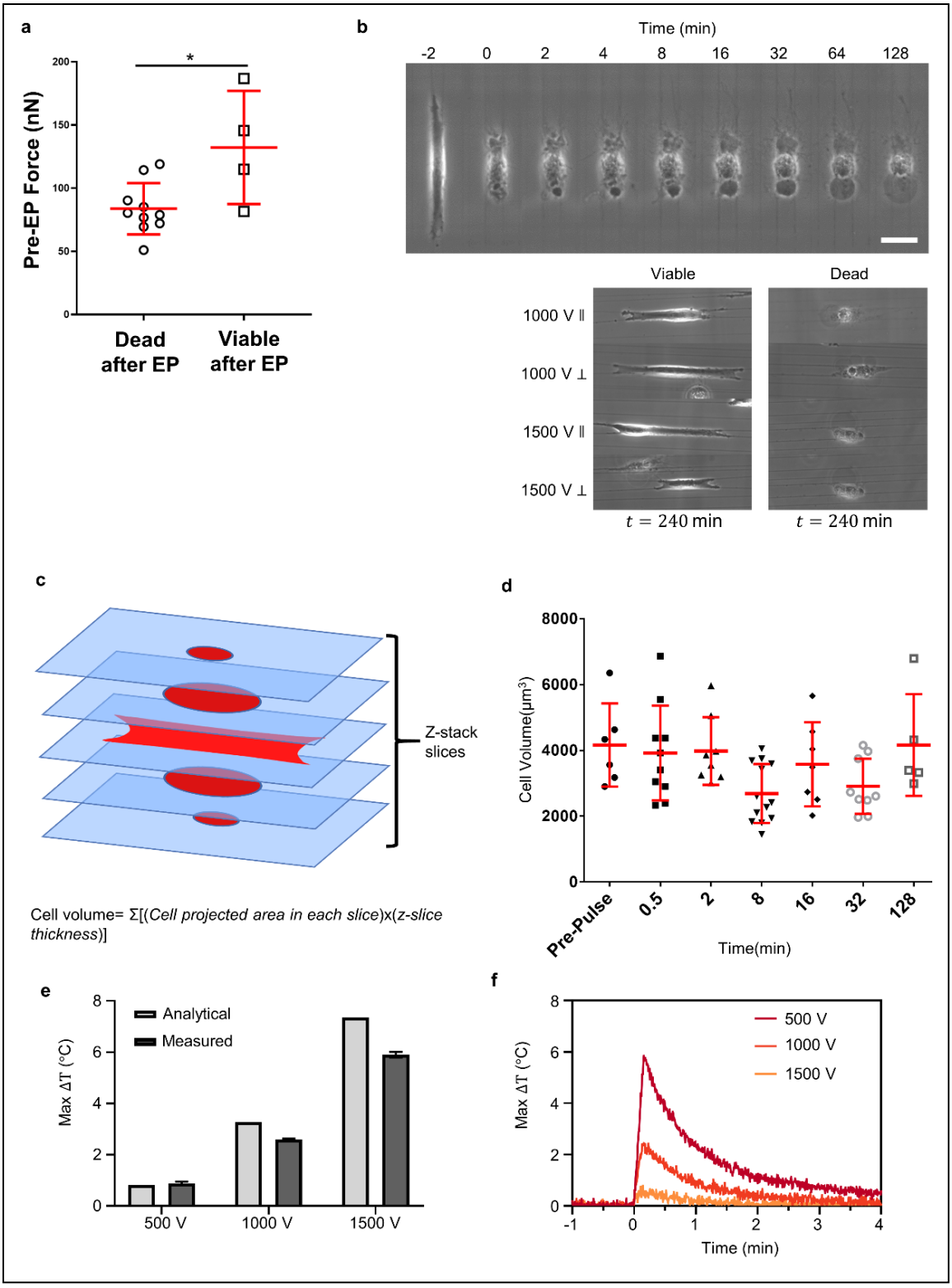
a
Pre-EP Force (nN)
200
150
100
50
0
*
Dead after EP
Viable after EP
b
Time (min)
-2
0
2
4
8
16
32
64
128
Viable
Dead
1000 V ∥
1000 V ⊥
1500 V ∥
1500 V ⊥
t = 240 min
t = 240 min
c
Z-stack slices
Cell volume= Σ[(Cell projected area in each slice)x(z-slice thickness)]
d
Cell Volume(μm³)
8000
6000
4000
2000
0
Pre-Pulse
0.5
2
8
16
32
128
Time(min)
e
Max ΔT (°C)
Analytical
Measured
500 V
1000 V
1500 V
f
Max ΔT (°C)
500 V
1000 V
1500 V
Time (min)

Supplementary Figure 6.S3. Additional analysis of cell death, cell volume, and Joule heating. a) Comparison of pre-electroporation forces for cells treated at 1500 V in the perpendicular orientation. The few cells that survived electroporation at 1500 V in the perpendicular orientation showed higher pre-electroporation forces than cells that did not survive electroporation b) This image panel shows an example of cell death by accidental cell death. Very soon after electroporation, the cell takes on visual signs of cell death such as a loss of contrast and large membrane blebs. Additionally, the cell rapidly losses contractility as shown by the lack of fiber deflection after electroporation. Scale bar 25 µm. c-d) Cell volume change during cell recovery. Volume was calculated in MATLAB using z-stacks of fluorescent images (stained for actin, microtubules, and the nucleus) of fixed cells. The 2D area of the cell in each slice was used to estimate cell volume. d) Cell volume seems to decrease after electroporation (1000 V ‖), with the greatest decrease between 8 and 32 minutes after electroporation. However, cell volume is not statistically significant between timepoints (ANOVA, α=0.05). (n = 6, 10, 8, 13, 7, 9 and 5 corresponding to pre-pulse, 0.5, 2, 8, 16, and 32-minute timepoints respectively) e-f) Joule heating due to the electric pulses results in a rapid increase in temperature that returns to near pre-electroporation levels within minutes. The maximum temperature increase within the device due to Joule heating was experimentally and analytically verified to be under 8 °C for all conditions. Experimental measurements of Joule heating within the device was measured *via* a fiber optic temperature probe placed through the PDMS sidewall into the center of the electrode regions. f) The maximum temperature occurs immediately after pulsing and then returns to near pre-electroporation levels within 5 minutes. Fiber optic data collected at room temperature.

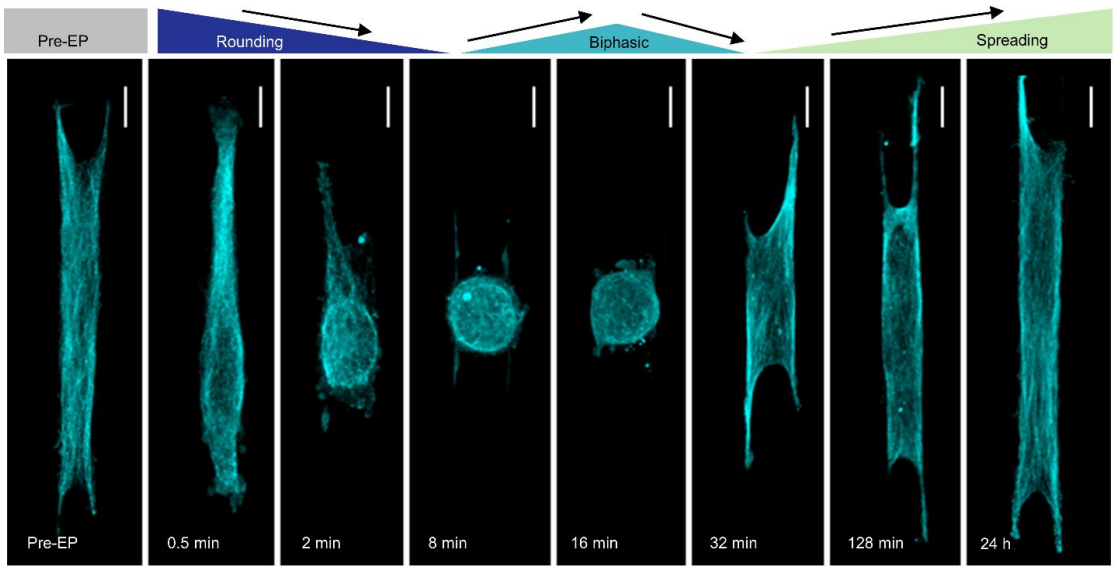

Supplementary Figure 6.S4. Microtubule dynamics after electroporation. a) Maximum intensity projections of cells stained for microtubules before electroporation and during various stages of recovery post-electroporation (1000 V Electroporated cells (1000 V ‖) show a loss of microtubule alignment as the cells round, localization of tubulin at membrane blebs, and an eventual recovery of structure within 2 hours. Scales bars 10 µm.

Chapter 7:

Impact and future directions

7.1 The Bigger Picture

It is now well-appreciated that cell behavior is not only regulated by chemical signals but is significantly influenced by the physical and mechanical properties of the cellular microenvironment. While previous studies have mostly elucidated the role of bulk mechanical properties of the extracellular matrix in regulation of force generation, migration and differentiation, but our understanding of the role of local fibrous ECM properties like fiber size, stiffness, alignment and pore sizes, remains highly limited. Fundamental knowledge of such cell-fiber interactions is particularly important in advancing our understanding of pathophysiological phenomenon like cancer metastasis, where malignantly transformed cells dissociate from the primary tumor site, interact with the highly fibrous tumor stroma to frequently adopt anisotropic shapes and migrate persistently and spread to distant parts within the body. Since cellular attachment, movements and generation of contractile forces leading to ECM remodeling, is primarily facilitated by the cell cytoskeleton, detailed investigation of the cytoskeletal remodeling in physiologically relevant fibrous environments in vitro, warrants for a better understanding of metastatic process.

In this study, we used the non-electrospinning Spinneret based Tunable Engineered Parameters (STEP) technique for design and manufacturing of suspended fiber networks with a wide range of fiber diameters, network architectures and stiffness to capture essential aspects of the native ECM. We demonstrate cytoskeletal caging of nucleus in

aligned fibers regulates nuclear shape and response in a fiber size, stiffness and density-dependent manner, with single fibers inducing nuclear envelope invaginations. Using bidirectional crossing fiber arrangements, we demonstrate control over the nature of cell migration, with dense crosshatch networks highly persistent migration in elongated morphologies, comparable to 3-dimensional environments, while sparse networks demonstrated slower 2D diffusive migration with well-spread cells. We utilize the fiber geometry-based tunable organization of interphase cell-ECM adhesions to investigate the role retraction fiber-mediated mechanical control of cell division dynamics and observe differential levels of mitotic spindle defects. Finally, we apply our knowledge of such mechanobiological responses to elucidate physical recovery mechanisms of single cells towards external electric fields.

Findings from this study provide detailed insights on how specific biophysical cues from the local cellular microenvironment can guide cell migration, division and nuclear mechanics, which constitute key behaviors in the broader context of cancer metastasis. Additionally, our findings on cytoskeletal disruption and reassembly during cellular recovery after intense-electric field application, demonstrates the incredible cellular adaptability to fibrous microenvironments and highlights how cancer can evade electric-field treatments and continue on their metastatic journey. Overall, our mechanobiological observations can potentially provide predictive data for *in vivo* cellular response, essential for development of cytoskeleton-targeting cancer therapies.

7.2 Future Directions

Specific Aim 1 (Mechanical regulation of cytoskeletal organization and nuclear shapes during cell spreading)

Results obtained from this specific aim demonstrate that a symmetric cytoskeletal caging structure lacking traditional apical-basal polarity, controls nuclear shapes and nuclear translocation of transcription factors, in a fiber diameter, stiffness and network density-dependent manner. In particular, cells attached to single fibers demonstrate distinct (1.5-3 μm) nuclear deformations or invaginations situated along the local region of cell-fiber contact, while those attached to multiple fibers in dense fiber matrices demonstrate high levels (~60% reduction from rounded nucleus thickness) of nuclear compression along with multiple invaginations. Such drastic nuclear shape deformations mediated by ECM fiber geometry raises an interesting question as to how these morphological changes contribute to alterations in chromatin condensation and overall transcriptional potential of cells. Currently, we have characterized the nuclear morphologies till the end of the spreading phase (~1-2 hours after initial cell-substrate contact), but typically changes in gene expression occur over a period of several hours to few days. Thus, future work will involve quantitative imaging for chromatin condensation and gene expression profiling after 24-48 hours of culturing cells in these suspended fibrous microenvironments.

Specific Aim 2 (Persistent cell migration on bidirectional crosshatch fiber matrices)

Results obtained from this specific aim suggest, that aligned ECM is not an essential requirement for achieving anisotropic cell shapes and persistent cell migration and dense fiber matrices in a crossing arrangement can induce elongated cell morphologies and

sustain persistent migration for long times. Specifically, we observe that based on the inter-fiber spacing, cells can show reduced migration (wide ~ 54 µm), 2D diffusive random-walk based migration (intermediate, ~18-36 µm) or enhanced and persistent motion (dense, ~ 3-6 µm). Since dense matrices were observed to be stiffer and offer more adhesive contact points to cells, this allows for investigation of durotaxis (mechanical stiffness based) and haptotaxis (adhesive ligand concentration based) of migrating cells. As a starting point, we have manufactured gradient-based crosshatch matrices (**Fig. 7.1**) with widely spaced fibers on one end, which decrease gradually to highly dense regions on the other side, thereby establishing durotactic/haptotactic gradients across the matrices.

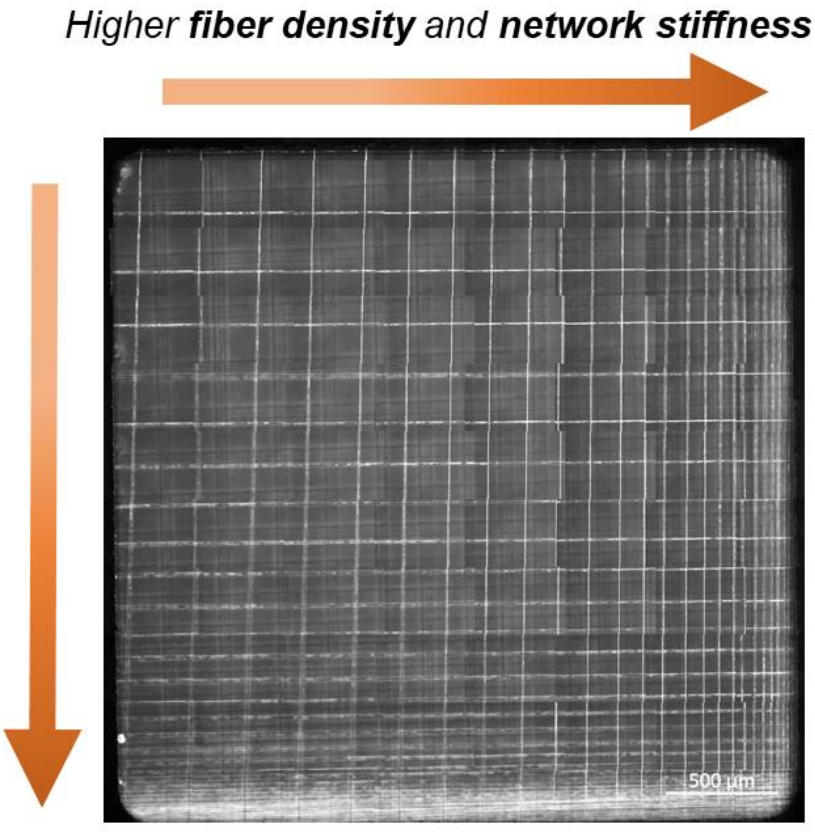

Figure 7.1: Gradient based scaffolds for investigating durotactic behavior of cells migrating on suspended fibers

It will be intriguing to understand how cells cultured on these fibrous environments establish their migration trajectories. Additionally within the native tumor microenvironment (TME), cells can sense and receive both biophysical and biochemical cues to regulative their migratory behavior. So, the next step is to place such a composite spacing scaffold within a microfluidic device with tunable gradients of chemotactic agents like TNF-α (tumor necrosis factor) and investigate the nature of migration under the actin of combined durotactic/chemotactic cues.

Specific Aim 3 (Mechanical force recovery after electroporation)

Results obtained from this specific aim demonstrate that elongated cells on suspended fibers, subjected to high-voltage short duration electric pulses (used to induce membrane – electroporation), demonstrate a multi-stage loss and recovery in elongation and contractility, which correlates with cytoskeletal disruption and reassembly. We also find such cells in anisotropic shapes, oriented along the electric field direction are particularly resilient as compared to their counterparts on flat cultures and can withstand voltages as high as 1500 V/cm with > 70% viability. Such behavior presents various opportunities to optimize reversible electroporation applications like cell electrofusion and intracellular delivery of plasmids.

i) Hybrid cancer stem cell generation using electrofusion

Recent studies indicate that tumor initiation and development can be attributed to formation of cancer stem cells which are known for their high proliferation capacity and their ability to self-renew. While the origin of cancer stem cells remain elusive, it is now well accepted that cell fusion between normal stem cells and malignantly transformed cells lead to their

formation. Here, we utilize the high viability of elongated cells on suspended fibers, to drive fusion of mesenchymal stem cells and cancer cells (HeLa cervical cancer cell line) using high voltage pulsed electric fields. As proof of concept, we carried out such electrofusion experiments in aligned fibers (**Fig. 7.2a**) and demonstrate successful formation of hybrid cancer stem cells (**Fig. 7.2b**). Future work will include extraction of such hybrid cells and detailed investigation of the long-term biophysical behavior (migratory and protrusive behavior, cell force generation) and gene expression profiling to ultimately elucidate the cellular reprogramming within cancer stem cells.

ii) Electroporation-induced intracellular cargo delivery in cells attached to suspended fibers

Intracellular delivery of foreign DNA is of great interest for various biological applications including gene transfection and anticancer treatments. While various techniques like microinjection and chemical transfection exist for such intracellular delivery, they have significant drawbacks such as low delivery efficiency and cell viability. While electroporation can achieve high delivery efficiencies with increasing electric field strengths, this often comes at the cost of low cell viability. On the other hand, higher electric fields are often necessary to generate sufficiently large membrane pores to enable entry of commonly used cargoes like plasmid DNA and cellular drugs. Thus, our findings of increased viability to electric fields, when cells are attached to suspended fibrous environments as compared to rounded cells in suspension, will allow us to utilize higher electric field strengths to efficiently drive the intracellular cargo delivery, while still maintaining a sufficiently high level of cell viability. Additionally, from our single cell force measurements, we identified a biphasic force recovery and loss stage, which lasted around 20-30 minutes for electric fields ~ 1000 V/cm, which was indicative of incomplete

pore resealing or a permeable cell membrane. Increased cell membrane permeability for such longer times (~30 minutes) offers a wider window of opportunity for delivery of cargo as compared to traditional electroporation-based transfection approaches with rounded cells in cuvettes, where the maximum resealing time of membrane pores is usually in the order of few hundred seconds[302–304].

As proof-of-concept, we have first tried to deliver high molecular weight FITC dextran and then pEF-GFP plasmids to elongated cells oriented along the electric field direction and attached to the suspended fiber networks. As shown in **Fig. 7.2 c,d** we demonstrate successful entry of both cargoes.

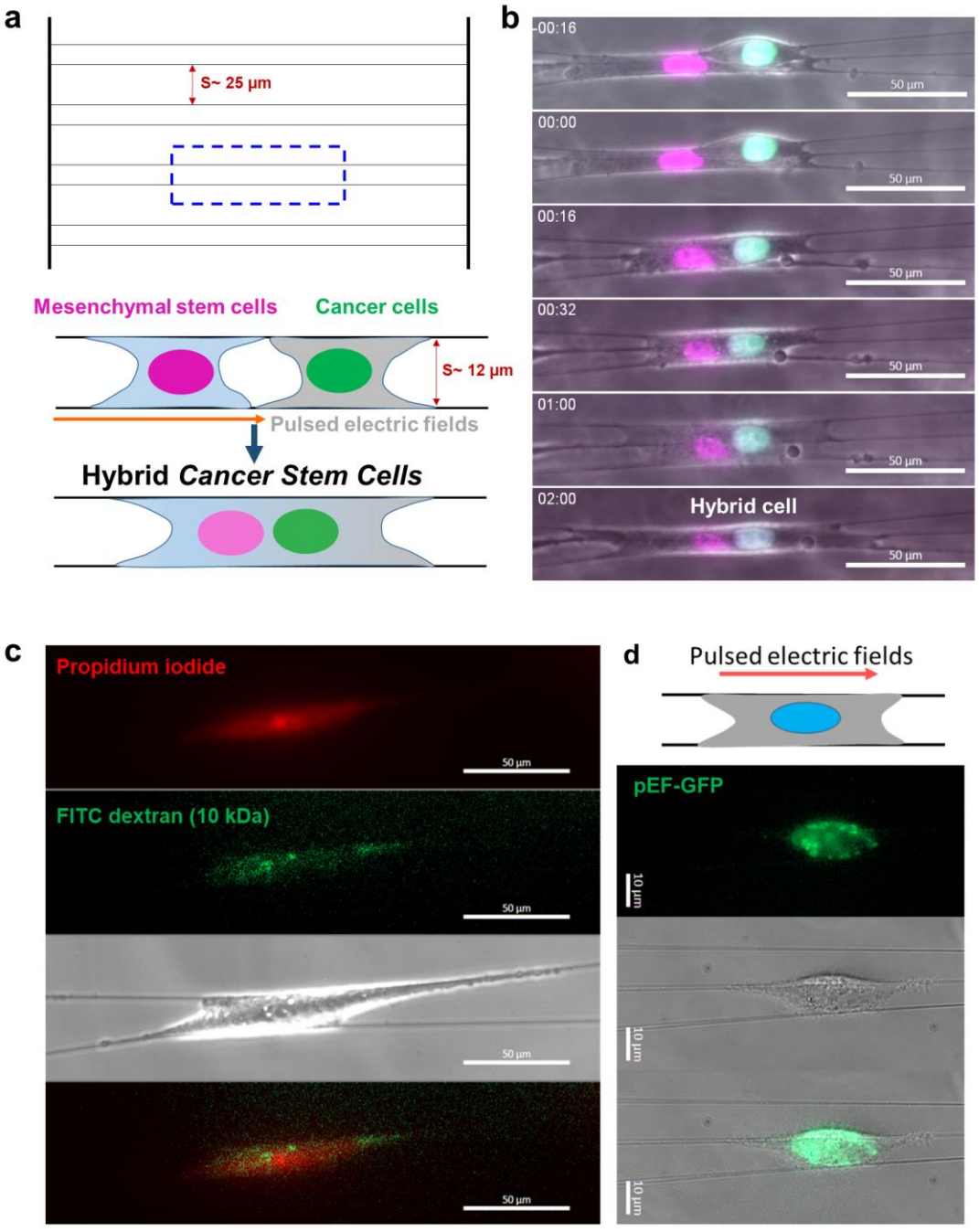

Figure 7.2: **Electrofusion and intracellular cargo delivery on cells attached to suspended fibers**, a) Aligned fibers to drive electric field-mediated fusion of stem cells and cancer cells to generate cancer stem cells, b) Electrofusion between mesenchymal stems and cancer cells (HeLa) leading to hybrid cell formation c,d) Intracellular delivery of FITC dextran (10 kDa) and pEF GFP plasmids

References

1. Mouw, J. K., Ou, G. & Weaver, V. M. Extracellular matrix assembly: a multiscale deconstruction. *Nat. Rev. Mol. Cell Biol.* **15**, 771–785 (2014).
2. Lu, P., Weaver, V. M. & Werb, Z. The extracellular matrix: a dynamic niche in cancer progression. *J. Cell Biol.* **196**, 395–406 (2012).
3. Wolf, K. & Friedl, P. Extracellular Matrix Determinants of Proteolytic and Non-Proteolytic Cell Migration. *Trends Cell Biol.* **21**, 736–744 (2011).
4. Thiery, J. P., Acloque, H., Huang, R. Y. J. & Nieto, M. A. Epithelial-mesenchymal transitions in development and disease. *Cell* **139**, 871–90 (2009).
5. Georgakopoulos-Soares, I., Chartoumpekis, D. V., Kyriazopoulou, V. & Zaravinos, A. EMT Factors and Metabolic Pathways in Cancer. *Front. Oncol.* **10**, 1–20 (2020).
6. Wong, I. Y. *et al.* Collective and individual migration following the epithelial-mesenchymal transition. *Nat. Mater.* **13**, 1063–1071 (2014).
7. Pathak, A. & Kumar, S. Biophysical regulation of tumor cell invasion: moving beyond matrix stiffness. *Integr. Biol. (Camb).* **3**, 267–78 (2011).
8. Siegel, R. L., Miller, K. D., Fuchs, H. E. & Jemal, A. Cancer Statistics, 2021. *CA. Cancer J. Clin.* **71**, 7–33 (2021).
9. Carey, S. P., D'Alfonso, T. M., Shin, S. J. & Reinhart-King, C. A. Mechanobiology of tumor invasion: Engineering meets oncology. *Crit. Rev. Oncol. Hematol.* **83**, 170–183 (2012).
10. Geiger, B., Spatz, J. P. & Bershadsky, A. D. Environmental sensing through focal adhesions. *Nat. Rev. Mol. Cell Biol.* **10**, 21–33 (2009).

11. Burridge, K. & Guilluy, C. Focal adhesions, stress fibers and mechanical tension. *Exp. Cell Res.* **343**, 14–20 (2016).

12. Burridge, K. & Wittchen, E. S. The tension mounts: Stress fibers as force-generating mechanotransducers. *J. Cell Biol.* **200**, 9–19 (2013).

13. Ridley, A. J. *et al.* Cell migration: integrating signals from front to back. *Science* **302**, 1704–9 (2003).

14. Lombardi, M. L. *et al.* The interaction between nesprins and sun proteins at the nuclear envelope is critical for force transmission between the nucleus and cytoskeleton. *J. Biol. Chem.* **286**, 26743–26753 (2011).

15. Bone, C. R., Chang, Y. T., Cain, N. E., Murphy, S. P. & Starr, D. A. Nuclei migrate through constricted spaces using microtubule motors and actin networks in C. elegans hypodermal cells. *Dev.* **143**, 4193–4202 (2016).

16. Jansen, K. A., Atherton, P. & Ballestrem, C. Mechanotransduction at the cell-matrix interface. *Semin. Cell Dev. Biol.* **71**, 75–83 (2017).

17. Iskratsch, T., Wolfenson, H. & Sheetz, M. P. Appreciating force and shape-the rise of mechanotransduction in cell biology. *Nat. Rev. Mol. Cell Biol.* **15**, 825–833 (2014).

18. Humphrey, J. D., Dufresne, E. R. & Schwartz, M. A. Mechanotransduction and extracellular matrix homeostasis. *Nat. Rev. Mol. Cell Biol.* **15**, 802–812 (2014).

19. Uroz, M. *et al.* Regulation of cell cycle progression by cell-cell and cell-matrix forces. *Nat. Cell Biol.* **20**, 646–654 (2018).

20. Nam, S. *et al.* Cell cycle progression in confining microenvironments is regulated by a growth-responsive TRPV4-PI3K/Akt-p27Kip1 signaling axis. *Sci. Adv.* **5**,

(2019).

21. Reinhart-King, C. A., Dembo, M. & Hammer, D. A. The dynamics and mechanics of endothelial cell spreading. *Biophys. J.* **89**, 676–689 (2005).

22. Puklin-Faucher, E. & Sheetz, M. P. The mechanical integrin cycle. *J. Cell Sci.* **122**, 575–575 (2009).

23. Kanchanawong, P. *et al.* Nanoscale architecture of integrin-based cell adhesions. *Nature* **468**, 580–4 (2010).

24. Tojkander, S., Gateva, G. & Lappalainen, P. Actin stress fibers - assembly, dynamics and biological roles. *J. Cell Sci.* **125**, 1855–1864 (2012).

25. Fournier, M. F., Sauser, R., Ambrosi, D., Meister, J.-J. & Verkhovsky, A. B. Force transmission in migrating cells. *J. Cell Biol.* **188**, 287–297 (2010).

26. Dix, C. L. *et al.* The Role of Mitotic Cell-Substrate Adhesion Re-modeling in Animal Cell Division. *Dev. Cell* **45**, 132-145.e3 (2018).

27. Théry, M. & Bornens, M. Cell shape and cell division. *Curr. Opin. Cell Biol.* **18**, 648–657 (2006).

28. Théry, M. & Bornens, M. Get round and stiff for mitosis. *HFSP J.* **2**, 65–71 (2008).

29. Petridou, N. I. & Skourides, P. A. A ligand-independent integrin β1 mechanosensory complex guides spindle orientation. *Nat. Commun.* **7**, (2016).

30. Matsumura, S. *et al.* Interphase adhesion geometry is transmitted to an internal regulator for spindle orientation via caveolin-1. *Nat. Commun.* **7**, (2016).

31. Maier, B., Kirsch, M., Anderhub, S., Zentgraf, H. & Krämer, A. The novel actin/focal adhesion-associated protein MISP is involved in mitotic spindle

positioning in human cells. *Cell Cycle* **12**, 1457–1471 (2013).

32. Bosman, F. T. & Stamenkovic, I. Functional structure and composition of the extracellular matrix. *J. Pathol.* **200**, 423–428 (2003).

33. Wade, R. J. & Burdick, J. A. Engineering ECM signals into biomaterials. *Mater. Today* **15**, 454–459 (2012).

34. Theocharis, A. D., Skandalis, S. S., Gialeli, C. & Karamanos, N. K. Extracellular matrix structure ☆. *Adv. Drug Deliv. Rev.* **97**, 4–27 (2016).

35. Gritsenko, P. G., Ilina, O. & Friedl, P. Interstitial guidance of cancer invasion. *J. Pathol.* **226**, 185–99 (2012).

36. Buehler, M. J. Nature designs tough collagen: Explaining the nanostructure of collagen fibrils. *Proc. Natl. Acad. Sci.* **103**, 12285–12290 (2006).

37. Zoumi, A., Yeh, A. & Tromberg, B. J. Imaging cells and extracellular matrix in vivo by using second-harmonic generation and two-photon excited fluorescence. **99**, (2002).

38. Weigelin, B., Bakker, G.-J. & Friedl, P. Intravital third harmonic generation microscopy of collective melanoma cell invasion. *IntraVital* **1**, 32–43 (2012).

39. Provenzano, P. P., Eliceiri, K. W. & Keely, P. J. Multiphoton microscopy and fluorescence lifetime imaging microscopy (FLIM) to monitor metastasis and the tumor microenvironment. *Clin. Exp. Metastasis* **26**, 357–370 (2009).

40. Alexander, D. C. *et al.* Orientationally invariant indices of axon diameter and density from diffusion MRI. *Neuroimage* **52**, 1374–89 (2010).

41. Gosline, J. *et al.* Elastic proteins: biological roles and mechanical properties. *Philos. Trans. R. Soc. Lond. B. Biol. Sci.* **357**, 121–32 (2002).

42. Mukherjee, A., Jana, A., Koons, B. & Nain, A. Design of Fiber Networks for Studying Metastatic Invasion. in 289–318 (Springer, Cham, 2018). doi:10.1007/978-3-319-95294-9_14.

43. Puls, T. J., Tan, X., Whittington, C. F. & Voytik-Harbin, S. L. 3D collagen fibrillar microstructure guides pancreatic cancer cell phenotype and serves as a critical design parameter for phenotypic models of EMT. *PLoS One* **12**, 1–25 (2017).

44. Conklin, M. W. *et al.* Aligned collagen is a prognostic signature for survival in human breast carcinoma. *Am. J. Pathol.* **178**, 1221–32 (2011).

45. Brett, E. A., Sauter, M. A., Machens, H.-G. & Duscher, D. Tumor-associated collagen signatures: pushing tumor boundaries. *Cancer Metab.* **8**, 1–5 (2020).

46. Van Helvert, S., Storm, C. & Friedl, P. Mechanoreciprocity in cell migration. *Nat. Cell Biol.* **20**, 8–20 (2018).

47. Weigelin, B., Bakker, G.-J. & Friedl, P. Intravital third harmonic generation microscopy of collective melanoma cell invasion. *IntraVital* **1**, 32–43 (2012).

48. Pelham, R. J. & Wang, Y. l. Cell locomotion and focal adhesions are regulated by substrate flexibility. *Proc. Natl. Acad. Sci. U. S. A.* **94**, 13661–5 (1997).

49. Huang, Z.-M., Zhang, Y.-Z., Kotaki, M. & Ramakrishna, S. A review on polymer nanofibers by electrospinning and their applications in nanocomposites. *Compos. Sci. Technol.* **63**, 2223–2253 (2003).

50. Nelson, M. T. *et al.* Preferential, enhanced breast cancer cell migration on biomimetic electrospun nanofiber 'cell highways'. *BMC Cancer* **14**, 825 (2014).

51. Rao, S. S. *et al.* Mimicking white matter tract topography using core-shell electrospun nanofibers to examine migration of malignant brain tumors.

Biomaterials **34**, 5181–90 (2013).

52. Beliveau, A., Thomas, G., Gong, J., Wen, Q. & Jain, A. Aligned Nanotopography Promotes a Migratory State in Glioblastoma Multiforme Tumor Cells. *Sci. Rep.* **6**, 1–13 (2016).

53. Nain, A. S. & Wang, J. Polymeric nanofibers: isodiametric design space and methodology for depositing aligned nanofiber arrays in single and multiple layers. *Polym. J.* **45**, 695–700 (2013).

54. Meehan, S. & Nain, A. S. Role of suspended fiber structural stiffness and curvature on single-cell migration, nucleus shape, and focal-adhesion-cluster length. *Biophys. J.* **107**, 2604–2611 (2015).

55. Sheets, K., Wunsch, S., Ng, C. & Nain, A. S. Shape-dependent cell migration and focal adhesion organization on suspended and aligned nanofiber scaffolds. *Acta Biomater.* **9**, 7169–7177 (2013).

56. Guilak, F., Tedrow, J. R. & Burgkart, R. Viscoelastic properties of the cell nucleus. *Biochem. Biophys. Res. Commun.* **269**, 781–786 (2000).

57. Swift, J. & Discher, D. E. The nuclear lamina is mechano-responsive to ECM elasticity in mature tissue. *J. Cell Sci.* **127**, 3005 (2014).

58. Skinner, B. M. & Johnson, E. E. P. Nuclear morphologies: their diversity and functional relevance. *Chromosoma* **126**, 195–212 (2017).

59. Uhler, C. & Shivashankar, G. V. Nuclear Mechanopathology and Cancer Diagnosis. *Trends in Cancer* **4**, 320–331 (2018).

60. Alam, S. G. *et al.* The nucleus is an intracellular propagator of tensile forces in NIH 3T3 fibroblasts. *J. Cell Sci.* **128**, 1901–1911 (2015).

61. Stephens, A. D. *et al.* Chromatin histone modifications and rigidity affect nuclear morphology independent of lamins. *Mol. Biol. Cell* **29**, 220–233 (2018).

62. Xia, Y. *et al.* Nuclear rupture at sites of high curvature compromises retention of DNA repair factors. *J. Cell Biol.* **217**, 3796–3808 (2018).

63. De vos, W. H. *et al.* Repetitive disruptions of the nuclear envelope invoke temporary loss of cellular compartmentalization in laminopathies. *Hum. Mol. Genet.* **20**, 4175–4186 (2011).

64. Alisafaei, F., Jokhun, D. S., Shivashankar, G. V. & Shenoy, V. B. Regulation of nuclear architecture, mechanics, and nucleocytoplasmic shuttling of epigenetic factors by cell geometric constraints. *Proc. Natl. Acad. Sci. U. S. A.* **116**, 13200–13209 (2019).

65. Elosegui-Artola, A. *et al.* Force Triggers YAP Nuclear Entry by Regulating Transport across Nuclear Pores. *Cell* **171**, 1397-1410.e14 (2017).

66. Kirby, T. J. & Lammerding, J. Emerging views of the nucleus as a cellular mechanosensor. *Nat. Cell Biol.* **20**, 373–381 (2018).

67. Damodaran, K. *et al.* Compressive force induces reversible chromatin condensation and cell geometry–dependent transcriptional response. *Mol. Biol. Cell* **29**, 3039–3051 (2018).

68. Mistriotis, P. *et al.* Confinement hinders motility by inducing RhoA-mediated nuclear influx, volume expansion, and blebbing. *J. Cell Biol.* **218**, 4093–4111 (2019).

69. Freedman, B. R. *et al.* Dynamic Loading and Tendon Healing Affect Multiscale Tendon Properties and ECM Stress Transmission. *Sci. Rep.* **8**, 1–13 (2018).

70. Provenzano, P. P. & Vanderby, R. Collagen fibril morphology and organization: Implications for force transmission in ligament and tendon. *Matrix Biol.* **25**, 71–84 (2006).

71. Järvinen, T. A. H., Józsa, L., Kannus, P., Järvinen, T. L. N. & Järvinen, M. Organization and distribution of intramuscular connective tissue in normal and immobilized skeletal muscles. An immunohistochemical, polarization and scanning electron microscopic study. *J. Muscle Res. Cell Motil.* **23**, 245–54 (2002).

72. Gillies, A. R. & Lieber, R. L. Structure and function of the skeletal muscle extracellular matrix. *Muscle and Nerve* **44**, 318–331 (2011).

73. Provenzano, P. P. *et al.* Collagen density promotes mammary tumor initiation and progression. *BMC Med.* **6**, 1–15 (2008).

74. Levental, K. R. *et al.* Matrix crosslinking forces tumor progression by enhancing integrin signaling. *Cell* **139**, 891–906 (2009).

75. Szulczewski, J. M. *et al.* Directional cues in the tumor microenvironment due to cell contraction against aligned collagen fibers. *Acta Biomater.* (2021) doi:10.1016/j.actbio.2021.04.053.

76. Starke, J., Maaser, K., Wehrle-Haller, B. & Friedl, P. Mechanotransduction of mesenchymal melanoma cell invasion into 3D collagen lattices: Filopod-mediated extension–relaxation cycles and force anisotropy. *Exp. Cell Res.* **319**, 2424–2433 (2013).

77. Doyle, A. D., Carvajal, N., Jin, A., Matsumoto, K. & Yamada, K. M. Local 3D matrix microenvironment regulates cell migration through spatiotemporal

dynamics of contractility-dependent adhesions. *Nat. Commun.* **6**, (2015).

78. Ushiki, T. Collagen fibers, reticular fibers and elastic fibers. A comprehensive understanding from a morphological viewpoint. *Arch. Histol. Cytol.* **65**, 109–126 (2002).

79. Fernández, M. *et al.* Small-angle x-ray scattering studies of human breast tissue samples. *Phys. Med. Biol.* **47**, 577–92 (2002).

80. Padhi, A. & Nain, A. S. ECM in Differentiation: A Review of Matrix Structure, Composition and Mechanical Properties. *Ann. Biomed. Eng.* **48**, (2020).

81. Keely, P. & Nain, A. Capturing relevant extracellular matrices for investigating cell migration. *F1000Research* **4**, (2015).

82. Wolf, K. *et al.* Physical limits of cell migration: Control by ECM space and nuclear deformation and tuning by proteolysis and traction force. *J. Cell Biol.* **201**, 1069–1084 (2013).

83. Friedl, P., Sahai, E., Weiss, S. & Yamada, K. M. New dimensions in cell migration. *Nat. Rev. Mol. Cell Biol.* **13**, 743–7 (2012).

84. Doyle, A. D., Wang, F. W., Matsumoto, K. & Yamada, K. M. One-dimensional topography underlies three-dimensional fi brillar cell migration. *J. Cell Biol.* **184**, 481–490 (2009).

85. Meehan, S. & Nain, A. S. Role of Suspended Fiber Structural Stiffness and Curvature on Single-Cell Migration, Nucleus Shape, and Focal-Adhesion-Cluster Length. *Biophys. J.* **107**, 2604–2611 (2014).

86. Koons, B. *et al.* Cancer Protrusions on a Tightrope: Nanofiber Curvature Contrast Quantitates Single Protrusion Dynamics. *ACS Nano* **11**, 12037–12048 (2017).

87. Mukherjee, A., Behkam, B. & Nain, A. S. Cancer Cells Sense Fibers by Coiling on them in a Curvature-Dependent Manner. *iScience* **19**, 905–915 (2019).

88. Singh, J., Pagulayan, A., Camley, B. A. & Nain, A. S. Rules of contact inhibition of locomotion for cells on suspended nanofibers. *Proc. Natl. Acad. Sci.* **118**, e2011815118 (2021).

89. Jana, A. *et al.* Crosshatch nanofiber networks of tunable interfiber spacing induce plasticity in cell migration and cytoskeletal response. *FASEB J.* **33**, 10618–10632 (2019).

90. Sheets, K., Wang, J., Zhao, W., Kapania, R. & Nain, A. S. Nanonet Force Microscopy for Measuring Cell Forces. *Biophys. J.* **111**, 197–207 (2016).

91. Sheets, K., Wunsch, S., Ng, C. & Nain, A. S. Shape-dependent cell migration and focal adhesion organization on suspended and aligned nanofiber scaffolds. *Acta Biomater.* **9**, 7169–77 (2013).

92. Nain, A. S., Sitti, M., Jacobson, A., Kowalewski, T. & Amon, C. Dry Spinning Based Spinneret Based Tunable Engineered Parameters (STEP) Technique for Controlled and Aligned Deposition of Polymeric Nanofibers. *Macromol. Rapid Commun.* **30**, 1406–1412 (2009).

93. Nain, A. S. & Wang, J. Polymeric nanofibers: Isodiametric design space and methodology for depositing aligned nanofiber arrays in single and multiple layers. *Polym. J.* **45**, 695–700 (2013).

94. Padhi, A. *et al.* Force-exerting perpendicular lateral protrusions in fibroblastic cell contraction. *Commun. Biol.* **3**, 1–11 (2020).

95. Graybill, P. M., Jana, A., Kapania, R. K., Nain, A. S. & Davalos, R. V. Single Cell

Forces after Electroporation. *ACS Nano* (2020) doi:10.1021/acsnano.0c07020.

96. Tu-Sekine, B. *et al.* Inositol polyphosphate multikinase is a metformin target that regulates cell migration. *FASEB J.* **33**, 14137–14146 (2019).

97. Wolfenson, H., Iskratsch, T. & Sheetz, M. P. Early events in cell spreading as a model for quantitative analysis of biomechanical events. *Biophysical Journal* vol. 107 2508–2514 (2014).

98. Li, Y. *et al.* Moving Cell Boundaries Drive Nuclear Shaping during Cell Spreading. *Biophys. J.* **109**, 670–686 (2015).

99. Katiyar, A. *et al.* Nuclear size changes caused by local motion of cell boundaries unfold the nuclear lamina and dilate chromatin and intranuclear bodies. *Soft Matter* **15**, 9310–9317 (2019).

100. Khatau, S. B. *et al.* A perinuclear actin cap regulates nuclear shape. *Proc. Natl. Acad. Sci. U. S. A.* **106**, 19017–22 (2009).

101. Ihalainen, T. O. *et al.* Differential basal-to-apical accessibility of lamin A/C epitopes in the nuclear lamina regulated by changes in cytoskeletal tension. *Nat. Mater.* **14**, 1252–1261 (2015).

102. Dupont, S. *et al.* Role of YAP/TAZ in mechanotransduction. *Nature* **474**, 179–184 (2011).

103. Kim, J. K. *et al.* Nuclear lamin A/C harnesses the perinuclear apical actin cables to protect nuclear morphology. *Nat. Commun.* **8**, 1–13 (2017).

104. Stephens, A. D., Banigan, E. J. & Marko, J. F. Chromatin's physical properties shape the nucleus and its functions. *Current Opinion in Cell Biology* vol. 58 76–84 (2019).

105. Buxboim, A. *et al.* Coordinated increase of nuclear tension and lamin-A with matrix stiffness outcompetes lamin-B receptor that favors soft tissue phenotypes. *Mol. Biol. Cell* **28**, 3333–3348 (2017).

106. Friedl, P. & Wolf, K. Plasticity of cell migration: A multiscale tuning model. *Journal of Cell Biology* vol. 188 11–19 (2010).

107. Doyle, A. D., Wang, F. W., Matsumoto, K. & Yamada, K. M. One-dimensional topography underlies three-dimensional fibrillar cell migration. *J. Cell Biol.* **184**, 481–90 (2009).

108. Carey, S. P., Kraning-Rush, C. M., Williams, R. M. & Reinhart-King, C. a. Biophysical control of invasive tumor cell behavior by extracellular matrix microarchitecture. *Biomaterials* **33**, 4157–65 (2012).

109. Reinhart-King, C. A., Dembo, M. & Hammer, D. A. The dynamics and mechanics of endothelial cell spreading. *Biophys. J.* **89**, 676–689 (2005).

110. Théry, M., Pépin, A., Dressaire, E., Chen, Y. & Bornens, M. Cell distribution of stress fibres in response to the geometry of the adhesive environment. *Cell Motil. Cytoskeleton* **63**, 341–355 (2006).

111. Cukierman, E., Pankov, R., Stevens, D. R. & Yamada, K. M. Taking Cell-Matrix Adhesions to the Third Dimension. *Science (80-.).* **294**, 1708–1712 (2001).

112. Hakkinen, K. M., Harunaga, J. S., Doyle, A. D. & Yamada, K. M. Direct comparisons of the morphology, migration, cell adhesions, and actin cytoskeleton of fibroblasts in four different three-dimensional extracellular matrices. *Tissue Eng. Part A* **17**, 713–24 (2011).

113. Balaban, N. Q. *et al.* Force and focal adhesion assembly: a close relationship

studied using elastic micropatterned substrates. *Nat. Cell Biol.* **3**, 466–72 (2001).

114. Versaevel, M., Grevesse, T. & Gabriele, S. Spatial coordination between cell and nuclear shape within micropatterned endothelial cells. *Nat. Commun.* **3**, 671 (2012).

115. Sugita, S., Adachi, T., Ueki, Y. & Sato, M. A novel method for measuring tension generated in stress fibers by applying external forces. *Biophys. J.* **101**, 53–60 (2011).

116. Katoh, K., Kano, Y., Masuda, M., Onishi, H. & Fujiwara, K. Isolation and Contraction of the Stress Fiber. *Mol. Biol. Cell* **9**, 1919–1938 (1998).

117. Lovett, D. B., Shekhar, N., Nickerson, J. A., Roux, K. J. & Lele, T. P. Modulation of nuclear shape by substrate rigidity. *Cell. Mol. Bioeng.* **6**, 230–238 (2013).

118. Sen, B. *et al.* Intranuclear Actin Structure Modulates Mesenchymal Stem Cell Differentiation. *Stem Cells* **35**, 1624–1635 (2017).

119. Davidson, P. M., Özçelik, H., Hasirci, V., Reiter, G. & Anselme, K. Microstructured surfaces cause severe but non-detrimental deformation of the cell nucleus. *Adv. Mater.* **21**, 3586–3590 (2009).

120. Badique, F. *et al.* Directing nuclear deformation on micropillared surfaces by substrate geometry and cytoskeleton organization. *Biomaterials* **34**, 2991–3001 (2013).

121. Denais, C. M. *et al.* Nuclear envelope rupture and repair during cancer cell migration. *Science (80-.).* **352**, 353–358 (2016).

122. Lohela, M. & Werb, Z. Intravital imaging of stromal cell dynamics in tumors. *Curr. Opin. Genet. Dev.* **20**, 72–78 (2010).

123. Andresen, V. *et al.* Infrared multiphoton microscopy: subcellular-resolved deep tissue imaging. *Curr. Opin. Biotechnol.* **20**, 54–62 (2009).

124. Han, W. *et al.* Oriented collagen fibers direct tumor cell intravasation. *Proc. Natl. Acad. Sci. U. S. A.* **113**, 11208–11213 (2016).

125. Paul, C. D., Mistriotis, P. & Konstantopoulos, K. Cancer cell motility: lessons from migration in confined spaces. *Nat. Rev. Cancer* **17**, 131–140 (2016).

126. Gilkes, D. M., Semenza, G. L. & Wirtz, D. Hypoxia and the extracellular matrix: drivers of tumour metastasis. *Nat. Rev. Cancer* **14**, 430–9 (2014).

127. Starke, J., Wehrle-Haller, B. & Friedl, P. Plasticity of the actin cytoskeleton in response to extracellular matrix nanostructure and dimensionality. *Biochem. Soc. Trans.* **42**, 1356–1366 (2014).

128. Clark, A. G. & Vignjevic, D. M. Modes of cancer cell invasion and the role of the microenvironment. *Current Opinion in Cell Biology* vol. 36 13–22 (2015).

129. Pickup, M. W., Mouw, J. K. & Weaver, V. M. The extracellular matrix modulates the hallmarks of cancer. *EMBO Rep.* **15**, 1243–1253 (2014).

130. Lambert, A. W., Pattabiraman, D. R. & Weinberg, R. A. Emerging Biological Principles of Metastasis. *Cell* **168**, 670–691 (2017).

131. Liliensiek, S. J., Nealey, P. & Murphy, C. J. Characterization of endothelial basement membrane nanotopography in rhesus macaque as a guide for vessel tissue engineering. *Tissue Eng. Part A* **15**, 2643–51 (2009).

132. Glentis, A. *et al.* Cancer-associated fibroblasts induce metalloprotease-independent cancer cell invasion of the basement membrane. *Nat. Commun.* **8**, 1–13 (2017).

133. Kim, D. H., Provenzano, P. P., Smith, C. L. & Levchenko, A. Matrix

nanotopography as a regulator of cell function. *J. Cell Biol.* **197**, 351–360 (2012).

134. Wolf, K. *et al.* Collagen-based cell migration models in vitro and in vivo. *Semin. Cell Dev. Biol.* **20**, 931–941 (2009).

135. Wu, P.-H., Giri, A. & Wirtz, D. Statistical analysis of cell migration in 3D using the anisotropic persistent random walk model. *Nat. Protoc.* **10**, 517–27 (2015).

136. Stokes, C. L., Lauffenburger, D. a & Williams, S. K. Migration of individual microvessel endothelial cells: stochastic model and parameter measurement. *J Cell Sci* **99 (Pt 2)**, 419–30 (1991).

137. Biela, S. A., Su, Y., Spatz, J. P. & Kemkemer, R. Different sensitivity of human endothelial cells, smooth muscle cells and fibroblasts to topography in the nano-micro range. *Acta Biomater.* **5**, 2460–6 (2009).

138. Li, S. *et al.* Effects of morphological patterning on endothelial cell migration. **38**, 101–108 (2001).

139. Ko, Y., Co, C. C. & Ho, C. Biomaterials Directing cell migration in continuous microchannels by topographical ampli fi cation of natural directional persistence. *Biomaterials* **34**, 353–360 (2013).

140. Pathak, A. & Kumar, S. Independent regulation of tumor cell migration by matrix stiffness and confinement. *Proc. Natl. Acad. Sci. U. S. A.* **2012**, (2012).

141. Irimia, D. & Toner, M. Quantitative biosciences from nano to macro Spontaneous migration of cancer cells under conditions of mechanical confinement w. **1**, (2009).

142. Dalton, B. A. *et al.* Modulation of epithelial tissue and cell migration by microgrooves. *J. Biomed. Mater. Res.* **56**, 195–207 (2001).

143. Kaiser, J.-P., Reinmann, A. & Bruinink, A. The effect of topographic characteristics on cell migration velocity. *Biomaterials* **27**, 5230–41 (2006).

144. Riching, K. M. *et al.* 3D Collagen Alignment Limits Protrusions to Enhance Breast Cancer Cell Persistence. *Biophys. J.* **107**, 2546–58 (2014).

145. Fraley, S. I. *et al.* Three-dimensional matrix fiber alignment modulates cell migration and MT1-MMP utility by spatially and temporally directing protrusions. *Sci. Rep.* **5**, 14580 (2015).

146. Dickinson, R. B., Guido, S. & Tranquillo, R. T. Biased cell migration of fibroblasts exhibiting contact guidance in oriented collagen gels. *Ann. Biomed. Eng.* **22**, 342–56.

147. Bredfeldt, J. S. *et al.* Computational segmentation of collagen fibers from second-harmonic generation images of breast cancer. *J. Biomed. Opt.* **19**, 016007 (2014).

148. Taylor, E. N., Hoffman, M. P., Aninwene, G. E. & Gilbert, R. J. Patterns of Intersecting Fiber Arrays Revealed in Whole Muscle with Generalized Q-Space Imaging. *Biophys. J.* **108**, 2740–2749 (2015).

149. Petrie, R. J., Doyle, A. D. & Yamada, K. M. Random versus directionally persistent cell migration. *Nat. Rev. Mol. Cell Biol.* **10**, 538–49 (2009).

150. Friedl, P. & Wolf, K. Proteolytic interstitial cell migration: a five-step process. *Cancer Metastasis Rev.* **28**, 129–35 (2009).

151. Condeelis, J. & Segall, J. E. Intravital imaging of cell movement in tumours. *Nat. Rev. Cancer* **3**, 921–30 (2003).

152. Sharma, P., Sheets, K., Elankumaran, S. & Nain, A. S. The mechanistic influence of aligned nanofibers on cell shape, migration and blebbing dynamics of glioma

cells. *Integr. Biol. (Camb).* **5**, (2013).

153. Ushiki, T. Collagen fibers, reticular fibers and elastic fibers. A comprehensive understanding from a morphological viewpoint. *Archives of Histology and Cytology* vol. 65 109–126 (2002).

154. McClendon, M. T. & Stupp, S. I. Tubular hydrogels of circumferentially aligned nanofibers to encapsulate and orient vascular cells. *Biomaterials* **33**, 5713–5722 (2012).

155. Nain, A. S. *et al.* Control of cell behavior by aligned micro/nanofibrous biomaterial scaffolds fabricated by spinneret-based tunable engineered parameters (STEP) technique. *Small* **4**, (2008).

156. Koons, B. *et al.* Cancer Protrusions on a Tightrope – Nanofiber Curvature Platform Reveals Protrusion Dynamics Independent of Cell Migration. **Manuscript**, 1–19 (2016).

157. Sharma, P. *et al.* Aligned fibers direct collective cell migration to engineer closing and nonclosing wound gaps. *Mol. Biol. Cell* **28**, 2579–2588 (2017).

158. Jolly, L. A. *et al.* Fibroblast-Mediated Collagen Remodeling Within the Tumor Microenvironment Facilitates Progression of Thyroid Cancers Driven by Braf ^{V600E} and Pten Loss. *Cancer Res.* **76**, 1804–1813 (2016).

159. Wang, J. & Nain, A. S. Suspended Micro/Nanofiber Hierarchical Biological Scaffolds Fabricated using Non-Electrospinning STEP Technique. *Langmuir* **30**, 13641–13649 (2014).

160. Sheets, K., Wang, J., Zhao, W., Kapania, R. & Nain, A. S. Nanonet Force Microscopy for Measuring Cell Forces. *Biophys. J.* **111**, 197–207 (2016).

161. Phillippi, J. A. *et al.* Basal and oxidative stress-induced expression of metallothionein is decreased in ascending aortic aneurysms of bicuspid aortic valve patients. *Circulation* **119**, 2498–506 (2009).

162. Wu, P.-H., Giri, A., Sun, S. X. & Wirtz, D. Three-dimensional cell migration does not follow a random walk. *Proc. Natl. Acad. Sci.* **111**, 3949–3954 (2014).

163. Nookaew, I. *et al.* A comprehensive comparison of RNA-Seq-based transcriptome analysis from reads to differential gene expression and cross-comparison with microarrays: a case study in Saccharomyces cerevisiae. *Nucleic Acids Res.* **40**, 10084–10097 (2012).

164. Love, M. I., Huber, W. & Anders, S. Moderated estimation of fold change and dispersion for RNA-seq data with DESeq2. *Genome Biol.* **15**, 550 (2014).

165. Väremo, L., Nielsen, J. & Nookaew, I. Enriching the gene set analysis of genome-wide data by incorporating directionality of gene expression and combining statistical hypotheses and methods. *Nucleic Acids Res.* **41**, 4378–4391 (2013).

166. Kim, D. H. & Wirtz, D. Focal adhesion size uniquely predicts cell migration. *FASEB J.* **27**, 1351–1361 (2013).

167. Théry, M. Micropatterning as a tool to decipher cell morphogenesis and functions. *J. Cell Sci.* **123**, 4201–13 (2010).

168. Versaevel, M., Grevesse, T. & Gabriele, S. Spatial coordination between cell and nuclear shape within micropatterned endothelial cells. *Nat. Commun.* **3**, 671 (2012).

169. Bischofs, I. B., Klein, F., Lehnert, D., Bastmeyer, M. & Schwarz, U. S. Filamentous Network Mechanics and Active Contractility Determine Cell and

Tissue Shape. doi:10.1529/biophysj.108.134296.

170. Kim, D.-H. *et al.* Mechanosensitivity of fibroblast cell shape and movement to anisotropic substratum topography gradients. *Biomaterials* **30**, 5433–44 (2009).

171. Chen, W.-T. Mechanism of the trailing edge during fibroblast movement. *J.Cell Biol.* **90**, 187–200 (1981).

172. http://doi.org/10.1242/jcs.144345-Hwee Kim, DongKim, D.-H., Cho, S., & Wirtz, D. (n. d.). T. coupling between nucleus, cell migration through the perinuclear actin cap. Journal of Cell Science., Cho, S. & Wirtz, D. Tight coupling between nucleus and cell migration through the perinuclear actin cap. *J. Cell Sci.* **127**, 2528–2541 (2014).

173. Nisenholz, N. *et al.* Active mechanics and dynamics of cell spreading on elastic substrates. *Soft Matter* **10**, 7234–7246 (2014).

174. Cuvelier, D. *et al.* The universal dynamics of cell spreading. *Curr. Biol.* **17**, 694–699 (2007).

175. Mukherjee, R. N., Chen, P. & Levy, D. L. Recent advances in understanding nuclear size and shape. *Nucleus* **7**, 167–186 (2016).

176. Woringer, M., Darzacq, X. & Izeddin, I. Geometry of the nucleus: a perspective on gene expression regulation. *Curr. Opin. Chem. Biol.* **20**, 112–119 (2014).

177. Zink, D., Fische, A. H. & Nickerson, J. A. Nuclear structure in cancer cells. *Nat. Rev. Cancer* **4**, 677–687 (2004).

178. Charras, G. & Sahai, E. Physical influences of the extracellular environment on cell migration. *Nat. Rev. Mol. Cell Biol.* **15**, 813–824 (2014).

179. Hung, W.-C. *et al.* Distinct signaling mechanisms regulate migration in unconfined

versus confined spaces. *J. Cell Biol.* **202**, 807–24 (2013).

180. Kim, D.-H. *et al.* Guided Cell Migration on Microtextured Substrates with Variable Local Density and Anisotropy. *Adv. Funct. Mater.* **19**, 1579–1586 (2009).

181. Park, J., Kim, D.-H. & Levchenko, A. Topotaxis: A New Mechanism of Directed Cell Migration in Topographic ECM Gradients. *Biophys. J.* **114**, 1257–1263 (2018).

182. Kutys, M. L. & Yamada, K. M. An extracellular-matrix-specific GEF-GAP interaction regulates Rho GTPase crosstalk for 3D collagen migration. *Nat. Cell Biol.* **16**, 909–17 (2014).

183. Chen, B., Kumar, G., Co, C. C. & Ho, C.-C. Geometric Control of Cell Migration. *Sci. Rep.* **3**, 2827 (2013).

184. Aubin, H. *et al.* Directed 3D cell alignment and elongation in microengineered hydrogels. *Biomaterials* **31**, 6941–6951 (2010).

185. Xu, W. *et al.* Cell Stiffness Is a Biomarker of the Metastatic Potential of Ovarian Cancer Cells. *PLoS One* **7**, (2012).

186. Swaminathan, V. *et al.* Mechanical stiffness grades metastatic potential in patient tumor cells and in cancer cell lines. *Cancer Res.* **71**, 5075–80 (2011).

187. Netti, P. A., Berk, D. A., Swartz, M. A., Grodzinsky, A. J. & Jain, R. K. Role of extracellular matrix assembly in interstitial transport in solid tumors. *Cancer Res.* **60**, 2497–503 (2000).

188. Grantab, R., Sivananthan, S. & Tannock, I. F. The Penetration of Anticancer Drugs through Tumor Tissue as a Function of Cellular Adhesion and Packing Density of Tumor Cells. *Cancer Res.* **66**, 1033–1039 (2006).

189. Hall, A. *et al.* Nanonet force microscopy for measuring forces in single smooth muscle cells of the human aorta. *Mol. Biol. Cell* **28**, 1894–1900 (2017).

190. Scholey, J. M., Brust-Mascher, I. & Mogilner, A. Cell division. *Nature* **422**, 746–752 (2003).

191. Théry, M. *et al.* The extracellular matrix guides the orientation of the cell division axis. *Nat. Cell Biol.* **7**, 947–953 (2005).

192. Zaidel-Bar, R. Atypical matrix adhesions guide cell division. *Nat. Cell Biol.* **20**, 1233–1235 (2018).

193. Lancaster, O. M. & Baum, B. Shaping up to divide: Coordinating actin and microtubule cytoskeletal remodelling during mitosis. *Semin. Cell Dev. Biol.* **34**, 109–115 (2014).

194. Petridou, N. I. & Skourides, P. A. FAK transduces extracellular forces that orient the mitotic spindle and control tissue morphogenesis. *Nat. Commun.* **5**, 5240 (2014).

195. Fink, J. *et al.* External forces control mitotic spindle positioning. *Nat. Cell Biol.* **13**, 771–8 (2011).

196. Fern, M. & Keyril, J. Small-angle x-ray scattering studies of human breast tissue samples. **47**, 577–592 (2002).

197. Doyle, A. D., Carvajal, N., Jin, A., Matsumoto, K. & Yamada, K. M. Local 3D matrix microenvironment regulates cell migration through spatiotemporal dynamics of contractility-dependent adhesions. *Nat. Commun.* **6**, 1–15 (2015).

198. Cukierman, E. Taking Cell-Matrix Adhesions to the Third Dimension. *Science (80-.).* **294**, 1708–1712 (2001).

199. Lancaster, O. M. *et al.* Mitotic Rounding Alters Cell Geometry to Ensure Efficient Bipolar Spindle Formation. *Dev. Cell* **25**, 270–283 (2013).

200. He, L. *et al.* Local 3D matrix confinement determines division axis through cell shape. *Oncotarget* **7**, 6994–7011 (2016).

201. Haydar, T. F., Ang, E. & Rakic, P. Mitotic spindle rotation and mode of cell division in the developing telencephalon. *Proc. Natl. Acad. Sci. U. S. A.* **100**, 2890–2895 (2003).

202. Stewart, M. P. *et al.* Hydrostatic pressure and the actomyosin cortex drive mitotic cell rounding. *Nature* **469**, 226–230 (2011).

203. Théry, M., Jiménez-Dalmaroni, A., Racine, V., Bornens, M. & Jülicher, F. Experimental and theoretical study of mitotic spindle orientation. *Nature* **447**, 493–496 (2007).

204. Sorce, B. *et al.* Mitotic cells contract actomyosin cortex and generate pressure to round against or escape epithelial confinement. *Nat. Commun.* **6**, (2015).

205. Vassilev, L. T. Cell cycle synchronization at the G2/M phase border by reversible inhibition of CDK1. *Cell Cycle* **5**, 2555–2556 (2006).

206. Broad, A. J., DeLuca, K. F. & DeLuca, J. G. Aurora B kinase is recruited to multiple discrete kinetochore and centromere regions in human cells. *J. Cell Biol.* **219**, (2020).

207. Tauchman, E. C., Boehm, F. J. & DeLuca, J. G. Stable kinetochore-microtubule attachment is sufficient to silence the spindle assembly checkpoint in human cells. *Nat. Commun.* **6**, 1–9 (2015).

208. Baudoin, N. C. & Cimini, D. A guide to classifying mitotic stages and mitotic

defects in fixed cells. *Chromosoma* **127**, 215–227 (2018).

209. Lock, J. G. *et al.* Reticular adhesions are a distinct class of cell-matrix adhesions that mediate attachment during mitosis. *Nat. Cell Biol.* **20**, 1290–1302 (2018).

210. Matthews, H. K. *et al.* Oncogenic Signaling Alters Cell Shape and Mechanics to Facilitate Cell Division under Confinement. *Dev. Cell* **52**, 563-573.e3 (2020).

211. Cadart, C., Zlotek-Zlotkiewicz, E., Le Berre, M., Piel, M. & Matthews, H. K. Exploring the function of cell shape and size during mitosis. *Dev. Cell* **29**, 159–169 (2014).

212. Chugh, P. *et al.* Actin cortex architecture regulates cell surface tension. *Nat. Cell Biol.* **19**, 689–697 (2017).

213. Desmaison, A. *et al.* Impact of physical confinement on nuclei geometry and cell division dynamics in 3D spheroids. *Sci. Rep.* **8**, 1–8 (2018).

214. Tse, H. T. K., Weaver, W. M. C. & Carlo, D. Increased asymmetric and multi-daughter cell division in mechanically confined microenvironments. *PLoS One* **7**, 1–8 (2012).

215. Cattin, C. J. *et al.* Mechanical control of mitotic progression in single animal cells. *Proc. Natl. Acad. Sci. U. S. A.* **112**, 11258–11263 (2015).

216. Cattin, C. J. *et al.* Mechanical control of mitotic progression in single animal cells. *Proc. Natl. Acad. Sci. U. S. A.* **112**, 1502029112- (2015).

217. Nam, S. & Chaudhuri, O. Mitotic cells generate protrusive extracellular forces to divide in three-dimensional microenvironments. *Nat. Phys.* **14**, 621–628 (2018).

218. Weaver, J. C. & Chizmadzhev, Y. A. Theory of electroporation: a review. *Bioelectrochemistry Bioenerg.* **41**, 135–160 (1996).

219. Kotnik, T., Rems, L., Tarek, M. & Miklavcic, D. Membrane Electroporation and Electropermeabilization: Mechanisms and Models. *Annu Rev Biophys* **48**, 63–91 (2019).

220. Potter, H. & Heller, R. Transfection by Electroporation. *Curr Protoc Mol Biol* **121**, 9 3 1-9 3 13 (2018).

221. Hu, N., Yang, J., Joo, S. W., Banerjee, A. N. & Qian, S. Cell electrofusion in microfluidic devices: A review. *Sensors Actuators B Chem.* **178**, 63–85 (2013).

222. Mali, B., Jarm, T., Snoj, M., Sersa, G. & Miklavcic, D. Antitumor effectiveness of electrochemotherapy: a systematic review and meta-analysis. *Eur J Surg Oncol* **39**, 4–16 (2013).

223. Davalos, R. V, Mir, I. L. & Rubinsky, B. Tissue ablation with irreversible electroporation. *Ann Biomed Eng* **33**, 223–231 (2005).

224. Scheffer, H. J. *et al.* Irreversible electroporation for nonthermal tumor ablation in the clinical setting: a systematic review of safety and efficacy. *J Vasc Interv Radiol* **25**, 997–1011; quiz 1011 (2014).

225. Geboers, B. *et al.* High-Voltage Electrical Pulses in Oncology: Irreversible Electroporation, Electrochemotherapy, Gene Electrotransfer, Electrofusion, and Electroimmunotherapy. *Radiology* **295**, 254–272 (2020).

226. Tsong, T. Y. Electroporation of cell membranes. in *Electroporation and Electrofusion in Cell Biology* 149–163 (Springer, 1989).

227. Rols, M. P. & Teissie, J. Electropermeabilization of mammalian cells. Quantitative analysis of the phenomenon. *Biophys J* **58**, 1089–1098 (1990).

228. Saulis, G., Venslauskas, M. S. & Naktinis, J. Kinetics of pore resealing in cell

membranes after electroporation. *J. Electroanal. Chem. Interfacial Electrochem.* **321**, 1–13 (1991).

229. Pavlin, M. & Miklavcic, D. Theoretical and experimental analysis of conductivity, ion diffusion and molecular transport during cell electroporation--relation between short-lived and long-lived pores. *Bioelectrochemistry* **74**, 38–46 (2008).

230. Teissie, J. Membrane Permeabilization Lifetime in Experiments. in *Handbook of Electroporation* 61–75 (Springer, 2017).

231. Weaver, J. C. & Vernier, P. T. Pore lifetimes in cell electroporation: Complex dark pores? *arXiv Prepr. arXiv1708.07478* (2017).

232. Berghofer, T. *et al.* Nanosecond electric pulses trigger actin responses in plant cells. *Biochem Biophys Res Commun* **387**, 590–595 (2009).

233. Hohenberger, P. *et al.* Plant actin controls membrane permeability. *Biochim Biophys Acta* **1808**, 2304–2312 (2011).

234. Harkin, D. G. & Hay, E. D. Effects of electroporation on the tubulin cytoskeleton and directed migration of corneal fibroblasts cultured within collagen matrices. *Cell Motil. Cytoskeleton* **35**, 345–357 (1996).

235. Kanthou, C. *et al.* The endothelial cytoskeleton as a target of electroporation-based therapies. *Mol Cancer Ther* **5**, 3145–3152 (2006).

236. Teissie, J. & Rols, M. P. Manipulation of cell cytoskeleton affects the lifetime of cell membrane electropermeabilization. *Ann N Y Acad Sci* **720**, 98–110 (1994).

237. Thompson, G. L., Roth, C., Tolstykh, G., Kuipers, M. & Ibey, B. L. Role of Cytoskeleton and Elastic Moduli in Cellular Response to Nanosecond Pulsed Electric Fields. in *Terahertz and Ultrashort Electromagnetic Pulses for*

Biomedical Applications (eds. Wilmink, G. J. & Ibey, B. L.) vol. 8585 (2013).

238. Louise, C., Etienne, D. & Marie-Pierre, R. AFM sensing cortical actin cytoskeleton destabilization during plasma membrane electropermeabilization. *Cytoskelet.* **71**, 587–594 (2014).

239. Pehlivanova, V. N., Tsoneva, I. H. & Tzoneva, R. D. Multiple effects of electroporation on the adhesive behaviour of breast cancer cells and fibroblasts. *Cancer Cell Int* **12**, 9 (2012).

240. Perrier, D. L. *et al.* Response of an actin network in vesicles under electric pulses. *Sci Rep* **9**, 8151 (2019).

241. Meulenberg, C. J. W., Todorovic, V. & Cemazar, M. Differential Cellular Effects of Electroporation and Electrochemotherapy in Monolayers of Human Microvascular Endothelial Cells. *PLoS One* **7**, 1–9 (2012).

242. Čemažar, M. Effects of Electroporation of Mammalian Cells on Cytoskeleton and Intercellular Connections. *Handb. Electroporation* 307–321 (2017).

243. Graybill, P. M. & Davalos, R. V. Cytoskeletal Disruption after Electroporation and Its Significance to Pulsed Electric Field Therapies. *Cancers (Basel)* **12**, 1132 (2020).

244. Pakhomov, A. G. *et al.* Disassembly of actin structures by nanosecond pulsed electric field is a downstream effect of cell swelling. *Bioelectrochemistry* **100**, 88–95 (2014).

245. Thompson, G. L., Roth, C., Tolstykh, G., Kuipers, M. & Ibey, B. L. Disruption of the actin cortex contributes to susceptibility of mammalian cells to nanosecond pulsed electric fields. *Bioelectromagnetics* **35**, 262–272 (2014).

246. Stacey, M., Fox, P., Buescher, S. & Kolb, J. Nanosecond pulsed electric field induced cytoskeleton, nuclear membrane and telomere damage adversely impact cell survival. *Bioelectrochemistry* **82**, 131–134 (2011).

247. Rols, M. P. & Teissie, J. Experimental evidence for the involvement of the cytoskeleton in mammalian cell electropermeabilization. *Biochim Biophys Acta* **1111**, 45–50 (1992).

248. Goswami, I. *et al.* Influence of Pulsed Electric Fields and Mitochondria-Cytoskeleton Interactions on Cell Respiration. *Biophys J* **114**, 2951–2964 (2018).

249. Xiao, D. *et al.* Effect of actin cytoskeleton disruption on electric pulse-induced apoptosis and electroporation in tumour cells. *Cell Biol Int* **35**, 99–104 (2011).

250. Steuer, A., Wende, K., Babica, P. & Kolb, J. F. Elasticity and tumorigenic characteristics of cells in a monolayer after nanosecond pulsed electric field exposure. *Eur Biophys J* **46**, 567–580 (2017).

251. Carr, L. *et al.* Calcium-independent disruption of microtubule dynamics by nanosecond pulsed electric fields in U87 human glioblastoma cells. *Sci Rep* **7**, 41267 (2017).

252. Mussauer, H., Sukhorukov, V. L., Haase, A. & Zimmermann, U. Resistivity of red blood cells against high-intensity, short-duration electric field pulses induced by chelating agents. *J Membr Biol* **170**, 121–133 (1999).

253. Neamtu, S., Morariu, V. V, Turcu, I., Popescu, A. H. & Copaescu, L. I. Pore resealing inactivation in electroporated erythrocyte membrane irradiated with electrons. *Bioelectrochem Bioenerg* **48**, 441–445 (1999).

254. Chopinet, L., Roduit, C., Rols, M. P. & Dague, E. Destabilization induced by

electropermeabilization analyzed by atomic force microscopy. *Biochim Biophys Acta* **1828**, 2223–2229 (2013).

255. Padhi, A. *et al.* Bioenergetics underlying single-cell migration on aligned nanofiber scaffolds. *Am J Physiol Cell Physiol* **318**, C476–C485 (2020).

256. Sundin, L. J. R., Guimaraes, G. J. & DeLuca, J. G. The NDC80 complex proteins Nuf2 and Hec1 make distinct contributions to kinetochore–microtubule attachment in mitosis. *Mol. Biol. Cell* **22**, 759–768 (2011).

257. Jolly, L. A. *et al.* Fibroblast-Mediated Collagen Remodeling Within the Tumor Microenvironment Facilitates Progression of Thyroid Cancers Driven by BrafV600E and Pten Loss. *Cancer Res.* **76**, (2016).

258. Bird, S. D. Calcium mediates cell shape change in human peritoneal mesothelial cells. *Cell Calcium* **72**, 116–126 (2018).

259. Mermelstein, C. S., Rebello, M. I., Amaral, L. M. & Costa, M. L. Changes in cell shape, cytoskeletal proteins and adhesion sites of cultured cells after extracellular Ca2+ chelation. *Braz J Med Biol Res* **36**, 1111–1116 (2003).

260. Sweeney, D. C. *et al.* Quantification of cell membrane permeability induced by monopolar and high-frequency bipolar bursts of electrical pulses. *Biochim Biophys Acta* **1858**, 2689–2698 (2016).

261. Schaub, S., Bohnet, S., Laurent, V. M., Meister, J. J. & Verkhovsky, A. B. Comparative maps of motion and assembly of filamentous actin and myosin II in migrating cells. *Mol Biol Cell* **18**, 3723–3732 (2007).

262. Pucihar, G., Kotnik, T., Valic, B. & Miklavcic, D. Numerical determination of transmembrane voltage induced on irregularly shaped cells. *Ann Biomed Eng* **34**,

642–652 (2006).

263. Suspended micro/nanofiber hierarchical biological scaffolds fabricated using non-electrospinning STEP technique.Wang, J. & Nain, A. S. Suspended micro/nanofiber hierarchical biological scaffolds fabricated using non-electrospinning STEP technique. *Langmuir* **30**, 13641–9 (2014).

264. Jana, A. *et al.* Crosshatch nanofiber networks of tunable interfiber spacing induce plasticity in cell migration and cytoskeletal response. *FASEB J.* **33**, 10618–10632 (2019).

265. Sheets, K., Wunsch, S., Ng, C. & Nain, A. S. Shape-dependent cell migration and focal adhesion organization on suspended and aligned nanofiber scaffolds. *Acta Biomater.* **9**, (2013).

266. Giannone, G. *et al.* Calcium rises locally trigger focal adhesion disassembly and enhance residency of focal adhesion kinase at focal adhesions. *J. Biol. Chem.* **279**, 28715–28723 (2004).

267. Gissel, H., Lee, R. C. & Gehl, J. Electroporation and cellular physiology. in *Clinical aspects of electroporation* 9–17 (Springer, 2011).

268. Sharma, P., Sheets, K., Elankumaran, S. & Nain, A. S. The mechanistic influence of aligned nanofibers on cell shape, migration and blebbing dynamics of glioma cells. *Integr. Biol. (Camb).* **5**, 1036–44 (2013).

269. Frandsen, S. K. *et al.* Direct therapeutic applications of calcium electroporation to effectively induce tumor necrosis. *Cancer Res* **72**, 1336–1341 (2012).

270. Conklin, M. W., Lin, M. S. & Spitzer, N. C. Local calcium transients contribute to disappearance of pFAK, focal complex removal and deadhesion of neuronal

growth cones and fibroblasts. *Dev Biol* **287**, 201–212 (2005).

271. D'Souza, R. S. *et al.* Calcium-stimulated disassembly of focal adhesions mediated by an ORP3/IQSec1 complex. *Elife* **9**, e54113 (2020).

272. Giannone, G., Ronde, P., Gaire, M., Haiech, J. & Takeda, K. Calcium oscillations trigger focal adhesion disassembly in human U87 astrocytoma cells. *J Biol Chem* **277**, 26364–26371 (2002).

273. Nesin, O. M., Pakhomova, O. N., Xiao, S. & Pakhomov, A. G. Manipulation of cell volume and membrane pore comparison following single cell permeabilization with 60- and 600-ns electric pulses. *Biochim Biophys Acta* **1808**, 792–801 (2011).

274. Ušaj, M., Trontelj, K., Hudej, R., Kandušer, M. & Miklavčič, D. Cell size dynamics and viability of cells exposed to hypotonic treatment and electroporation for electrofusion optimization. *Radiol. Oncol.* **43**, 108–119 (2009).

275. Steuer, A., Schmidt, A., Laboha, P., Babica, P. & Kolb, J. F. Transient suppression of gap junctional intercellular communication after exposure to 100-nanosecond pulsed electric fields. *Bioelectrochemistry* **112**, 33–46 (2016).

276. Kanduser, M., Sentjurc, M. & Miklavcic, D. Cell membrane fluidity related to electroporation and resealing. *Eur Biophys J* **35**, 196–204 (2006).

277. Saulis, G. Pore disappearance in a cell after electroporation: theoretical simulation and comparison with experiments. *Biophys J* **73**, 1299–1309 (1997).

278. Kotnik, T., Pucihar, G. & Miklavcic, D. Induced transmembrane voltage and its correlation with electroporation-mediated molecular transport. *J Membr Biol* **236**, 3–13 (2010).

279. Hibino, M., Itoh, H. & Kinosita Jr, K. Time courses of cell electroporation as

revealed by submicrosecond imaging of transmembrane potential. *Biophys. J.* **64**, 1789–1800 (1993).

280. Maswiwat, K., Wachner, D. & Gimsa, J. Effects of cell orientation and electric field frequency on the transmembrane potential induced in ellipsoidal cells. *Bioelectrochemistry* **74**, 130–141 (2008).

281. Teissie, J. & Rols, M. P. An experimental evaluation of the critical potential difference inducing cell membrane electropermeabilization. *Biophys J* **65**, 409–413 (1993).

282. Towhidi, L. *et al.* Variability of the minimal transmembrane voltage resulting in detectable membrane electroporation. *Electromagn Biol Med* **27**, 372–385 (2008).

283. Sozer, E. B., Pocetti, C. F. & Vernier, P. T. Asymmetric Patterns of Small Molecule Transport After Nanosecond and Microsecond Electropermeabilization. *J Membr Biol* **251**, 197–210 (2018).

284. Tekle, E., Astumian, R. D. & Chock, P. B. Selective and asymmetric molecular transport across electroporated cell membranes. *Proc Natl Acad Sci U S A* **91**, 11512–11516 (1994).

285. Pucihar, G., Miklavcic, D. & Kotnik, T. A time-dependent numerical model of transmembrane voltage inducement and electroporation of irregularly shaped cells. *IEEE Trans Biomed Eng* **56**, 1491–1501 (2009).

286. Rems, L. *et al.* Cell electrofusion using nanosecond electric pulses. *Sci. Rep.* **3**, 3382 (2013).

287. Krassowska, W. & Filev, P. D. Modeling electroporation in a single cell. *Biophys J* **92**, 404–417 (2007).

288. Sweeney, D. C., Weaver, J. C. & Davalos, R. V. Characterization of cell membrane permeability in vitro part I: Transport behavior induced by single-pulse electric fields. *Technol. Cancer Res. Treat.* **17**, 1–15 (2018).

289. Yu, M. & Lin, H. Modeling transport across the electroporated membrane. in *Handbook of Electroporation* 1089–1110 (Springer International Publishing, 2017).

290. Charras, G. T., Hu, C. K., Coughlin, M. & Mitchison, T. J. Reassembly of contractile actin cortex in cell blebs. *J Cell Biol* **175**, 477–490 (2006).

291. Chikina, A. S., Svitkina, T. M. & Alexandrova, A. Y. Time-resolved ultrastructure of the cortical actin cytoskeleton in dynamic membrane blebs. *J. Cell Biol.* **218**, 445–454 (2019).

292. Guo, M. *et al.* Cell volume change through water efflux impacts cell stiffness and stem cell fate. *Proc. Natl. Acad. Sci. U. S. A.* **114**, E8618–E8627 (2017).

293. Platonova, A. *et al.* Role of cytoskeleton network in anisosmotic volume changes of intact and permeabilized A549 cells. *Biochim Biophys Acta* **1848**, 2337–2343 (2015).

294. Chen, Y.-T. *et al.* The ER Ca2+ sensor STIM1 regulates actomyosin contractility of migratory cells. *J. Cell Sci.* **126**, 1260–1267 (2013).

295. Jarm, T., Cemazar, M., Miklavcic, D. & Sersa, G. Antivascular effects of electrochemotherapy: implications in treatment of bleeding metastases. *Expert Rev Anticancer Ther* **10**, 729–746 (2010).

296. Chen, C. *et al.* Fluidization and resolidification of the human bladder smooth muscle cell in response to transient stretch. *PLoS One* **5**, 16–21 (2010).

297. Krishnan, R. *et al.* Fluidization, resolidification, and reorientation of the endothelial cell in response to slow tidal stretches. *Am. J. Physiol. - Cell Physiol.* **303**, 368–375 (2012).

298. Krishnan, R. *et al.* Reinforcement versus fluidization in cytoskeletal mechanoresponsiveness. *PLoS One* **4**, (2009).

299. Lan, B. *et al.* Transient stretch induces cytoskeletal fluidization through the severing action of cofilin. *Am J Physiol Lung Cell Mol Physiol* **314**, L799–L807 (2018).

300. Lee, S. L. *et al.* Physically-Induced Cytoskeleton Remodeling of Cells in Three-Dimensional Culture. *PLoS One* **7**, (2012).

301. Nekouzadeh, A., Pryse, K. M., Elson, E. L. & Genin, G. M. Stretch-activated force shedding, force recovery, and cytoskeletal remodeling in contractile fibroblasts. *J Biomech* **41**, 2964–2971 (2008).

302. Ruzgys, P., Jakutavičiūtė, M., Šatkauskienė, I., Čepurnienė, K. & Šatkauskas, S. Effect of electroporation medium conductivity on exogenous molecule transfer to cells in vitro. *Sci. Rep.* **9**, 1–10 (2019).

303. Demiryurek, Y. *et al.* Transport, resealing, and re-poration dynamics of two-pulse electroporation-mediated molecular delivery. *Biochim. Biophys. Acta - Biomembr.* **1848**, 1706–1714 (2015).

304. Stern, J. V., Gowrishankar, T. R., Smith, K. C. & Weaver, J. C. Broad pore lifetime distributions: A fundamental concept for cell electroporation. 1–7 (2017).